

UNCLASSIFIED

AD NUMBER

AD611257

CLASSIFICATION CHANGES

TO: UNCLASSIFIED

FROM: SECRET

LIMITATION CHANGES

TO:

Approved for public release; distribution is unlimited. Document partially illegible.

FROM:

Distribution authorized to U.S. Gov't. agencies and their contractors;
Administrative/Operational Use; DEC 1960. Other requests shall be referred to Defense Atomic Support Agency, Sandia Base, Albuquerque, NM.
Document partially illegible.

AUTHORITY

21 Jun 1961 DASA per document marking; 21 Jun 1961 DASA per document marking

THIS PAGE IS UNCLASSIFIED

AD611257

UNCLASSIFIED



WT-1403

This document consists of 134 pages.

No. 182 of 210 copies, Series A

OP

OPERATION

PLUMBBOB



NEVADA TEST SITE
MAY-OCTOBER 1957

TECHNICAL LIBRARY
of the
AUG 9 1961
DEFENSE ATOMIC
SUPPORT AGENCY

COPY 1 OF 1
HARD COPY \$ 4.00
MICROFICHE \$ 7.00

132p

Project 1.3

Classification (Cancelled) () to
By Authority of DASASC-3 Memo, dtd 21 Jun 61
By *Byeller* Date AUG 11 1961

UNCLASSIFIED

AIR-BLAST PHENOMENA in the
HIGH-PRESSURE REGION (U)

THIS REPORT HAS BEEN APPROVED FOR OPEN PUBLICATION.

Issuance Date: December 15, 1960

HEADQUARTERS FIELD COMMAND
DEFENSE ATOMIC SUPPORT AGENCY
SANDIA BASE, ALBUQUERQUE, NEW MEXICO

DDC
RECEIVED
MAR 1 1965
DDG E

FORMERLY RESTRICTED DATA

Handle as Restricted Data in foreign dissemination.
Section 144b, Atomic Energy Act of 1954.

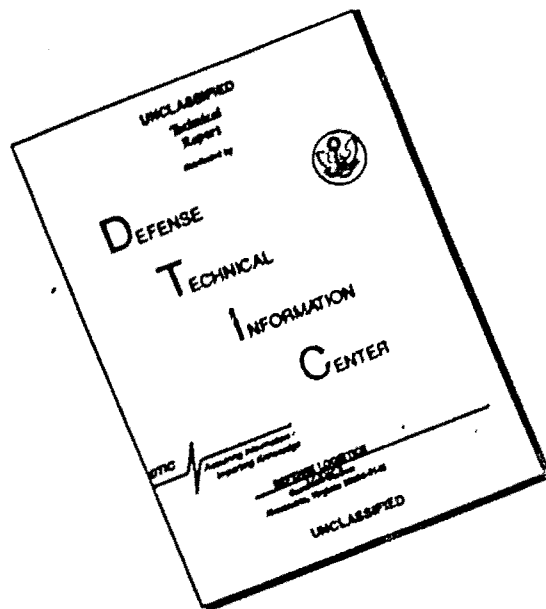
This material contains information affecting
the national defense of the United States
within the meaning of the espionage laws,
Title 18, U. S. C., Secs. 793 and 794, the
transmission or revelation of which in any
manner to an unauthorized person is pro-
hibited by law.

ARCHIVE COPY

UNCLASSIFIED

PROCESSING COPY

DISCLAIMER NOTICE



THIS DOCUMENT IS BEST QUALITY AVAILABLE. THE COPY FURNISHED TO DTIC CONTAINED A SIGNIFICANT NUMBER OF PAGES WHICH DO NOT REPRODUCE LEGIBLY.

Inquiries relative to this report may be made to

Chief, Defense Atomic Support Agency
Washington 25, D. C.

When no longer required, this document may be
destroyed in accordance with applicable security
regulations.

THIS REPORT HAS BEEN APPROVED FOR O. EN PUBLICATION.

DO NOT RETURN THIS DOCUMENT

**CLEARINGHOUSE FOR FEDERAL SCIENTIFIC AND TECHNICAL INFORMATION, CFSTI
INPUT SECTION 410.11**

**LIMITATIONS IN REPRODUCTION QUALITY OF TECHNICAL ABSTRACT BULLETIN
DOCUMENTS, DEFENSE DOCUMENTATION CENTER (DDC)**

AD 611257

- 1. AVAILABLE ONLY FOR REFERENCE USE AT DDC FIELD SERVICES.
COPY IS NOT AVAILABLE FOR PUBLIC SALE.
- 2. AVAILABLE COPY WILL NOT PERMIT FULLY LEGIBLE REPRODUCTION.
REPRODUCTION WILL BE MADE IF REQUESTED BY USERS OF DDC.
 - A. COPY IS AVAILABLE FOR PUBLIC SALE.
 - B. COPY IS NOT AVAILABLE FOR PUBLIC SALE.
- 3. LIMITED NUMBER OF COPIES CONTAINING COLOR OTHER THAN BLACK
AND WHITE ARE AVAILABLE UNTIL STOCK IS EXHAUSTED. REPRODUCTIONS
WILL BE MADE IN BLACK AND WHITE ONLY.

TSL-121-2/64

DATE PROCESSED: *3 mar 65*

PROCESSOR: *gabriel*

UNCLASSIFIED

~~SECRET~~

WT-1403

OPERATION PLUMBBOB—PROJECT 1.3

*AIR-BLAST PHENOMENA in the
HIGH-PRESSURE REGION (U)*

L. M. Swift, Project Officer
D. C. Sachs
A. R. Kriebel

Stanford Research Institute
Menlo Park, California

THIS REPORT HAS BEEN APPROVED FOR OPEN PUBLICATION.

FORMERLY RESTRICTED DATA

Handle as Restricted Data in foreign dissemination. Section 144b, Atomic Energy Act of 1954.

This material contains information affecting the national defense of the United States within the meaning of the espionage laws, Title 18, U.S.C., Secs. 793 and 794, the commission or revelation of which in any manner to an unauthorized person is prohibited by law.

UNCLASSIFIED

3

~~SECRET~~

FOREWORD

This report presents the final results of one of the 46 projects comprising the military-effects program of Operation Plumbbob, which included 24 test detonations at the Nevada Test Site in 1957.

For overall Plumbbob military-effects information, the reader is referred to the "Summary Report of the Director, DOD Test Group (Programs 1-9)," ITR-1445, which includes: (1) a description of each detonation, including yield, zero-point location and environment, type of device, ambient atmospheric conditions, etc.; (2) a discussion of project results; (3) a summary of the objectives and results of each project; and (4) a listing of project reports for the military-effects program.

ABSTRACT

Surface level and aboveground static overpressures, near-surface differential pressures (pitot-tube), and near-surface total pressures were measured on a low-burst-height nuclear explosion (Shot Priscilla) 700 feet, 36.6 kt). Gages were placed at ground ranges from 450 feet to 4,500 feet, with a concentration of measurements in the high-pressure region. Blast switches, which measured arrival time only, were placed at several ranges, the closest at 100-foot range. Usable records were obtained on 39 of the 47 electronic channels.

A precursor wave formed near 500-foot ground range, and dissipated between 2,000 and 2,500 feet. Shot Priscilla shock velocity agrees with the ideal except between 500- and 2,000-foot ranges where it exceeds the ideal. Computed preshock arrival surface temperatures are significantly higher than those computed for Shot 12, Operation Teapot.

At high pressures, overpressures agree well with those predicted over an ideal surface, although surface maxima are depressed below the ideal curve. Maximum precursor overpressures out to about 1,000 feet are approximately one tenth the peak overpressure and decrease with ground range at about the same rate as the peak overpressure.

Total-head pressures obtained in the Mach reflection region agree with the ideal until 850 feet. From 850 to 2,500 feet, peak total pressure is significantly higher than the ideal.

Maximum differential pitot-tube pressures are higher than predicted over an ideal surface. Maximum differential pressure is computed from total-head pressure and overpressure measurements. Maximum dynamic (air-plus-dust) pressure computed from Mach number and surface overpressure is lower than ideal at close-in stations, agrees with ideal at mid-ranges, and exceeds ideal at 2,500 feet and beyond.

Differential pressure wave-form classifications based on the degree of deviation from the corresponding overpressure wave form indicates that at close-in scaled ground ranges total-head pressure wave forms follow fairly closely those of the overpressure. The greatest deviations are concentrated between 450 and 900 feet scaled ground range and 100 and 300 feet scaled burst height.

Comparison of Hess' stagnation bubble theory with precursor phenomena suggests that this theory can be used to describe precursor formation.

PREFACE

The planning and execution of Project 1.3 were under the direction of Mr. L. M. Swift with Mr. W. M. Wells serving as field supervisor and Mr. L. H. Inman as field party chief. Other members of the field party included V. E. Krakow, C. M. Westbrook, R. V. Ohler, H. C. Wuner, R. E. Aumiller, and J. Milless. This report was written by Dr. D. C. Sachs. Data reduction, analysis, and report preparation were undertaken by Miss Barbara Ames, Miss Sherry Ward, Mrs. Barbara Wells, Mrs. Betty Hearns, and Miss Phyllis Flanders.

CONTENTS

FOREWORD	4
ABSTRACT	5
PREFACE	6
CHAPTER 1 INTRODUCTION	11
1.1 Objectives	11
1.2 Background	11
1.3 Pressure Phenomenology and Theory	12
1.3.1 Precursor Formation	12
1.3.2 Effects of Dust upon the Precursor	13
1.3.3 Effects of Dust upon Dynamic Pressure	13
1.3.4 Mach Number in Dust-Laden Air	16
CHAPTER 2 PROCEDURE	19
2.1 Predictions	19
2.1.1 Precursor Formation Criteria and Overpressure Wave Forms	19
2.1.2 Peak Overpressure	21
2.1.3 Peak Dynamic Pressure	22
2.2 Instrumentation	22
2.2.1 Central Station	22
2.2.2 Pressure Gages	25
2.2.3 Arrival Time Gage	29
2.2.4 Beam Devices	30
2.2.5 Gage Coding	31
2.2.6 Instrument Response	31
2.2.7 Calibration	31
2.3 Field Operations	32
CHAPTER 3 RESULTS	33
3.1 Instrument Performance	33
3.2 Data Reduction	33
3.2.1 General	33
3.2.2 Gage Corrections and Auxiliary Calculations	34
3.3 Gage Records	35
3.4 Wave Forms	35
3.5 Tables of Results	46
CHAPTER 4 DISCUSSION	50
4.1 Arrival-Time Data	50
4.1.1 Arrival Time and Shock Velocity	50
4.1.2 Wave-Front Orientation	52
4.2 Pressure Measurements	55
4.2.1 Overpressure	55

4.2.2 Total-Head Pressure - - - - -	61
4.2.3 Differential Pitot-Tube Pressure - - - - -	62
4.3 Mach Number and Computed Dynamic (Air-plus-Dust) Pressure (q^*) - - - - -	63
4.4 Precursor Phenomena - - - - -	66
4.4.1 Background - - - - -	72
4.4.2 Computed Preshock-Arrival Temperature - - - - -	73
4.4.3 Precursor Formation and Development - - - - -	74
4.4.4 Comparison with Hess' Theory - - - - -	77
4.4.5 Dynamic Pressure Wave Forms - - - - -	80
CHAPTER 5 CONCLUSIONS - - - - -	86
5.1 Instrument Performance - - - - -	86
5.2 Arrival Time and Shock Velocity - - - - -	86
5.3 Precursor Formation and Pressures - - - - -	87
5.4 Main-Wave Pressures and Wave Forms - - - - -	87
5.4.1 Overpressure - - - - -	87
5.4.2 Total-Head Pressure - - - - -	87
5.4.3 Dynamic Pressure - - - - -	87
CHAPTER 6 RECOMMENDATIONS - - - - -	88
APPENDIX A DEFINITIONS OF SYMBOLS IN CLEAN AND DIRTY SUBSONIC AND SUPERSONIC AIRBLAST FLOWS - - - - -	89
A.1 Clean Airblast Flows - - - - -	89
A.2 Dirty Airblast Flows - - - - -	89
APPENDIX B OVERPRESSURE WAVE-FORM CLASSIFICATION - - - - -	90
APPENDIX C DESIGN ANALYSIS OF TOTAL-PRESSURE PROBE - - - - -	92
APPENDIX D TEAPOT DATA REPROCESSED BY METHODS AGREED UPON BY PARTICIPANTS IN AFSWP- SPONSORED MEETING 12 and 13 AUGUST 1958 - - - - -	96
REFERENCES - - - - -	131
FIGURES	
1.1 Early stage of precursor flow - - - - -	13
1.2 Error in calculating Mach number after moving shock because of suspended dust ($m \approx n$) - - - - -	16
2.1 Initial precursor arrival times as function of height-of-burst - - - - -	20
2.2 Height-of-burst chart for surface-level overpressure wave forms, NTS desert surface - - - - -	21
2.3 Predicted maximum overpressure, Shot Priscilla - - - - -	23
2.4 Predicted maximum overpressure and limits of deviation, Shot Priscilla - - - - -	24
2.5 Predicted maximum dynamic pressure, Shot Priscilla - - - - -	25
2.6 Modified Sandia-Wiancko subsonic pitot-tube gage - - - - -	26
2.7 Stanford Research Institute - - - - -	27
2.8 Typical gage installation: ground baffle, total-head gage, and Sandia-Wiancko pitot-tube - - - - -	27
2.9 Close-up of total-head gage installed on tower - - - - -	27
2.10 Pressure gage layout - - - - -	28
2.11 Arrival time switch - - - - -	29
2.12 Arrival time switch mount - - - - -	29

2.13	Arrival time gage layout	30
2.14	Beam device	31
3.1	Surface-level overpressure versus time, Stations 1 to 8, Shot Priscilla	36
3.2	Surface-level overpressure versus time, Stations 9 to 12, Shot Priscilla	37
3.3	Overpressure versus time, 3- and 10-foot levels, Stations 8 and 9, Shot Priscilla	38
3.4	Overpressure versus time, 3- and 10-foot levels, Stations 10 to 12, Shot Priscilla	39
3.5	Total-head pressure versus time, 3-foot level, Stations 1 to 4, Shot Priscilla	40
3.6	Total-head pressure versus time, 3-foot level, Stations 5 to 7, Shot Priscilla	41
3.7	Total-head pressure versus time, 3-foot level, Stations 9 and 10, Shot Priscilla	42
3.8	Dynamic pressure versus time, 3- and 10-foot levels, Stations 6 to 8, Shot Priscilla	43
3.9	Dynamic pressure versus time, 3- and 10-foot levels, Stations 9 and 10, Shot Priscilla	44
3.10	Dynamic pressure versus time, 3- and 10-foot levels, Stations 11 and 12, Shot Priscilla	45
4.1	Arrival time, surface level, Shot Priscilla	51
4.2	Shock velocity, surface level, Shot Priscilla	53
4.3	Wave-front orientation, Shot Priscilla	54
4.4	Maximum overpressure, Shot Priscilla	56
4.5	Maximum overpressure, Upshot-Knothole Shot 10 and Shot Priscilla	57
4.6	Decay of overpressure behind shock front, Stations 1 to 5, Shot Priscilla	58
4.7	Decay of overpressure behind shock front, Stations 6 to 12, Shot Priscilla	59
4.8	Positive-phase duration versus overpressure, A-scaled, various shots	60
4.9	Positive impulse versus overpressure, A-scaled, various shots	61
4.10	Total-head pressure, 3-foot level, Shot Priscilla	62
4.11	Maximum differential pressure, Shot Priscilla	63
4.12	Mach number versus time, Stations 1 to 7, Shot Priscilla	65
4.13	Mach number versus time, Stations 8 and 9, Shot Priscilla	67
4.14	Mach number versus time, Stations 10 to 12, Shot Priscilla	68
4.15	Dynamic pressure (q^*) versus time, Stations 10 to 12, Shot Priscilla	69
4.16	Dynamic pressure (q^*) versus time, Stations 7 and 8, Shot Priscilla	70
4.17	Dynamic pressure (q^*) versus time, Stations 9 to 12, Shot Priscilla	71
4.18	Calculated dynamic pressure (q^*), Shot Priscilla	72
4.19	Computed preshock arrival temperature versus arrival time, Teapot Shot 12 and Plumbbob Shot Priscilla	76
4.20	Arrival time versus slant range, A-scaled, Shot Priscilla	76
4.21	Arrival time versus slant range, A-scaled, Buster-Charlie, Tumbler 4, Upshot-Knothole 10	77
4.22	Comparison of Hess' theory and field results, Upshot-Knothole 10 and Teapot Shot 12	78

4.23 Precursor length versus ground range -----	80
4.24 Comparison of Hess' theory and field results, various shots -----	81
4.25 Dynamic-pressure wave forms, various shots -----	82
C.1 Total-pressure probe design -----	93
C.2 Particle velocity ratio versus distance -----	94
C.3 Error versus pressure ratio -----	94

TABLES

2.1 Surface Constants for Various NTS Surfaces -----	20
2.2 Predicted Surface-Level Overpressure Wave Forms at Selected Ground Ranges, Shot Priscilla -----	21
2.3 Project 1.3 Gage Layout -----	28
3.1 Overpressure, Shot Priscilla -----	47
3.2 Total-Head Pressure, Shot Priscilla -----	48
3.3 Dynamic Pressure, Shot Priscilla -----	48
4.1 Blast Switches, Shot Priscilla -----	51
4.2 Shock-Front Velocity, Surface Level, Shot Priscilla -----	52
4.3 Wave-Front Orientation Data, Shot Priscilla -----	53
4.4 Calculated Mach Number and Dynamic Pressure, Shot Priscilla -----	64
4.5 Computed Preshock Temperatures, Shot Priscilla -----	75
4.6 Predicted and Measured Wave Forms, Shot Priscilla -----	75
4.7 Bubble Stagnation Versus Ground Range, Various Shots -----	79
4.8 Dynamic Pressure Wave-Forms, Various Shots -----	83
D.1 Overpressure, Shot 12, Desert Line -----	97
D.2 Overpressure, Shot 12, Water Line -----	98
D.3 Overpressure, Shot 12, Asphalt Line -----	99
D.4 Overpressure, Shot 6, Asphalt Line -----	100
D.5 Overpressure, Shot 6, Desert Line -----	100
D.6 Dynamic Pressure, Shot 12, Desert Line -----	101
D.7 Dynamic Pressure, Shot 12, Water Line -----	102
D.8 Dynamic Pressure, Shot 12, Asphalt Line -----	103
D.9 Dynamic Pressure, Shot 6, Desert Line -----	104
D.10 Dynamic Pressure, Shot 6, Asphalt Line -----	104
D.11 Calculated Mach Number and Dynamic Pressure, Shot 12, Desert Line -----	105
D.12 Calculated Mach Number and Dynamic Pressure, Shot 12, Asphalt Line -----	106
D.13 Calculated Mach Number and Dynamic Pressure, Shot 6, Desert Line -----	107
D.14 Calculated Mach Number and Dynamic Pressure, Shot 6, Asphalt Line -----	107
D.15 Calculated Mach Number and Dynamic Pressure, Shot 12, Water Line -----	108

~~SECRET~~

~~SECRET~~

Chapter 1

INTRODUCTION

1.1 OBJECTIVES

The basic objective was to obtain data on the variation with time and ground range of over-pressure and dynamic pressure resulting from a nuclear explosion. Particular emphasis was on phenomena in the regions of high pressure (above 50 psi) and disturbed (non-classic) blast waves. A secondary objective was to provide detailed data on blast arrival time versus ground (or slant) range, especially at close-in ground ranges.

The experiment was designed to provide data and subsequent analyses to serve three purposes: (1) to extend the range of predictions of nuclear air-blast effects to include higher pressure ranges; (2) to provide data for correlation with other shots; and (3) to provide input data for other projects concerned with both aboveground and underground phenomena.

1.2 BACKGROUND

Pressure studies similar to this project have formed a part of practically all nuclear military-effects tests. From the results of such projects have come generalized prediction techniques for military applications and for operations planning. Cumulative data taken in regions of low pressure (less than 10 psi) and normal blast waves are satisfactorily precise for any known purpose; information is lacking, however, in regions of high pressures (greater than 50 psi) and nonideal wave forms.

Beginning with Operations Buster-Jangle (Reference 1) and Tumbler-Snapper (Reference 2), it became obvious that for weapons in the 20-kt range at moderate heights of burst, serious disturbances occur in wave forms and peak pressures at pressure levels above 8 to 10 psi. Because of higher-than-normal propagation velocities of these disturbed waves, these phenomena were denoted by the general term of precursor.

Results of Program 1 studies of precursor phenomenology on Operations Upshot-Knothole (Reference 3) and Teapot (Reference 4), and results of other tests permit reasonably accurate prediction of precursor phenomena over a limited range of yields. Limited information is available on peak pressures and wave forms at pressures above 100 psi because of high incidence of damage to conventional structures and gage towers subjected to very high pressures. Operation Teapot experience indicated, however, that gage mounts and towers could be designed to withstand blast-wave inputs where overpressures were in excess of 250 psi which meant that pressure measurements could be taken in regions of very-high pressures with greater probability of success than hitherto possible.

It has recently been required that consideration be given to construction of both aboveground and underground structures more resistant to blast than have been previously considered feasible for overall planning. It has become necessary, therefore, to provide structural planners with predictions of free-field loads to be expected in very-high pressure regions, including peak values, wave forms, and duration in time and space. This project was designed to help fulfill these needs.

~~SECRET~~

~~FORMERLY RESTRICTED DATA~~

1.3 PRESSURE PHENOMENOLOGY AND THEORY

Rigorous mathematical analyses have been made (References 5, 6, and 7) which describe adequately spherical shock-wave phenomena from a nuclear explosion in free air. However, perturbations introduced by the surface, when it is exposed to intense thermal radiation before and during the blast wave, and particularly when the surface is dust-producing, often make direct application of these analyses impossible.

1.3.1 Precursor Formation. Many mechanisms of precursor formation have been postulated; however, none has fully explained all of the observed phenomena. Most of these postulates are based on the assumed existence of a relatively thick thermal layer near the surface prior to blast-wave arrival, caused by the fireball impinging on the surface. It has been difficult to explain how this thermal layer is formed in the time before blast arrival; attempts to measure pre-shock air temperature near the ground surface have been inconclusive.

It appears now that there may be an alternative explanation for the close-in precursor region, i. e., the region of Types 1 and 2 surface-level overpressure wave forms (see Appendix B and Reference 4). Theoretical considerations suggest that a thermal disturbance is formed when a threshold, determined by the rate of heat transfer from the ground to the medium, is passed. According to the inverse square law for thermal radiation and the time dependency of radiant flux, this threshold is not exceeded at all points simultaneously; normally the time will be a function of ground range. Hence the disturbance will have an apparent propagation velocity which at some points may be extremely high.

At greater ground ranges this threshold is not exceeded, but by this time the disturbance (precursor) has far outrun the main blast wave, raising behind it a thick thermal layer caused by convective transfer of thermal energy from the surface (and surface dust) to the medium. Here, the mechanism may revert to distortion of the main pressure wave as observed photographically in full- and model-scale tests.

The stage of this mechanism at a given ground range controls the rise time and wave form at that range. Pressure-time wave forms observed at various ground ranges on a precursor-forming shot, such as Teapot Shot 12 (Reference 4), show a relatively orderly development of various types of wave form throughout the precursor region, eventually developing into an essentially classic wave form at distant ground ranges. The appearance of these wave forms implies that no distortion would be expected at very-short ground ranges; and, in fact, some pressure-versus-time records which are essentially classic have been obtained in close-in regions. If this is true, it may be expected that very-high dynamic pressures (with respect to ideal pressures) observed in the precursor zone do not exist at very-close ground ranges and that here the flow conditions, in general, approach those of the ideal case. These close-in effects importantly affect the predictions of loading and damage in the high-pressure regions.

As stated previously, one of the obvious characteristics of the precursor wave form is its abnormally high propagation velocity. Arrival times, obtained by photographic methods, are available on many shots on which pressure-time data are not available. Arrival-time data from a large number of shots fired at the Nevada Test Site have been analyzed in conjunction with wave form data (see Section 2.1). There is definite evidence from this analysis that it is possible to predict the ground range for precursor formation and the types of overpressure wave form to be expected for a wide range of heights of burst and yield. The same analysis can be extended to describe the shot geometry required for precursor formation.

The emphasis given in this study to prediction of precursor formation and characteristics is engendered not only by the necessity for reasonably accurate prediction of overpressure and dynamic pressure but also by the importance of the pressure-time wave form in the establishment of damage criteria. This is true for aboveground and underground structures.

The subsurface accelerations produced by passage of a blast wave over the surface are affected significantly by the wave form and the rise time of the blast wave. Some knowledge of this wave form is therefore necessary to predict underground effects on structural elements or on experiments where acceleration forces are important.

1.3.2 Effects of Dust upon the Precursor. Field tests of atomic weapons consistently indicate that precursors are accompanied by flows of dust clouds moving behind the precursor wave front. Time-sequence photographs of precursor waves indicate that typical flow patterns during early development can be represented as shown in Figure 1.1. The oblique shock generated from the leading edge of the visible dust cloud indicates that the flow of air is at least partially diverted

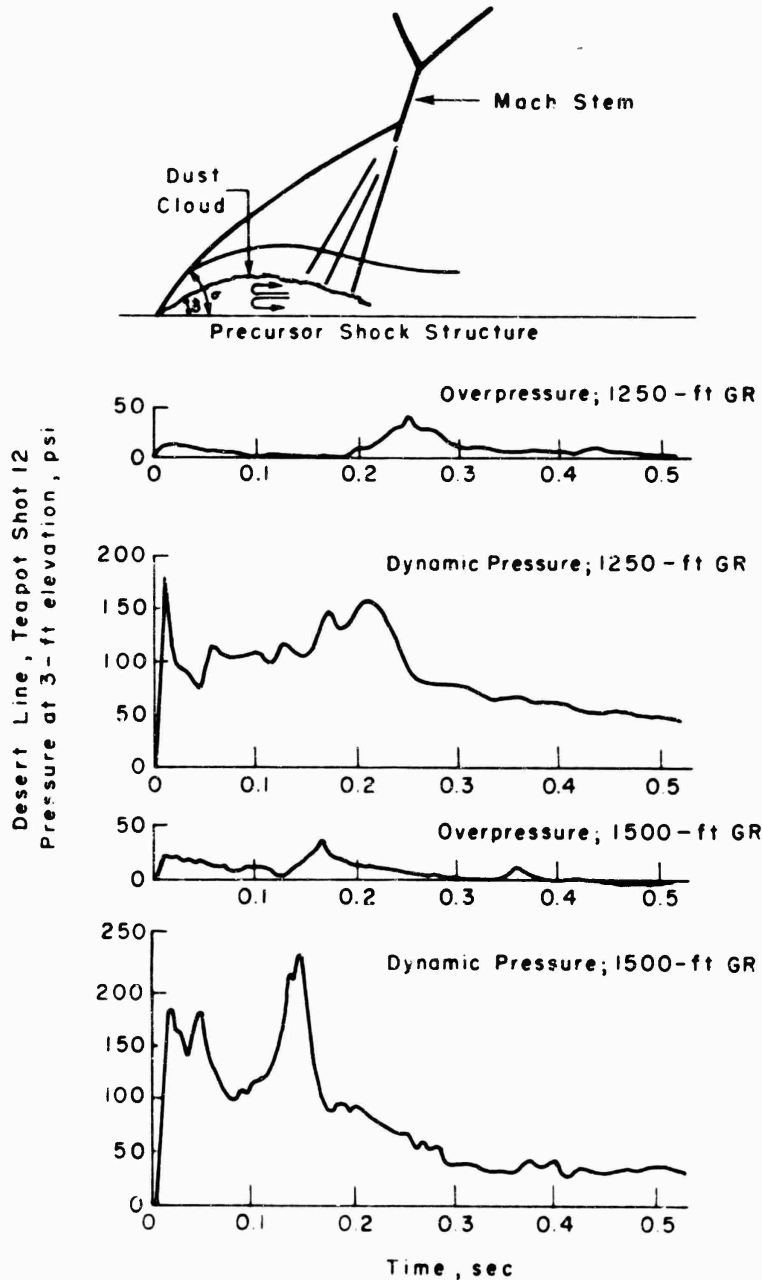


Figure 1.1 Early stage of precursor flow.

over the dust cloud. An analysis of precursor-type flows caused by a layer of air which is pre-heated by thermal radiation before shock arrival indicates that under certain conditions the layer cannot be a throughgoing layer but must be accumulated into a bubble under the Mach stem as shown in Figure 1.1 (Reference 8).

With addition of heat to a compressible flow the total pressure must decrease, and the total or stagnation density must decrease even more (Reference 9). The requirement for bubble formation is that the total pressure of the heated layer must be less than the down-stream pressure of the external flow. Therefore, the process of bubble formation described in Reference 8 can be enhanced by the raising of dust within the bubble leading to rapid absorption of thermal radia-

tion, even though the heat is added after shock arrival. It may be that only a small part of the heat absorbed by the dust is absorbed after it is raised into the air. Possibly the predominant mechanism for heating the bubble is a thin layer of dust, heated to a very high temperature on the ground prior to shock arrival, raised and mixed into the bubble.

The presence of dust in the bubble shown in Figure 1.1 is certain to affect the shape of the bubble and therefore the flow over it. Since the dust which is raised into the bubble has an initial relative velocity, the circulation within the bubble (discussed in Reference 8) is affected by the initial momentum of the dust. The addition of dust increases the density of the mixture and therefore effects changes in internal pressure gradients and bubble shape. Intense thermal radiation on the dust-laden bubble may significantly increase its temperature, decrease the density, and thereby alter the shape and size of the bubble. This is indicated by the air density measurements obtained at Teapot (Reference 10), which increased after the arrival of the first shock, then decreased to values lower than ambient upon arrival of the dust cloud.

It is probable that the addition of dust greatly enhances the development of a bubble-type precursor. In fact, dust may be necessary for the existence of this type of precursor if preheating of the air (see Reference 1) is not sufficient. It is not known whether most of the dust is raised by the initial formation of the bubble and carried out to greater ground ranges, or if there is a steady flow of dust into the front of the bubble. If the second condition exists, precursor development over surfaces which are uniformly dusty should be more complete than over surfaces which are dusty in patches. For the first condition, only the surface near ground zero needs to be dusty for this effect to be important in precursor development.

In any description of dust effects, whenever the dust may be considered to be in velocity and temperature equilibrium with the air, only the ratio of dust to air density influences the flow, i. e., the flow is independent of particle size. Particle size is of importance, however, when equilibrium does not exist; drag and heat transfer coefficients for particles depend upon their size during the flow around objects. Furthermore, it can be shown (Reference 11) that for flow of a mixture of gas and particles which can be considered to be in velocity and temperature equilibrium, the mixture may be treated as a gas, so that

$$R' = \frac{R}{1 + m} \quad (1.1)$$

where R' is the effective gas constant of the mixture, R is the gas phase constant, and m is the ratio of mass flow of particles to the mass flow of gas. Also,

$$K' = \frac{K(n + 1)}{nK + 1} \quad (1.2)$$

where K' is the ratio of the specific heats of the mixture, K is the ratio of specific heats of the gas phase, and n is m times the ratio of specific heat of particles to specific heat of the gas phase, both at constant pressure.

1.3.3 Effects of Dust upon Dynamic Pressure. Rankine-Hugoniot equations describing the relationships between overpressure and dynamic pressure hold true in regions of classical shock-wave behavior, at least immediately behind the shock front. However, in the precursor region measured dynamic pressures are usually much higher than would be calculated from measured overpressure and Rankine-Hugoniot relations; and no fixed quantitative relationships between these two pressures have been established. Even a cursory examination of measured dynamic pressure versus time in the precursor region shows rapid variations of dynamic pressure not associated with similar variations of overpressure. It is not known whether the high dynamic pressure and the variations between overpressure and dynamic pressure result from excessive particle velocity or from increased density caused by suspended dust, but it is probable that both contribute. This contention is supported by the results at Teapot (Reference 10). At present there appears to be no method of distinguishing between the effects of velocity variation and dust variation, and consequently no method of calculation of either function from test data. Efforts at independent measurement of these parameters, using the beta densitometer and cen-

tripetal density gages, have been almost completely unsuccessful. In any case, it is concluded that the influence of suspended particulate matter and/or increased particle velocity are closely tied to the design of the measuring instrument employed.

Although it is clear that dust cannot be raised from the ground by aerodynamic forces without alteration of the flow of air, increments in measured values of dynamic pressure which are charged to dust effects have been attributed to increased density alone with the implied assumption that air flow is unaffected by the raising of the dust.

That this assumption can be misleading is illustrated by an interesting example. If a shock in air travels down a tube with velocity

$$V_S = 3KRT_1 \quad (1.3)$$

the normal shock equations yield

$$\frac{\Delta p}{P_0} = 2.3$$

$$\frac{q}{P_0} = 1.5$$

However, for the same value of V_S : if a layer of dust on the floor of the tube is raised by the shock and becomes uniformly mixed and in equilibrium with the air downstream of the shock; if the final mass flow of dust is one half the flow of air; and if the specific heat of the dust is equal to that of air; then (using equations from Reference 11)

$$\frac{\Delta p}{P_0} = 4.5$$

$$\frac{q}{P_0} = 3.6$$

These figures indicate that a 50 percent increase in density due to dust causes a greater increase in dynamic pressure than in overpressure behind a shock because of the effect upon the flow of air.

Dynamic pressure is usually determined by measuring the difference between total and static pressure. When an appreciable amount of dust is suspended in a flow of gas, the value of total pressure which is measured depends upon the shape and size of the probe and the shape and size of the dust particles. This is due to the fact that the particles are not in velocity equilibrium with the gas in the vicinity of the probe. As the probe size increases and the particle size decreases, the particles follow the gas-flow pattern more closely. For the limiting case (and for low Mach number), the large probe senses a total pressure,

$$P_t = P_s + \frac{1}{2} \rho_g V^2 + \frac{1}{2} \rho_p V^2 \quad (1.4)$$

where ρ_g is the gas density and ρ_p is the mass of particles divided by volume of mixture. As the probe size decreases and the particle size increases the particle trajectories become closer to straight lines in the vicinity of the probe, with less deviation due to air drag. In the limit, the small probe senses a total pressure,

$$P_t = P_s + \frac{1}{2} \rho_g V^2 \quad (1.5)$$

near the inlet of the total pressure tube, and

$$P_t = P_s + \frac{1}{2} \rho_g V^2 + \rho_p V^2 \quad (1.6)$$

far downstream of the inlet.

The effect of suspended particles upon static pressure is found by kinetic theory to be

$$\Delta p = \frac{\text{no. of particles}}{\text{volume}} \bar{RT} \quad (1.7)$$

Since the number of suspended particles is much less than the number of gas molecules, suspended dust contributes negligibly to static pressure. However, the static pressure (along

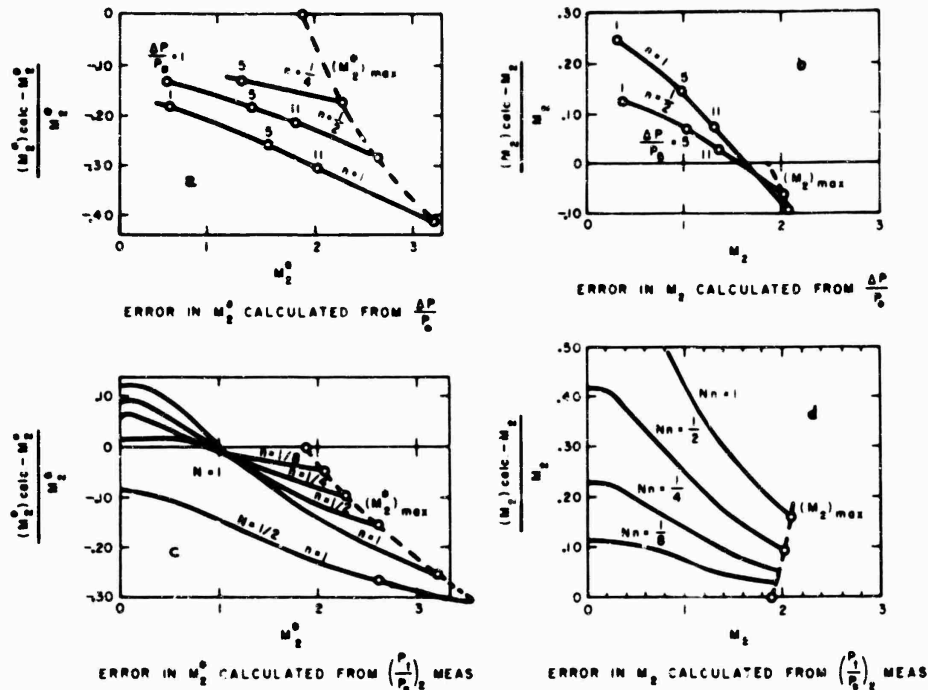


Figure 1.2 Error in calculating Mach number after moving shock because of suspended dust ($m \approx n$).

with all other gas properties) can be changed appreciably as the particles are ingested into the flow and before they attain velocity and temperature equilibrium with the gas.

1.3.4 Mach Number in Dust-Laden Air. In analysis of pressure effects from nuclear explosions, it is desirable to determine the afterflow Mach number (the ratio of the flow velocity to the local velocity of sound) as a function of time and space. Information on Mach number is necessary for (1) purposes of gage compressibility correction, and (2) the determination of the drag coefficients of various targets or target shapes.

Using pressure measurements which may be obtained in the field, there are four ways to determine M_2 , the afterflow Mach number; they are:

1. To measure $\left(\frac{P_t}{P_s}\right)$ in the afterflow = $f_1(M_2)$
(i. e., total pressure method)
2. To measure $\left(\frac{\Delta p}{P_0}\right) = f_2(M_2)$
(i. e., overpressure method)
3. To measure $\left(\frac{P_t}{P_0}\right) = f_3(M_2)$
4. To measure shock velocity from arrival times = $f_4(M_2)$.

Since there is a large error in calculation of M_2 by Method 3, and since there is not sufficiently detailed arrival-time data from previous shots for use of Method 4, only the first two methods will be discussed. Each of the two methods cited is affected by suspended dust in a different

manner. Also, there are two alternate definitions of M_2 based upon the speed of sound in clear air (M_2) or the speed of sound in the mixture (M_2^*) as shown by Appendix E, Reference 11.

Since the free-stream conditions are affected by suspended dust, both methods must consider these effects. The mixture is in equilibrium approximately 1 foot or 1 msec after shock arrival; outside this region the mixture may be considered to be a new medium with the ratio of specific heats, gas constant, and speed of sound (Reference 11) determined by only two parameters,

$$m = \frac{\rho_d}{\rho_a} \text{ and } n = \frac{\rho_d c_p (\text{dust})}{\rho_a c_p (\text{air})} \quad (1.8)$$

In addition, the total pressure method is affected by the fact that a gage correction for dust must be applied to measured P_t (References 10 and 12). The correction depends upon particle shape and size and upon gage shape and size. In addition to the dynamic pressure of the air the probe senses $N\rho_d V^2$, where N is the dust registry coefficient, and $0 \leq N \leq 1$.

The relationships of M_2 and M_2^* to the total pressure in the afterflow are (Reference 11):

$$M_2^2 = \frac{V_2^2}{KRT_2} = \frac{2}{(K-1)} \left[\left(\frac{P_t}{P_s} \right)_2 \frac{K-1}{K} - 1 \right] \quad (1.9)$$

$$M_2^{*2} = \frac{(mK+1)V_2^2}{KRT_2} = \frac{2(mK+1)}{K-1} \left[\left(\frac{P_t}{P_s} \right)_2 \frac{K-1}{K(m+1)} - 1 \right] \quad (1.10)$$

where

$$\left(\frac{P_t}{P_s} \right)_2 = \left(\frac{P_{t2}}{P_{s2}} \right)^* - NmKM_2^2 \quad (1.11a)$$

$$= \frac{P_{t2}}{P_{s2}} - \frac{NmK}{mK+1} (M_2^*)^2 \quad (1.11b)$$

The starred quantities refer to measurements in the presence of dust.

The Mach numbers may also be related to the overpressure across the shock.

$$M_2^2 = \frac{mK+1}{(m+1)^2 K^2 \left(1 + \frac{P_0}{\Delta p} \right) \left(\frac{K-1}{K(m+1)} + \frac{P_0}{\Delta p} \right)} \quad (1.12)$$

$$(M_2^*)^2 = \frac{(mK+1)^2}{(m+1)^2 K^2 \left(1 + \frac{P_0}{\Delta p} \right) \left(\frac{K-1}{K(m+1)} + \frac{P_0}{\Delta p} \right)} \quad (1.13)$$

In Equations 1.9 to 1.13 the specific heat of the dust has been assumed to be equal to the specific heat (at constant pressure) of air, i.e., $m = n$.

A comparison of errors in calculating M_2 and M_2^* by the total pressure and overpressure methods is indicated in Figure 1.2. In each case M_2 (calculated) results from arbitrarily setting $M = 0$ in Equations 1.9 to 1.13. The Mach correction on P_t is neglected, which affects this error analysis only if $M > 1$ and then only slightly. The plots shown in Figures 1.2b and 1.2d using M_2 (calculated) rather than M_2^* (calculated) seem to be superior from an error standpoint.

Other reasons for using M_2 rather than M_2^* are that:

1. Near an obstacle the real Mach number is less than M_2^* and greater than M_2 because the dust is not in velocity equilibrium with the air; therefore, using M_2 avoids over-correcting for Mach number.

2. Physically, M_2 is the Mach number in the afterflow if the dust were removed. Any response other than that caused by M_2 should be attributed to the dust directly and not considered to be a Mach correction; this additional response depends upon the size and shape of the particles and the obstacle, which are not flow properties.

It should be pointed out that the total-pressure method requires measurement (or knowledge) of two quantities (P_{t2} , P_{s2}) and possibly a third quantity (angle, depending on probe used), whereas the overpressure method requires only one measurement, Δp , and no corrections. However, in regions of thermal layers, bubble formation, and supersonic flows, the total-pressure method is more generally valid.

The conclusion is that the best compromise for Mach number calculation is to calculate M_2 (not M_2^*) by the total-pressure method, that is, using Equation 1.9.

Chapter 2 PROCEDURE

In planning an experiment of this type it is necessary that peak values be predicted with reasonable accuracy so that suitable gage settings may be selected. It is also necessary to determine expected frequency components of importance so that proper choice of instrumentation may be made. Even more important in this project was the prediction of air-blast phenomena to formulate pretest predictions of underground phenomena to be measured by others (Projects 1.4, 1.5, and Program 3). In these measurements, the expected wave forms and rise times greatly affect the magnitude of some of the underground phenomena.

For early planning for Shot Priscilla, essentially empirical extrapolations of scaled Teapot Shot 12 and Upshot-Knothole Shot 10 data were prepared. These peak values were used in the selection of ground ranges for gage stations for this and other projects. Although some of the shot parameters were changed after these ground ranges were selected, only minor modifications to the experiment plan were necessary.

2.1 PREDICTIONS

2.1.1 Precursor Formation Criteria and Overpressure Wave Forms. Peak pressure and wave-form predictions were based on the prediction of both the ground range of precursor formation and its various stages of development. The criterion for precursor formation was derived from an empirical analysis of precursor arrival times developed in the interpretation of results of Operation Teapot. The analytical procedures leading to correlation of arrival time and wave-form data are presented in Reference 4; results of that investigation may be summarized as follows:

Arrival times of the precursor wave during its early stages of development obey the empirical equation

$$t_i = C_S H^{1/2} R^{3/2} \quad (2.1)$$

where t_i is the A-scaled¹ arrival time in seconds, H the A-scaled height-of-burst in feet, R the A-scaled slant range in feet, and C_S a constant depending on the type of surface (Table 2.1). Equation 2.1 is consistent with data on nine precursor-producing shots as shown in Figure 2.1.

Using the constants of Table 2.1, correlation of arrival time data was achieved in the precursor region, provided the surface-level overpressure wave form was Type 4 (see Appendix B and Reference 4) or less. When wave form was plotted as a parameter in this correlation, Type 1 wave forms extend to a scaled slant range corresponding to

$$R = 2.8 \times 10^{-3} \quad (2.2)$$

Other wave form classifications overlap on an A-scaled slant-range basis and hence correspond to a different scaling criterion.

For a particular surface and scaled height-of-burst, the range at which the precursor forms may be found from the intersection of the t_i curve, Equation 2.1, and the ideal arrival-time curve. Using the Frenchman Flat constants and the shot conditions for Priscilla, the ground range for precursor formation was predicted to be 600 to 650 feet.

¹A-scaling is the use of $W^{1/3}$ scaling to normalize all values to 1 kt at sea level.

The extent of the Type 1 wave-form region may be determined from Equation 2.2. Since both Equations 2.1 and 2.2, and the ideal arrival curve are functions of A-scaled height-of-burst and slant range, a height-of-burst chart may be constructed for precursor formation and the extent of the Type 1 wave-form region. Figure 2.2 shows the results of these calculations for an aver-

TABLE 2.1 SURFACE CONSTANTS FOR VARIOUS NTS SURFACES

Surface	C_S , A-scaled ft-sec
Frenchman Flat area	6.10×10^{-7}
Yucca Area	5.85×10^{-7}
Asphalt, Teapot Shot 12	5.42×10^{-7}
Asphalt, Teapot Shot 6	5.17×10^{-7}

age Nevada Test Site (NTS) desert surface, i.e., the average of Frenchman Flat and Yucca areas. Although the surface-constant analysis yields a distinct difference between these two areas, this difference is small; and for the purpose of consolidating wave-form material, the average surface constant was used. Also shown in Figure 2.2 are wave-form data from 14 shots over NTS

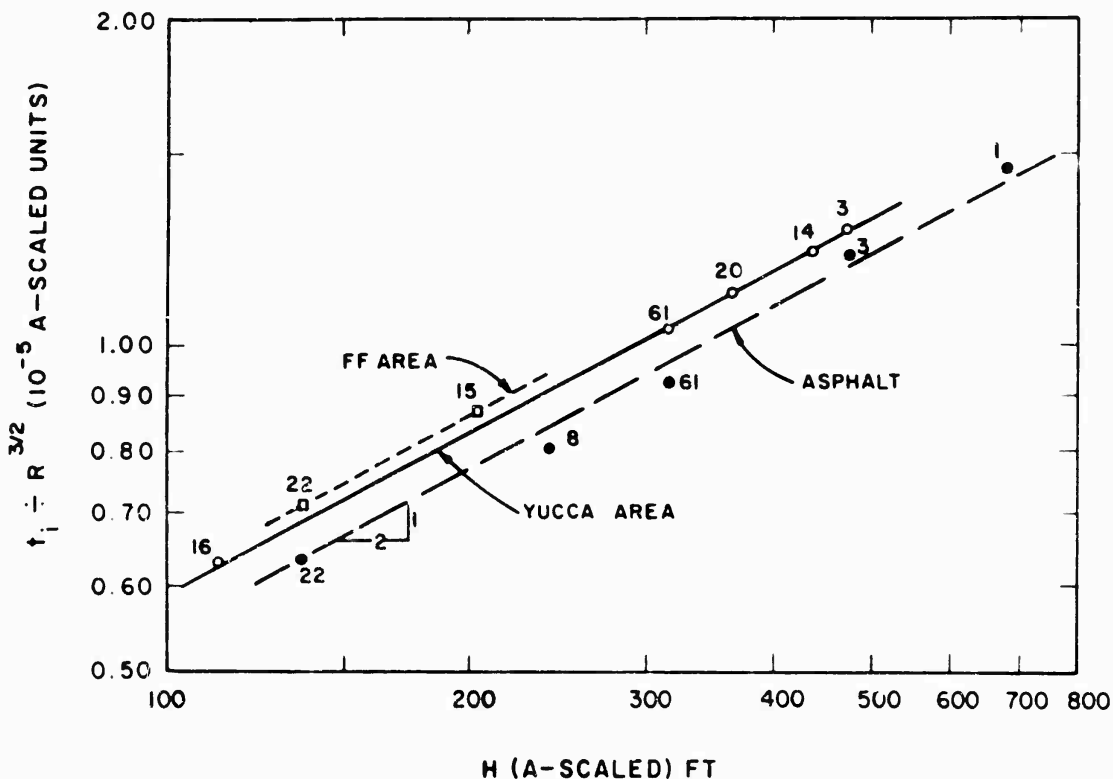


Figure 2.1 Initial precursor arrival times as function of height of burst.

desert surfaces. Underlined numbers indicate wave-form types derived from Ballistic Research Laboratory (BRL) mechanical gage results during Operation Teapot (Reference 5). Observations of Type 1 wave forms are in agreement with the computed region; wave forms of higher order, when viewed in toto, fall into definable regions on the height-of-burst chart.

The Type 1+ and Type 2- are shadings of the parent wave forms (see Appendix B). Type 1+ indicates a first peak only slightly less than the second, and Type 2- indicates peaks of equal magnitudes. Parentheses indicate some doubt about wave-form type either due to possible gage malfunction or to similarity between some wave-form types.

In Figures 2.1 and 2.2 shot yields, to the nearest kt, are indicated at their corresponding height-of-burst. The almost random order of yields demonstrates the nondependency on yield per se; that is, yield dependence comes about only through A-scaling.

Figure 2.2 forms the basis of wave-form prediction. Table 2.2 gives predicted surface-level overpressure wave forms for Priscilla preshot A-scaled height-of-burst (197 feet).

TABLE 2.2 PREDICTED SURFACE-LEVEL OVERPRESSURE WAVE FORMS AT SELECTED GROUND RANGES, SHOT PRISCILLA

Ground Range ft	Wave Form
450	0
550	0
650	1
1,650	1
2,000	1+ or 2-
2,500	3
3,000	4 or 5
3,500	6
4,500	7 or 8

2.1.2 Peak Overpressure. From the standpoint of A-scaled burst height, Priscilla is close to Upshot-Knothole Shot 10 (202 feet A-scaled), although the yield of the latter detonation was only about 15 kt. The predicted peak overpressure curve presented in Figure 2.3 is based largely upon data from the Upshot-Knothole Shot 10 and Teapot Shot 12. From ground zero to

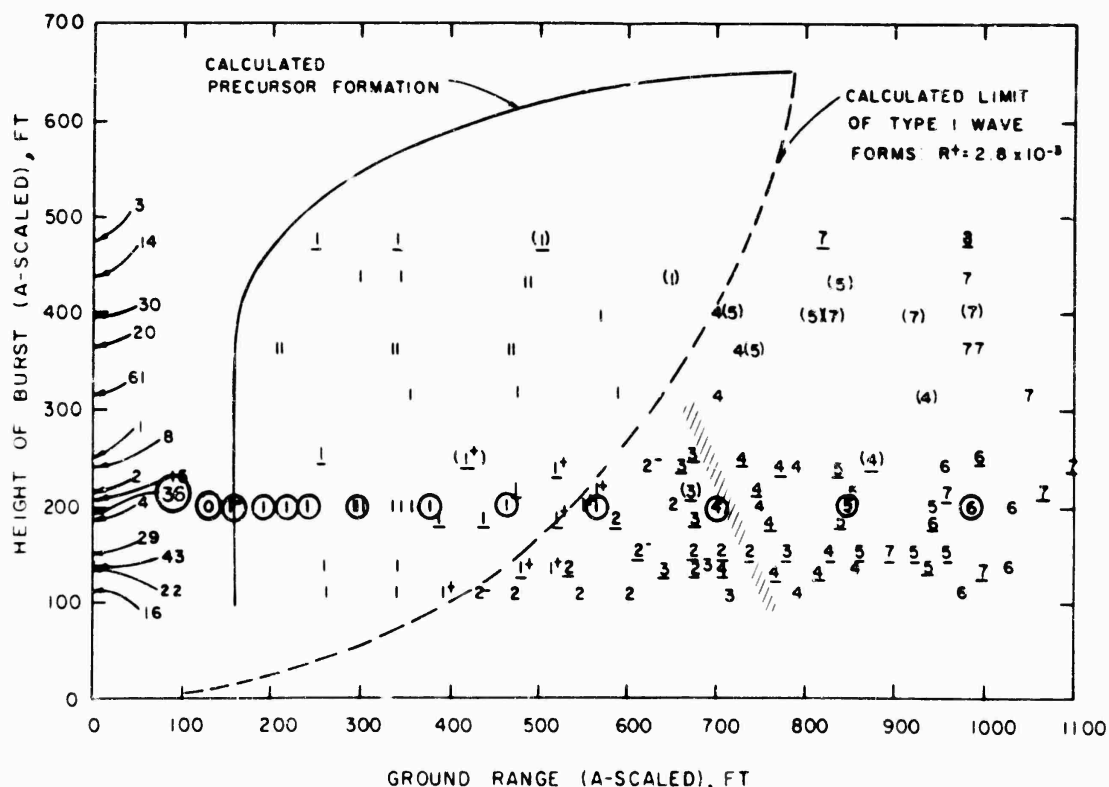


Figure 2.2 Height-of-burst chart for surface-level overpressure wave forms, NTS desert surface (Priscilla wave forms circled).

the beginning of the precursor (600- to 650-foot ground range), the prediction was computed from the standard free-air data and ideal reflection factors. It should be noted that ideal Mach stem formation occurs at about 600 feet also; however, it was likely that for this high yield, a thermal Mach would form at a smaller range. From 150 to 30 psi, composite Upshot-Knothole

10 data points were used; but, to account for yield dependence, the curve was depressed about 10 percent in this region. From 30 to 8 psi, an average curve through the Teapot 12 (desert) and Upshot-Knothole 10 data was used. Also, ideal peak overpressures were used from 8 to 1 psi.

To make the predictions more useful to other projects, it was suggested that approximate deviation limits be assigned to the curve. These limits, based upon the magnitude of the scatter of available data, are shown in Figure 2.4.

2.1.3 Peak Dynamic Pressure. For predictions of peak dynamic pressure, it was decided that in the region of regular reflection (less than 600-foot ground range) the pressure would be based upon ideal behavior of shock wave as shown in Figure 2.5. In the Mach reflection region, use was made of the ratios of measured-to-ideal peak dynamic pressure observed on Teapot 12 (desert). These ratios, coupled with the ideal curve for Priscilla, gave the prediction of Figure 2.5 beyond 600 feet. In the region of Mach stem formation, data from Operation Redwing (Reference 13) indicate that measured values should "fair" into the ideal curve; however, the prediction curve was not changed in this region. Referring to Figure 2.5, it is necessary to point out that peak dynamic pressures predicted there correspond to measurements obtained using the conventional blunt-nosed (Sandia) pitot-static tube and correcting the measurement for Mach number and pitch angle based upon Cornell data (Reference 14). Finally, it must be recognized that although the total-head gage of new design was used at ground range stations closer than 1,000 feet, the equivalence of the new SRI gage and the Sandia pitot-tube gage was not established prior to the test.

2.2 INSTRUMENTATION

2.2.1 Central Station. All channels of instrumentation were essentially identical to those used on previous operations (Reference 3). Wiancko balanced variable-reluctance pressure transducers or Ultradyne variable-reluctance pressure transducers were connected through modified Wiancko equipment to William J. Miller Corporation oscillograph recorders. Provisions were included for applying automatically a synthetic calibrating signal to each channel immediately prior to zero time for purposes of comparison of the final deflection on the record with the deflection produced by the same signal at the time of calibration. A highly accurate timing signal of 100 and 1,000 cps was also applied to all recorders simultaneously from a single source, having a time accuracy of better than 10 parts per million. This provided means for accurate time correlation of events on separate records.

The prime power supply for all instruments during the shots was a bank of storage batteries. Suitable converters were used to produce 115 volts for those components requiring this power source. An individual converter was used for each rectifier power supply, thus minimizing the probability of gross failure due to converter failure.

Forty-seven gage channels were connected, of which twelve were connected to dual recording systems consisting of one galvanometer on each of two recorders. These dual channels were assigned to minimize loss of data due to any single recorder failure. On five of these twelve channels, one of the galvanometers had a natural frequency of 300 cps. The channels incorporating one 200-cps galvanometer were used on gages where the uncertainty of the predicted peak was greatest and where the expected signal would not be degraded appreciably by the reduced frequency response of the lower-frequency galvanometer. Since there was an appreciable difference in the sensitivity of the two galvanometers thus used on a single channel, a wider range of input signals could be accommodated without loss of data.

Instruments were powered at given times before zero time by Edgerton, Germeshausen, and Grier (EG&G) relay circuits, with lock-in relays controlled by a time-delay relay, allowing continued operation for approximately one minute after zero time even though EG&G relays dropped out sooner. Utmost attention was paid to circuitry and procedures to insure maximum reliability of operation. Dual relay contacts or dual relays were used wherever feasible. A

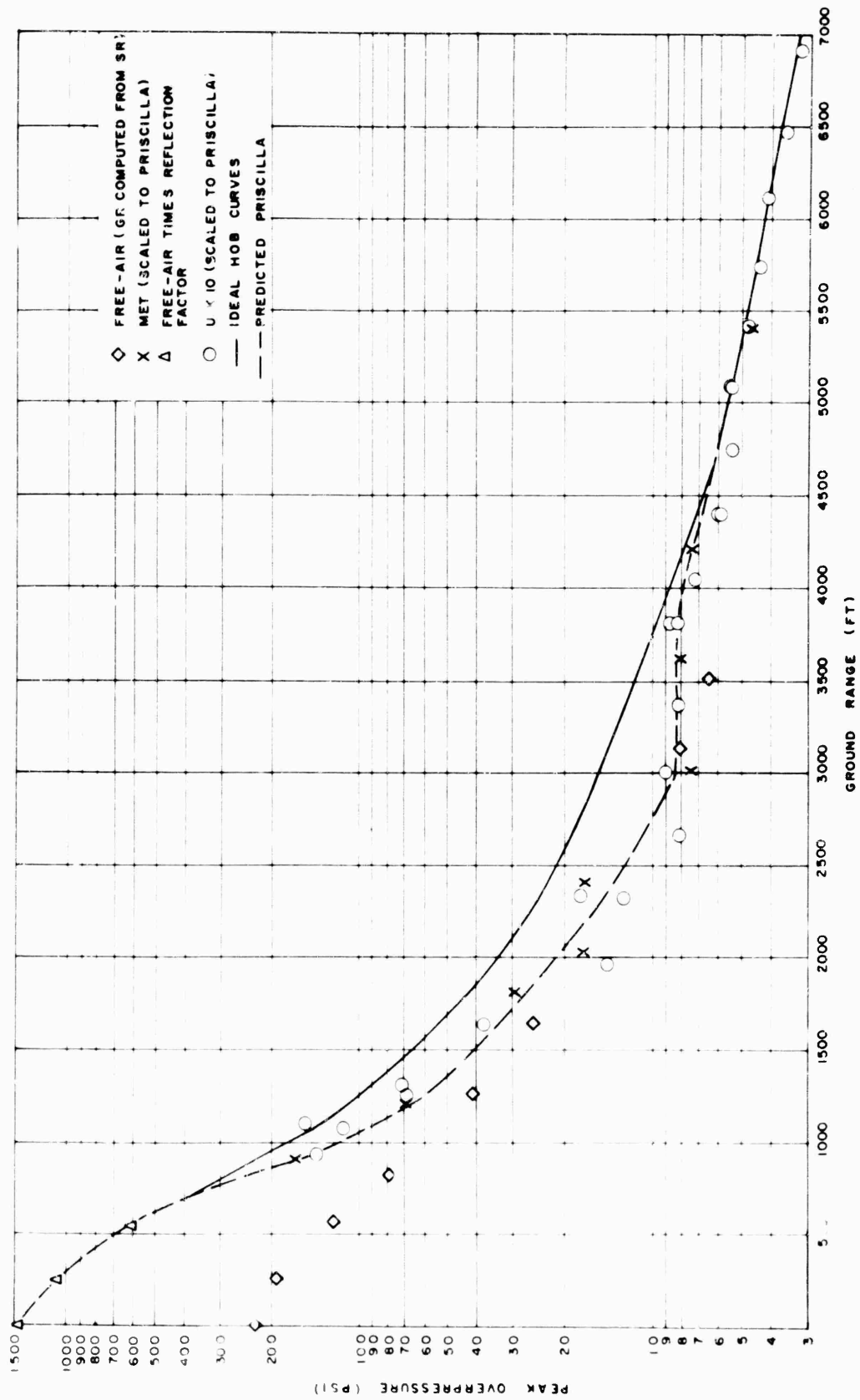


Figure 2.3 Predicted maximum overpressure, Shot Priscilla.

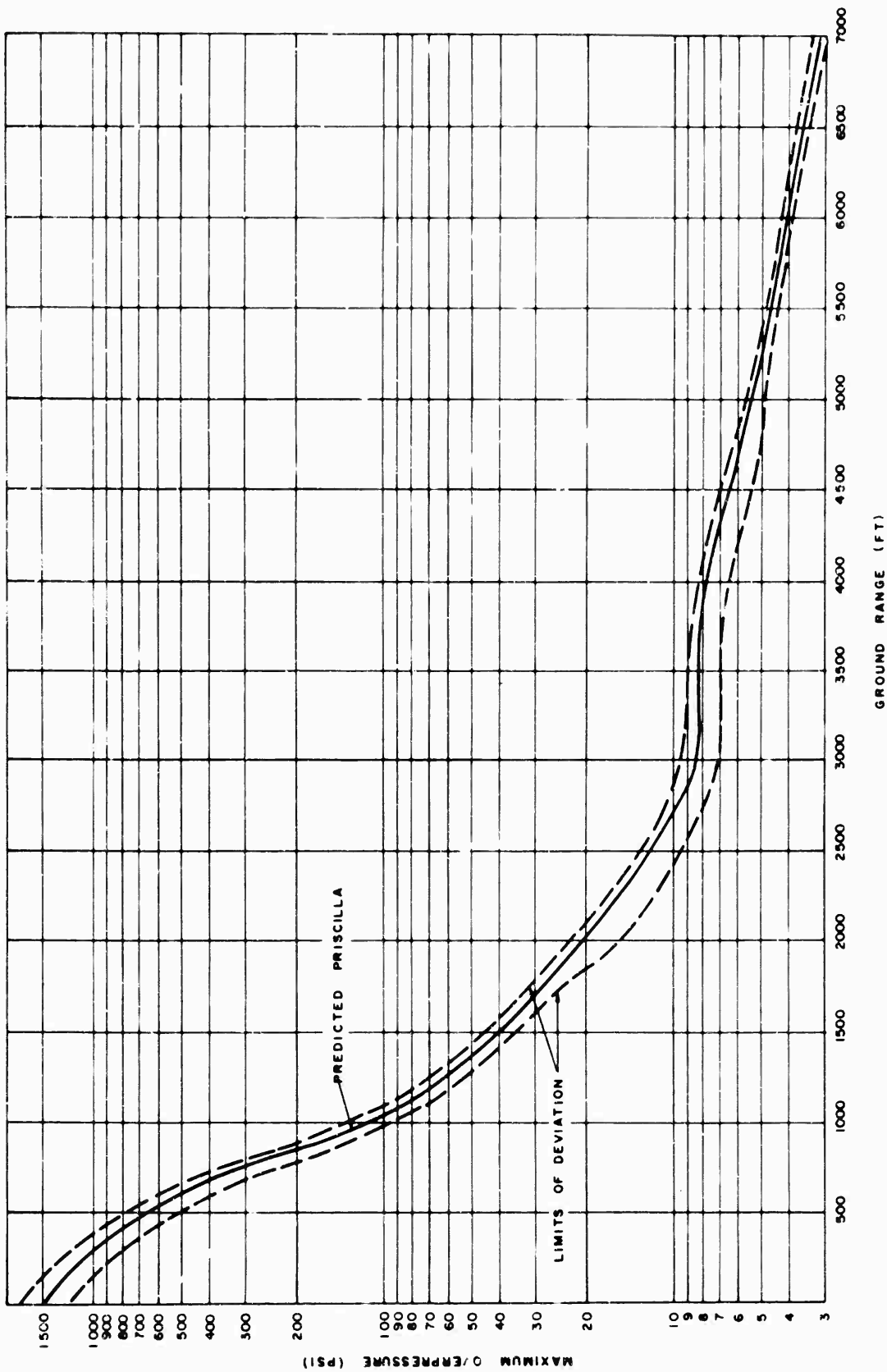


Figure 2.4 Predicted maximum overpressure and limits of deviation, Shot Priscilla.

multipen recorder was connected to provide a record of operating time and sequence of various elements so that any failure might be traced to its source in a posttest study.

To minimize possible damage from heavy transient currents flowing at zero time (the induction signal or electromagnetic pulse) the signal circuit of each gage channel was grounded during zero time. A number of multicontact relays were used with one contact connected between each signal lead and ground. Circuits were arranged so that these relays were energized at approximately -5 seconds and were de-energized after a short delay by the signals from an EG&G blue

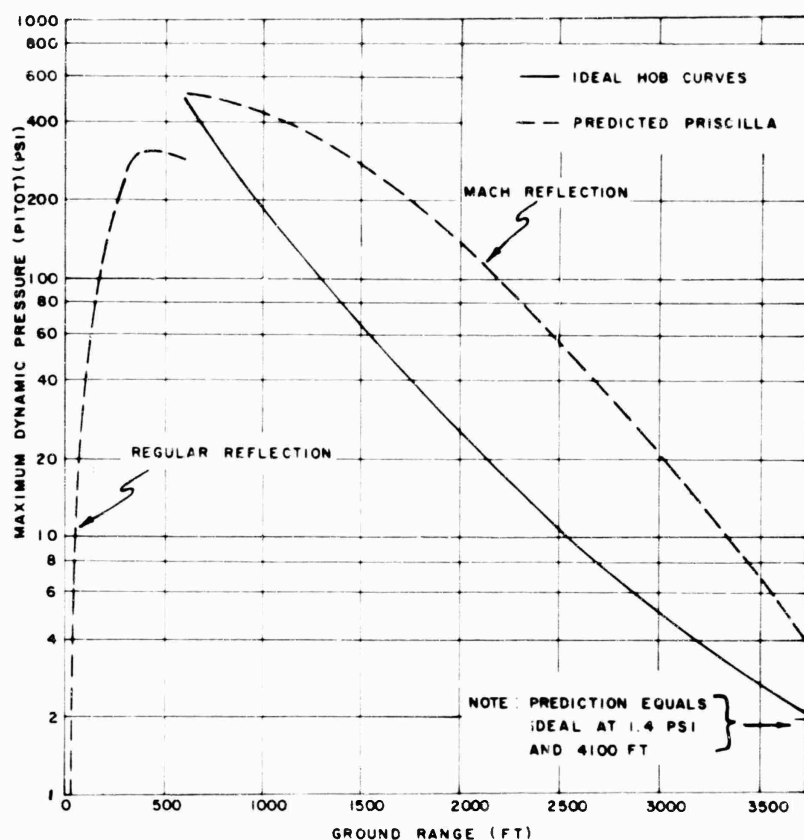


Figure 2.5 Predicted maximum dynamic pressure, Shot Priscilla.

box mounted above the shelter. The blue-box signal results from the detection of the bomb light by a photocell. This protection system was used successfully on Operations Upshot-Knothole and Teapot.

The recording shelter, F-223, housed all central station equipment used for this project as well as for Projects 1.4, 3.5, and 1.7.1. The recording shelter was buried to a depth sufficient to reduce the integrated radiation dosage within the shelter to below 10 r. This radiation level had been chosen to represent that which would preclude fogging of the Type 809 recording paper; for more information on radiation fogging, see Reference 15.

2.2.2 Pressure Gages. Blast Gage. At pressure levels below approximately 200 psi, Wiancko pressure gages mounted at the center of a 17-inch-diameter cast aluminum baffle were used to measure surface-level overpressure. This baffle was cemented flush with the earth's surface and was held in place with a buried anchor. At high pressure levels, a gage similar in principle but different in construction to the Wiancko, manufactured by Ultradyn Manufacturing Company of Albuquerque, New Mexico, was mounted in a 9-inch heavy steel baffle set flush with the surface of a concrete abutment.

Subsonic Pitot-Tube Gage. The pitot-tube gages for measurement of aboveground overpressure and dynamic pressure were a modified form of the Sandia-Wiancko pitot-tube gage used on Operation Teapot (Reference 2). On that operation some of the gages failed to operate satisfactorily during the latter part of the positive phase because dust entered the gage mecha-

nism itself and, in some cases, was carried into the gaps between the armature and the coil forms. For Operation Plumbbob, the gage design was changed to provide more indirect entry to the gage cavity itself and to allow use of a more effective filter to remove the dust collection (Figure 2.6). This increased the fill time of the gage cavity but did not appreciably affect the overall response time of the differential gage system since that is primarily determined by the difference in fill time of the two cavities. The pressure entry into the second gage used for overpressure was not modified.

The pitot-tube gages were mounted identically to those used on Operation Teapot (Reference 4), since this mount had proved satisfactory on that operation.

Supersonic Total-Head Gage. The Sandia-Wiancko pitot-tube gage described above was designed primarily for use in flows less than Mach 1. The hemispherical shape of the nose

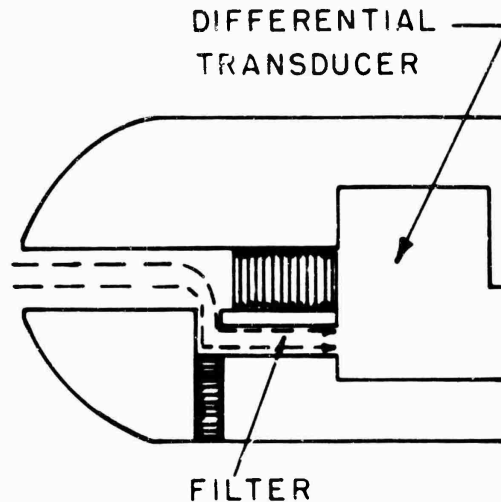


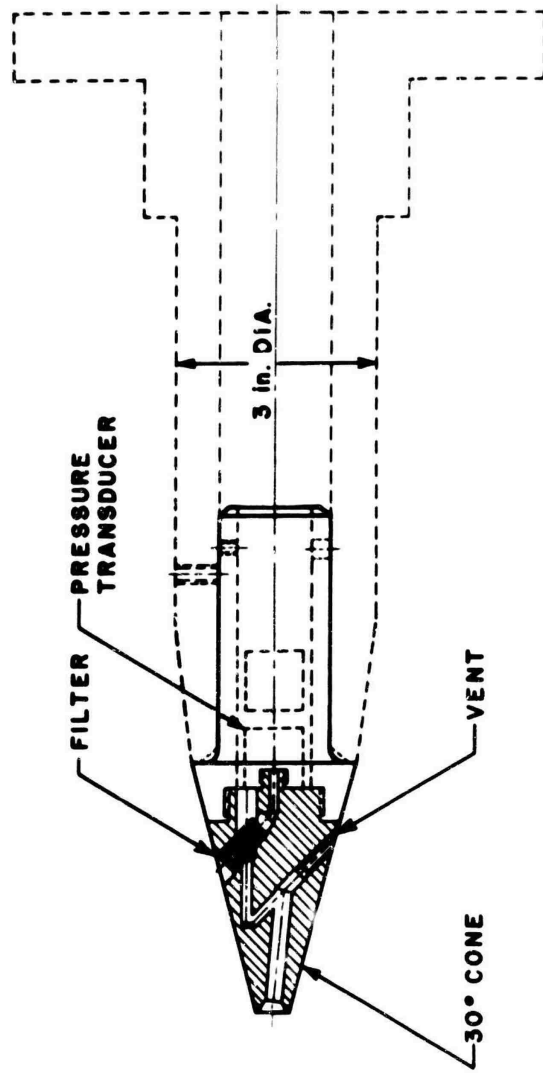
Figure 2.6 Modified Sandia-Wiancko subsonic pitot-tube gage.

of this gage and the location of the side entry ports caused the correction for Mach number to become large at Mach numbers above approximately 0.9. Wind-tunnel calibrations are available up to this Mach number (Reference 14), but use of this gage in higher Mach flows required extrapolation of the correction curve and resulted in serious probable errors in the reduced data. In addition, the hemispherical nose caused the pitch or yaw corrections to be large, particularly for Mach numbers approaching unity.

In the original planning of this experiment, a new gage was designed for use in the supersonic region. The basis of this design is described in Appendix C. The final form of this gage is shown in Figure 2.7. This gage is designed to measure total-head pressure only, with dynamic pressure derived during data reduction by subtraction of the overpressure measured nearby. The decision to measure total-head pressure was made because use of side ports on supersonic pitot-tube gages requires a very long space between side ports and the nose of the gage which would lead to instruments mechanically too weak to withstand the loads expected in the high-pressure region. Elimination of the side ports permitted use of shorter mountings with resultant improved ruggedness. Since the design of the gage provided a high degree of resistance to pitch or yaw angle effects, no separate pitch gages were required.

The towers supporting these and other aboveground gages were designed by the Program 1 staff, Field Command, AFSWP. They were essentially extrapolations of the designs originally made for similar towers on Operation Teapot where no tower failures were experienced. Typical gage installations on towers are shown in Figures 2.8 and 2.9.

Pressure Gage Layout. The gage layout (Figure 2.10 and Table 2.3) was designed to cover the regions of interest as thoroughly as possible and to make use of existing gage towers wherever possible. The blast line followed the desert line of the Frenchman Flat area used for several previous shots (Upshot-Knothole 9 and 10, and Teapot 12), and ground zero was at the same location as for these shots.



SRI TOTAL PRESSURE GAUGE

Figure 2.7 Stanford Research Institute supersonic total-head gage.



Figure 2.9 Close-up of total-head gage installed on tower.



Figure 2.8 Typical gage installation: ground baffle, total-head gage, and Sandia-Wiancko pitot-tube.

TABLE 2.3 PROJECT 1.3 GAGE LAYOUT

Station Number	Ground Range ft	Gage Code*	Predicted Peak psi	Galvanometer Frequency cps
0		OB	1,500	300
1	450'	1B	750	300
		1Z3	1,320	300, 300
2	550'	2B	600	300
		2Z3	1,150	300, 200
3	650'	3B	450	300
		3Z3	1,450	300
4	750'	4B	320	300
		4Z3	1,240	300, 200
5	850'	5B	200	300
		5Z3	1,000	300, 200
6	1,050'	6B	100	300
		6Z3	730	300, 300
		6Q3	630	300
7	1,350'	7B	50	300
		7Z3	465	300, 300
		7Q3	415	300
8	1,650'	8B	33	300
		8P3	33	300
		8Q3	270	300
		8P10	33	300
		8Q10	270	300, 300
9	2,000'	9B	21	300
		9Z3	175	300
		9P3	21	300
		9Q3	155	300
		9P10	21	300
		9Q10	155	300, 300
10	2,500'	10B	12.5	300
		10Z3	71	300
11	3,000'	10P3	12.5	300
		10Q3	56	300
		10P10	12.5	300
		10Q10	56	300, 300
		10F3	—	300
12	3,500'	11B	8.4	300
		11P3	8.4	300
		11Q3	21	300
		11P10	8.4	300
		11Q10	21	300, 300
13	4,500'	12B	8.3	300
		12P3	8.3	300
		12Q3	7	300
		12P10	8.3	300
		12Q10	7	300, 300
13	4,500'	13B	6.5	300

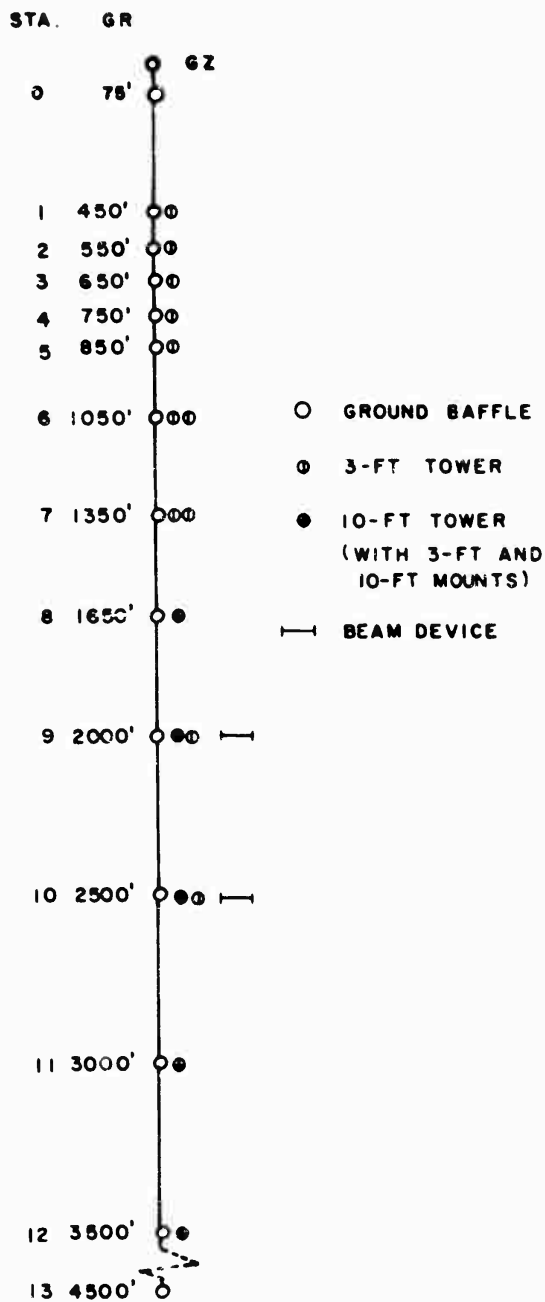


Figure 2.10 Pressure gage layout.

* Station number, gage type, and gage height. B = surface-level, baffle-mounted pressure gage; P = side-on (overpressure) component, pitot-tube; Q = subsonic pitot-tube, dynamic pressure, and Z = supersonic total-pressure gage.

Station locations were chosen on the basis of early predictions of peak overpressures and to correspond to pressure levels of interest to other projects. At ground ranges beyond 2,000 feet, station locations were chosen to utilize existing towers.

Surface-level air pressure was measured at all stations including a station near ground zero. Total stagnation pressure (dynamic pressure plus overpressure) was measured with the supersonic total-head gage mounted at 3-foot height at all ground ranges between 450 and 1,350 feet and, for correlating purposes, at 2,000 and 2,500 feet. Dynamic pressure and overpressure at 3- and 10-foot heights were measured by the standard pitot-tube gage at all ground ranges between 1,650 and 3,500 feet and, for correlation purposes, at 3-foot heights at 1,050- and 1,350-foot ground range. The overlap between the two methods of measurement of dynamic pressure was introduced to obtain direct evidence of their correlation.

2.2.3 Arrival Time Gage. Blast switches with a high degree of accuracy in recording arrival times were included on this project for extension of arrival-time data normally available from pressure-time records.

The arrival time switches consisted of a one-inch hollow cube of brass sheet, with a thin glass plate (microscope slide cover) forming one side of the cube (Figure 2.11). This plate was

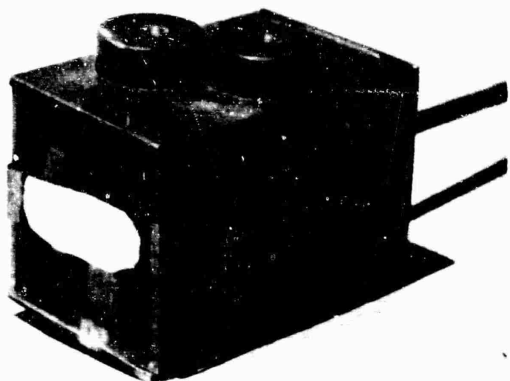


Figure 2.11 Arrival time switch.



Figure 2.12 Arrival time switch mount.

supported on two opposite edges by the brass box, the other two edges having a minimum of clearance but no support. A strip of conducting paint was applied to the inner surface of the glass plate and was contacted by two light spring contacts insulated from the box. Tests showed that the glass would break and open the circuit within 50 μ sec or less when subjected to a blast wave of over two or three psi. Precautions were taken both in the design and installation of the switches to avoid re-closure of the circuit after it was opened by the breaking of the glass. Pull-out connectors were used at the switches themselves, and at the point where the cable left the surface of the ground, on aboveground switches.

The switches were mounted with the glass plate on a side of the box at right angles to the line to ground zero to minimize thermal effects (Figure 2.12). All portions of the switch and exposed wiring were covered with aluminum foil for the same purpose. At stations where there was an instrument tower, aboveground switches were clamped to the pitot-tube gage. Where no fixed tower was available, aboveground gages were mounted on light wooden towers arranged so that the switch projected about three feet forward from the base and so that the "toe" of the sloping wave-front would not move the mount before the front arrived at the aboveground switch. No effort was made to protect the switches or mounts from the blast wave — the majority of them were expected to be destroyed after they operated.

Twenty-six of these switches, with suitable resistors in series with each, were connected in two parallel groups of thirteen each to a single three-conductor cable to form a balanced half-bridge circuit. The bridge was supplied by a bank of 24-volt storage batteries. The physical layout was designed to connect successive switches on opposite sides of the line, so that in op-

eration, the bridge would be unbalanced successively in alternate directions. Two such groups of 26 gages were installed.

The pulses produced by the successive operation of the switches were recorded on a magnetic recorder running at 60 in/sec, along with a 10-kc timing signal on a third channel. The system:

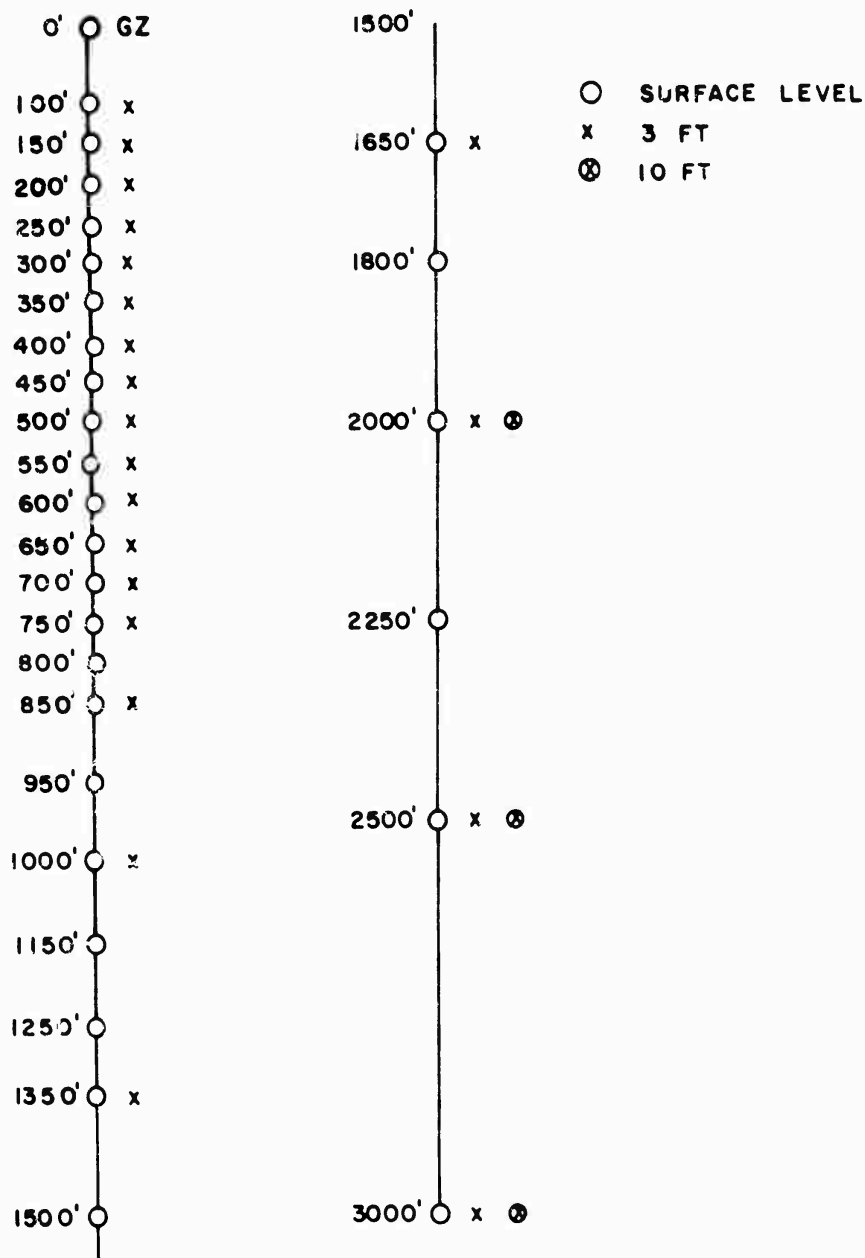


Figure 2.13 Arrival time gage layout.

was designed for playback of the record at 15 in/sec onto an oscillograph recorder running at 100 in/sec, for optimum time resolution.

The line on which these gages were located is coincident with the other blast line and is shown separately (Figure 2.13) for convenience only.

2.2.4 Beam Devices. The two beam devices, at 2,000- and 2,500-foot ground range, whose loadings were recorded on Channels 9F3 and 10F3, were those which were installed on Operation Teapot, Project 3.2 (Reference 4). The Teapot experiment was repeated to obtain better records than were recorded before, particularly in the later part of the trace. It was hoped that more accurate data would be obtained by providing foil shielding for the gages so that sensitive elements

of the transducer and its mount would not be heated by reflected thermal radiation after zero time. Figure 2.14 shows a general view of one of these structures.

2.2.5 Gage Coding. To identify channels and recorded traces with their proper gages, a coding system was adopted. Station numbers were assigned to each ground range on each blast line. These numbers were used as a first part of the gage code. The second part of the gage code was a letter indicating the type of measurement. In this project, B was used for air-blast overpressure measured by conventional surface-level baffle-mounted gages; P for air-blast overpressure measured as the side-on component of the pitot-tube gage; Q for measured dynamic pressures with the subsonic pitot-tube gages; and Z for total pressure measured by the supersonic total-head gage. A third part of the gage code, where necessary, indicated the height of a gage above the surface in feet. Typical gage code numbers then would be: 8B, a blast gage at

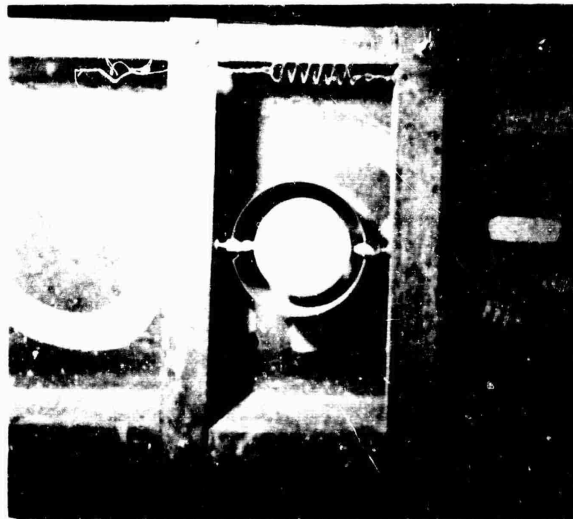


Figure 2.14 Beam device.

Station 8, surface level; 9Q10, a dynamic (differential) pressure gage at Station 9, 10-foot height, and so forth.

2.2.6 Instrument Response. Response time of the pressure-gage recording system was determined by the characteristics of the recording galvanometers. The (nominal) 300-cps galvanometers had an actual undamped natural frequency of from 200 to 230 cps and were similarly damped, giving a nominal rise time of approximately 1.8 msec. Since the rise time of the Wiancko and Ultradyn transducer, when properly adjusted, is appreciably smaller than either of these figures, the transducer frequency response does not enter into the characteristics of the final records.

The Wiancko gage system is basically flat down to steady-state conditions. To avoid drift due to temperature changes, or to changes in ambient pressure, the lower-range gages, however, are provided with a "bleed plug" in the gage casing. Thus, any pressure difference between the inside and outside of the case is equalized over a period of several seconds. The time constant of this bleed plug is adjusted to a minimum of 30 seconds so that it will have no effect on the recording of a blast wave of normal duration. As a consequence, the low-frequency response of the gage system may be considered as completely flat.

Response time of the arrival-time blast switch system is not yet proven completely, but it is believed that a time resolution of 25 μ sec can be obtained. This resolution time permits final reduction of data to a degree of precision not attainable by methods used in the past.

2.2.7 Calibration. Each pressure gage was calibrated in the field by the application of several values of static pressure after the gage had been installed in its final location and connected to its

associated equipment. After the shot, a postshot calibration was performed on all possible gages to check stability of the system.

In the calibration procedure several pressures, ranging from zero to well above the expected peak, were applied to the gage in sequence. For each pressure the galvanometer deflection was noted and recorded. In addition, the deflection caused by an artificial signal injected into the gage circuit was recorded. From the former deflection, a calibration curve of deflection versus pressure was constructed; the latter deflection served to correct for any changes of sensitivity in the recording system between the calibration and the final tests, since an identical signal was injected on the final record about 10 seconds before zero time.

2.3 FIELD OPERATIONS

Field operations were concurrent with and were performed by the same personnel as those for Projects 1.4, 3.5, and the instrumentation phase of 1.7. A common recording shelter was used, and the data channels were intermingled; common cable trenches were used in most cases.

The field crew arrived at NTS approximately 2 months before the scheduled shot date. The severe general flood of the Frenchman Flat area flooded the excavations made for the gage tower placement; these holes had to be redug.

The recording shelter was ready for occupancy on April 26 and equipment was installed in approximately one week. Cable trenching, which took about 2 weeks, was late in completion; this made it necessary to carry out field calibration of gages in piecemeal fashion. It is not certain whether this procedure had any effect on the accuracy of the calibrations, but it is certainly not optimum.

With calibration and gage placement completed, the instrument shelter was "buttoned-up" during the late evening of D-1 day. The shot, originally scheduled for June 15, was fired on June 24, 1957.

Chapter 3

RESULTS

3.1 INSTRUMENT PERFORMANCE

Of the 47 normal electronic recording channels installed on this shot, 39 channels produced usable records, although 5 of them were incomplete due to cable breaks during the positive phase. In addition, the records from the force gages on the Teapot 3.2 beam devices produced records so large that the significant portions of the records were off the paper and lost.

Of the 8 channels producing no records, 6 were lost due to failure of one oscillograph recorder to pull paper throughout the run. This machine ran for about 10 seconds (until -5 seconds) before the recording paper tore and jammed. One gage was apparently destroyed by the induction signal. Another gage (9Z3) gave no response, for undetermined reasons.

The 2 channels of arrival-time gages, consisting of a total of 52 gage circuits, developed too much noise to be read on the directly recorded traces, although some useful data can be obtained from playback of the magnetic tape records.

Mechanically, there was no shock or blast damage to any central station equipment, and the only gage tower used on this project which showed blast damage was that at 2,500 feet, a guyed 40-foot tower. This tower was bent at a point approximately 20 feet from the ground but not broken. The 10-foot tower at 1,650 feet, which had been moved intact, showed that the foundation had moved slightly in the loose backfill. At the 3-foot towers at 450, 550, and 650 feet (the closest towers to ground zero), the soil covering the cable entrance to the tower foundation was scooped away by the blast exposing the cables at this point, even though the loose soil piled on the foundation to cover arrival-time cables was still in place. This appears to have been the source of at least some of the cable breaks. It emphasizes the necessity for precautions in cable installations in high-pressure regions.

3.2 DATA REDUCTION

3.2.1 General. After each gage record was identified on the oscillograph, it was "read" (inches of deflection of the trace versus time) with an electromechanical reader, Benson-Lehner Oscar Model J. The reader output was fed into an IBM card punch, which produced the data cards. These deflection-versus-time data cards, along with the appropriate calibration data cards, were processed on an IBM 650 electronic computer. The reduced data were in the form of pressure-versus-time listings corresponding to each gage record. The plots of these listings were the primary data upon which this report was based.

The magnetic tape upon which the blast-switch data was recorded was played back at the home laboratory. The playback was at one-eighth the speed used in recording and included a 10-kilo-cycle timing signal from the same oscillator providing timing to the pressure-time records. At zero time, the timing signal was lost for about two msec, apparently due to tape saturation by the transient induction signal; however, as indicated by the direct signals, the timing oscillator did not stop. Fortunately, the paper speed is constant, and one can measure back to zero with some confidence.

The records from the blast-switch gages were rather difficult to reduce due to false arrivals caused by intermittent electrical shorts occurring in the switch case shortly after shock arrival. However, with the aid of arrival-time data from the pressure-time records, it was possible to obtain some useful data from the magnetic tape playback.

3.2.2 Gage Corrections and Auxiliary Calculations. At a meeting of the nuclear-blast-measurement agencies called early in 1958 by the Armed Forces Special Weapons Project (AFSWP), the several agencies explained their problems and agreed upon a common course of action for the future (Reference 16). These agencies included Sandia Corporation (SC), Stanford Research Institute (SRI), Ballistic Research Laboratories (BRL), and Naval Ordnance Laboratory (NOL).

It was recognized by all the meeting participants that the measurements that had been made in dusty blasts were questionable, and even if fully understood, would not completely answer the structural engineer's question, "What will be the expected free-stream forces that will act on a structure at a given distance from a given yield and burst geometry?" The meeting results which are most pertinent to Project 1.3 data-reduction procedures are reviewed here.

In referring to the data recorded directly by the Project 1.3 gages (i. e., pitot-static differential gage, SRI total-head gage, and surface-level baffle gage), standard nomenclature will be used (Appendix A). It has been decided that this is the nomenclature to be used on all future reports on blast pressures to avoid misunderstanding.

For the pitot-static gage and the total-head gage, the value of the dust-registry coefficient, n , is unknown. For this reason probably more than for any other, the measurements made with these gages in dusty blasts are highly suspect. It is reasonable to assume that the dynamic pressure values that have been obtained do not include the total dust contribution to the dynamic pressure, and just what percentage of the total they do include is unknown. Consequently, q_c cannot be determined from the measured values, which give the sum $(q_c + n\phi_d)'$ and $n\phi_d$ is unknown. Only the Greg and Snob gage results, for which n is known approximately, offer hope for reclaiming the bulk of the data obtained in dusty regions. Unfortunately, Greg and Snob gage measurements are few and far between; therefore, the bulk of the available data must be reduced in a manner consistent with the amount of information now available, i. e., assuming the dust-registry coefficient is unknown.

On Plumbbob, Project 1.3 data included measurements of: (1) $\Delta p_g'$; (2) $q_c' (= [\Delta p_p - \Delta p'])$ for clean air; (3) $\Delta p_p - \Delta p^{*'} = q_c^{*'} (= [q_c + n\phi_d]')$ for dusty air; (4) $\Delta p'$; (5) $\Delta p_p'$ for clean air; and (6) $\Delta p_p^{*}'$ for dusty air. In the above, (1) refers to the ground baffle overpressure gage, (2), (3), and (4) to the Sandia pitot-static gage, and (5) and (6) to the SRI total-head gage. In this discussion it is assumed that all flows were dusty, and $q_c^{*'}$ and $\Delta p_p^{*'}$ only will be discussed.

Ground-Baffle Overpressure ($\Delta p_g'$). It is assumed that the ground-baffle overpressure is unaffected by dust and Mach number or direction of the flow; therefore, these data are used without correction.

Differential Pitot-Tube Pressure ($q_c^{*'}$). The Mach number of the flow is calculated using the method outlined in Section 1.3.4, where $P_t = q_c^{*' + \Delta p^{*' + P_0}$ and $P_s = \Delta p_g' + P_0$. The Cornell Aeronautical Laboratory (Reference 14) has calibrated in their wind tunnel a model of the field pitot-tube gage. The results of these clean-air measurements present gage corrections as a function of angles of pitch and yaw to ± 45 degrees and as a function of Mach number to $M = 0.85$. Since no pitch or yaw measurements were taken on Plumbbob, the $q_c^{*'}$ measurements can only be corrected for Mach number to produce q_c^* .

Pitot-Tube Overpressure ($\Delta p^{*'}$). Once the Mach number has been calculated as explained in Section 1.3.4, the pitot-tube overpressure can be corrected for the gage (Reference 14) to produce Δp^* .

Total-Head Pressure ($\Delta p_p^{*'}$). The SRI total-head gage was designed on the basis of National Advisory Committee for Aeronautics (NACA) wind-tunnel tests (References 17 and 18). These tests indicated that for pitch and yaw angles of ± 18 degrees and Mach numbers up to 1.26 the gage corrections for clean air were less than 3 percent; hence, it was decided that pending further wind-tunnel and/or shock-tube tests of the gage, no correction should be applied. The total-head gage measurements were used to compute Mach number and then q^* from the relation

$$q^* = \frac{\gamma P_s M^2}{2}$$

As outlined in Reference 16, the data from Project 1.3 were processed as follows:

1. At each station, q^* and M_2 are calculated as if the air were clean. The error will be small in regions of light dust loading and larger as dust loading increases. When these calculations use the 3-foot-high total-head data and the ground-baffle overpressure, no gage corrections are applied. When it is necessary to use the pitot-tube data for obtaining M_2 , the gage corrections (Reference 14) must be applied to obtain q_c^* and Δp^* ; then, a new calculation of M_2 is made.
2. Where possible, q_c^* as obtained from the pitot-tube data will be compared with the total-head $(\Delta p_p^* - \Delta p_g)^*$ data.
3. For gages located above 3-foot elevation, the side port values of Δp should be used to obtain q_c^* .
4. At 2,000-foot ground range (SRI Station 9), Project 34.1 made some measurements with Snob, Greg, and pitot-static gages. These data will be used to determine the approximate dust registry coefficient of the pitot-tube.

3.3 GAGE RECORDS

Figures 3.1 through 3.10 present the significant portions of the gage records obtained on Project 1.3. The records are arranged by gage type in the order (1) surface-level baffle, (2) pitot-tube static port, (3) total head, and (4) pitot-tube differential port. All records are plotted from the listings obtained from the computer; no smoothing of the original records was done.

These records represent the primary data upon which this report is based.

3.4 WAVE FORMS

Reference to the gage records of Figures 3.1 through 3.10 indicates that in a purely qualitative sense the forms of the records change considerably with increasing ground range. Thus, before discussing the qualitative results of the measurements, the wave forms will be investigated for evidence of effects of surface conditions and burst characteristics upon the blast wave.

The classification of the wave forms separates logically into two main groups: one dealing with the overpressure-time measurements, and the other with those measurements involving dynamic pressure. In the SRI Teapot report (Reference 4) some success was experienced with classification of overpressure-time wave forms; the classification system which was devised allowed for a consistent analysis of the bulk of the available data. This overpressure wave-form classification is summarized in Appendix A, where typical examples are given. The classification system for dynamic pressure measurements (Reference 4) has been revised and is presented in Section 4.4.5 of this report.

Referring to the surface level overpressure wave forms of Figures 3.1 and 3.2, it is seen that the form at Station 1 (1B) is almost classic, exhibiting a rapid rise to a sharp pressure peak; however, it may be argued that the rise time is noticeably longer than would be expected for a truly classic shock. Nevertheless, the 1B record is a Type 0 form by SRI notation. Subsequent records of Figure 3.1 show the development of the precursor wave with increasing ground range; these are all Type 1 forms. There is no significant change in form until Station 10 (10B) where it is difficult to choose between Types 3 and 4; Type 3 is chosen because there is a late pressure maximum which is characteristic of this form. Station 11 and 12 records (Figure 3.2) exhibit the "clean-up" forms, Types 5 and 6. No Types 7 and 8 were observed because the 13B record was lost and measurements did not extend to larger ranges.

Generally, the wave form for the aboveground overpressure records (Figures 3.3 and 3.4) follows the surface-level records rather closely. The significant difference is that the aboveground records appear more "hashy" than do the surface-level measurements. This may be due either to a real increase in flow disturbance above the ground surface or to the fact that the measurement was taken using a side port of the pitot tube where the tube itself could disturb the flow somewhat.

The total-head records of Figures 3.5, 3.6, and 3.7 indicate wave forms much like the overpressure results. The total-head records are a bit more hashy after Station 5 (Figure 3.6), but

(Text continued on Page 46)

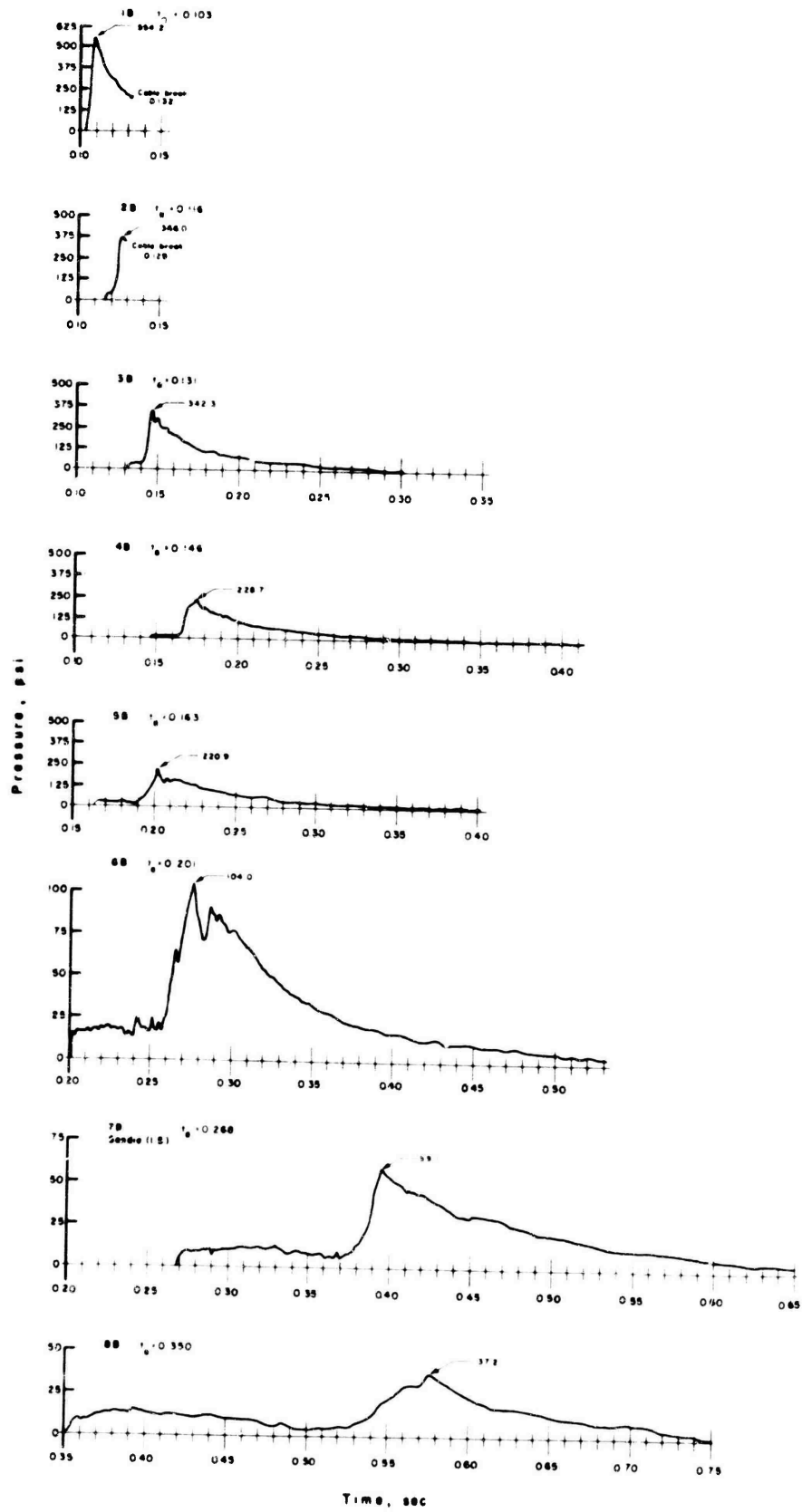


Figure 3.1 Surface-level overpressure versus time, Stations 1 to 8, Shot Priscilla.

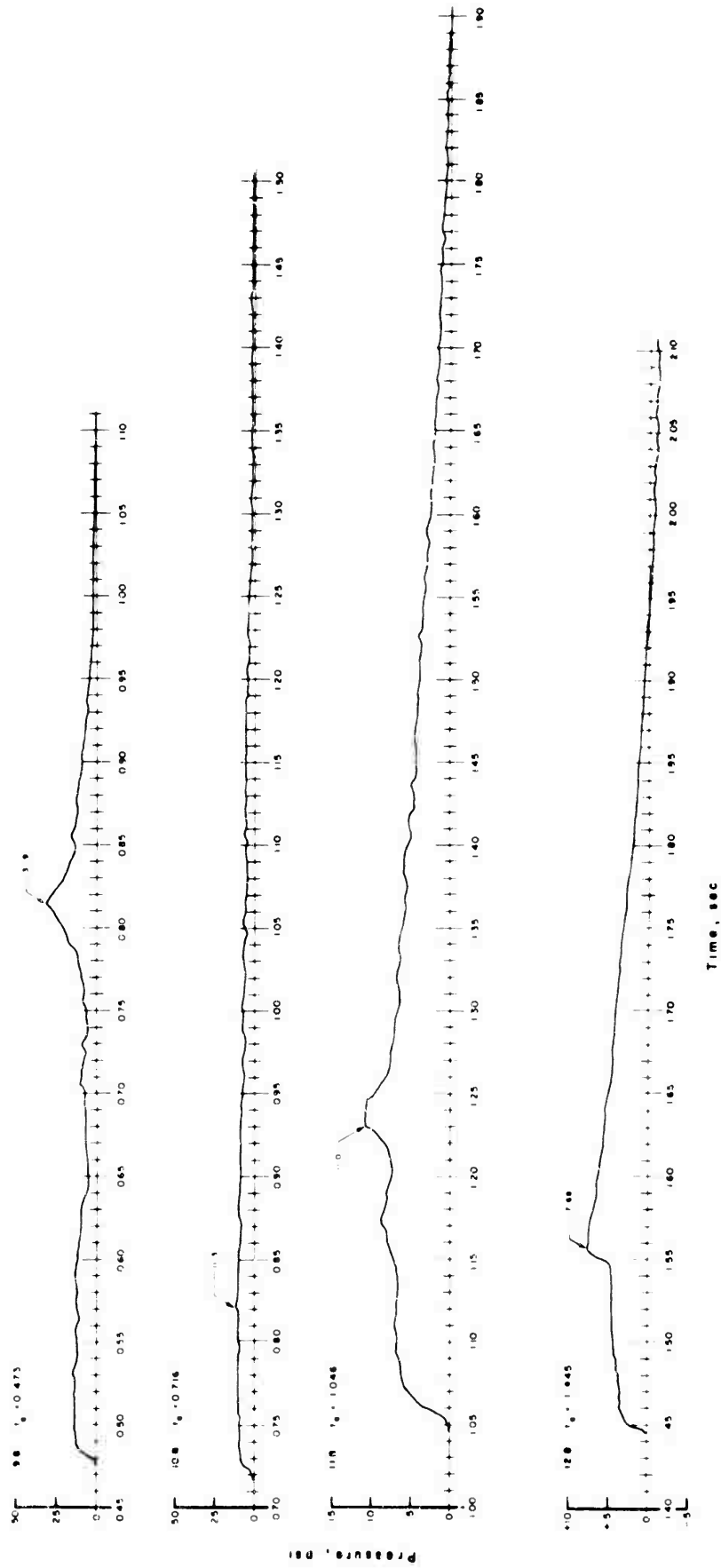


Figure 3.2 Surface-level overpressure versus time, Stations 9 to 12, Shot Priscilla.

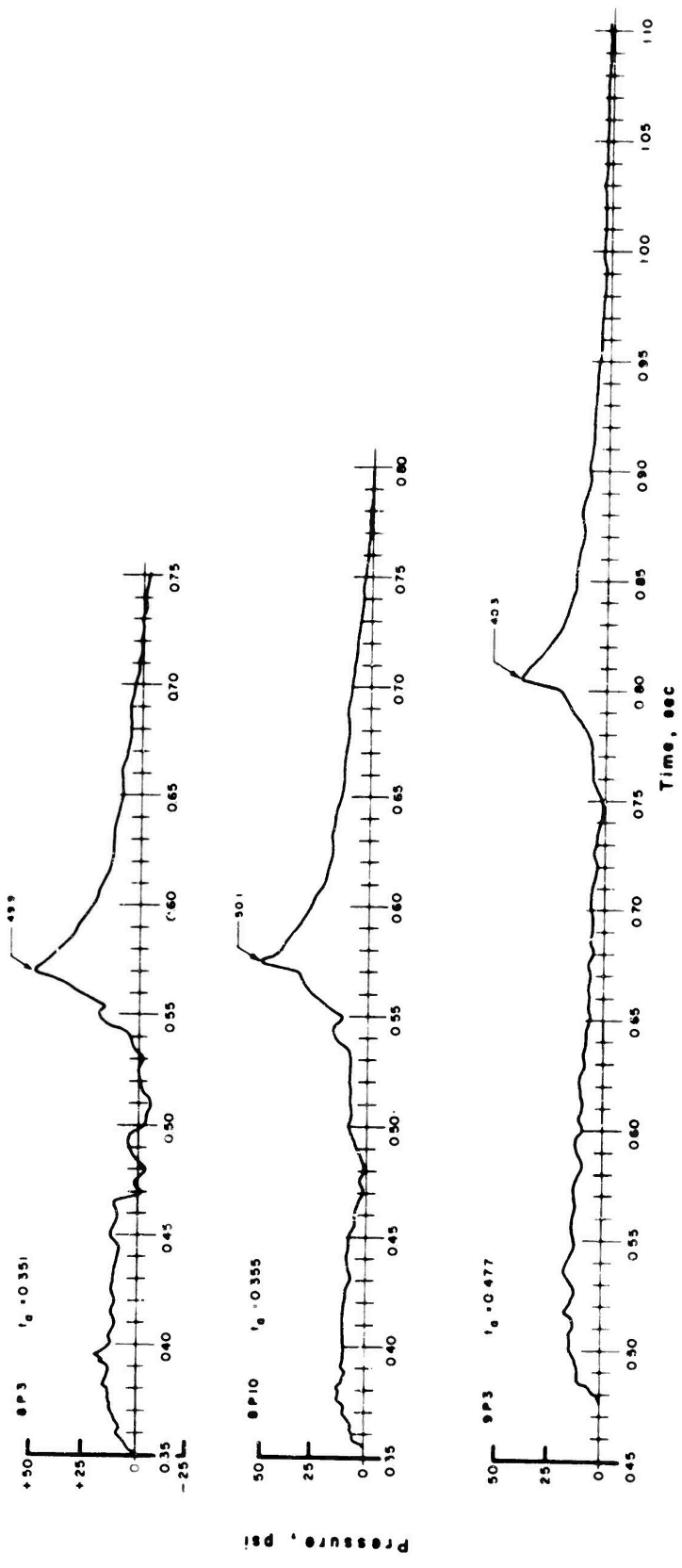


Figure 3.3 Overpressure versus time, 3- and 10-foot levels, Stations 8 and 9, Shot Priscilla.

9 P 10 No Record

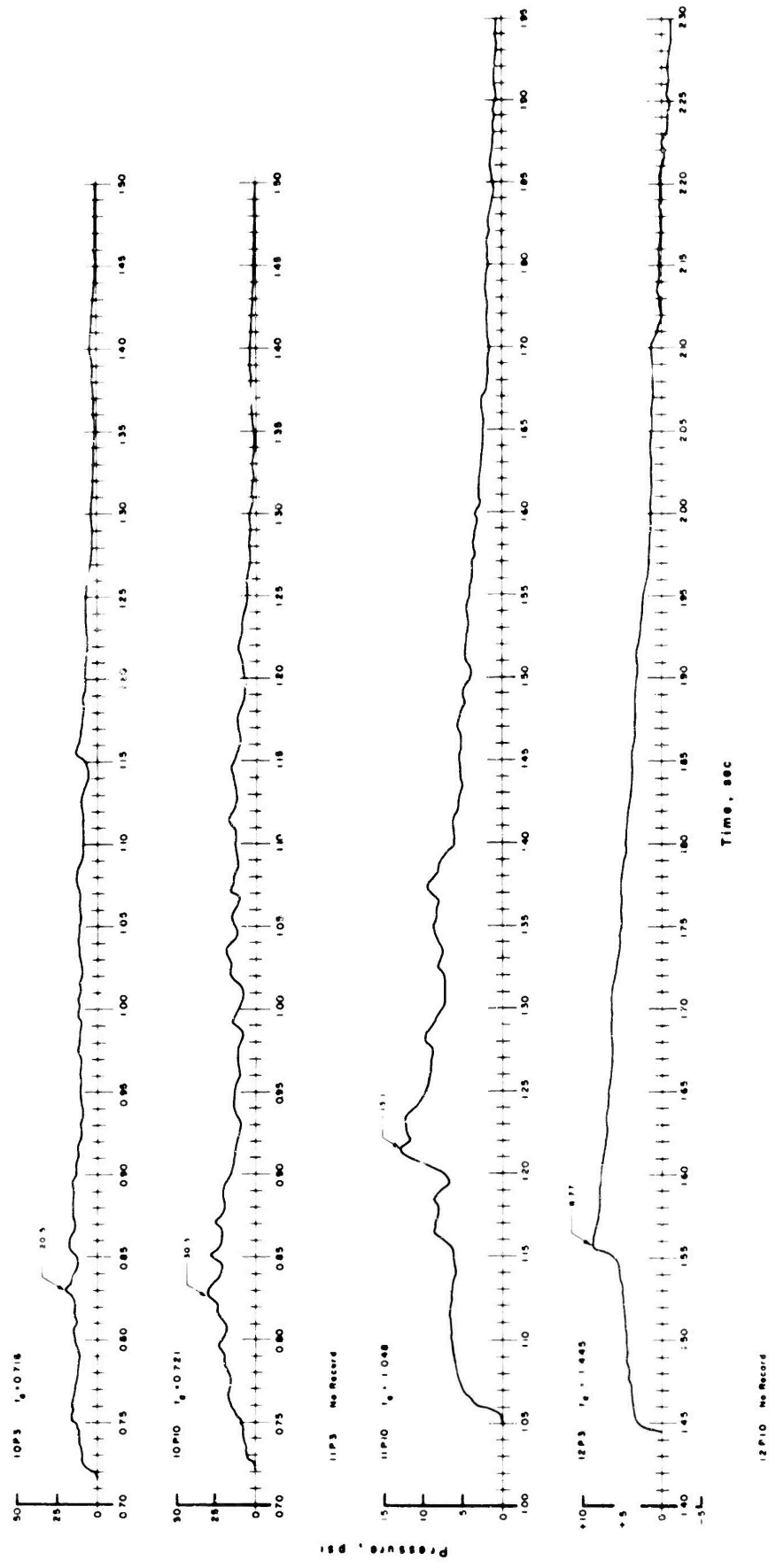


Figure 3.4 Overpressure versus time, 3- and 10-foot levels, Stations 10 to 12, Shot Priscilla.

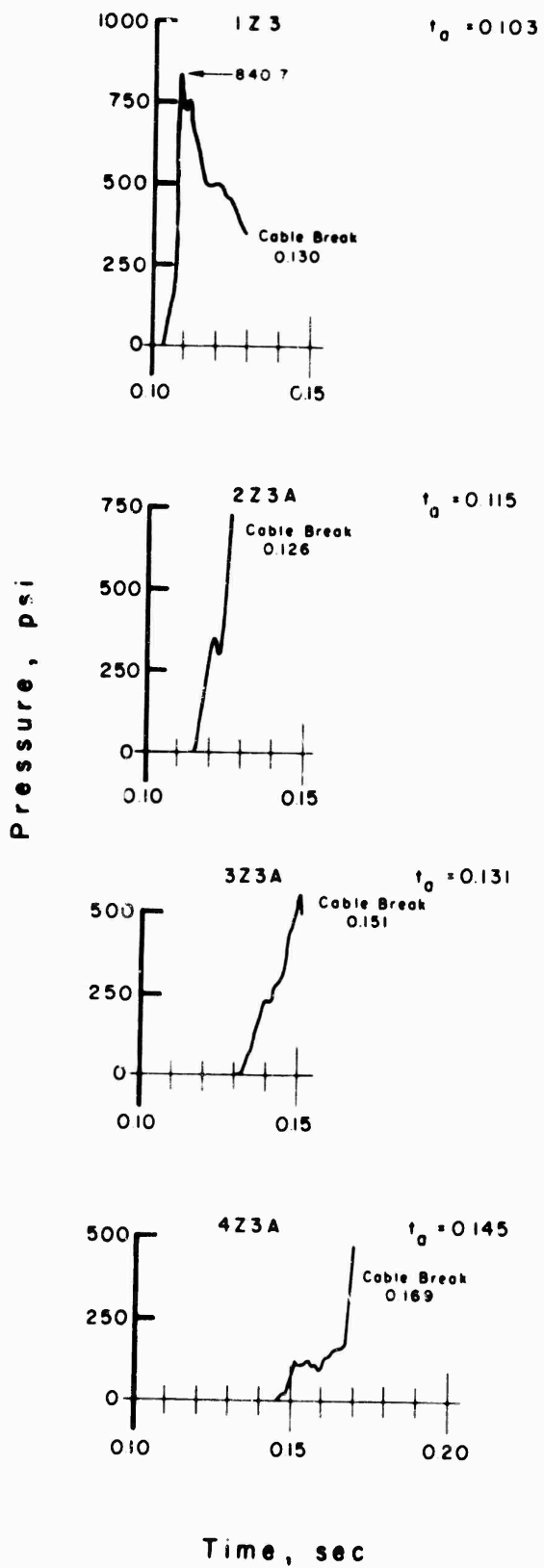


Figure 3.5 Total-head pressure versus time, 3-foot level, Stations 1 to 4, Shot Priscilla.

~~SECRET~~

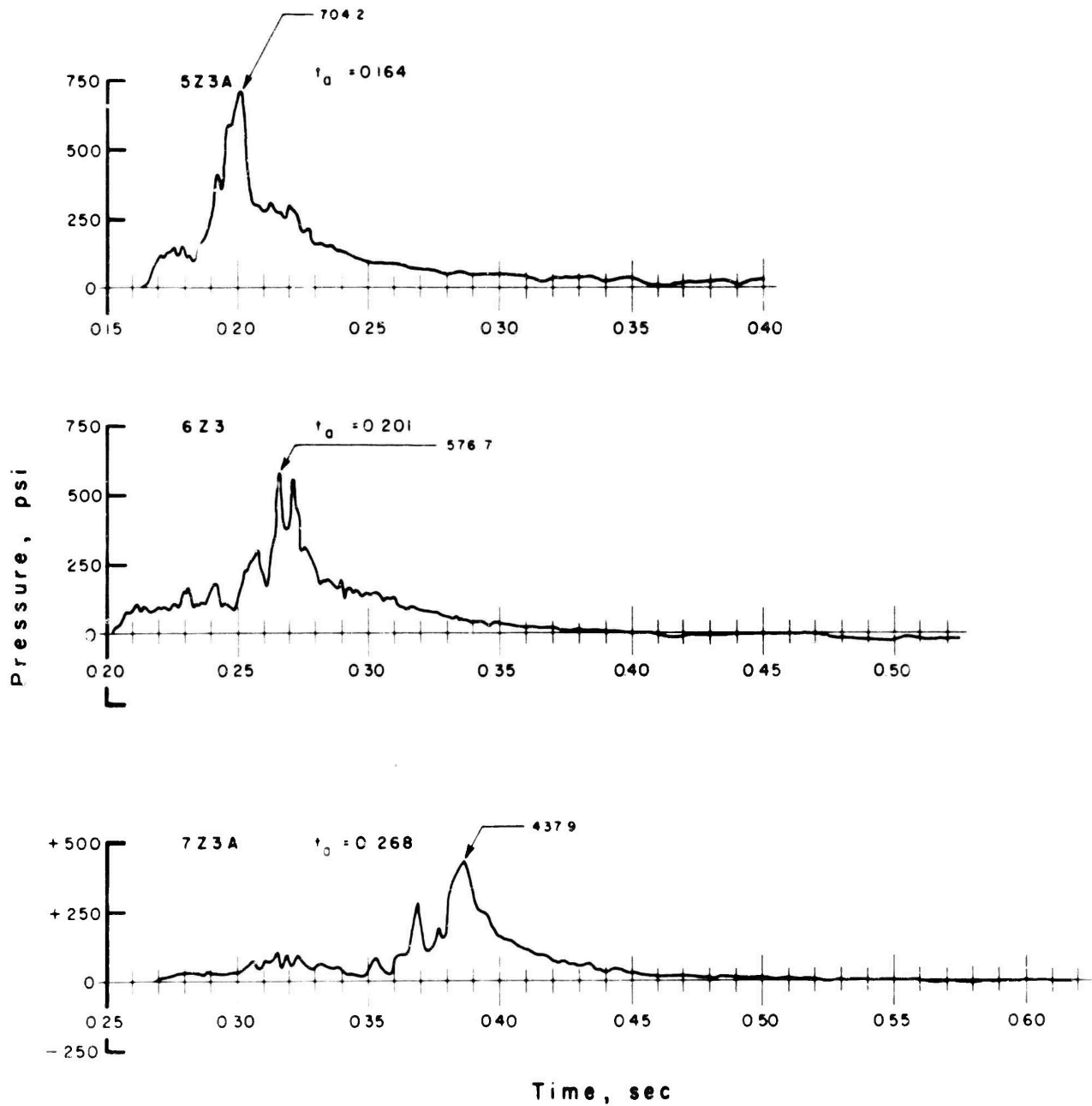


Figure 3.6 Total-head pressure versus time, 3-foot level, Stations 5 to 7, Shot Priscilla.

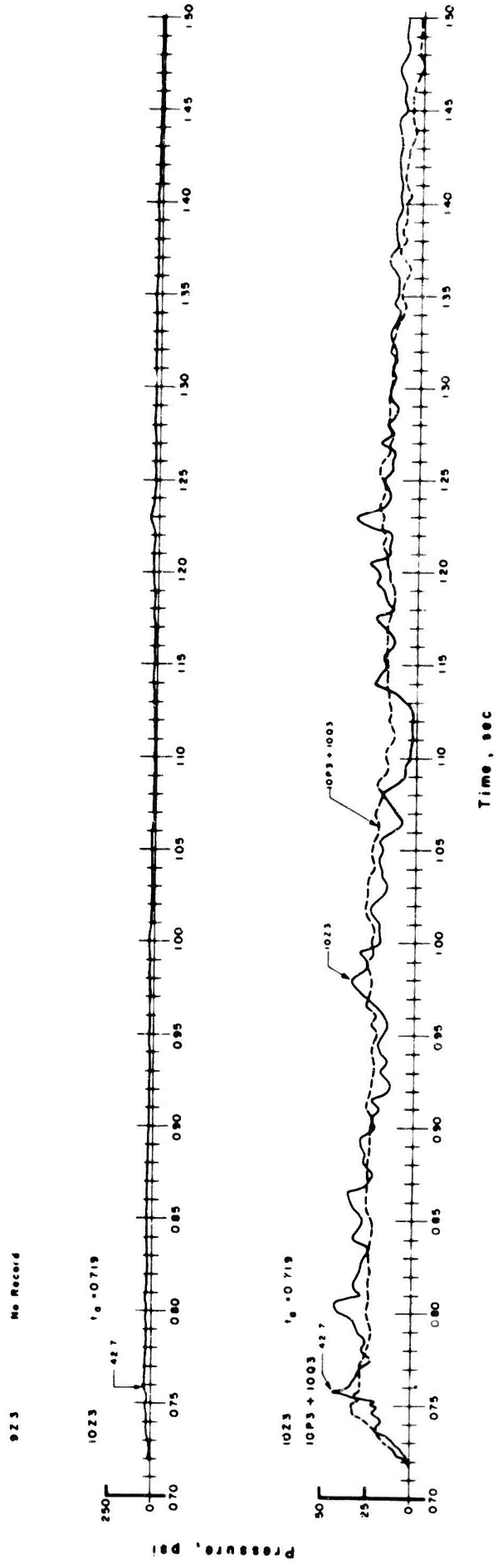


Figure 3.7 Total-head pressure versus time, 3-foot level, Stations 9 and 10, Shot Priscilla.

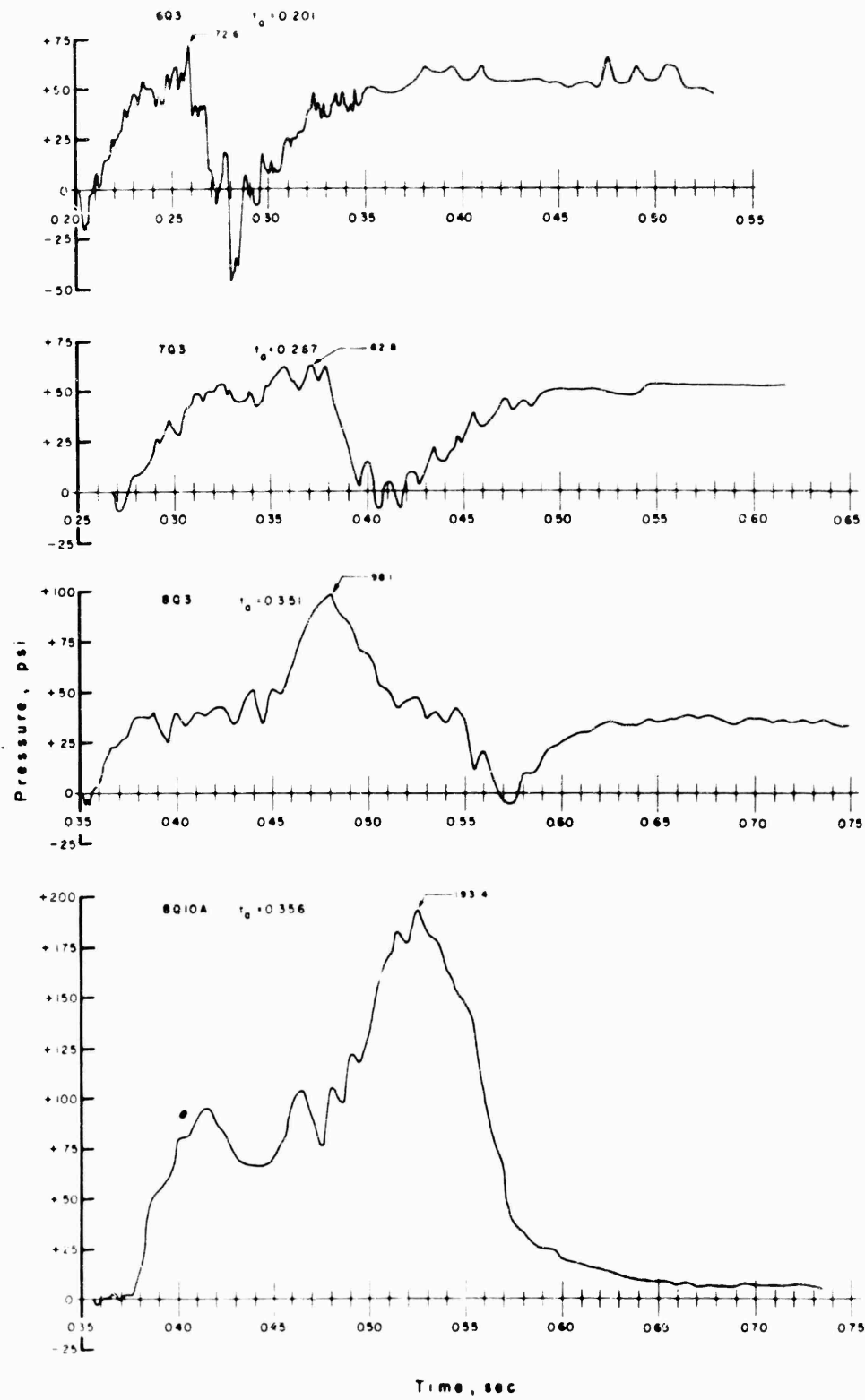


Figure 3.8 Dynamic pressure versus time, 3- and 10-foot levels, Stations 6 to 8, Shot Priscilla.

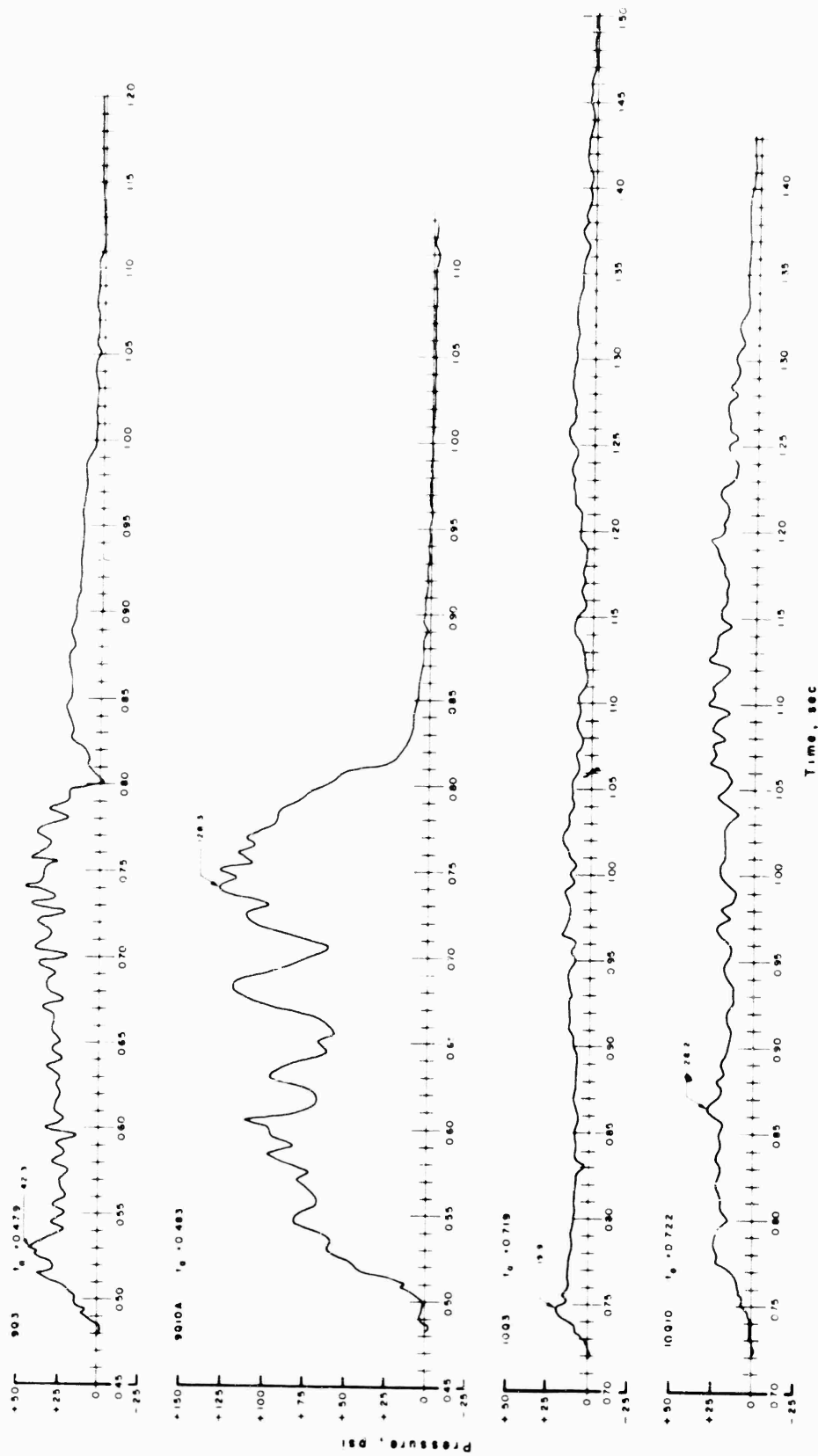


Figure 3.9 Dynamic pressure versus time, 3- and 10-foot levels, Stations 9 and 10, Shot Priscilla.

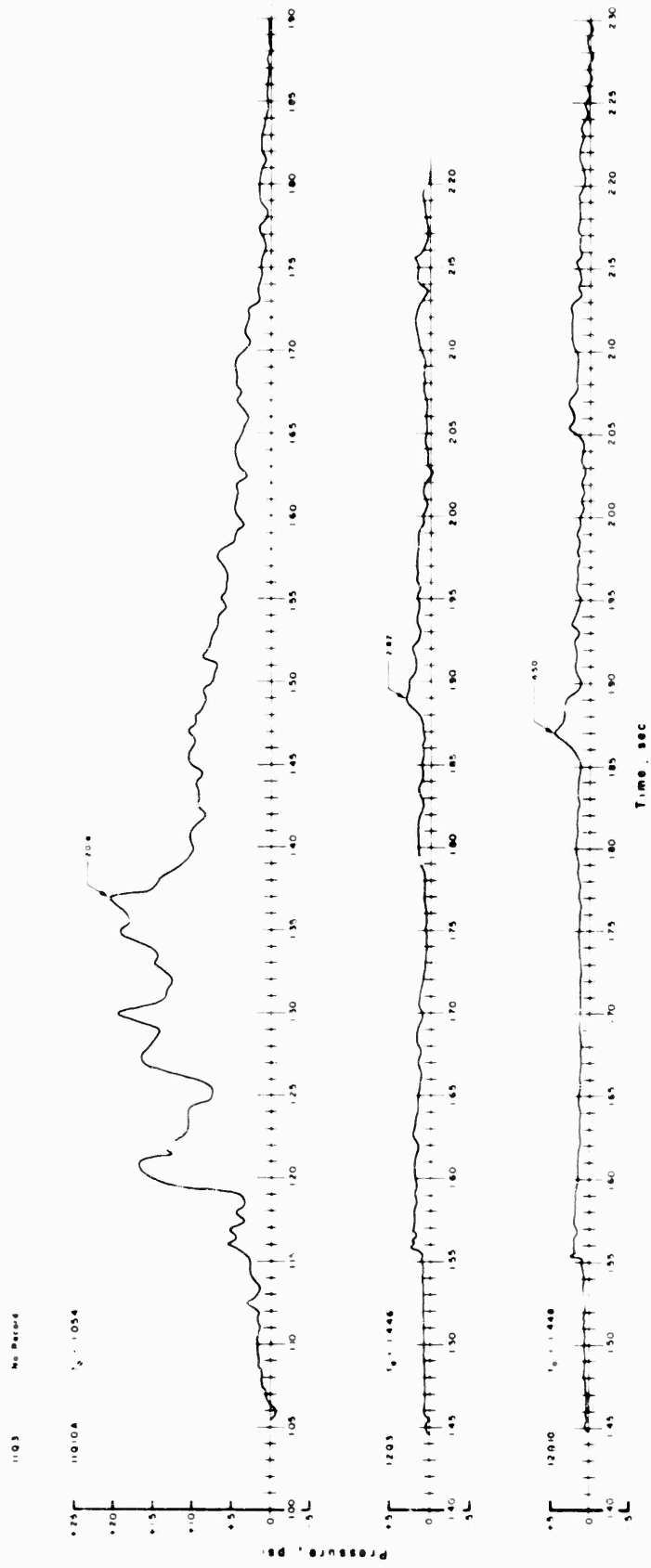


Figure 3.10 Dynamic pressure versus time, 3- and 10-foot levels, Stations 11 and 12, Shot Priscilla.

the general forms are similar. Turning to the differential gage records of Figures 3.8, 3.9 and 3.10, the picture is not as straightforward. First, most of the records begin with a short negative onset, which indicates that the fill time of the front port is longer than that of the side port. Therefore, the differential gage registered pressure on the rear end before the pressure signal arrived through the front port.

Records 6Q3, 7Q3, and 8Q3 (Figure 3.8) show evidence of plugging with dust shortly after signal arrival. This plugging probably stops the flow of air at the front port so that when the side-on overpressure rises rapidly, the differential reading falls abruptly and later assumes the relatively constant positive plugged pressure after the overpressure has decayed. This hypothesis is borne out quantitatively: the 6Q3 record shows an abrupt decrease in differential pressure near 0.270 second of slightly less than 100 psi, whereas the 6B gage record (Figure 3.1) at this station indicates a rise of about 85 psi at the same time. Also, the Station 7 (7Q3) and Station 8 (8Q3) records check similarly well with the rise in overpressure recorded at these stations. The 8Q10A record shows no definite evidence of dust plugging; it appears to decay to almost zero differential pressure as one would expect if the orifice were clear.

As far as the wave forms of Figure 3.8 are concerned, the 6Q3 and 7Q3 records bear little resemblance to their overpressure counterparts, even before the gages were plugged with dust. However, the much slower rise times observed on the differential gage records might well be attributed to the long fill time of the front opening. For these two records, the best that can be said is that the peak recorded pressures can be associated with the precursor wave only, and, that if it were not for plugging, the recorded peak pressures would have been much higher. The records at Station 8, although their form is similar to the corresponding 8P3 and 8P10 overpressures, display a much shorter pressure plateau (before the rise to peak pressure) than do the overpressure forms. From this result and the fact that the differential measurement is known to be sensitive to the dust carried along by the blast wave, it could be concluded that the dust precedes the main blast-wave arrival at this station.

Proceeding to Figure 3.9, there is some evidence of dust plugging on the 9Q3 record, but the remaining records show no such evidence. The differential gage records at Station 9 (9Q3 and 9Q10A) do not exhibit the same form as the overpressure records (9B and 9P3); that is, all significant portions of the pitot record can be identified with the precursor wave only. At Station 10 (Figure 3.9), the differential-gage record is similar in form to the corresponding overpressures (10P3 and 10P10). In this case the arrival of the so-called main wave cannot be distinguished.

Finally, the wave forms of Figure 3.10 indicate a rather close correlation with their overpressure counterparts. At Station 11, although the two wave forms (11Q10A and 10P10) are similar, the 11Q10A record exhibits a much larger increase in response upon arrival of the main shock, which is probably the result of entrained dust in the wave. There is no evidence of plugging. The Station 12 records (12Q3 and 12Q10) follow closely the overpressure (12P3) wave form. The origin of the later peaks near 1.90 seconds on the Q records is unknown, but these will be discussed further in Chapter 4.

3.5 TABLES OF RESULTS

The primary data obtained from all usable Project 1.3 records on Shot Priscilla are contained in Tables 3.1 through 3.3. The tables represent the as-read and A-scaled data; they include gage designation, ground range, gage height, arrival time, maximum pressure (precursor and main shock), time of maximum pressure positive-phase impulse duration (overpressure only), positive-phase impulse, and wave-form classification.

For comparison with other nuclear detonations, it is convenient to normalize the blast data for the Priscilla shot to a common base by scaling all values. This procedure involves reducing data to a standard atmosphere at sea level for 1 kt of radiochemical yield. Conventional cube-root-yield scaling is used in conjunction with Sachs correction factors for atmospheric pressures and temperatures at the gage (modified Sachs scaling). The following scaling relations apply:

TABLE 3.1 OVERPRESSURE, SHOT PRISCILLA

CB, cable break at or near time of peak; CF, camera failure; NP, no precursor; NR, no record.

Gage	Ground Range	Gage Height	Arrival Time	Maximum Precursor	Time of Maximum Precursor	Maximum Pressure	Time of Maximum Pressure	Positive-Phase Duration	Positive-Phase Impulse	Wave-form Type
	ft	ft	sec	psi	sec	psi	sec	sec	psi-sec	
As-read										
OB	75	0	NR	NR	NR	NR	NR	NR	NR	NR
1B	450	0	0.103	NP	—	554 CB	0.108	—	—	0
2B	550	0	0.116	39.2	0.118	366 CB	0.126	—	—	1-
3B	650	0	0.131	31.4	0.134	342	0.146	0.149	12.2	1
4B	750	0	0.146	26.0	0.150	229	0.175	0.164	10.1	1
5B	850	0	0.163	25.6	0.166	221	0.201	0.197	> 11.2	1
6B	1,050	0	0.201	20.5	0.223	104	0.275	0.314	> 9.15	1
7B	1,350	0	0.268	12.1	0.318	59.1	0.394	0.357	6.62	1
8B	1,650	0	0.350	15.7	0.392	37.2	0.575	0.375	5.02	1
8P3	1,650	3	0.351	20.3	0.396	49.9	0.570	0.354	4.35	1
8P10	1,650	10	0.355	13.0	0.382	50.1	0.575	0.395	> 4.98	1
9B	2,000	0	0.475	14.2	0.492	31.9	0.815	0.570	5.82	1
9P3	2,000	3	0.477	18.4	0.535	40.3	0.805	0.568	> 5.70	1
9P10	2,000	10	CF	CF	CF	CF	CF	CF	CF	CF
10B	2,500	0	0.716	9.23	0.138	11.3	0.820	0.774	> 4.54	3
10P3	2,500	3	0.716	16.6	0.752	20.5	0.830	0.749	6.86	3
10P10	2,500	10	0.721	7.67	0.750	30.3	0.825	0.605	8.24	3
11B	3,000	0	1.046	6.94	1.094	10.9	1.230	0.789	3.66	5
11P3	3,000	3	CF	CF	CF	CF	CF	CF	CF	CF
11P10	3,000	10	1.048	6.85	1.115	13.1	1.215	0.807	> 4.23	5
12B	3,500	0	1.445	3.61	1.462	7.68	1.558	0.490	1.67	6
12P3	3,500	3	1.445	3.89	1.464	8.77	1.558	0.675	3.07	6
12P10	3,500	10	CF	CF	CF	CF	CF	CF	CF	CF
13E	4,500	0	CF	CF	CF	CF	CF	CF	CF	CF
A-scaled to 1-kt radiochemical release at sea level										
OB	—	0	NR	NR	NR	NR	NR	NR	NR	NR
1B	131	0	0.0296	NP	—	615 CB	0.0312	—	—	0
2B	160	0	0.0335	43.5	0.0341	406 CB	0.0364	—	—	1-
3B	189	0	0.0378	34.9	0.0387	380	0.0422	0.043	3.91	1
4B	218	0	0.0422	28.9	0.0433	254	0.0506	0.048	3.24	1
5B	247	0	0.0471	28.4	0.0480	245	0.0581	0.057	> 3.59	1
6B	305	0	0.0581	22.8	0.0644	115	0.794	0.091	> 2.93	1
7B	392	0	0.0774	13.4	0.0919	65.6	0.1136	0.103	2.12	1
8B	479	0	0.1011	17.4	0.1132	41.3	0.1661	0.108	1.61	1
8P3	479	0.87	0.1014	22.5	0.1144	55.4	0.1647	0.102	1.40	1
8P10	479	2.90	0.1026	14.4	0.1104	55.6	0.1861	0.114	> 1.60	1
9B	581	0	0.1372	15.8	0.1421	35.4	0.2355	0.165	1.87	1
9P3	581	0.87	0.1378	20.4	0.1546	44.7	0.2326	0.164	> 1.83	1
9P10	581	2.90	CF	CF	CF	CF	CF	CF	CF	CF
10B	726	0	0.2069	10.2	0.2132	12.5	0.2361	0.224	> 1.46	3
10P3	726	0.87	0.2069	18.4	0.2173	22.7	0.2398	0.216	> 2.20	3
10P10	726	2.90	0.2083	8.51	0.2167	33.6	0.2383	0.175	2.64	3
11B	871	0	0.3022	7.70	0.3161	12.1	0.3553	0.228	1.17	5
11P3	871	0.87	CF	CF	CF	CF	CF	CF	CF	CF
11P10	871	2.90	0.3028	7.60	0.3221	14.5	0.3510	0.233	> 1.36	5
12B	1,016	—	0.4175	4.01	0.4224	8.52	0.4501	0.142	0.54	6
12P3	1,016	0.87	0.4175	4.32	0.4229	9.73	0.4501	0.195	0.98	6
12P10	1,016	2.90	CF	CF	CF	CF	CF	CF	CF	CF
13B	—	—	CF	CF	CF	CF	CF	CF	CF	CF

TABLE 3.2 TOTAL-HEAD PRESSURE, SHOT PRISCILLA

CB, cable break, at or near time of peak, NP, no precursor, NR, no record.

Gage	Ground Range ft	Gage Height ft	Arrival Time sec	Maximum Precursor psi	Time of		Maximum Pressure* psi	Time of Maximum Pressure sec
					Maximum Precursor sec	Maximum Pressure*		
As-read								
1Z3	450	3	0.103	NP	—		848 CB	0.109
2Z3	550	3	0.115	356	0.121		804 CB	0.126
3Z3	650	3	0.131	231	0.140		559 CB	0.150
4Z3	750	3	0.145	125	0.152		530 CB	0.169
5Z3	850	3	0.164	149	0.179		716	0.201
6Z3	1,050	3	0.201	104	0.211		569	0.266
7Z3	1,350	3	0.268	104	0.314		438	0.386
9Z3	2,000	3	NR	NR	NR		NR	NR
10Z3	2,500	3	0.719	19.0	0.736		42.7	0.758
A-scaled to 1-kt radiochemical release at sea level								
1Z3	131	0.87	0.0298	NP	—		941 CB	0.0315
2Z3	160	0.87	0.0332	395	0.0350		892 CB	0.0364
3Z3	189	0.87	0.0378	256	0.0404		620 CB	0.0433
4Z3	218	0.87	0.0419	139	0.0439		588	0.0488
5Z3	247	0.87	0.0474	165	0.0517		695	0.0581
6Z3	305	0.87	0.0581	115	0.0610		632	0.0768
7Z3	392	0.87	0.0774	115	0.0907		486	0.1115
9Z3	581	0.87	NR	NR	NR		NR	NR
10Z3	726	0.87	0.2077	21.1	0.2126		47.4	0.2190

* Average of alternate and standard gages whenever possible.

TABLE 3.3 DYNAMIC PRESSURE, SHOT PRISCILLA

NA, not able to determine; CF, camera failure.

Gage	Ground Range ft	Gage Height ft	Arrival Time sec	Maximum Precursor psi	Time of		Maximum Precursor psi	Time of Maximum Pressure sec	Wave-form Type
					Maximum Precursor sec	Maximum Pressure			
As-read									
6Q3	1,050	3	0.201	NA	—		72.6	0.258	—
7Q3	1,350	3	0.267	NA	—		62.8	0.370	1b
8Q3	1,650	3	0.351	36.7	0.382		98	0.480	1c
8Q10	1,650	10	0.356	95.7	0.415		193	0.525	1c
9Q3	2,000	3	0.479	NA	—		42.3	0.530	1d
9Q10	2,000	10	0.483	NA	—		128	0.740	1d
10Q3	2,500	3	0.719	NA	—		19.9	0.746	3c
10Q10	2,500	10	0.722	1.74	0.736		28.2	0.865	3c
11Q3	3,000	3	CF	CF	CF		CF	CF	NR
11Q10	3,000	10	1.054	1.69	1.098		20.6	1.370	5c
12Q3	3,500	3	1.446	0.50	1.462		2.81	1.890	6b
12Q10	3,500	10	1.448	0.53	1.472		4.47	1.870	6b
A-scaled to 1-kt radiochemical release at sea level									
6Q3	305	0.87	0.0581	NA	—		80.6	0.0745	—
7Q3	392	0.87	0.0771	NA	—		69.7	0.1069	1b
8Q3	479	0.87	0.1014	40.7	0.1104		109	0.1387	1c
8Q10	479	2.90	0.1028	106	0.1199		214	0.1517	1c
9Q3	581	0.87	0.1384	NA	—		47.0	0.1531	1d
9Q10	581	2.90	0.1395	NA	—		142	0.2138	1d
10Q3	726	0.87	0.2077	NA	—		22.1	0.2155	3c
10Q10	726	2.90	0.2086	1.93	0.2126		31.5	0.2499	3c
11Q3	871	0.87	CF	CF	CF		CF	CF	NR
11Q10	871	2.90	0.3045	1.88	0.3172		22.9	0.3958	5c
12Q3	1,016	0.87	0.4177	0.55	0.4224		3.12	0.5460	6b
12Q10	1,016	2.90	0.4183	0.59	0.4253		4.96	0.5402	6b

Pressure: $S_p = \frac{14.7}{P_0}$

Distance: $S_d = \left(\frac{P_0}{14.7}\right)^{1/3} \left(\frac{1}{W}\right)^{1/3}$

Time: $S_t = \left(\frac{T}{288}\right)^{1/2} \left(\frac{P_0}{14.7}\right)^{1/3} \left(\frac{1}{W}\right)^{1/3}$

Impulse: $S_i = \left(\frac{T}{288}\right)^{1/2} \left(\frac{14.7}{P_0}\right)^{2/3} \left(\frac{1}{W}\right)^{1/3}$

Where: P_0 = ambient pressure at the gage, psi
T = absolute temperature at the gage, C
W = total yield, kt.

The modified Sachs correction factors for Shot Priscilla are listed below:

$$S_p = 1.110$$

$$S_d = 0.2904$$

$$S_t = 0.2914$$

$$S_i = 0.3227$$

In Appendix D are Teapot data (tables and plots) reprocessed by methods agreed upon by AFSWP, BRL, SC, NOL, and SRI at a meeting 12 and 13 August 1958, in Albuquerque, New Mexico.

Chapter 4

DISCUSSION

In this chapter, Project 1.3 data are discussed under the following main subjects: (1) quantities derived from arrival-time data; (2) peak pressure measurements and Mach number calculations; and (3) precursor phenomena and predictions.

The analyses and discussion of Priscilla results are supplemented by data from previous nuclear weapons-effects tests.

4.1 ARRIVAL-TIME DATA

Arrival time of the pressure wave at the electronic pressure gages is probably the least ambiguous of the quantities measured on Project 1.3. Using these data and those obtained from the blast switches, it is possible to derive several useful quantities such as shock velocity and wave-front orientation.

4.1.1 Arrival Time and Shock Velocity. Arrival-time data from surface-level overpressure gages and blast switches on Priscilla are included in Tables 3.1 and 4.1, respectively. These arrival-time data are summarized in Figure 4.1; included in the figure is the arrival-time-versus-ground-range curve for an ideal surface and also the arrival times of the so-called main blast wave. The curves indicate that at the first instrumented station (Station 1, 450-foot ground range) the arrival time agrees with that predicted over an ideal surface. Also, since no precursor wave is apparent at this station, the first arrival is the main wave arrival. At subsequent gage stations, the first arrival is the precursor wave. As the curves of Figure 4.1 indicate, the precursor wave always precedes the ideal surface prediction, whereas the main wave arrival lags behind it; only at Stations 10, 11, and 12 (2,500-, 3,000-, and 3,500-foot ground range) do the main wave arrivals approximate those predicted over an ideal surface. It is significant that the main wave arrivals show an abrupt change between Stations 9 and 10 (2,000- to 2,500-foot ground range); this will be discussed in Section 4.4, Precursor Phenomena. It is worth noting that the arrival-time-versus-ground-range curve for the precursor has a cusp near 500-foot ground range.

To obtain shock velocity as a function of ground range, it is necessary to differentiate the time-of-arrival curve (precursor) of Figure 4.1. This is done by a five-point numerical method outlined in Reference 19. Since an upper bound for the residual of the expansion is not known, a maximum limit of the error term cannot be determined analytically. However, from a practical standpoint, an estimate of the total error can be made.

Let total error be $E + e$, where E is the error inherent in the time-versus-distance curve (Figure 4.1), and where e is the error inherent in the numerical differentiation method used to determine shock velocity.

The value of e may be determined as follows: In choosing tabular values of ground range from the curve, a reading error of ± 1 foot is assumed. Then considering the central point formula, the maximum error is

$$e_{\max} = 150 \text{ ft/sec.}$$

Similarly, considering the end point formulas, the maximum error is

$$e_{\max} = 1,067 \text{ ft/sec,}$$

for one pair of end points and

TABLE 4.1 BLAST SWITCHES, SHOT PRISCILLA

Nominal Ground Range ft	Arrival Time		Arrival Time for Ideal Surface msec
	0-ft msec	3-ft msec	
100	70.8	69.8	70
150	NR	NR	—
200	NR	NR	75
250	81.7	81.0	80
300	85.6	84.9	—
350	NR	NR	90
400	NR	NR	—
450	104.7	104.2	104
500	NR	NR	112
550	NR	NR	—
600	NR	NR	—
650	NR	NR	135
700	NR	NR	—
750	NR	147.7	—
800	NR	NR	161
850	132.4	166.1	181
950	182.2	—	—
1,050	NR	NR	238
1,150	221.3	—	—
1,250	242.4	—	308
1,350	266.7	272.0	—
1,500	305.7	—	401
1,650	350.4	353.7	—
1,800	402.3	—	536
2,000	NR	NR	623
2,200	NR	—	755
2,500	721.4	723.8	893
3,000	NR	NR	1,046
3,500	NR	NR	1,445

NR, no record

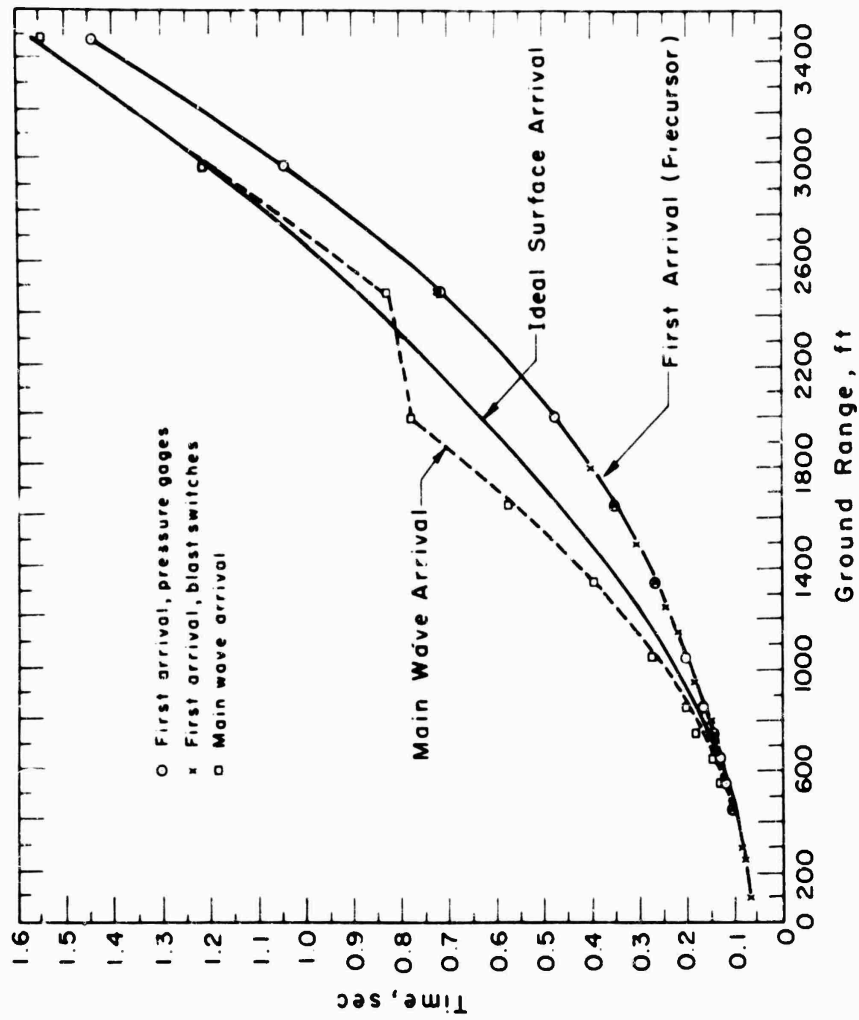


Figure 4.1 Arrival time, surface level, Shot Priscilla.

$$e_{\max} = 317 \text{ ft/sec,}$$

for the other pair.

An attempt was made to examine the shock velocity in greater detail around the area of the cusp found on the arrival-time curve; however, the attempt increased the inherent reading error three-fold and the results were not reliable.

The shock velocity versus ground range is listed in Table 4.2 and shown in Figure 4.2. Also included on Figure 4.2 is the velocity curve derived from the arrival times over an ideal surface. It is evident that for the close-in ranges, less than about 300 feet, the computed trace velocities would agree closely with those predicted over an ideal surface. However, near 500-foot range the Priscilla curve begins to deviate markedly from the ideal surface curve. From overpressure-time data (Figure 3.1), it is concluded that the precursor developed between 450- and 550-foot

TABLE 4.2 SHOCK-FRONT VELOCITY, SURFACE LEVEL, SHOT PRISCILLA

Ground Range ft	Shock Velocity ft/sec	Ground Range ft	Shock Velocity ft/sec	Ground Range ft	Shock Velocity ft/sec
113	17,717	1,319	4,267	1,941	2,550
254	11,200	1,361	4,100	1,966	2,450
349	8,283	1,401	3,942	1,990	2,350
427	7,558	1,440	3,850	2,017	2,300
503	7,633	1,478	3,750	2,046	2,218
579	7,333	1,515	3,650	2,077	2,120
649	6,775	1,551	3,558	2,106	2,065
715	6,442	1,586	3,400	2,136	2,005
778	6,158	1,619	3,233	2,165	1,980
838	5,800	1,651	3,200	2,196	1,930
894	5,433	1,683	3,150	2,228	1,880
947	5,192	1,714	3,100	2,257	1,850
998	5,000	1,745	3,058	2,286	1,800
1,047	4,792	1,775	2,950	2,315	1,750
1,094	4,633	1,804	2,900	2,346	1,700
1,140	4,583	1,832	2,850	2,375	1,650
1,186	4,550	1,861	2,808	2,407	1,600
1,233	4,508	1,888	2,692	2,435	1,540
1,276	4,342	1,915	2,658	2,463	1,480

range, which is consistent with the sharp kink in the velocity curve of Figure 4.2. It is significant that the Priscilla velocity curve, at ranges exceeding 2,300 feet, dips below the ideal-surface curve; the explanation for this is deferred to Section 4.4, Precursor Phenomena.

4.1.2 Wave-Front Orientation. The calculations involved in determining wave-front orientation from arrival-time data can be described as follows:

1. The as-read arrival times for each gage are corrected for differences in actual location of the surface and aboveground gages using the horizontal shock velocity (Figure 4.2) at each station. This procedure assumes that all portions of the front are moving with the same velocity, an assumption which is verified when aboveground trace velocities are computed.
2. Using the corrected arrival times and the arrival at the surface gage (or blast switch) as the station reference, the time interval (Δt) for each level is determined.
3. The Δt values corresponding to each level are multiplied by the shock velocity to obtain ΔR , which defines the orientation of the wave front.

The results of these calculations for Priscilla are shown in Table 4.3 and plotted in Figure 4.3.

The wave-front orientations derived from the close-in blast-switch arrivals are shown in Figure 4.3. Since these measurements were taken in the regular reflection region, they repre-

TABLE 4.3 WAVE-FRONT ORIENTATION DATA, SHOT PRISCILLA

Gage	Nominal Ground Range ft	Trace Velocity ft/sec	Gage Height ft	Arrival Time msec	Exact Ground Range ft	At Nominal Range	
						Δt msec	ΔR ft
BS-0	100	18,000	0.1	70.8	100.2	0	0
BS-3			3.0	69.8	100.2	1.0	18.0
RS-0	250	11,200	0.1	81.7	250.6	0	0
BS-3			3.0	81.0	250.6	0.7	7.8
BS-0	300	9,600	0.1	85.6	300.4	0	0
FS-3			3.0	84.9	300.4	0.7	6.7
RS-0	450	7,600	0.1	104.7	450.8	0	0
BS-3			2.7	104.2	450.8	0.5	3.8
BS-0	750	6,300	0.1	NR	751.0	—	—
4B			0.0	146	750.3	0	0
BS-3			2.7	147.7	751.0	1.7	-9.9
BS-0	850	5,700	0.1	162.4	850.2	0	0
BS-3			2.7	166.1	850.2	3.7	-21.0
5B	850	5,700	0.0	163	849.0	0	0
BS-0			2.7	166.1	850.2	3.1	-16.5
BS-0	1,350	4,150	0.1	266.7	1,350.5	0	0
BS-3			2.7	272.0	1,350.5	5.3	-22.0
7B	1,350	4,150	0.0	268	1,349.0	0	0
BS-3			2.7	272.0	1,350.5	4.0	-15.1
BS-0	1,650	3,200	0.1	350.4	1,650.4	0	0
BS-3			2.7	353.7	1,650.4	3.3	-10.5
8B	1,650	3,200	0.0	350	1,650.2	0	0
BS-3			2.7	353.7	1,650.4	3.7	-11.6
9B	2,000	2,300	0.0	475	2,000.8	0	0
9P3			0.0	477	2,000.4	2.0	-5.0
9P10			10.0	481*	2,000.4	6.0	-14.2
BS-0	2,500	1,400	0.1	721.4	2,499.2	0	0
BS-3			2.7	723.8	2,499.2	2.4	-3.4
BS-10			9.7	724.6	2,499.2	3.2	-4.5

* Estimated from differential gage arrival.

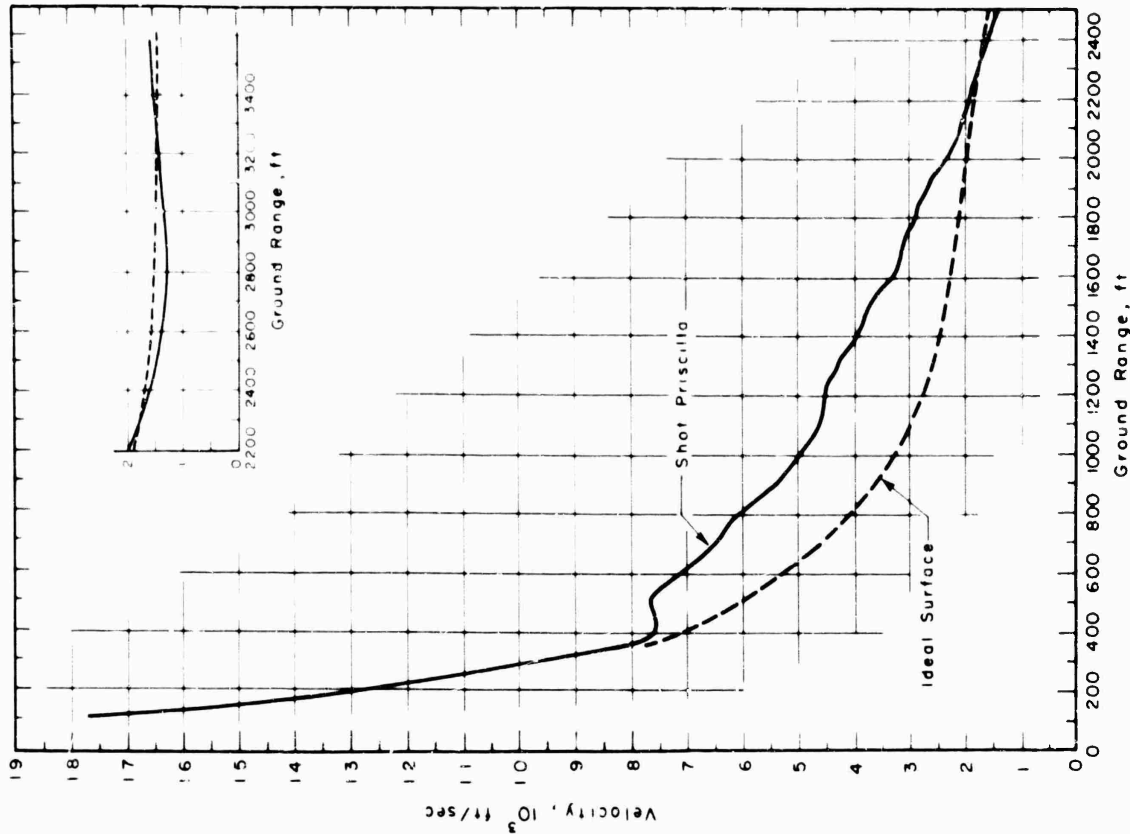


Figure 4.2 Shock velocity, surface level, Shot Priscilla.

sent the angle of the incident wave at these ranges. The dashed line indicates the geometric angle to the burst point at each station; it is evident that the computed orientations of the incident wave agree well with this geometric angle. As the wave travels to increased ranges, the precursor precedes all other phenomena and at 750-foot range (Figure 4.3) the characteristic "toe"

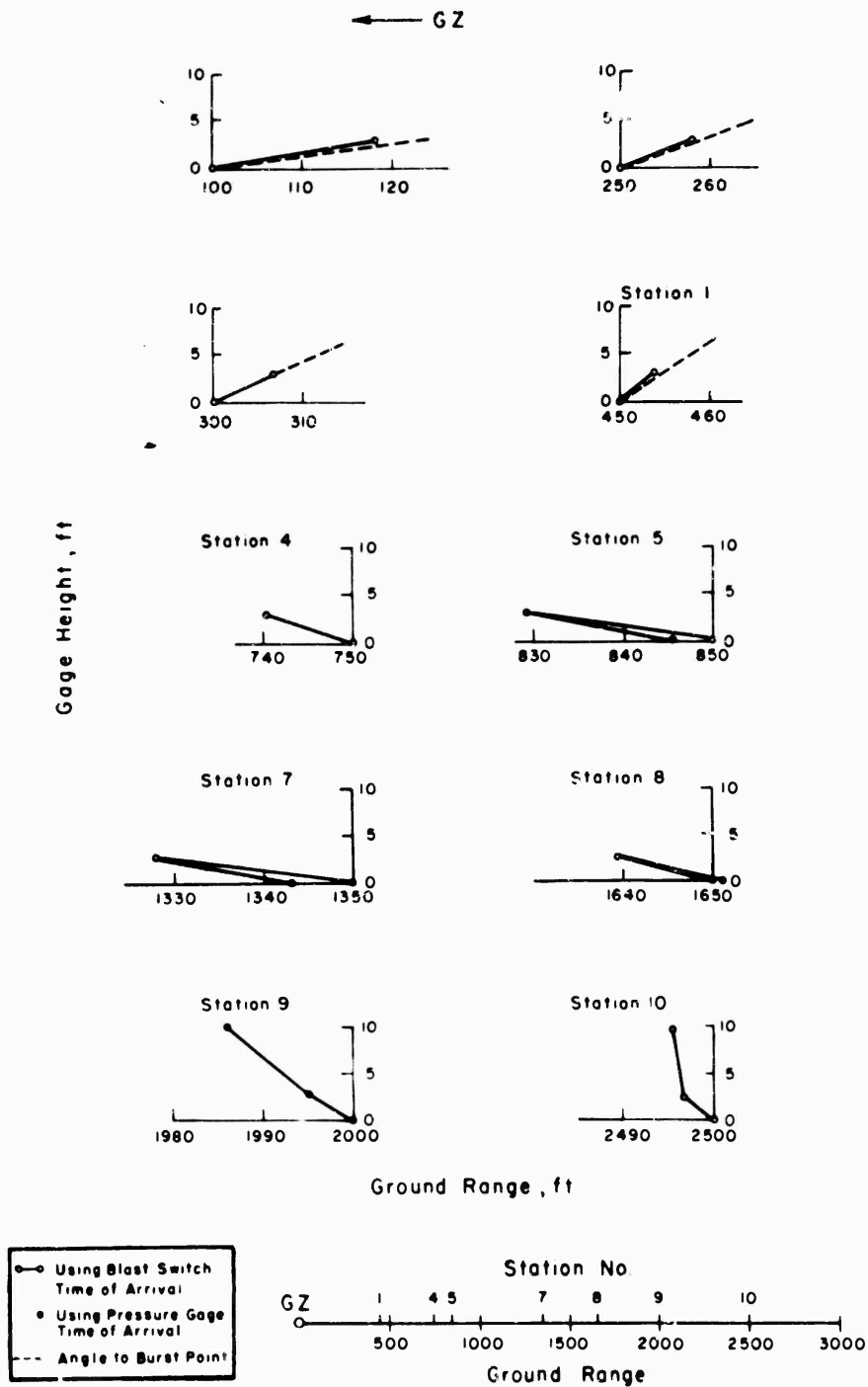


Figure 4.3 Wave-front orientation, Shot Priscilla.

of the precursor wave front is evident. At 850 feet, the effect becomes more pronounced with blast-switch and pressure-gage data yielding similar results. At subsequent ground ranges (Figure 4.3), it is evident that the precursor angle decreases slowly. From orientation data alone, one would conclude that the precursor wave is fully developed between ranges of about 850 and 1,350 feet, whereas it begins to "clean up" rapidly between 2,000 and 2,500 feet. It is

interesting to note here that between 2,000 and 2,500 feet the wave forms of overpressure-time records (Table 3.1) change from Type 1 to Type 3, which indicates that the precursor wave is dissipating rapidly in this region.

4.2 PRESSURE MEASUREMENTS

4.2.1 Overpressure. In early weapon-effects tests, because the pressure records were mostly classical in form, it was possible to describe unambiguously the essential characteristics of the overpressure results using a few physical quantities such as peak pressure, positive-phase duration, and pressure impulse. With these data, plots of peak pressure versus ground range, etc., were constructed and became the bases for military planning, damage analysis, and comparisons with other test results.

More-recent tests have produced pressure records which are markedly nonclassical in form. The classical physical quantities seldom have corresponding counterparts on a disturbed (non-classical) air-blast record. That is, a quantity such as peak overpressure loses much of its value as a dependable and useful parameter when, for disturbed blast waves, the maximum pressure may occur almost any time after blast arrival and may be associated with either a sharp-peaked or a broad-humped pressure rise. For this reason, a revised method of data presentation was introduced in the Teapot report (Reference 4). This method combined maximum pressure data with data on wave-form classification; that is, associated with each datum point is the designation of the type of wave form from which the data are obtained.

Maximum Overpressure. Maximum overpressure data for Shot Priscilla are presented in Figure 4.4; also included in the figure is the peak overpressure over an ideal surface from Shelton's calculations (Reference 20) and the peak precursor overpressures measured on Priscilla.

It is evident from Figure 4.4 that, at the highest recorded pressures, the Priscilla results agree well with those that would be predicted over an ideal surface. The depression of peak overpressure measured at the surface, so characteristic of precursor-producing shots, is manifest on Priscilla beginning at Station 6 (1,050-foot range). Except for data at 2,000 feet, the surface measurements are consistently less than indicated by the ideal curve. It is expected that the measurements, if they had been obtained at ground ranges exceeding 3,500 feet, would eventually show approximate agreement with the ideal. On previous shots this agreement was reached near 7 or 8 psi overpressure. There is no apparent explanation for the agreement with the ideal surface curve at 2,000 feet; at this station Type 1 wave form has reached the limit of its development and is about to change form.

The aboveground pressure measurements all indicate higher peak pressures than those measured at the ground surface; also, where 10-foot-level data are available, they indicate even higher peak pressures than those observed at the 3-foot level. This latter result is similar to observations from previous precursor-forming shots; however, the Priscilla Project 1.3 data show no significant wave-form differences with increased height aboveground, as has been observed in the past.

The maximum precursor overpressure data from Priscilla shown in Figure 4.4 indicate that within ranges of about 1,000 feet of ground zero the precursor pressures were about one tenth the peak overpressure and decreased with ground range at about the same rate. However, from 1,350- to 2,500-foot range the maximum precursor pressure decays very little, after which it drops off similarly to the peak-overpressure decrease with range. Comparing the surface level and aboveground precursor maxima leads to no definite conclusions; although the maxima at the 3-foot level are larger than at the surface, the data at 10 feet are all slightly less than at the surface. It should be mentioned that in the wave-form classification system employed here the Type 6 form is the last form to possess two maxima—one of which can be identified with the precursor wave, i.e., Types 7 and 8 are both single-peaked forms. Therefore, since the Priscilla records at 3,500-foot range are both Type 6 forms, it is concluded that the data at 4,500 feet, although lost, would have yielded no additional precursor-wave data. Further, it should be noted that of all the pressure measurements obtained on this project, the overpressure

measurements are probably least affected by the presence of suspended particulate matter (mainly dust) in the airflow. This is a commentary on the sensitivity of the gage to entrained dust but says nothing of the role of dust in the formation and propagation of the precursor wave.

Comparison with Upshot-Knothole Shot 10. To compare the Priscilla data with previous results, a logical choice appears to be Shot 10 of Operation Upshot-Knothole.

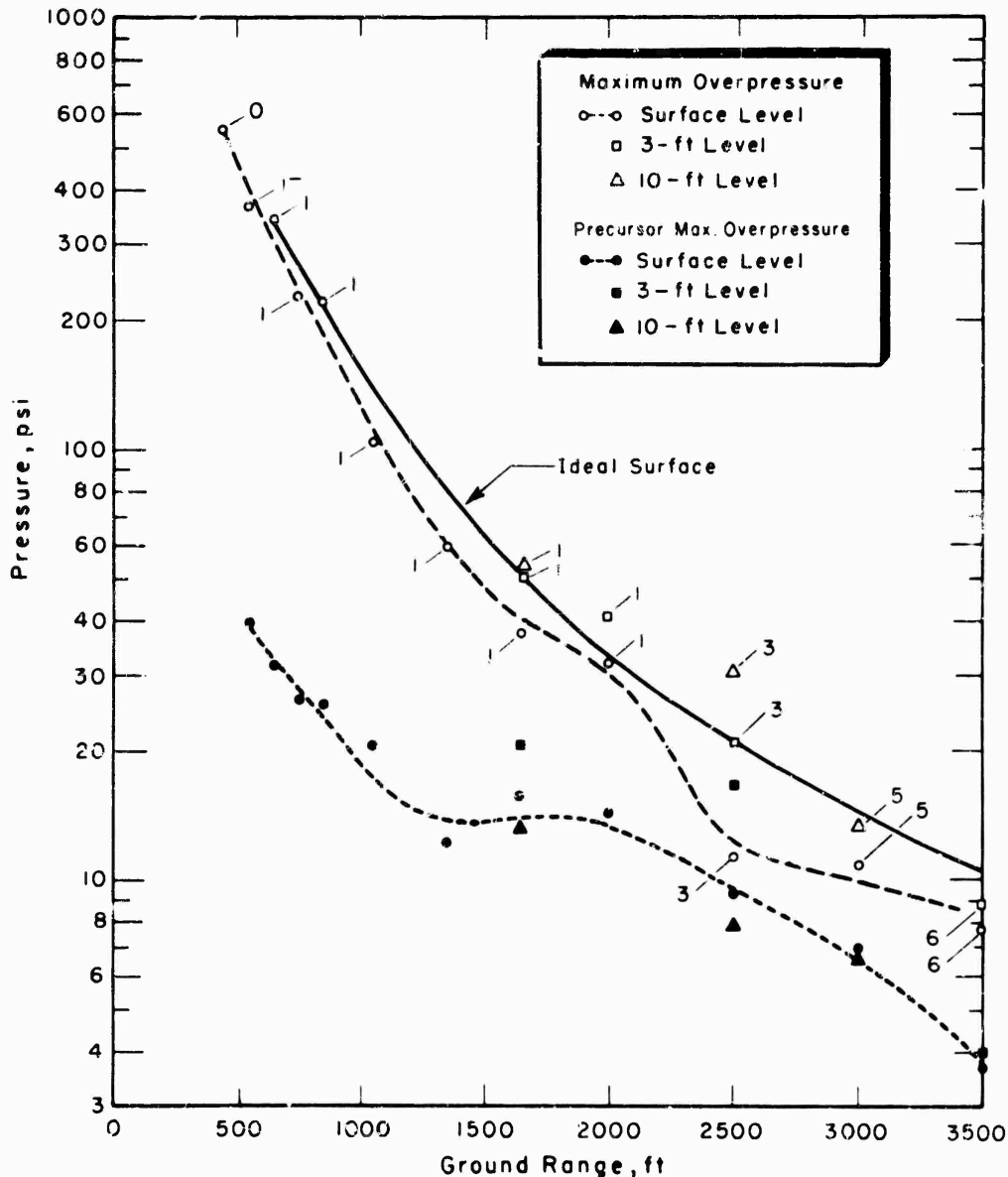


Figure 4.4 Maximum overpressure, Shot Priscilla.

This latter shot was smaller in yield than Priscilla (14.9 kilotons compared with 36.6 kilotons), but was fired at almost exactly the same scaled burst height (204 against 202 feet).

The comparison between the two shots is shown pictorially in Figure 4.5, where the Priscilla curves from Figure 4.4 are included as well as the Upshot-Knothole-10 data, scaled to Priscilla yield conditions. Except for the closest station where the Upshot-Knothole gage was evidently overloaded, Upshot-Knothole peak-overpressure data agree well with the Priscilla data out to about the 1,600-foot range. However, between 1,600 feet and about 2,600 feet, the Upshot-Knothole data appear to fall significantly lower than Priscilla, recovering at the longer ranges, beyond 2,800 feet.

Comparison on the basis of wave form is very consistent between the two shots. For this scaled burst height (~200 feet) and yield interval one can expect Type 1 forms out to about 3,000-

foot range and no farther. Also, it appears likely that one would have observed a Type 2 form on Priscilla if a gage had been positioned between the 2,000 and 2,500-foot stations. Finally, looking at both Figures 4.4 and 4.5, it is evident that the changes from Types 2 to 3 to 4 occur in short intervals of ground range, which explains why it is rare that all three of these wave-form types are observed on a single shot.

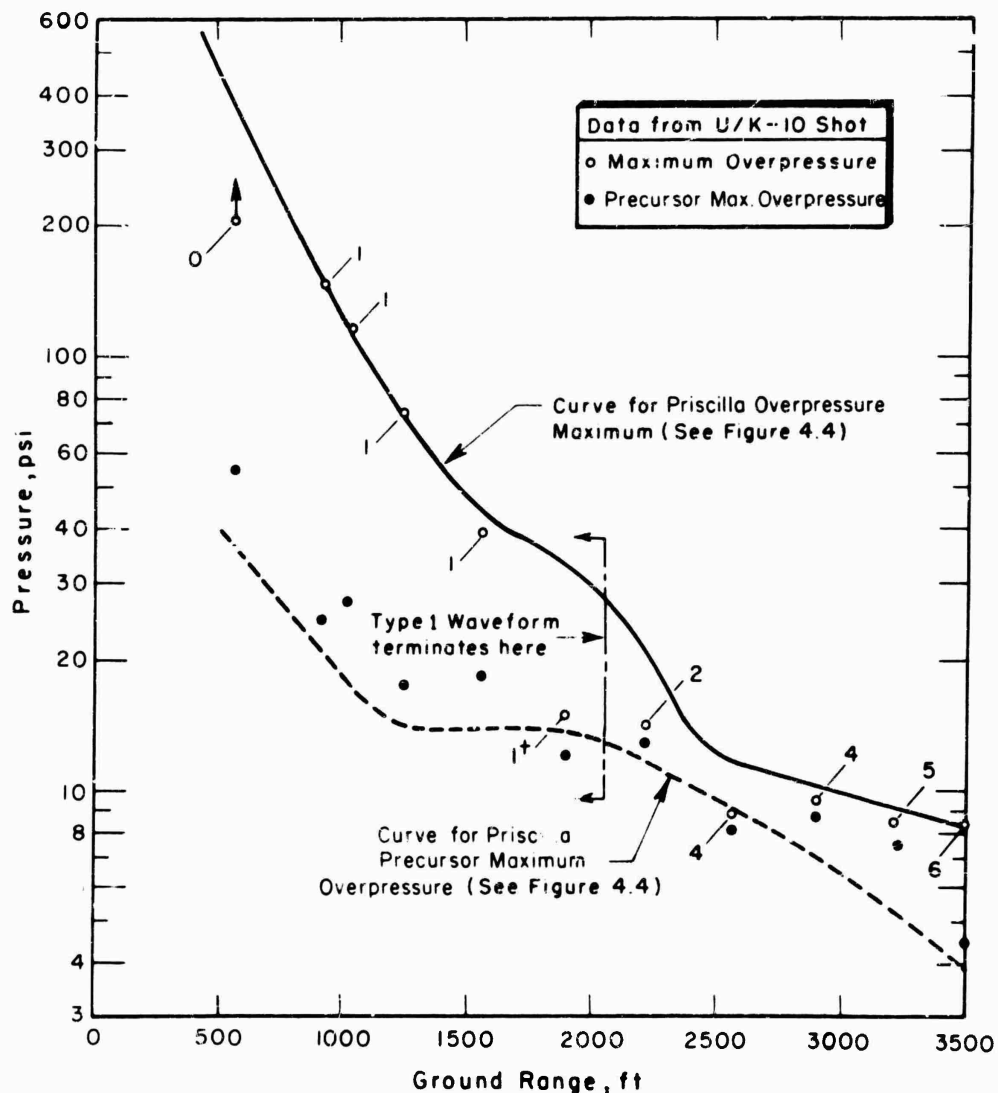


Figure 4.5 Maximum overpressure, Upshot-Knothole Shot 10 and Shot Priscilla.

The maximum precursor overpressures shown in Figure 4.5 indicate that the Upshot-Knothole-10 pressures were somewhat higher than comparable Priscilla results. The differences are not believed to be significant, and the decay of maxima with distance appears to be similar for the two shots.

Overpressure Decay behind Shock Front. An analytical representation of the overpressure profile (Reference 21) of the classical shock wave at a given distance from an explosion is provided by:

$$\Delta p = \Delta p_m (1 - t/\Delta t) e^{-t/\Delta t} \quad (4.1)$$

Where: Δp = the overpressure at time t ,
 Δp_m = the peak value of overpressure at $t = 0$,
 t = the time measured from shock arrival, and
 Δt = the positive-phase duration of the blast wave.

Equation 4.1 is approximately valid for overpressure maxima not exceeding 25 psi. In his paper on strong-shock spherical blast waves, Brode (Reference 5) derives some relations for the pressure decay behind a spherical shock moving through an ideal gas medium. Brode shows that for peak overpressures above one atmosphere the decay is not a simple exponential, since the early

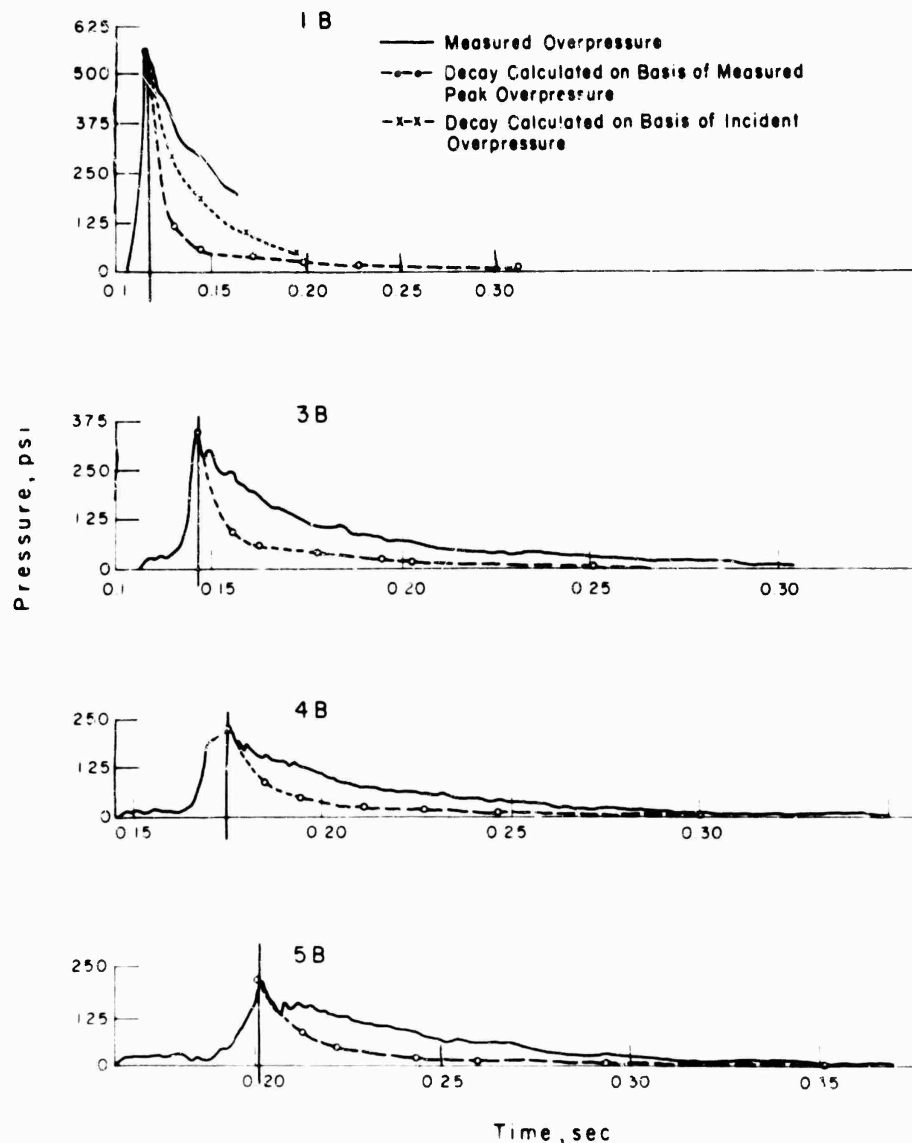


Figure 4.6 Decay of overpressure behind shock front, Stations 1 to 5, Shot Priscilla.

portion of the pressure-time function decays more rapidly than do the later parts. The results obtained by Brode and Equation 4.1 become identical when

$$\frac{\Delta p_m}{P_0} = 0.5 \quad (4.2)$$

where P_0 is the ambient pressure in front of the shock front.

Both these methods of computation are strictly limited to the case of free-air wave propagation. Thus, any application of the methods to shock phenomena which are influenced by a ground plane (in either regular or Mach reflection regions) necessarily involves an approximation of unknown magnitude. Nevertheless, some interesting comparisons come out of a look at the Priscilla data.

Comparisons of the calculated and measured decay of overpressure versus time on Priscilla are presented in Figures 4.6 and 4.7. Since the data at Station 1 (1B record) were probably taken in the region of regular reflection, the decay was calculated in two ways. First, the decay was

computed using peak pressure as measured (i. e., reflected pressure), with these calculations plotted as circles. Second, considering the incident pressure only (about 125 psi at this range), the decay was recomputed and the results plotted as fractions of the peak incident pressure (shown as crosses on Figure 4.6). The first calculation shows a theoretical pressure decay much steeper than measured; in addition, the second computation, although its results are closer to measured decay, indicates a steeper decay than the measurement. This means that assuming ideal surface conditions, the measured decay is even slower than that calculated on the basis of

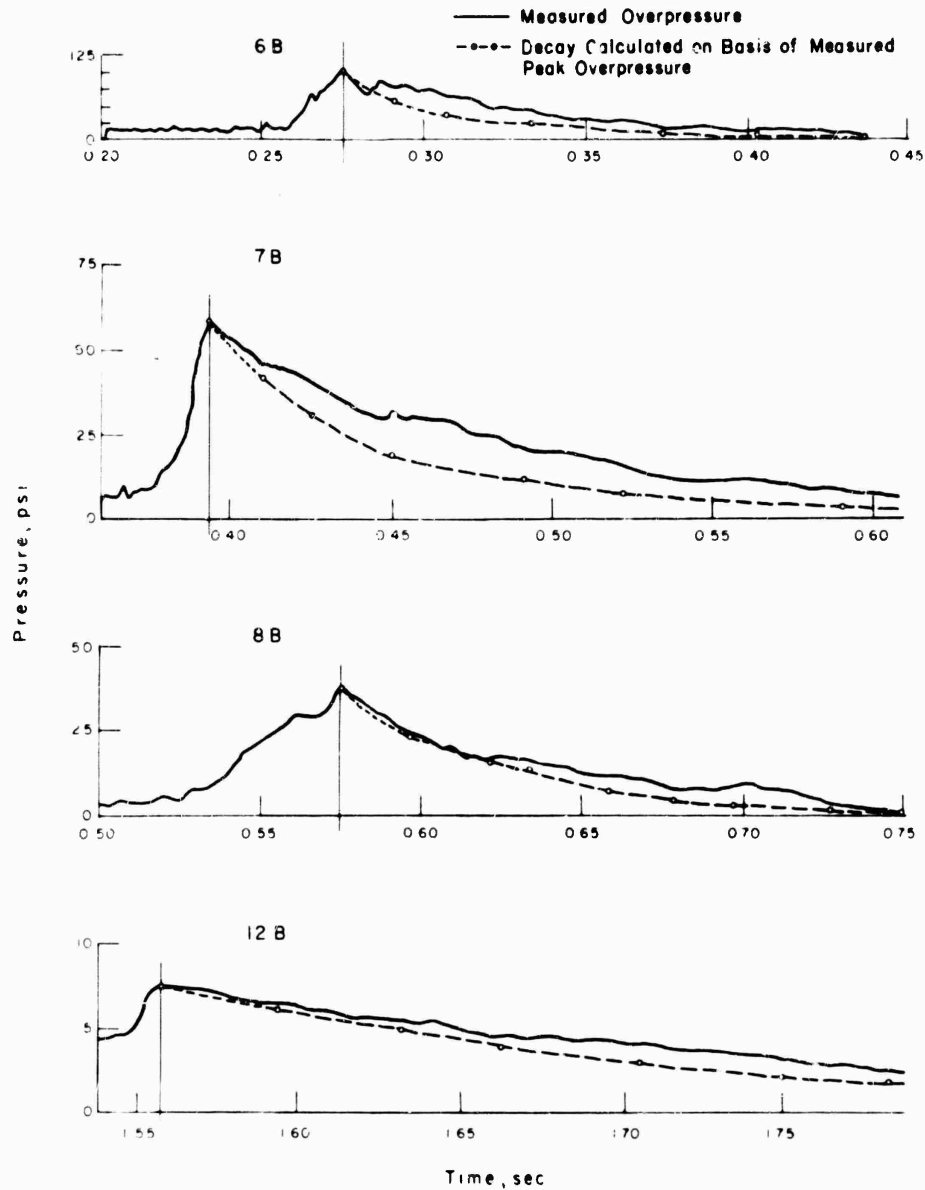


Figure 4.7 Decay of overpressure behind shock front, Stations 6 to 12, Shot Priscilla.

incident overpressure—a result that suggests the influence of thermal disturbance upon the blast wave.

The subsequent examples of comparing calculations with measurements indicate the same general behavior, i. e., the calculations show sharper pressure decay than do the pressure-time records. The 2B record is not considered because of the cable break. Records 3B through 6B show a very early decay which agrees well with calculations, but after 5 or 10 msec the gage record appears to "hump up" and decay more slowly. At Station 8 (8B, Figure 4.7) the calculated decay agrees quite well with the measured; even here, however, the gage record displays the characteristic hump after an initial smooth decay. The last comparison, at Station 12, is

not unlike the 8B comparison, but here again the evidence is strong that the blast wave is disturbed.

The analysis indicates the magnitude of the deviations from classical decay observed in the precursor region. Actually one might use such a deviation as one measure of the severity of the precursor disturbance. For Shot Priscilla (Figures 4.6 and 4.7), one would conclude that the disturbance to classic conditions peaked at about Station 3 (650-foot ground range) and began to dissipate rapidly with increased range.

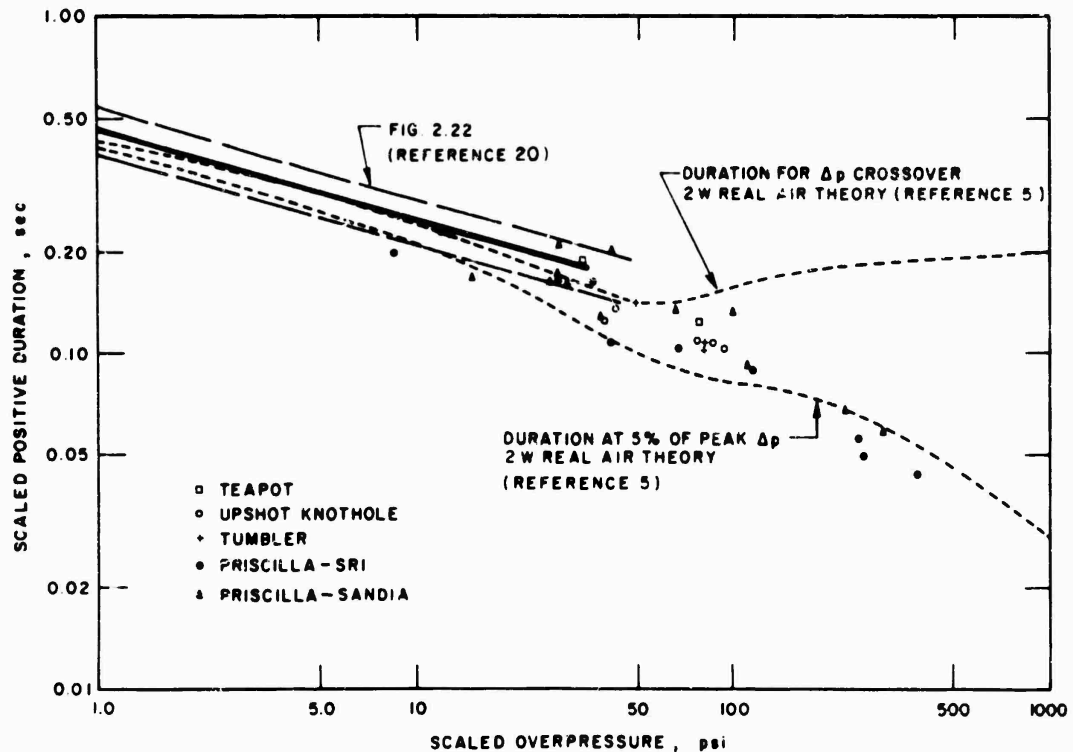


Figure 4.8 Positive-phase duration versus overpressure, A-scaled, various shots.

Overpressure Positive Duration and Impulse. In Reference 20, overpressure positive-phase duration and positive impulse as a function of peak pressure from all nuclear air bursts prior to Upshot-Knothole are A-scaled and plotted; subsequently, Teapot data were added to the plots (Reference 4). Although the pre-Upshot-Knothole data scatter a good deal, it is found that about 90 percent of the datum points fall within ± 15 percent deviation from an average curve. Also, it is found that the curve did not fit well with data corresponding to overpressures higher than about 30 psi (A-scaled).

Figures 4.8 and 4.9 present the major portion of available data on duration and impulse for overpressures greater than 10 psi. As a guide in extrapolating previous correlations, the results obtained by Brode (Reference 5) are included in the figures, modified by the 2W theory (surface bursts).

The data on duration (Figure 4.8) do not follow the theoretical calculations for overpressures greater than 100 psi. This may be because of limitations of the instrumentation; to prevent the maximum overpressure from over-ranging the gage or recording medium, the sensitivity of the system must be reduced at high pressures. A check of the SRI system indicates that the error of reading pressure from camera records amounts to approximately 5 percent of the peak overpressure. Using this criterion, a theoretical duration curve has been constructed for the time at which the overpressure reached 5 percent of its peak value. This curve deviates markedly from the theoretical duration curve (associated with zero overpressure) as the pressure increases. However, over 95 percent of the overpressure total positive impulse is included before the overpressure drops to 5 percent of the peak overpressure. Hence, the theoretical curve of Figure 4.8 is believed to be a legitimate guide in the high-pressure region provided allowance is made

for the increased duration in the 10- to 100-psi region due to precursor action. Priscilla data appear to agree well with the theoretical 5 percent curve; in addition to Project 1.3 data, useful data from Projects 34.1 and 1.5 (References 22 and 23) are plotted. It is significant that some of the data at very-high pressures fall below the theoretical curve; the 2W theory approximation is not expected to hold where the ground range is less than or comparable with the burst height.

In Figure 4.9, Priscilla impulse data are in agreement with the theoretical curve at high pressures. At intermediate pressures (10 to 100 psi) measured impulse is from 0 to 50 percent greater (due to precursor action) than 2W theory predicts. While it is understood that 2W theory does not apply theoretically to air bursts, the impulse resulting from 2W theory will probably be a lower limit. It should be noted that although the duration data (Figure 4.8) at high pressures fall below the theoretical curve, the impulse data agree well. A look at the decay of pressure

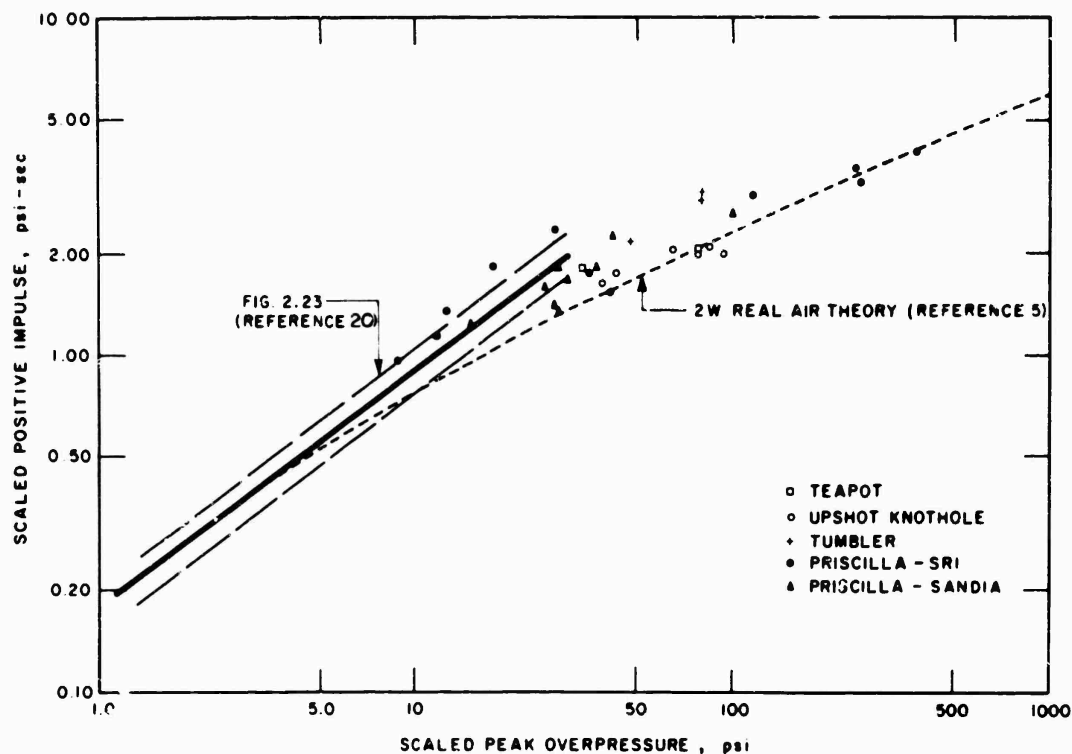


Figure 4.9 Positive impulse versus overpressure, A-scaled, various shots.

behind the shock front (Figure 4.6) will resolve this apparent anomaly; it is evident that thermal disturbances at close-in ranges effect changes in total impulse (i.e., slower pressure decay behind shock front) while not changing the duration significantly.

4.2.2 Total-Head Pressure. Peak total-head pressures are presented in Figure 4.10. Because of cable breaks early in the pressure-time history, data at Stations 2 and 4 (see Figure 3.5) are rather indefinite. All data are at the 3-foot level. Also shown on the plot of Figure 4.10 are the ideal surface curves for both maximum dynamic pressure and total-head pressure: there is a sharp jump in the ideal values at the ground range corresponding to transition from regular to Mach reflection.

Figure 4.10 reveals that the only data obtained in the region of regular reflection agree well with the ideal surface prediction. Although it is difficult to evaluate the data from gages which suffered a cable break, the points appear to be reasonably consistent with the ideal curve. However, at Station 5 (850-foot ground range) the peak total pressure is significantly higher than the curve; this behavior is maintained at 1,050- and 1,350-foot ranges to an even more pronounced degree. The data at 2,000 feet (9Z3) were lost, but at 2,500 feet the maximum total-head pressure agrees fairly well with ideal. Only at Station 10 are both total-head and pitot-tube gage data available; Figure 3.7 presents the comparison between the 10Z3 record and the sum of the

10P3 and 10Q3 records. Unfortunately, the wave form is like Type 3, which is a highly disturbed form not amenable to correlation. However, the peak total-head pressures obtained with these two gages check closely (Figure 4.10) with each other and with the ideal curve.

Also plotted on Figure 4.10 are the total-head precursor maxima, which show similar behavior to that of the peak pressure. At close-in ranges, the precursor total pressures decrease steeply with increased ground range, then level off near 100 psi between the 850- and 1,350-foot range, and finally decrease sharply at 2,500 feet.

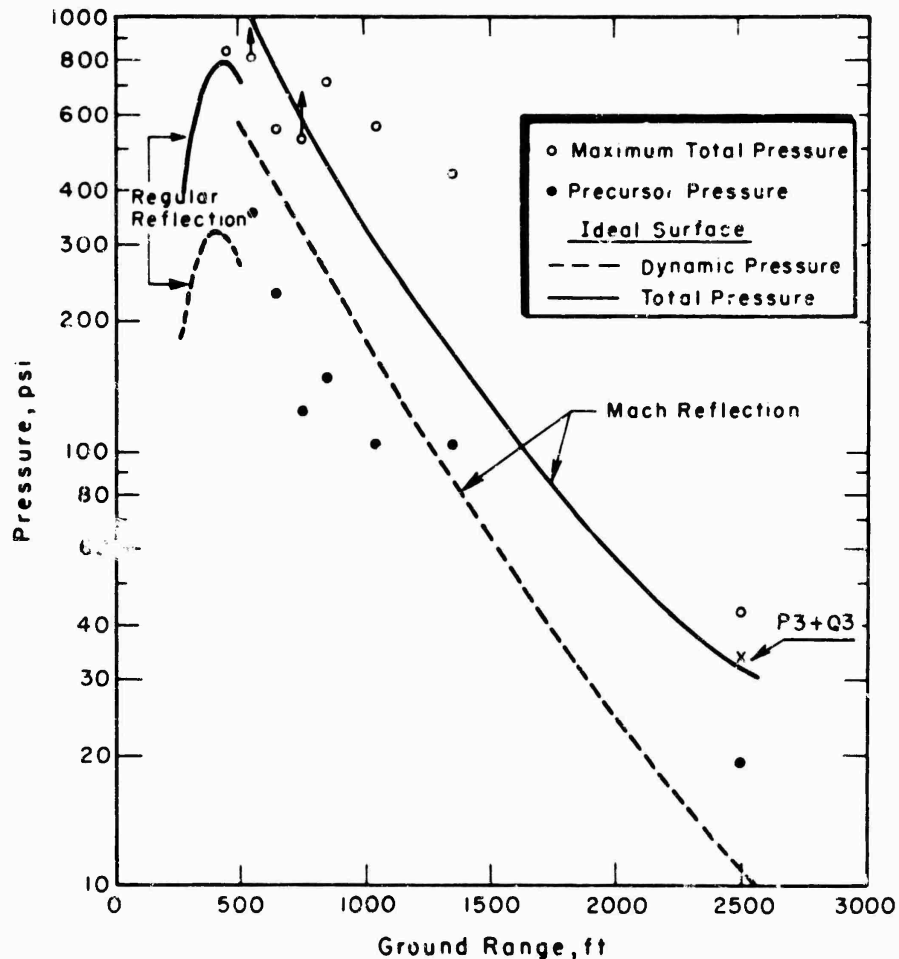


Figure 4.10 Total-head pressure, 3-foot level, Shot Priscilla.

4.2.3 Differential Pitot-Tube Pressure. Figure 4.11 presents the measurements of Priscilla differential pitot-tube pressure. As was pointed out in Section 3.4 (Figures 3.8 through 3.10), many of the differential (front) ports of the pitot tubes were obviously plugged with dust shortly after shock front arrival. This seriously limits the usefulness of the data. For instance, no maximum differential pressure was obtained at Stations 6 and 7; the peak pressures recorded can be identified with the precursor wave. However, reference to Figure 4.11 allows some pertinent conclusions. Maximum differential pressures are higher than predicted over an ideal surface, with the 10-foot-level data appreciably larger than those at the 3-foot level. This is in contrast to the experience during Teapot Shot 12 (Reference 4) where lower differential pressures were observed at the higher levels. Approximate curves have been fitted to the datum points; however, there are too few measurements to attach much significance to the curves.

It is possible, with both the total-head pressure and the static overpressure measured on separate gages, to compute a maximum differential pressure (3-foot level) as measured at the close-in ground ranges. These results are plotted in Figure 4.11, where the behavior is similar to that observed for total-head pressure. The data agree well with ideal out to the 750-foot range, after which the peak pressure jumps to 2 to 4 times ideal. The single datum point at 2,500 feet

indicates that the calculated differential pressure is somewhat higher than that measured by the pitot-tube.

Finally, it is pertinent to obtain the total-head-minus-static-pressure results for the precursor wave. These data are also plotted in Figure 4.11. It is significant that these data do not display the rise to higher pressures as does the main wave between 850- and 1,350-foot range.

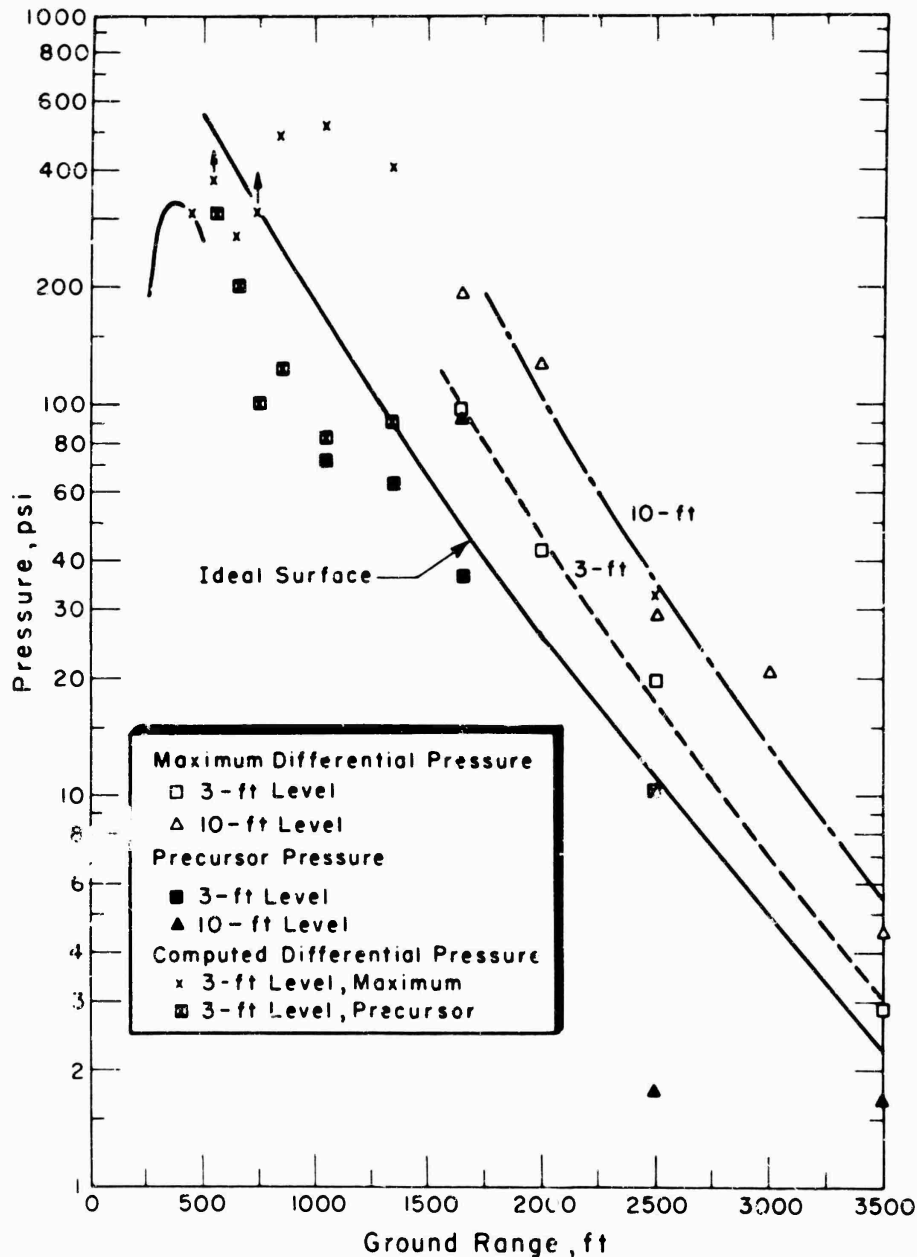


Figure 4.11 Maximum differential pressure, Shot Priscilla.

4.3 MACH NUMBER AND COMPUTED DYNAMIC (AIR-PLUS-DUST) PRESSURE (q^*)

The Mach number of the flow behind the shock front as a function of time for each gage station was computed according to the method outlined in Section 1.3.4 (Figures 4.12 to 4.14). Maximum Mach numbers are listed in Table 4.4. It should be noted that the calculation (see Equation 1.9) becomes uncertain for $\Delta p_g = 0$ or for $(\Delta p_p + P_0)/(\Delta p_g + P_0) < 1$; for these cases, no results are plotted on the figures and an appropriate symbol indicates the nature of the uncertainty. At the stations where no total-head measurement was available, the sum $([\Delta p_p - P_s] + \Delta p)$ obtained from the pitot-tube was used to compute the Mach number.

TABLE 4.4 CALCULATED MACH NUMBER AND DYNAMIC PRESSURE, SHOT PRISCILLA

Station	Ground Range	Gage Height	Mach No. Cal-culation Method	Maximum Mach No.	Time of Maximum Mach No.	Maximum Dynamic Pressure		Time of Maximum Differential Pressure (pitot)	Maximum Differential Pressure		Time of Maximum Differential Pressure (pitot)	Maximum Total-Head Minus Static Pressure		Time of Maximum Total-Head Minus Static Pressure
						psi	sec		psi	sec		psi	sec	
As-read														
1	450	3	Z	0.93*	0.124	258	0.109	—	—	—	—	310	0.112	
2	550	3	Z	1.89*	0.119	287	0.126	—	—	—	—	373	0.126	
3	650	3	Z	1.73*	0.139	211	0.150	—	—	—	—	270	0.150	
4	750	3	Z	1.63*	0.163	211	0.169	—	—	—	—	308	0.169	
5	850	3	Z	1.88	0.192	309	0.201	—	—	—	—	498	0.200	
6	1,050	3	Z	2.17	0.257	225	0.271	—	—	—	—	519	0.266	
7	1,350	3	Z	2.33	0.382	143	0.390	—	—	—	—	412	0.386	
8	1,650	3	$\Delta p+Q$	1.81	0.480	44.1	0.475	98.1	0.480	—	—	—	—	
8	1,650	10	$\Delta p+Q$	2.27	0.525	72.6	0.545	193	0.525	—	—	—	—	
9	2,000	3	$\Delta p+Q$	1.42	0.740	29.0	0.530	42.3	0.530	—	—	—	—	
10	2,500	3	Z	1.26	1.230	23.1	0.758	19.9	0.746	—	—	32.5†	0.758	
10	2,500	3	$\Delta p+Q$	1.09	1.260	18.0	0.750	19.9	0.746	—	—	—	—	
10	2,500	10	$\Delta p+Q$	1.36	1.110	27.7	0.825	28.2	0.865	—	—	—	—	
11	3,000	10	$\Delta p+Q$	1.15	1.370	17.5	0.370	20.6	1.370	—	—	—	—	
12	3,500	3	$\Delta p+Q$	0.74	1.890	5.31	1.890	2.81	1.890	—	—	—	—	
A-scaled to 1-kt radiochemical release at sea level														
1	131	0.87	Z	0.93*	0.0358	286	0.0315	—	—	—	—	344	0.0324	
2	160	0.87	Z	1.89*	0.0344	319	0.364	—	—	—	—	414	0.0364	
3	189	0.87	Z	1.73*	0.0402	234	0.0433	—	—	—	—	300	0.0433	
4	218	0.87	Z	1.63*	0.0471	234	0.0488	—	—	—	—	342	0.0433	
5	247	0.87	Z	1.88	0.0555	343	0.0581	—	—	—	—	553	0.0578	
6	305	0.87	Z	2.17	0.0742	250	0.0783	80.6	0.0745	—	—	576	0.0768	
7	392	0.87	Z	2.33	0.1104	159	0.1127	69.7	0.1069	—	—	457	0.1115	
8	479	0.87	$\Delta p+Q$	1.81	0.1381	490	0.1372	109	0.1387	—	—	—	—	
8	479	2.90	$\Delta p+Q$	2.27	0.1507	80.6	0.1575	214	0.1517	—	—	—	—	
9	581	0.87	$\Delta p+Q$	1.42	0.2138	32.2	0.1531	47.0	0.1531	—	—	—	—	
10	726	0.87	Z	1.26	0.3553	25.6	0.2190	22.1	0.2155	—	—	36.1†	2.190	
10	726	0.87	$p+Q$	1.09	0.3640	20.0	0.2167	22.1	0.2155	—	—	—	—	
10	726	2.90	$p+Q$	1.36	0.3207	30.7	0.2383	31.3	0.2499	—	—	—	—	
11	871	2.90	$p+Q$	1.15	0.3958	19.1	0.3958	22.9	0.3958	—	—	—	—	
12	1,016	0.87	$p+Q$	0.74	0.5460	5.89	0.5460	3.12	0.5460	—	—	—	—	

* Cable break, at or near time of peak.

† Maximum Z- Δp = 28.7, time of maximum Z- Δp = 1.230 — as read.

‡ Maximum Z- Δp = 31.9, time of maximum Z- Δp = 0.3553 — A-scaled.



As indicated in Section 1.3.4 and Figure 1.2d, the errors involved in calculating Mach number (M_2) by this method are dependent upon (1) the mass ratio of dust to air of the flow mixture and (2) the dust registry coefficient of the gage. Figure 1.2d shows that the errors in M_2 calculation from these factors are always in the direction of increasing the calculated M_2 over that for clean

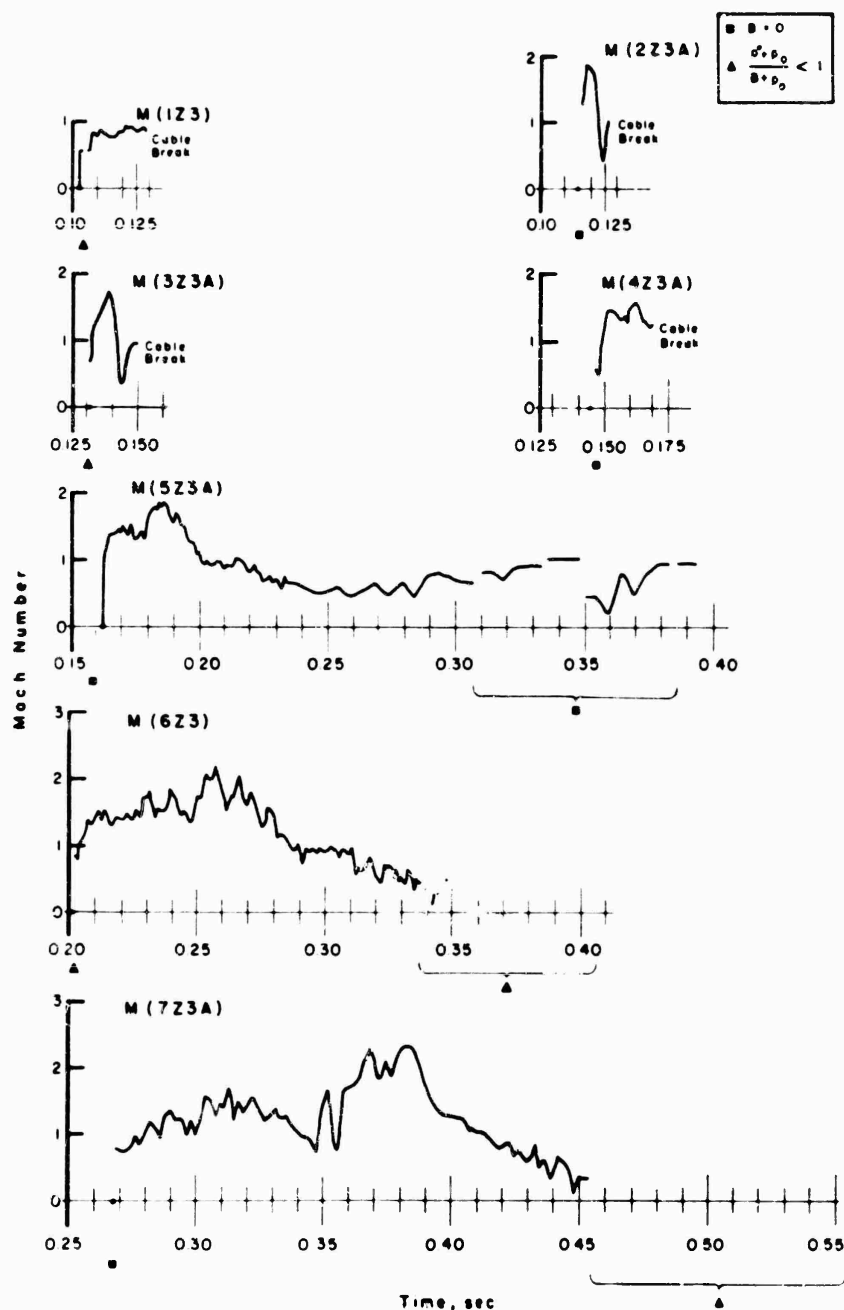


Figure 4.12 Mach number versus time, Stations 1 to 7, Shot Priscilla.
(For explanation of symbols, see text.)

air. From these remarks, one must conclude, first, that the M_2 calculations using total-head and pitot-tube results are not strictly equivalent; second, that one must be cautious about ascribing increases in calculated M_2 to an increase in flow velocity behind the shock front, when increased dust densities can produce the same effect.

Analysis of the Mach number-time plots of Figure 4.12 leads to some rather unusual conclusions. The calculations of Mach number at the first four stations are terminated abruptly due to cable breaks at either the total-head or the surface-overpressure gages. Taking these stations

separately, it is probable that the Station 1 calculation would show no later maxima even if the gage cables had not broken. The situation is quite different at Station 2 because the total-head pressure appears to be increasing at the break while the static overpressure (2B) has begun to decay; hence, it is possible that the computed Mach number at some later time would have been larger than the first peak. Station 3 is not unlike Station 2, although there is a definite indication that the total-head pressure was decaying before the cable broke; thus, it is unlikely that any secondary maxima would exceed the first peak. At Station 4, because the total-head record shows no decay before the cable break, there are possibly later maxima of the Mach number-time plot which are larger than the first peak shown. Subsequent plots of Figure 4.12 are unambiguous. The interesting conclusion one obtains from this figure is that the maximum computed Mach number occurs at Stations 6 or 7 rather than at the close-in range station. Figures 4.13 and 4.14 indicate that at Stations 8 through 12 the trend is toward decreasing maximum Mach number with increasing range; at Stations 8 and 10, where both 3- and 10-foot-level data are available, the 10-foot data yield slightly higher Mach numbers. In general, the Mach number-time plots show very little structure and no characteristic form; hence, for results at Stations 8 through 12, it would not be difficult to determine an average Mach number, averaged over the time of significant pressure measurement.

Presented in Figures 4.15 through 4.17 are the results of computing q^* ($= \frac{1}{2}\rho v^2$) from the Mach number and surface overpressure as outlined in Section 3.2.2. Also shown on these figures, for comparison, are plots of total-head pressure minus surface overpressure versus time. Since the q^* calculation is comparatively insensitive to the entrained dust in the flow and since the surface overpressure measurement is not affected by dust, one can conclude that the differences between the dotted- and solid-line records of Figures 4.15 and 4.16 can be ascribed to the response of the total-head gage to the dust in the flow. Of course, with no data on the actual mass flow versus time or particle size distribution versus time of the dust at each station, this response cannot be converted into quantitative results. However, it can be concluded from the evidence that the effect of dust upon the total-head measurement is rather small at the close-in stations, increasing markedly at Station 5 (850-foot ground range) and beyond. The comparison at Station 10 (Figure 4.17) indicates that the computed q^* results are considerably smoother in wave form than the corresponding total-head-minus-static-pressure plot. At this station, there appears to be no significant difference between using the static overpressure at the surface level or at 3-foot level (pitot tube).

Figure 4.18 presents the maximum values of calculated q^* compared with the ideal surface curve for dynamic pressure. In general appearance the calculated values are somewhat lower than ideal at close-in stations, agree with ideal in mid-ranges, and exceed ideal at 2,500 feet and beyond. At Station 10, the only station where both total-head and pitot-tube measurements were obtained, the calculated q^* maximum values using the two results agree well, although the total-head value is larger (the differential pitot gage probably has a higher dust registry coefficient than the total-head gage). Where both 3- and 10-foot-level data are available at the same station, the 10-foot data indicate higher maxima.

Phenomenologically, it is difficult to evaluate the quantity q^* (calculated). Until more is known about the sensitivity of the gages to dust, Mach number, and pitch angle, and until field measurements are available for dust mass flow and size distribution versus time at each gage station, calculated q^* must be regarded as a very approximate measure of the air-phase dynamic pressure. In order to use these numbers to determine the forces on structures enveloped by the blast wave, one must add the effect of the entrained dust. Further work is needed to establish the magnitude of the forces due to dust loading as a function of Mach number, structure Reynolds number, etc.

4.4 PRECURSOR PHENOMENA

The most significant air-blast results of Priscilla, and more specifically, all the results of Project 1.3, were obtained where air-blast behavior departed from ideal. Such departures have

$$\frac{B \cdot O}{A \frac{B^2 + B_0^2}{B + B_0}} <$$

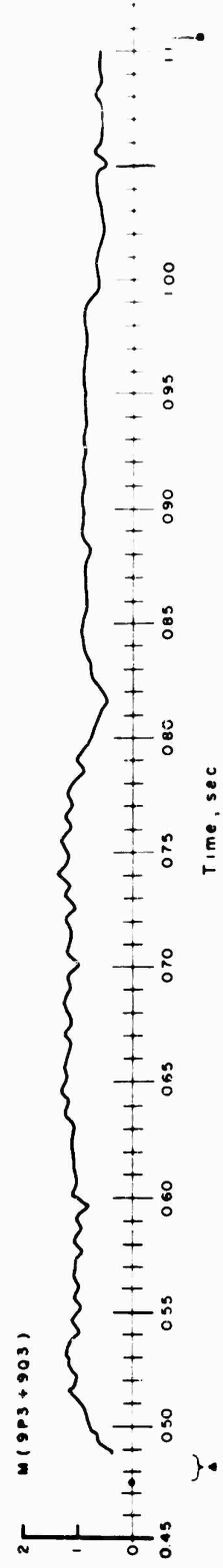
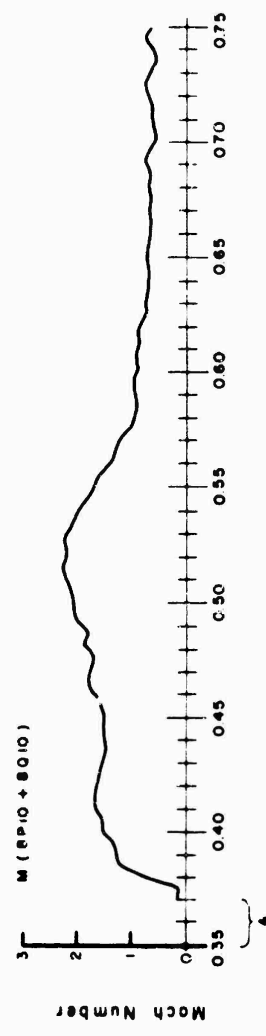
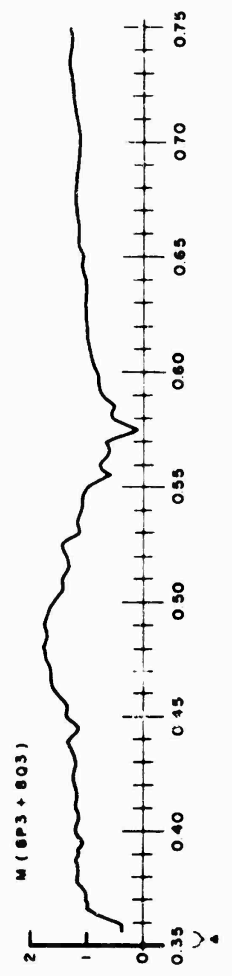


Figure 4.13 Mach number versus time, Station 8 and 9, Shot Priscilla.
(For explanation of symbols, see text.)

$$\Delta \frac{P_1 P_2}{B + P_2}$$

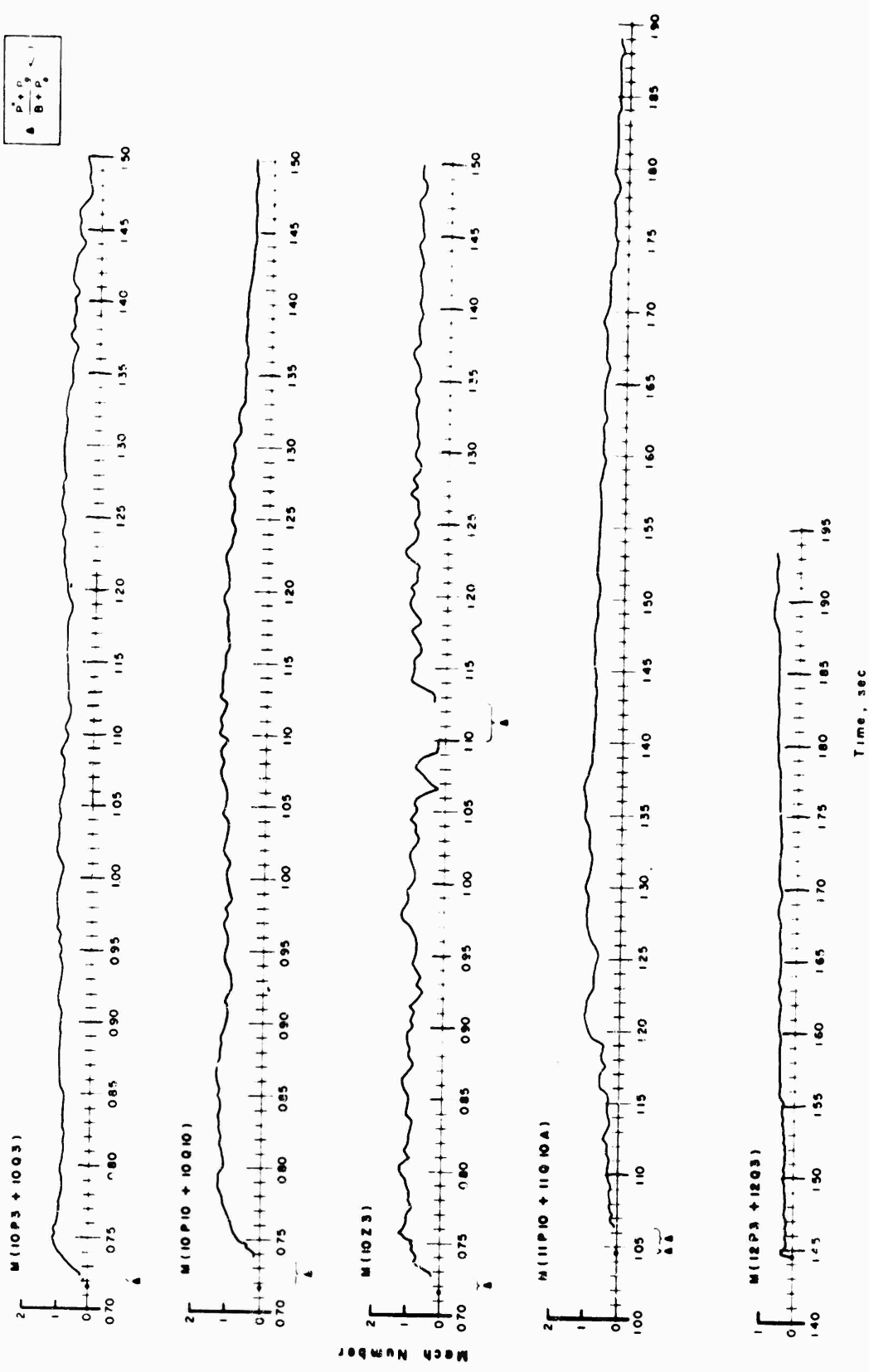


Figure 4.14 Mach number versus time, Stations 10 to 12, Shot Priscilla.
 (For explanation of symbols, see text.)

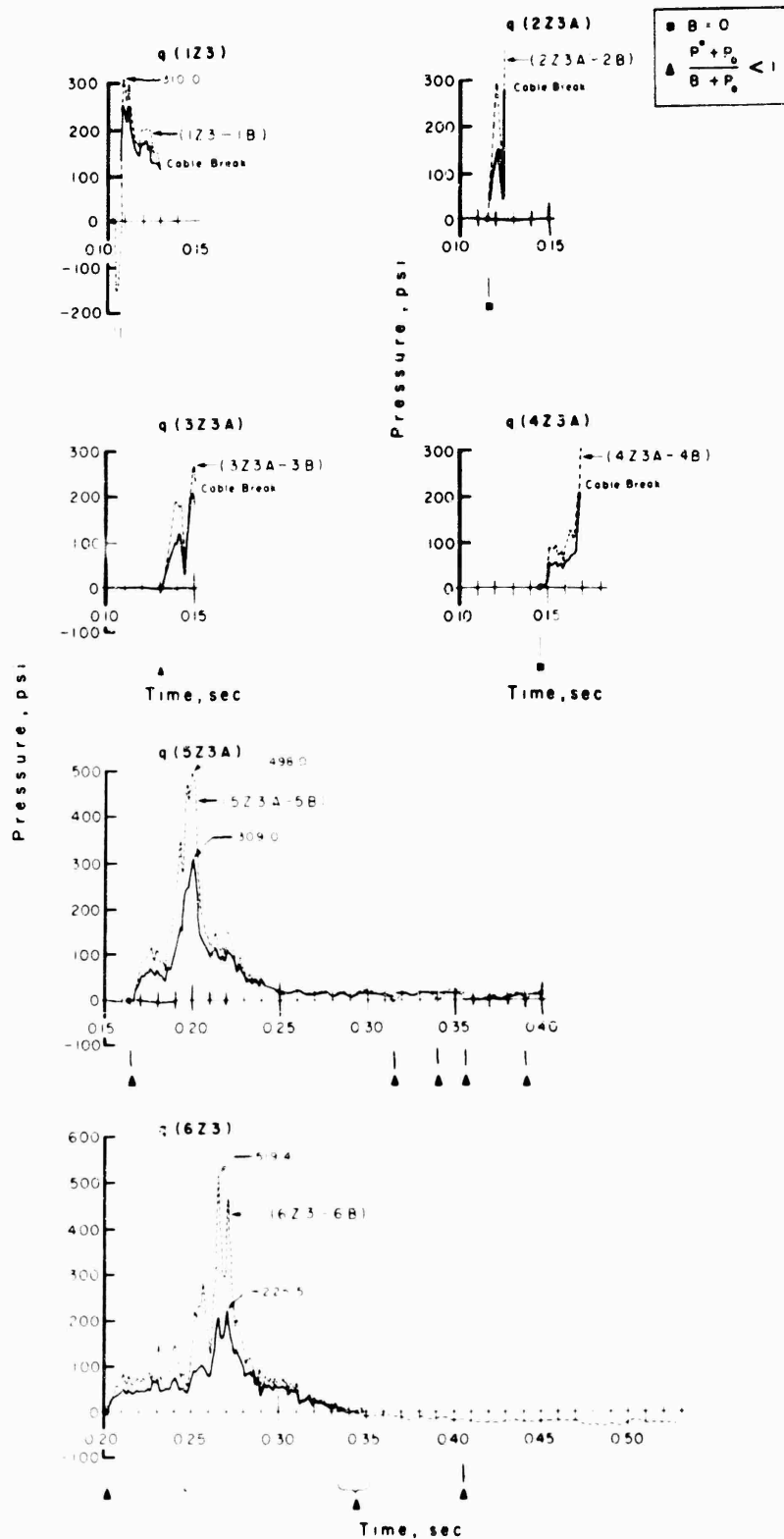


Figure 4.15 Dynamic pressure (q^*) versus time, Stations 10 to 12, Shot Priscilla. (For explanation of symbols, see text.)

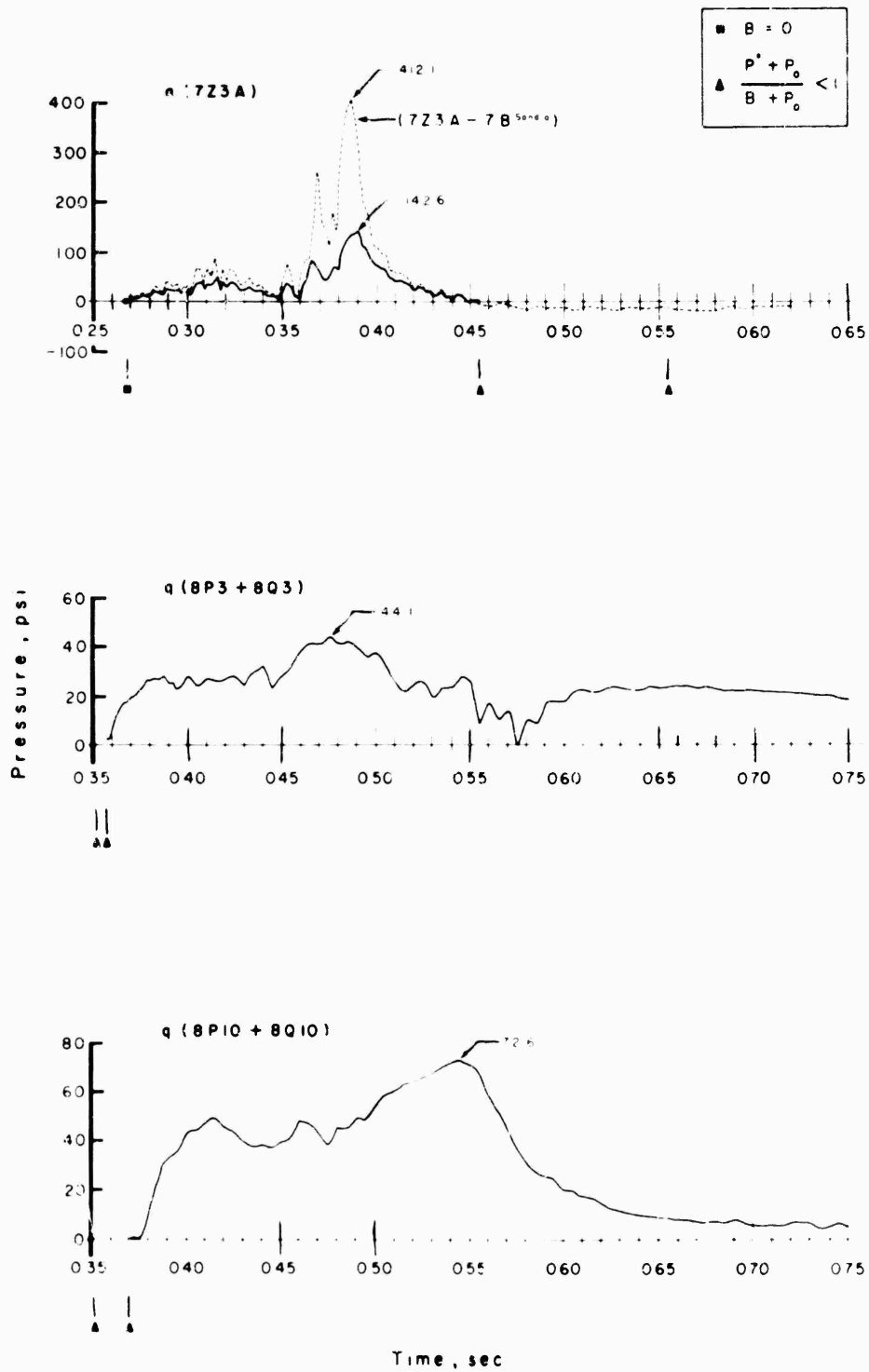


Figure 4.16 Dynamic pressure (q^*) versus time, Stations 7 and 8, Shot Priscilla. (For explanation of symbols, see text.)

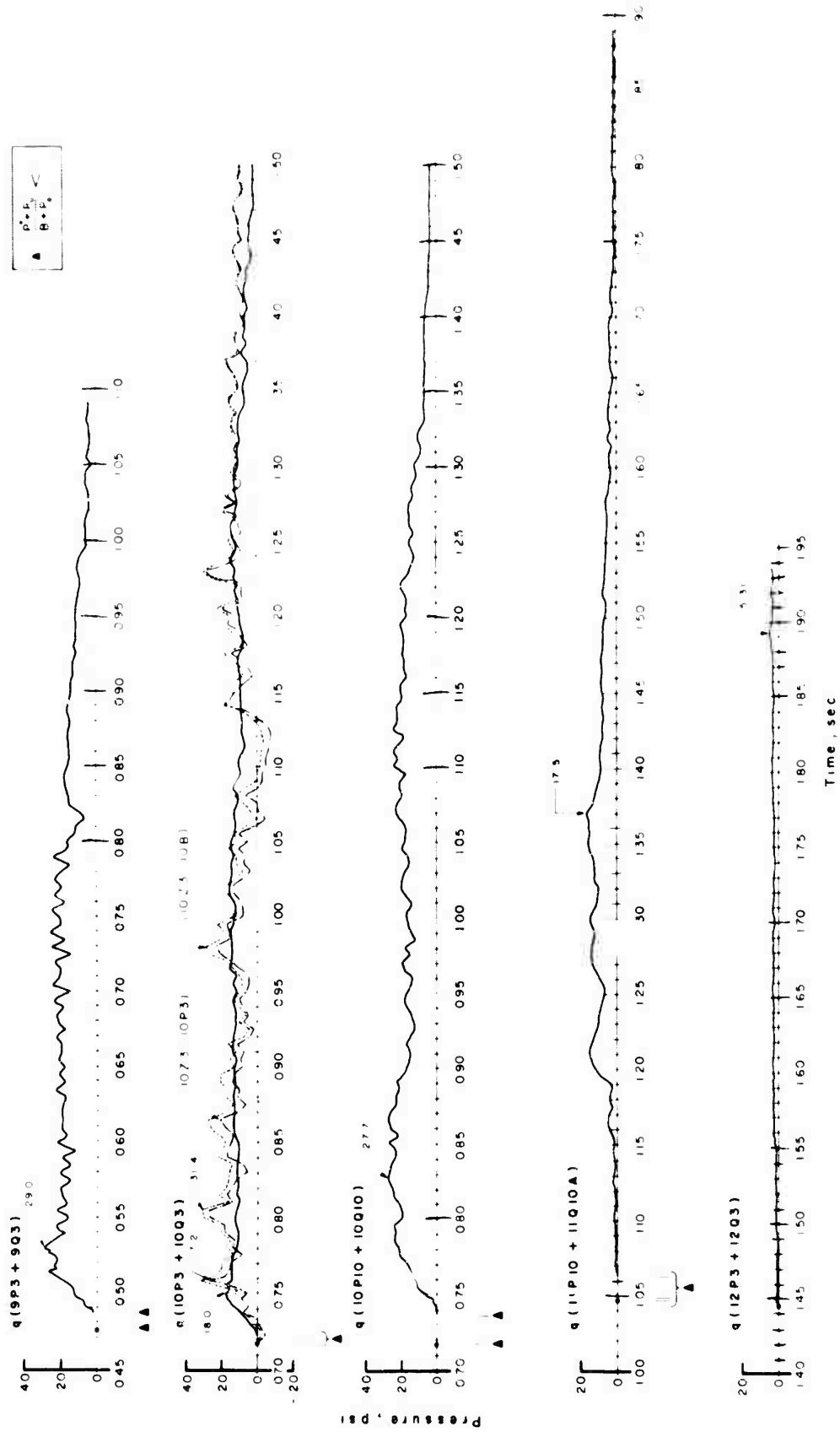


Figure 4.17 Dynamic pressure (q^*) versus time, Stations 9 to 12, Shot Priscilla. (For explanation of symbols, see text.)

SECRET

been attributed to surface and/or thermal effects on the blast wave, effects which result in the formation of the precursor wave.

4.4.1 Background. High explosives tests, which have negligible accompanying thermal radiation, show minor blast effects due to differences in surface mechanical reflection properties (such as water content and degree of compaction) and dust. Surface nuclear explosions, where geometry limits the thermal radiation incident on the reflecting surface, give results similar to

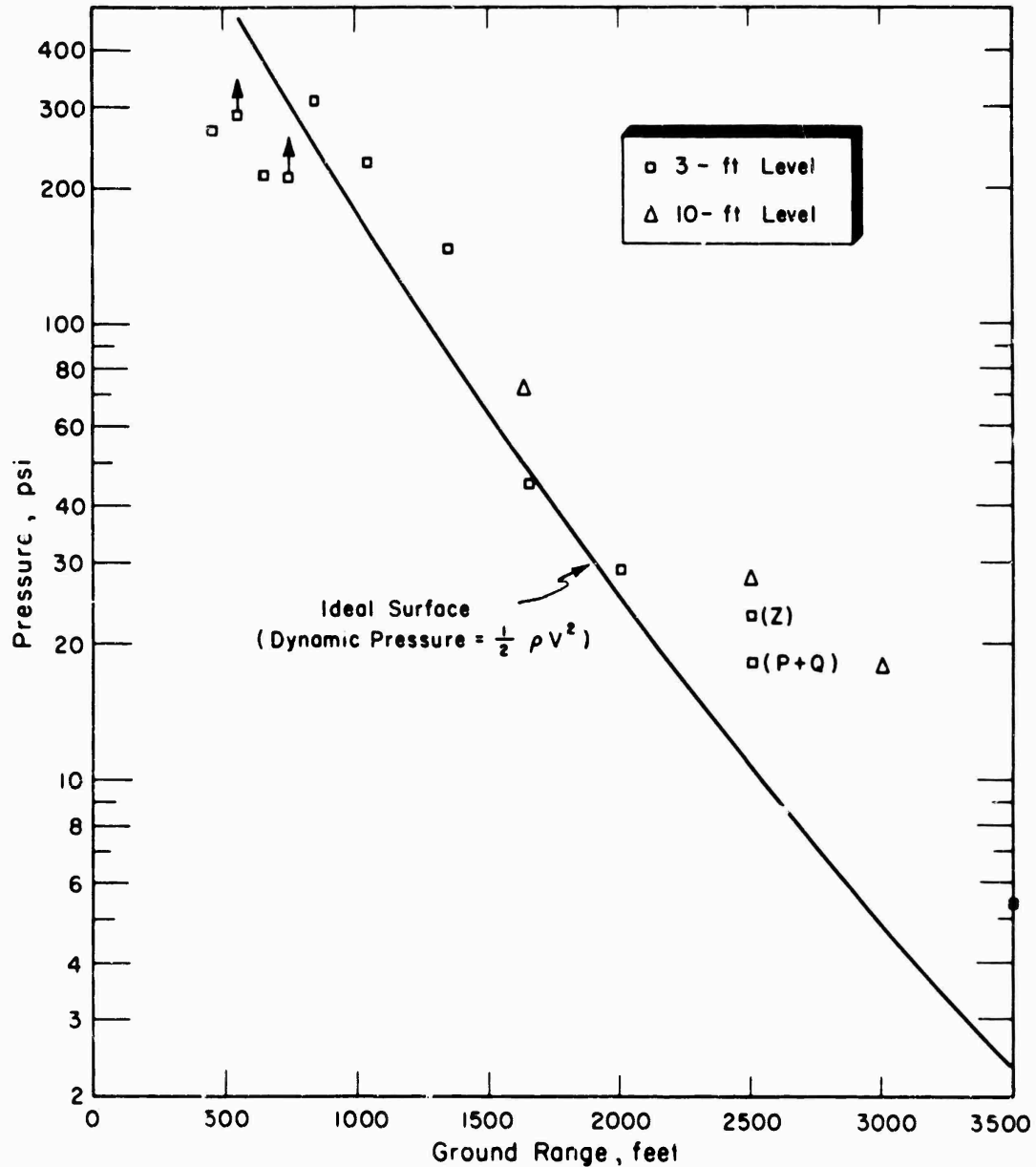


Figure 4.18 Calculated dynamic pressure (q^*), Shot Priscilla.

TNT tests. In any case, the extreme deviations from ideal blast phenomena which were observed on several low burst-height nuclear detonations are far greater than the perturbations observed for scaled TNT tests or for surface nuclear tests over the same kind of surfaces. It therefore appears safe to assume that thermal radiation is the principal cause of blast-wave departures from ideal. Of course, the mechanical properties of the surface, including dust, can have a profound influence upon the degree to which the thermal radiation affects blast.

An operational definition for the precursor can be stated: A separate and distinct pressure wave whose front travels at velocities appreciably higher than classical shock velocities over the same surface. It must be noted that the disturbing effects on blast can be significant with-

cut the actual generation of a precursor wave, or outside the range of the precursor region. In these circumstances the term non-ideal is used to describe this behavior.

The role of thermal effects on blast was first clearly delineated on Tumbler-Snapper (1952), where the precursor phenomena was identified. Subsequent re-examination of Buster (1951) and Greenhouse (1951) blast measurements confirmed precursor existence and showed similar thermal perturbations on blast. It remained for the Upshot-Knothole series (1953) to investigate the effects of such nonideal blast waves on targets and to study further the associated basic-blast phenomena. It was the objective of Teapot (1955) to put the thermal phenomena on a firmer quantitative basis and to aid in the prediction of the blast behavior of nuclear weapons (at low burst heights) over surfaces other than those characteristic of desert areas. The Plumbbob series (1957), and Shot Priscilla in particular, was directed toward obtaining air-blast measurements at close-in distances to better observe the formation of the precursor wave and the evolution of the phenomena in regions of strong precursor action.

The blast disturbances observed during previous test operations have been explained in part, qualitatively, by the hypothesis that the thermal radiation creates a heated layer of air adjacent to the ground surface prior to shock arrival at the point of observation. Analytical considerations and some supporting shock-tube experiments indicate that a conventional shock wave is markedly influenced by passage into a region of nonuniform temperature or, more particularly, nonuniform sonic velocity.

Experimental measurements on previous nuclear-explosion tests were designed to investigate the properties of the thermal layer prior to shock arrival. Such measurements were only moderately successful; general instrumentation problems (plus turbulence and atmospheric instability effects characteristic of the heated region being investigated) reduced the value of these measurements in a quantitative sense. Therefore, although measurements verified the existence of a preshock thermal disturbance near the ground, details of temperatures, temperature gradients, and height of the effective layer at shock arrival are inconclusive.

4.4.2 Computed Preshock-Arrival Temperature. A sizable fraction of the total energy released from a nuclear detonation is emitted in the form of thermal radiation. Large amounts of thermal radiation are incident upon the ground before shock arrival, and thus the existence of a near-surface thermal layer appears to be a sound assumption.

If a near-surface thermal layer is assumed to exist prior to shock arrival, it is possible to set up analytic relationships which can be used to deduce the general characteristic of the thermal layer from the observed blast behavior. Temperatures computed in this manner are, at best, gross averages and apply only to conditions which exist just prior to shock arrival at the range in question. The relationships based upon blast parameters can be divided into three main classifications: (1) those using shock-wave equations, measured initial overpressures, and some average wave-front orientation angle (called pressure calculation); (2) those using the assumption that wave-propagation velocity equals the sonic velocity characteristic of the medium (called sonic calculation); and (3) those using only angle of shock wave-front orientation (called angle-of-front calculation). These three methods of approach are discussed in detail in a previous report (Reference 4) and the methods are merely summarized here.

1. Pressure Calculation. With a shock front moving through a medium of constant γ (ratio of specific heats), analysis yields:

$$\frac{\Delta p_2}{\Delta p_1} = \frac{2\gamma}{\gamma + 1} \left[\left(\frac{v \sin \theta}{c_1} \right)^2 - 1 \right] \quad (4.3)$$

Where: Δp_2 initial overpressure (first rise) behind the shock front
 v horizontal trace velocity of the front
 θ acute angle which the shock front makes with the ground surface
 c_1 sonic velocity in the medium just ahead of the shock front
 Δp_1 pressure of the medium just ahead of the shock front.

From the measured overpressures and information on the orientations of the shock fronts, Equation 4.3 may be used to compute c_1 . Then the preshock absolute temperature, T_1 , is related to c_1 by:

$$\left(\frac{c_1}{c}\right)^2 = \frac{T_1}{T} \quad (4.4)$$

Where: c = sonic velocity corresponding to ambient atmospheric conditions.

T = absolute temperature corresponding to ambient atmospheric conditions.

2. Sonic Calculation. This method is based upon the existence of a compression-type acoustic wave. If this condition is fulfilled, the propagation velocity of the initial disturbance (pressure) equals the sonic velocity of the medium, and Equation 4.4 is immediately applicable for the temperature calculation. Hence:

$$\left(\frac{v \sin \theta}{c}\right)^2 = \frac{T_1}{T} \quad (4.5)$$

and for a wave normal to the ground surface,

$$\left(\frac{v}{c}\right)^2 = \frac{T_1}{T} \quad (4.6)$$

This calculation (which assumes the wave-propagation velocity to be the same as the sonic velocity), if applied erroneously to a shock wave, yields temperatures much larger than those computed from the pressure-calculation or angle-of-front methods.

3. Angle-of-Front Calculation. This method can be applied to either shock or compression-type wave fronts. The equations reduce to:

$$\frac{c_A}{\sin \theta_A} = \frac{c_B}{\sin \theta_B}; \quad c_B = \frac{\sin \theta_B}{\sin \theta_A} c_A \quad (4.7)$$

Where: c_A, c_B = sonic velocities ahead of the front at points A and B

θ_A, θ_B = orientation angles of the front to the horizontal at points A and B.

The preshock temperature calculations at stations where wave-front orientation data are available are presented in Table 4.5, along with the number of the particular equation used for each calculation. The last column of the table lists what is considered to be the best value of computed temperature; this choice is based upon the types of pressure-time record observed at each station, i. e., a shock-type pressure rise would suggest that the best temperature calculation is either the pressure method or angle-of-front method, whereas a compression-type, pressure-time history points to the sonic method. Naturally, the transition form of record presents a problem; however, since the angle-of-front method is equally applicable to shock or compression waves, this fact would influence the "best" choice.

Computed Priscilla preshock surface temperatures are plotted versus time of shock arrival in Figure 4.19. For comparison, the computed temperature data obtained over the desert line of Teapot Shot 12 are also included in the figure. It is obvious that the Priscilla temperatures are significantly larger than those from Teapot Shot 12 at comparable arrival times. It should be noted that the Priscilla detonation was higher in yield (36.6 kilotons against 22 kilotons) and was detonated at a somewhat higher burst height (700 feet against 400 feet). Both of these factors, for close-in ground ranges, contribute to the higher thermal input of Priscilla.

4.4.3 Precursor Formation and Development. Although much attention has been directed toward the study of the precursor wave, its formation and development, the origins and mechanisms responsible for this phenomenon have not been clearly explained.

The predicted and measured wave forms for Priscilla surface-level overpressures are presented in Table 4.6. The predictions agree well with the actual measurements, which indicate

that the diagram of Figure 2.2 is consistent with the Priscilla data—thus making the diagram more useful for prediction purposes.

In Reference 4, a rather thorough empirical analysis was made with data from known precursor-forming shots. It was found that if arrival-time data are plotted versus slant range on logarithmic

TABLE 4.5 COMPUTED PRESHOCK TEMPERATURES, SHOT PRISCILLA

Ground Range	Arrival Time	Gage Height	Equation 4.3	Equation 4.5	Equation 4.6	Equation 4.7	Type of Wave	Best Value
ft	sec	ft	C	C	C	C		C
550	0.116	0	3,000	11,270	12,780	—	Shock	3,000
750	0.145	0	10	500	8,930	3,800	Trans	3,800
850	0.163	0	-200	-75	7,290	2,850	Trans	2,850
1,350	0.268	0	-240	-220	3,710	1,960	Trans	1,960
2,000	0.475	0	-70	60	1,110	950	Compr	950 to 1,110
2,500	0.716	0	-160	-110	180	185	Compr	185
—	—	3	-35	36	—	—	Compr	—
—	—	10	36	170	—	—	Compr	—

coordinates, some details of behavior are revealed which are not apparent in Figure 4.1. Figure 4.20 shows precursor-arrival data from Project 1.3 and the arrival-time curve for an ideal surface. Figure 4.20 indicates that the initial slope, corresponding to the ideal surface arrivals, is only slightly less than 5/2, whereas the precursor data indicate a 3/2 slope in the initial portions.

TABLE 4.6 PREDICTED AND MEASURED WAVE FORMS, SHOT PRISCILLA

Ground Range	Predicted Wave-form Type	Measured Wave-form Type
ft		
450	0	0
550	0	1-
650	1	1
750	1	1
850	1	1
1,050	1	1
1,350	1	1
1,650	1	1
2,000	1+ or 2-	1
2,500	3	3
3,000	4-5	5
3,500	6	6

This behavior is consistent with the analysis of other precursor-forming shots included in References 4 and 25.

The intersection of the precursor curve with the ideal gives a good indication of the time (and ground ranges) at which the precursor forms. For Priscilla, the intersection occurs at about 510-foot ground range and the arrivals begin to deviate from the 3/2 slope near 450-foot A-scaled slant range (or 1,350-foot ground range). Comparison of this with the data from Upshot-Knothole Shot 10 (Figure 4.21) shows the arrivals deviating from the 3/2 slope near 500-foot A-scaled slant range (or 1,170-foot ground range). In many respects the Priscilla and Upshot-Knothole Shot 10 curves are similar: (1) the arrivals of Types 0 and 1 wave forms agree well with the ideal (the Priscilla Type 0 form is in the region of regular reflection) (2) most of the arrivals associated with Type 1 form fall on the 3/2 slope, and deviation from this slope corresponds to a change in form; and (3) the arrivals of the Type 6 form (and succeeding forms) agree well with the ideal

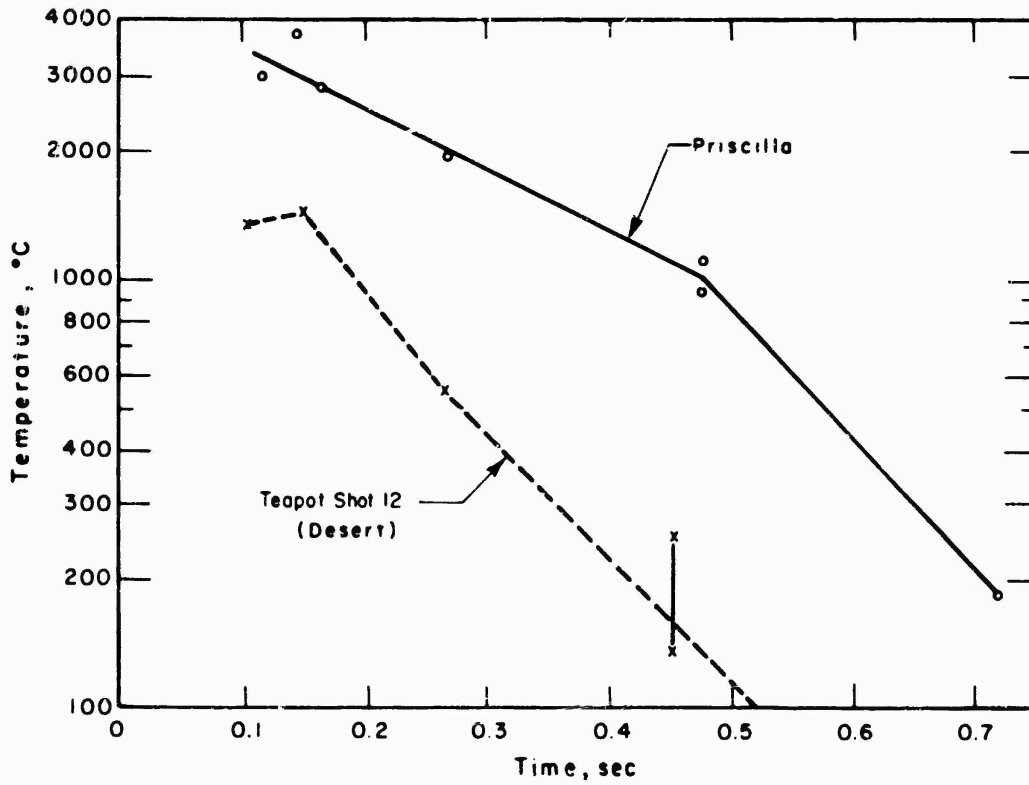


Figure 4.19 Computed preshock arrival temperature versus arrival time, Teapot Shot 12 and Plumbbob Shot Priscilla.

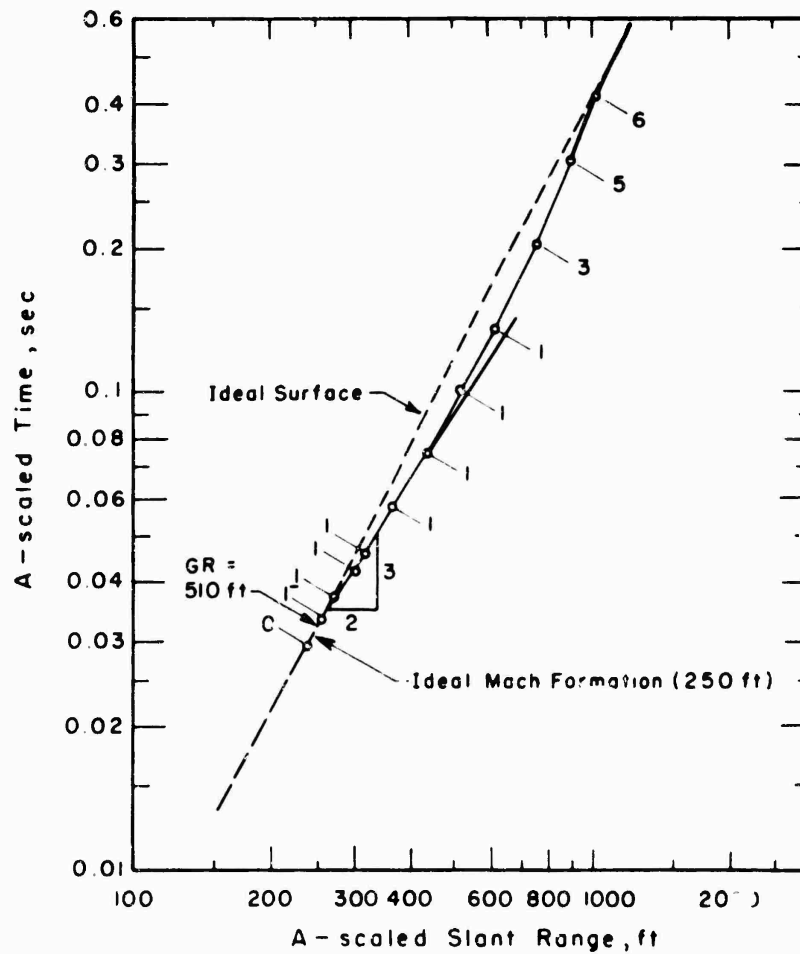


Figure 4.20 Arrival time versus slant range, A-scaled, Shot Priscilla.

arrivals. The above conclusions are also borne out by the data from Buster Charlie shot and Tumbler Shot 4 (Figure 4.21).

4.4.4 Comparison with Hess' Theory. It is significant to look carefully at Hess' bubble theory in the light of data obtained on precursor-forming shots.

On page 53 of Reference 8 is a plot which shows the temperature and Mach-number conditions required for the formation of a "stagnation bubble" under a normal shock wave (or Mach stem)

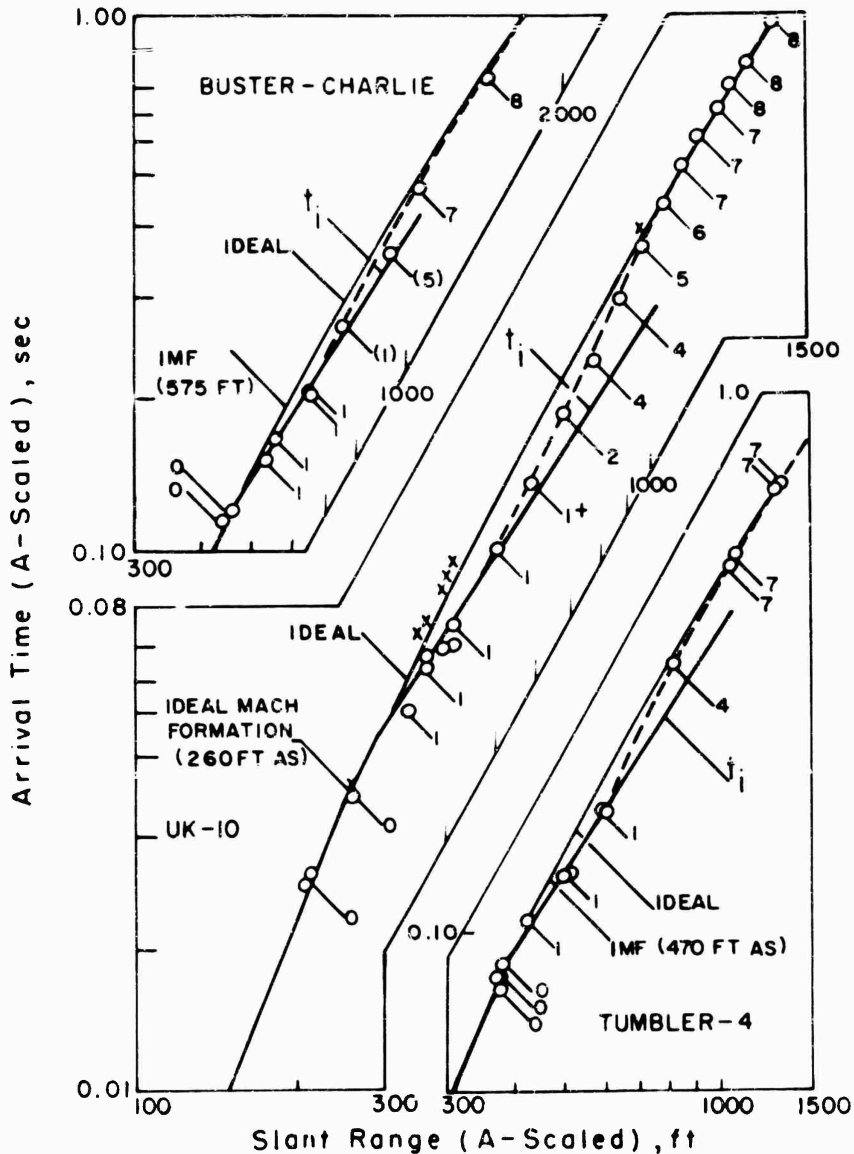


Figure 4.21 Arrival time versus slant range, A-scaled, Buster-Charlie, Tumbler 4, Upshot-Knothole 10.

moving over a heated layer. Hess shows that a bubble forms when the stagnation pressure in the heated layer is less than the static pressure downstream of the shock. In Figure 4.22, Curve 1 shows this condition plotted as overpressure, which is a more convenient parameter to measure than temperature. Curve 1 simply shows the overpressure ratio for a normal shock at Mach number M_c in the cold gas. Bubbles exist above Curve 1 where the first step in overpressure (the precursor wave) is less than the normal shock overpressure. Throughgoing layers lie on Line 1, and there are no bubbles below Line 1. Curve 2 indicates the transition from a strong to a weak oblique shock over the bubble, and Curve 3 shows when the flow over the bubble becomes supersonic.



Also shown in Figure 4.22 are precursor overpressure data from Priscilla and other shots. The data indicate that: (1) at the same scaled ground range, points from Priscilla and Upshot-Knothole Shot 10 very nearly coincide; (2) at 2,150 feet on Upshot-Knothole Shot 10 and 3,000 feet on Priscilla (or at a scaled ground range of about 810 feet) measured overpressures indicate

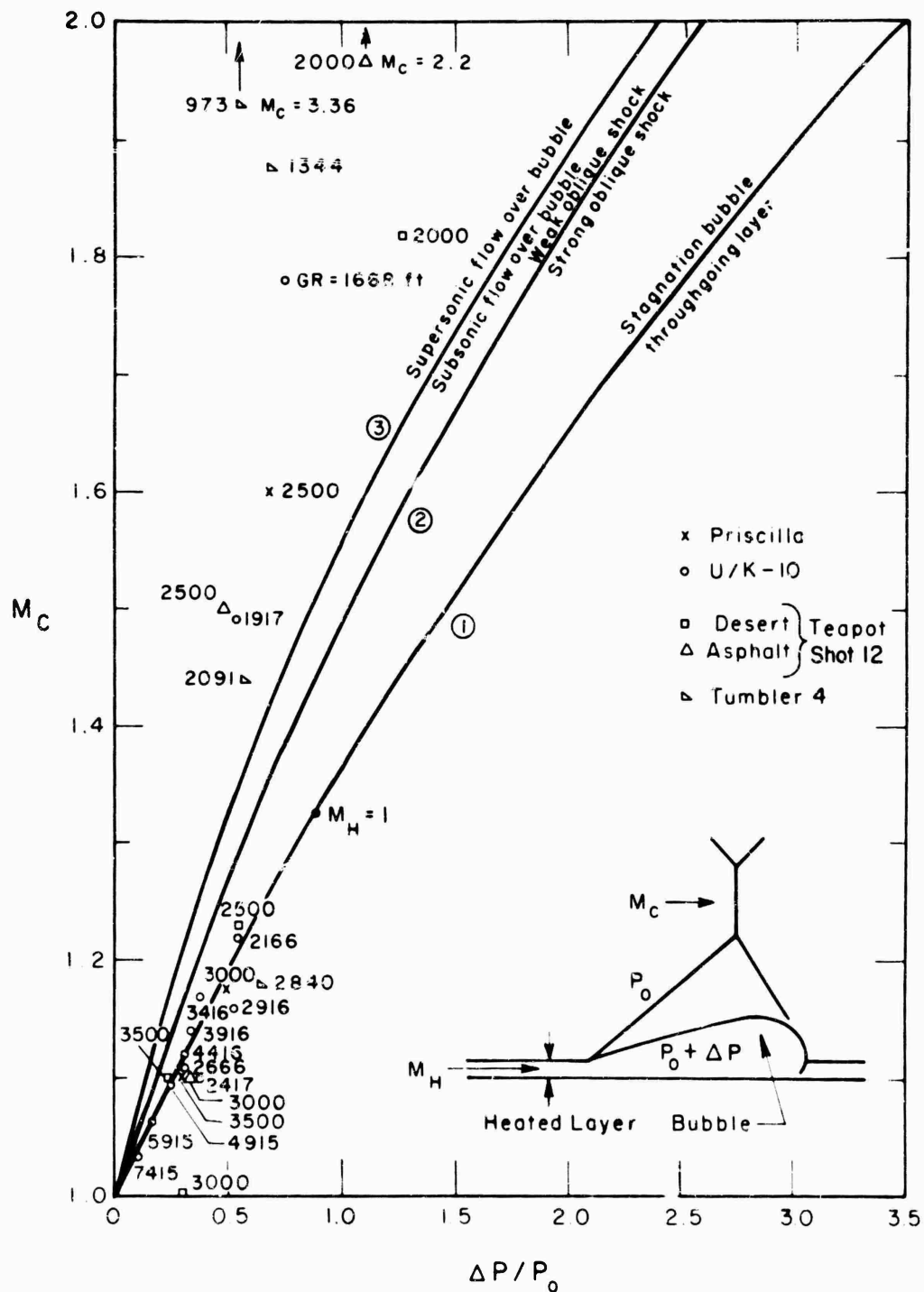


Figure 4.22 Comparison of Hess' theory and field results, Upshot-Knothole 10 and Teapot Shot 12.

that the bubble should have begun to lag behind the Mach stem and transition to a throughgoing layer should have started, after which datum points should lie on Curve 1. The NOL photography of Upshot-Knothole Shot 10 (Reference 24) indicates that the dust cloud did in fact begin to lag behind the Mach stem at about 2,100 feet. The pressure wave forms of the two shots indicate that at the time of transition the two steps in pressure become indistinguishable (Types 3 and 4

wave forms). However, after transition, a second step in overpressure (Types 5 and 6 wave forms) and an initial step in differential pitot pressure reappear. But in contrast with earlier wave forms, the first step in differential pressure is smaller than the second and both steps in pressure arrive well before the dust cloud.

It is not clear, therefore, what the shock structure is that causes the two steps in pressure after transition to a throughgoing layer. It may well be a dynamic phenomenon associated with the collapse of the shock structure over the bubble. This problem is not treated by Hess since he assumes quasi-steady flow and does not consider the dynamics of bubble collapse. However, the mechanism of transition is indicated in Figure 4.22, i.e., there is first a supersonic flow over the bubble with two shocks, then a weak oblique shock with subsonic flow over the bubble, a strong oblique shock, and finally a throughgoing layer.

Data from Teapot 12 and Tumbler Shot 4 (both precursor shots) are included in Figure 4.22. The data on the ground range where transition to throughgoing layer occurs are summarized in Table 4.7. It is noted that the A-scaled values for all shots bunch around 800-foot A-scaled

TABLE 4.7 BUBBLE STAGNATION VERSUS GROUND RANGE, VARIOUS SHOTS

Shot	Yield	A-Scaled Burst Height	Bubble Stagnation Ground Range	A-Scaled Stagnation Ground Range
	kt	ft	ft	ft
Priscilla	36.6	204	3,000	810
Upshot-Knothole Shot 10	14.9	202	2,150	775
Teapot Shot 12 (desert)	22.0	147	2,550	835
Teapot Shot 12 (asphalt)	22.0	147	2,900	915
Tumbler Shot 4	19.6	363	2,500	800

range. This range corresponds to the transition from Type 4 to 5 overpressure wave forms shown in Figure 2.2. The Teapot 12 asphalt data yield a higher value (915-foot A-scaled) which is consistent with the precursor action over this surface. In the final analysis, it appears that the precursor wave collapses from the rear, i.e., the second disturbance suddenly increases in velocity. From Figure 4.22 and the NOL photographic data on Upshot-Knothole Shot 10 (Reference 24) this is well before transition to a throughgoing layer should (or did) occur. It must therefore be associated with some alteration in shape of the bubble and shock structure, possibly due to a change in the rate of radiation on the bubble.

This explanation of the behavior throws some light on the reason for the sudden increase in main wave velocity observed on Priscilla between Stations 9 and 10 (shown in Figure 4.1). Here again the velocity increase occurred before the transition to the throughgoing layer.

In Figure 4.23 is shown the length of the precursor versus ground range for Upshot-Knothole Shot 10 and Priscilla. The length is the distance between the steps in overpressure as determined from arrival times and average shock velocity. Note that the growth and collapse of this length is nearly linear with ground range and that the maximum length is at the point of transition to a throughgoing layer, i.e., when the dust cloud begins to lag the Mach stem. Also, the length very nearly scales for these two shots with the maximum length approximately equal to the height of burst in both cases.

A blown-up view of a portion of Figure 4.22 is presented as Figure 4.24; here, Upshot-Knothole Shot 10 and Teapot Shot 12 (desert) data which fall close to the stagnation line are plotted. The interesting feature of this plot is the indication that the data appear to cross the stagnation line, make a loop, cross the line again, and finally follow this line closely out to the farthest range instrumented. One explanation for this is that when the bubble is left behind (i.e., throughgoing layer begins), the shock front near the ground is probably still oblique (see the wave-front orien-

tation at 2,500-foot range in Figure 4.3). Therefore, the first effect is an apparent decrease in trace velocity as the bubble dissipates, which is an explanation for the computed trace velocity of the front dipping below the ideal surface prediction (see Section 4.1.1). However, the oblique shock front must evolve into a normal shock; also, the precursor wave is losing velocity rapidly and the main wave begins to influence an increased pressure at the front. Both these factors

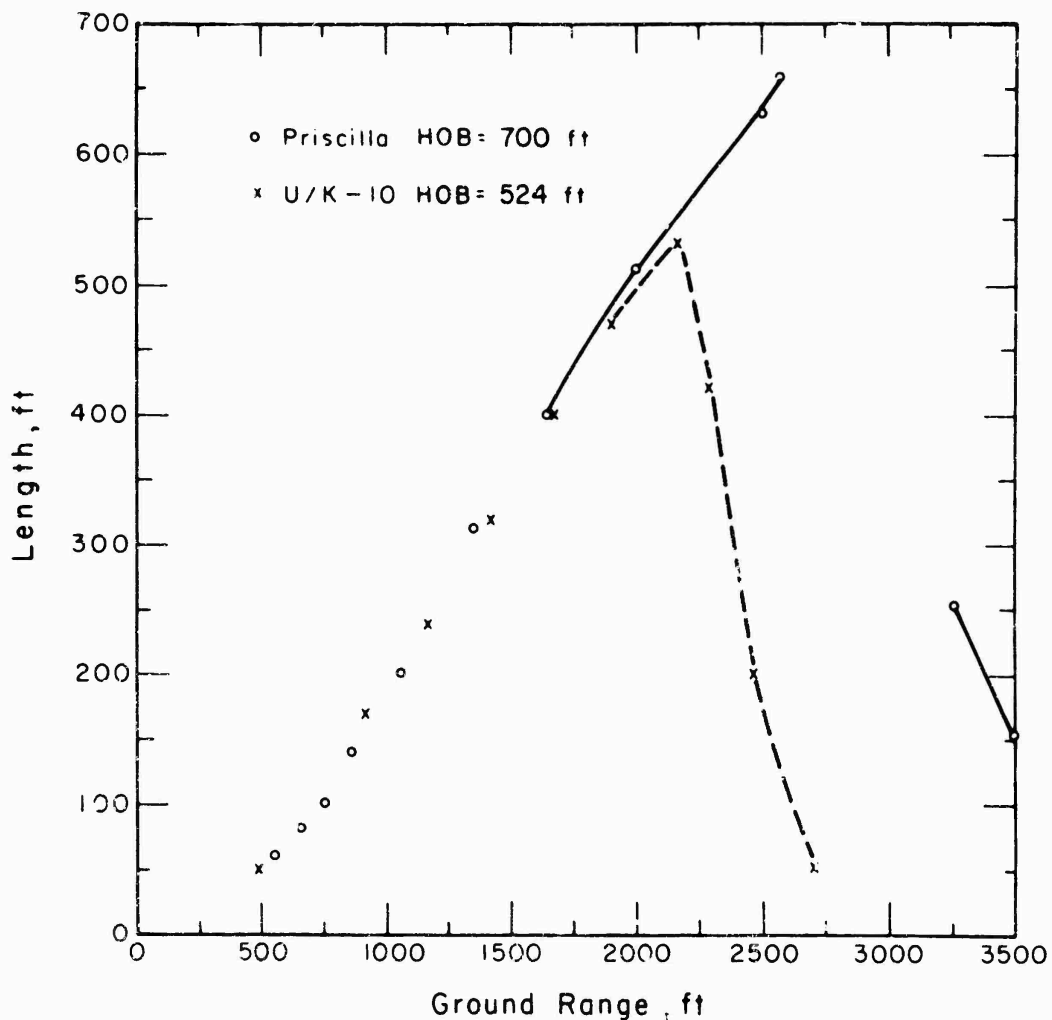


Figure 4.23 Precursor length versus ground range.

result in the loop observed on Figure 4.24; subsequent development finds the normal shock travelling near ideal sonic velocities and complete dissipation of the precursor.

4.4.5 Dynamic Pressure Wave Forms. Under conditions of ideal compressible gas flow and ideal surfaces there is a one-to-one correspondence between dynamic pressure and static overpressure at the shock front (Rankine-Hugoniot). Although the two quantities decay with time somewhat differently behind the front, it can be assumed that gage records of both would exhibit similar wave forms. Further, it has been found that, in regions where classical shock waves are observed in nuclear tests, the differential pitot pressure-time data agree well in wave form with records of static overpressure. However, on precursor-forming shots, because the differential-pressure measurement is obviously more sensitive to particulate matter entrained in the airflow and to localized inhomogeneities of temperature and particle velocity, there is poor correspondence between these wave forms.

In designating dynamic pressure wave-form types, the gage used to obtain the measurement will necessarily influence the wave form and thus the system of classification. The records from Sandia Snob and Greg gages (Reference 10) bear this out; since the Greg gage is sensitive to almost all the entrained dust and the Snob to very little, the wave forms are dissimilar.

Therefore, it is desirable to make the system of wave-form classification independent of the gage used for the measurement.

One possible method of classification which may be advanced is based upon the use of Hess' analysis and Figure 4.22. That is, the classifications of dynamic pressure wave forms could be defined by the various regions on the graph, e. g., a change in classification in going from

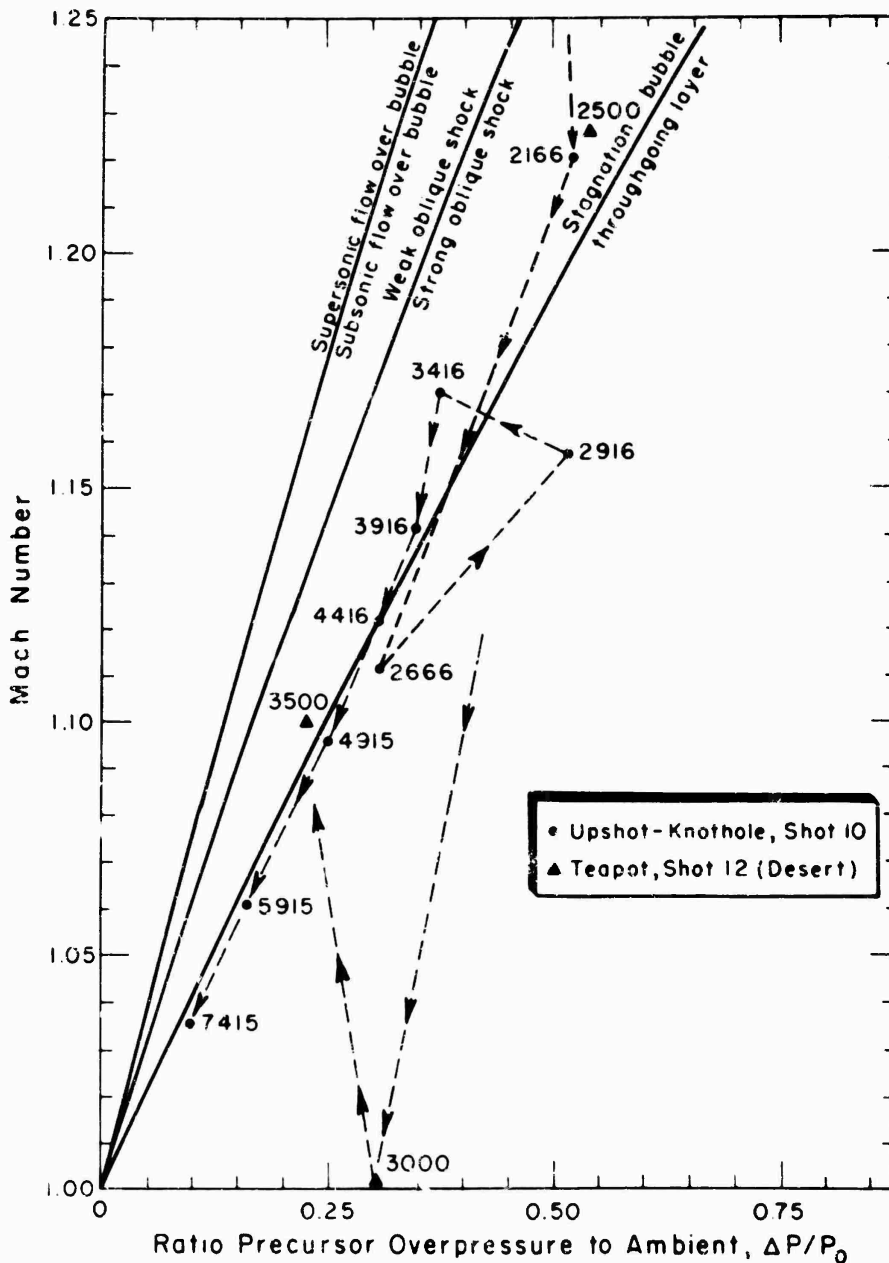


Figure 4.24 Comparison of Hess' theory and field results, various shots.

supersonic to subsonic flow over the bubble, another when crossing from weak to strong oblique shock, etc. This type of classification system would be independent of the gage employed, and the regions on the graph would be fixed by the static overpressure data. However, in Figure 4.22 practically all of the data fall either in the supersonic region or the throughgoing-layer region. This leads to the conclusion that the precursor wave goes through the transitions necessary to change from supersonic flow over the bubble to throughgoing layer in a very short ground-range interval. This also suggests that, unless one is satisfied with only two wave-form classes, a classification method based upon Figure 4.22 will not be very fruitful for prediction purposes.

Another suggestion, which unfortunately is not completely independent of the measuring gage, is to base the dynamic-pressure classes upon the overpressure wave forms. This system has

the advantage of reference to a fairly well proven system, the overpressure wave-form classifications. Also, it is believed that the most useful information to be retained about dynamic pressure wave forms is their degree of deviation from the corresponding overpressure form. Priscilla total-head and differential-pitot wave forms correspond fairly well with the forms for overpressure. It is only at Stations 6, 7, and 8 that the differential forms indicate wide difference; comparisons are somewhat limited due to gage plugging at Stations 6 and 7.

As explained in the discussion of the Greg and Snob gages, any classification system which is

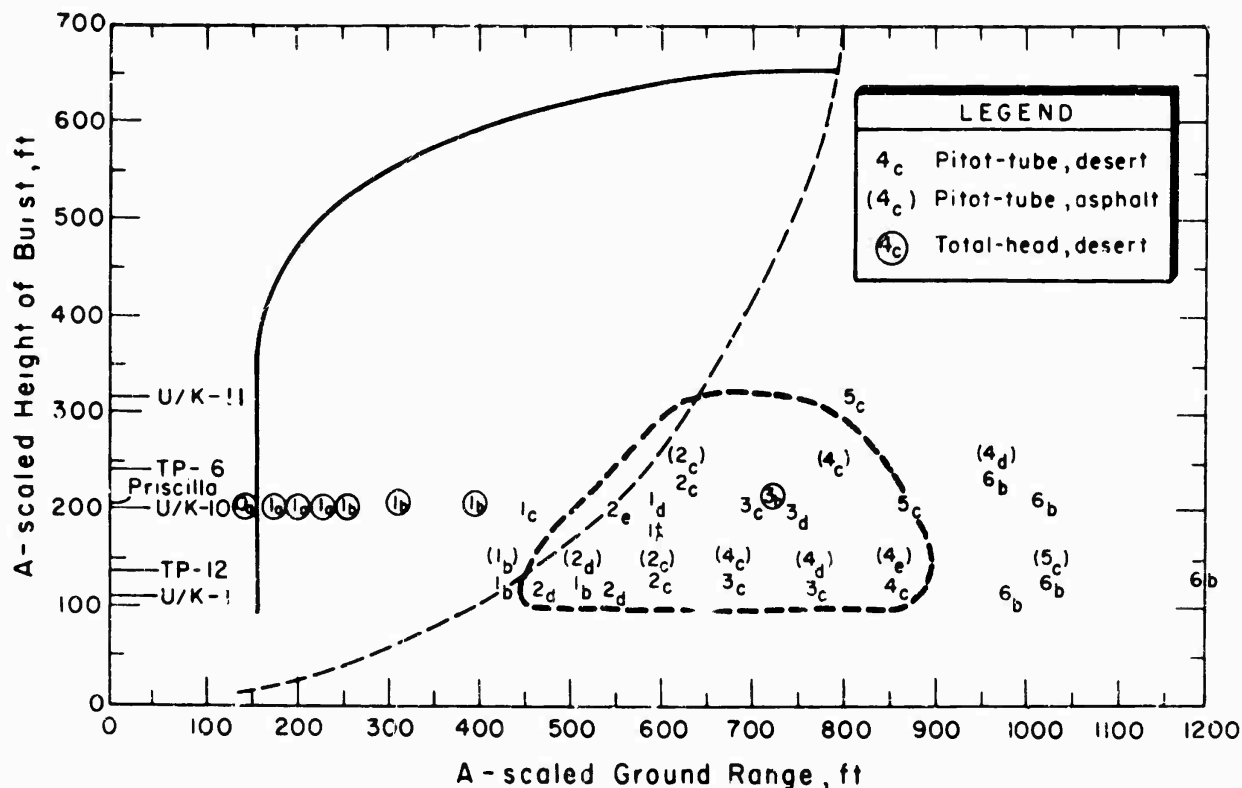


Figure 4.25 Dynamic-pressure wave forms, various shots.

based upon the degree of deviation from an expected form is not independent of the gage. The indices for degree of deviation are as follows:

- a = the same wave form as the overpressure-time counterpart
- b = similar wave form--with a few minor differences in the form of hashy appearance or small sharp peaks
- c = similar wave form--with obvious differences in time sequence of peaks and much more hashy
- d = decidedly different wave form--with some characteristics of the parent form
- e = no similarity to the parent form.

In designating the classifications of all total-head or differential-pressure wave forms the corresponding overpressure-time (parent form) class is given first and then the index for the degree of deviation, e.g., 1a, 2b, 4d, and 1+c.

All known measurements (at NTS) of total-head and differential pressure taken over desert and asphalt surfaces have been assigned appropriate wave-form designations (Table 4.8). It was clear when this review was undertaken that many of the violent deviations from ideal behavior noted on the records obtained on Upshot-K. 0thole could be cited as instrumental difficulties. The pitot-tube differential-gage port fill times were obviously quite long (10 to 20 msec) and many gages became clogged shortly after shock arrival. With these instrumental problems in mind, every effort was made to carefully classify each gage record according to the foregoing criteria.

The results listed in Table 4.8 are plotted in Figure 4.25 on the same coordinates used for Figure 2.2. There are insufficient data for firm conclusions, but some pertinent observations

TABLE 4.8 DYNAMIC PRESSURE WAVE FORMS, VARIOUS SHOTS

Q, pitot-tube differential pressure; NR, no record; S, Snob-gage differential pressure; G, Greg-gage pressure; T, total-head pressure.

Shot A-scaled Height of Burst	Ground Range ft	A-scaled Ground Range ft	Gage Type	Gage Height ft	Wave-form Type	Remarks	
U/K-1 (112 ft)	1,250	470	Q	10	2d	Gage believed clogged	
	1,450	546	Q	10	2d	Gage believed clogged	
	2,600	979	Q	13	6b		
U/K-9 (763 ft)	827	263	Q	11	—	Poor record	
			Q	9	NR		
	1,087	342	Q	13	7Rd		
	1,300	410	Q	10	7Rc	No response to incident pressure	
	1,473	465	Q	13	7Rd	Negative response to incident pressure	
	1,712	540	Q	10	7Rc	Negative response to incident pressure	
	2,160	680	Q	10	7Rc		
			Q	25	7Rc	No response to incident pressure	
			Q	40	7Rc	Negative response to incident pressure	
			Q	40	7Rc	Negative response to incident pressure	
U/K-10 (202 ft)	4,075	1,285	Q	8.5	8b		
	6,460	2,035	Q	10	8c		
			Q	35	8b		
			Q	60	8b		
			Q	60	8b		
	6,545	2,060	Q	10	8b		
			Q	35	8b		
	U/K-10 (202 ft)	1,169	454	Q	13	1 + c	Gage believed clogged
		1,422	553	Q	10	—	Gage believed clogged
				Q	40	2e	
Q							
Q							
1,920		746	Q	10	3d		
1,920		746	Q	25	3d		
			Q	40	3c		
3,918	1,520	Q	8.5	8b			
6,417	2,490	Q	10	8b			
		Q	35	8b			
U/K-11 (316 ft)	3,437	810	Q	5	5c		
Teapot-12 (desert) (137 ft)	1,250	428	Q	3	1b		
	1,500	514	Q	3	1b	Gage believed clogged	
			Q	10	2c		
			Q	3	3c		
			Q	10	3c		
	2,000	685	S	3	3c		
			G	3	3c	Cable break; partial record	
	2,250	770	Q	10	3c		
	2,500	856	Q	3	4d		
			Q	10	5d		
Q			25	4d			
Q			40	4d			
S			3	4d			
G			3	4d			

TABLE 4.8 CONTINUED

Q, pitot-tube differential pressure; NR, no record; S, Snob-gage differential pressure; G, Greg-gage pressure; T, total-head pressure.

Shot A-scaled Height of Burst	Ground Range ft	A-scaled Ground Range ft	Gage Type	Gage Height ft	Wave-form Type	Remarks
	2,750	942	Q	10	NR	
	3,000	1,027	Q	3	6b	
			Q	10	NR	
	3,500	1,198	Q	10	6b	
	4,000	1,370	Q	10	7b	
	4,500	1,541	Q	3	7b	
	8,000	2,740	Q	10	8a	
Teapot-6 (desert) (240 ft)	1,300	624	Q	10	2c	
	1,650	792	Q	10	NR	
	2,000	961	Q	10	6b	
Priscilla (204 ft)	450	131	T	3	0a	
	550	160	T	3	1-a	
	650	189	T	3	1a	
	750	218	T	3	1a	
	850	247	T	3	1b	
	1,050	305	T	3	1b	
			Q	3	—	Gage believed clogged
	1,350	392	Q	3	1b	
			Q	3	—	Gage believed clogged
	1,650	479	Q	3	1c	
			Q	10	1c	
	2,000	581	T	3	NR	Project 34.1 Reference 22
			Q	3	1c	
			Q	10	1c	
			Q	3	NR	
			Q	10	1+c	
			S	3	1+b	
			S	10	1+c	
			G	3	1+c	
			G	10	1+c	
	2,500	726	T	3	3b	
			Q	3	3c	
			Q	10	3c	
	3,000	871	Q	3	NR	
			Q	10	5c	
	3,500	1,016	Q	3	6b	
			Q	10	6b	
Teapot-12 (asphalt) (13. ft)	1,250	428	Q	3	1b	
	1,500	514	Q	3	2-d	Gage believed clogged
			Q	10	2c	
	1,750	599	Q			
	1,750	599	Q	10	2c	
	2,000	685	Q	3	4c	
			Q	10	4d	
			S	3	4b	
			G	3	NR	
	2,250	770	Q	10	4d	



TABLE 4.8 CONTINUED

Q, pitot-tube differential pressure; NR, no record; S, Snob-gage differential pressure;
G, Greg-gage pressure; T, total-head pressure.

Shot A-scaled Height of Burst	Ground Range ft	A-scaled Ground Range ft	Gage Type	Gage Height ft	Wave-form Type	Remarks
	2,500	856	Q	3	4e	
			Q	10	4e	
			Q	25	4d	
			Q	40	4d	
			S	3	4d	
			G	3	4c	Cable break; partial record
	2,750	942	Q	3	NR	
	3,000	1,027	Q	3	5c	Gage believed clogged
Teapot-6 (asphalt)	1,300	624	Q	10	2c	
(137 ft)	1,650	792	Q	10	4c	
	2,000	961	Q	10	4d	

can be made. The only really close-in measurements are the total-head results and these wave forms are all a or b indices; these measurements probably reflect somewhat the gage design, which is probably less sensitive than the pitot tube to entrained dust. The data plotted in Figure 4.25 indicate that there is an area (enclosed by heavy-dashed line) in which the c, d, and e types are concentrated; that is, at the ground ranges and burst heights corresponding to this area one would expect the pitot-tube differential pressure wave forms to deviate most markedly from their overpressure counterparts. It should be noted that the area designated on Figure 4.25 is based upon available data; therefore, as more data are taken, this area will be more clearly defined and will probably grow in size.

It will be noted in Figure 4.25 and Table 4.8 that there are few c, d, or e designations associated with overpressure forms of Types 6, 7, and 8; it appears that the greatest deviations are associated with Types 2, 3, and 4. The data taken over asphalt appear to be more disturbed than corresponding data over the desert; also, the disturbances (or deviations) seem to persist to larger ground ranges over the asphalt.



Chapter 5

CONCLUSIONS

5.1 INSTRUMENT PERFORMANCE

Project 1.3 obtained usable records on 39 of its 47 electronic recording channels, although 5 of these were incomplete due to cable breaks during the positive phase. Of the 8 lost records, 6 were due to jamming of paper in one oscillograph, 1 was destroyed by the induction signal, and 1 was lost for undetermined reasons.

5.2 ARRIVAL TIME AND SHOCK VELOCITY

Shock-arrival time agrees well with that predicted over an ideal surface at 450 feet. At subsequent ranges, the first arrival is the precursor which always precedes the ideal surface prediction, whereas the main wave lags it. Only at 2,500- and 3,000-foot ranges, after precursor dissipation, do main-wave arrivals approximate those predicted over an ideal surface.

At the closest stations, the computed trace velocity, based on arrival-time data from pressure gages and blast switches, agrees with that predicted over an ideal surface. Farther out, at about 500 feet, Priscilla shock velocity begins to deviate markedly from the ideal, exceeding the ideal surface velocities out to about 2,000-foot range, where there is agreement. Computations of preshock-arrival surface temperatures yield values significantly higher than those computed for Teapot Shot 12.

5.3 PRECURSOR FORMATION AND PRESSURES

The precursor wave began between 450 and 550 feet, peaked at around 650 feet, was fully developed between 850 and 1,350 feet, and dissipated rapidly between 2,000 and 2,500 feet.

Maximum precursor overpressures out to about 1,000 feet were approximately one tenth the peak overpressure and decreased with ground range at about the same rate as the peak overpressure.

Comparison of maximum precursor overpressure of Upshot-Knothole Shot 10 and Priscilla (approximately same scaled height of burst) shows Upshot-Knothole Shot 10 pressures to be somewhat higher than those for Priscilla.

Total-head precursor maxima show similar behavior to that of the peak main-wave pressure, with precursor pressures decreasing steeply with increasing ground range, leveling off between 850 and 1,350 feet, and finally decreasing abruptly at 2,500 feet.

Pitot-tube differential pressures (total-head minus static) for the precursor do not rise to high pressures (above 200 psi) as does the main wave between 850 and 1,350 feet.

Analyses (Reference 8) of precursor-type flows caused by a layer of air which is preheated by thermal radiation before shock arrival indicates that this layer cannot be a "throughgoing" layer but must be accumulated into a bubble under the Mach stem when the stagnation pressure in the heated layer is less than the static pressure downstream of the shock. The transition to a throughgoing layer occurs when the dust cloud begins to lag the Mach stem. When the occurrence of transition predicted by this theory is compared with data from precursor-forming shots, theory and experimental results are in close agreement.

The dynamics of bubble collapse are not treated by the theory, but the mechanism of transition appears to be first a supersonic flow over the bubble with two shocks, then a weak oblique shock with subsonic flow over the bubble, a strong oblique shock, and finally a throughgoing layer.

It appears that the precursor collapses from the rear with a sudden increase in main wave velocity. Since this occurs well before transition to a throughgoing layer on Upshot-Knothole Shot 10 and Priscilla, it is suggested that collapse must be associated with some change in the shape of the bubble and shock structure possibly due to a change in the rate of heating of the bubble.

5.4 MAIN-WAVE PRESSURES AND WAVE FORMS

5.4.1 Overpressure. At the highest recorded pressures, Priscilla results agree well with those predicted over an ideal surface. Surface peak-overpressure measurements exhibit the depression below the ideal curve which is characteristic of precursor action. Aboveground measurements are all higher than surface pressures and show increases in pressure with increases in height of measurement.

If the theoretical duration is suppressed to be consistent with the sensitivity of the overall pressure measuring system, Priscilla positive duration data agree with 2W theory, although at very high pressures some data fall below the theoretical curve. Priscilla impulse data agree with the 2W theoretical curve at high pressures. The reason for the difference in duration and impulse at high pressures is that thermal disturbances close-in create a change in the total-impulse (slower pressure decay) without significantly changing the duration.

Type 1 overpressure wave forms predominate to 2,000 feet; Type 3 are evident at 2,500 feet, Type 5 at 3,000 feet, and Type 6 at 3,500 feet. Comparison of wave forms between Upshot-Knothole Shot 10 and Priscilla show good agreement. No significant wave-form differences with increased height aboveground noted on previous shots are found on Priscilla.

5.4.2 Total-Head Pressure. The only data obtained in the region of regular reflection agree well with the ideal surface prediction of dynamic pressure. In the Mach reflection region, there is agreement with the ideal until 850 feet. From this range onward the peak total pressure is significantly higher than the ideal out to 2,500 feet.

5.4.3 Dynamic Pressure. Differential Pitot-Tube Pressure. The data are limited because the front ports of the pitot tubes were clogged with dust; however, the measured maximum pressures are higher than predicted over an ideal surface, with the 10-foot-level pressures appreciably higher than the 3-foot. Maximum differential pressure computed from total-head pressure and overpressure measurements agrees with the ideal to 750 feet, after which the peak pressure jumps to 2 to 4 times the ideal.

Mach Number and Dynamic (air-plus-dust) Pressure. Maximum computed Mach number occurs at ~1,200 feet rather than at close-in ranges. Maximum dynamic (air-plus-dust) pressure computed from Mach number and surface overpressure is somewhat lower than ideal at close-in stations, agrees with ideal at mid-ranges, and exceeds ideal at 2,500 feet and beyond. Until field measurements of dust mass flow and size distribution versus time at each station are available, dynamic pressure calculated in this way is only a very approximate measure of air-phase dynamic pressure.

Wave Forms. A wave-form classification system for differential pressure based on the degree of deviation from the corresponding overpressure wave form indicates that at close-in scaled ground ranges total-head pressure wave forms follow fairly closely those of overpressure. The greatest deviations are concentrated between 450 and 900 feet scaled ground range and between 100 and 300 feet scaled burst heights.

Chapter 6

RECOMMENDATIONS

It is recommended that laboratory investigations be pursued concurrently with field operations to establish the following:

1. The magnitude of the forces due to dust as a function of dust density, Mach number of flow, and target Reynolds number.
2. The mechanisms which are responsible for the formation and the subsequent development and decay of the precursor wave.
3. The dust registry coefficients of all gages which have been used on previous operations to measure differential (dynamic) pressure or total pressure.

In addition it is recommended that a gage be developed which combines the capabilities of the Snob and the Greg gages in a single probe so that both the air phase and air-plus-dust phase dynamic pressure can be measured on the same elemental volume of flow.

Appendix A

DEFINITIONS of SYMBOLS in CLEAN and DIRTY SUBSONIC and SUPERSONIC AIRBLAST FLOWS

A.1 CLEAN AIRBLAST FLOWS

q \equiv dynamic air pressure = $\frac{1}{2}\rho u^2$

$q_c \equiv (P_p - P_s)$

$M \equiv u/c$ - local free stream Mach number of flow behind blast front

P_t = free stream total pressure (absolute)

P_p = total head pitot pressure (absolute)

$$\begin{cases} M < 1, & P_p = P_t \\ M > 1, & P_p \neq P_t \end{cases}$$

P_s = free stream static pressure (absolute)

P_0 = ambient preshock static pressure (absolute)

Δp = free stream static overpressure = $P_s - P_0$

Δp_g = free stream-static overpressure, measured by ground baffle

Δp_p = total-head pitot overpressure = $P_p - P_0$

ρ = air density (local)

u = particle speed of air (local)

c = speed of sound in air (local)

γ = ratio of specific heats

Primes are used to denote uncorrected, as-read gage values, thus

$$q'_c = (P_p - P_s)'$$

A.2 DIRTY AIR-BLAST FLOWS

q^* \equiv dynamic air-plus-dust pressure in free stream = $q + \varphi_d$

$q_c^* \equiv q_c + \varphi_d$

$q_c^{*'} \equiv (q_c + n\varphi_d)'$

φ_d = momentum flux of dust = $\rho_d u_d^2$

N = dust registry coefficient of gage, $0 \leq N \leq 1$

ρ_d = mass of suspended dust per unit volume of mixture (local)

u_d = particle speed of dust (local)

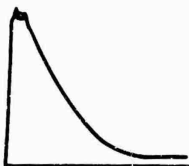

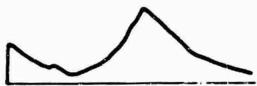

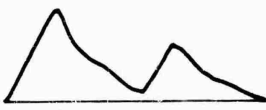
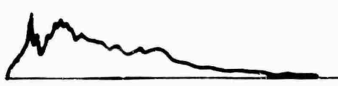


δ = specific gravity of dust particles $\cong 2.5$

starred (*) values refer to mixture and contain air and dust components, thus

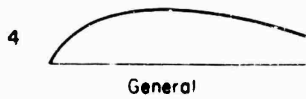
$$\Delta p_p^{*'} = [\Delta p_p (\text{air}) + N \varphi_d]'$$

Appendix B

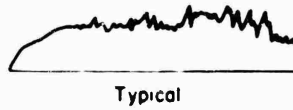
OVERPRESSURE WAVE - FORM CLASSIFICATION

Type	Description of Form	Relation to Previous Type
0	A sharp rise to a double-peaked maximum; peaks close together in time and approximately equal in amplitude.	In its ideal form, it is the classical single-peaked shock wave but is usually recorded as a double-peaked wave.
	 <p>General</p>	 <p>Typical</p>
1	A sharp rise to first low peak followed by either a plateau or a slight decay, then a higher second peak preceding the rapid decay. Time interval between first and second peaks can vary significantly; shock-like rises are evident.	The first low peak indicates the existence of a disturbance which travels faster than the main wave. This type is distinctly nonclassical.
	 <p>General</p>	 <p>Typical</p>
2	Same as Type 1 except that second peak is less than first.	The second peak has decayed to a lower value than the first and has become more rounded and less distinct. Second peak finally disappears.
	 <p>General</p>	 <p>Typical</p>
3	A first large, rounded maximum followed by decay; then a later, usually smaller, second peak. Pressure rises may be slower than for Type 2.	The first peak of Type 2 has developed to become the rounded maximum, while the second peak has decreased in magnitude with respect to the first.
	 <p>General</p>	 <p>Typical</p>

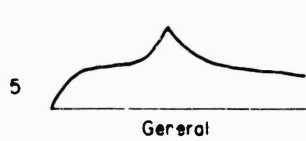
- 4 A long-rise-time flat-topped form which exhibits a long decay time and much hash.



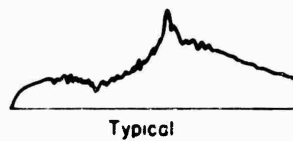
The relatively sharp pressure rise of Type 3 has been replaced by a slow rise and the second peak has disappeared.



- 5 A pressure rise to a rounded plateau which is followed by a slow rise to a second, higher peak.



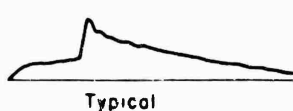
The single-peaked hashy form of Type 4 seems to develop a compression-type second peak, which may be the first indication of the return of the main wave.



- 6 A clear-cut double peak form with a rise to a plateau which slopes upward, then a shock rise to a peak.



This is clearly a cleaned-up Type 5, with the compression-type second peaks becoming shocks.



- 7 A shock rise to a peak followed by either a slight gentle rise, a plateau, or in later examples, a slow decay.



The second peak of Type 6 has overtaken the first peak, resulting in a wave form which is close to classic; sharp, single peak is not evident.



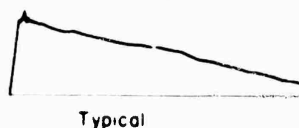
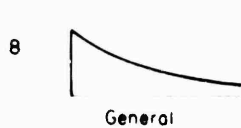
- 7R Refers to Type 7 in region of regular reflection where a second (reflected) shock front is evident.

Second rise due to reflected wave.



- 8 A classical wave form.

Sharp single-peaked form, followed by classic decay.



- 8R Refers to classical wave form in region of regular reflection.

Second rise due to reflected wave.



Appendix C

DESIGN ANALYSIS of TOTAL-PRESSURE PROBE

by A. R. Kriebel

The presence of solid particles in a gas stream effectively makes its total pressure greater than that of the gas phase alone. It is desirable that the measured value of total pressure, p_m , indicate this effect. Reference 12 describes a probe for measuring the effect of water droplets on the total pressure of a subsonic gas stream. The basis for the present probe design, shown in Figures 2.7 and C.1, is the work of Doussard and Shapiro (Reference 12).

Air flows through the probe and out a vent where the contraction of area is 4/1. The upstream velocity of the dust particles is taken to be u_1 , the upstream air velocity. After a dust particle enters the probe, it is decelerated by a drag force; and u_d , the velocity of a dust particle after it has moved a distance x inside the probe, approaches u_2 , the air velocity inside the probe (assumed constant).

From the results reported in Reference 12 and the fact that in supersonic flow ($M_1 > 1$) streamlines are not disturbed by the probe upstream of the shock wave which is close to the inlet of the probe, it is assumed that the collection efficiency of the probe is 100 percent; i. e., all dust particles which enter the probe have trajectories which are straight lines upstream of the pressure tap.

The fact that the inlet passage is flared and inclined to the axis of the probe, which in turn may not be aligned with the flow, is not taken into account in the analysis below. The inlet is flared because of the results of tests described in Reference 17 which indicate that flaring decreases the sensitivity of the probe to misalignment with the flow (in clean air).

The necessity for venting the probe can be shown by calculating the thickness of dust, L , which would accumulate in a blind hole. The following assumptions are made:

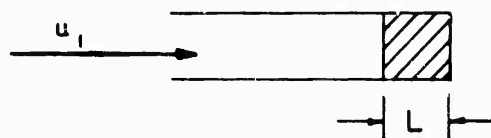
D = solid dust density = 160 lb/ft³

ρ_{d1} = upstream weight of dust per unit volume = 0.2 lb/ft³

ρ_1 = upstream air density = 0.1 lb/ft³

t = duration of flow = 0.1 sec

u_1 = upstream velocity = 2,100 ft/sec



Then

$$L = \left(\frac{\rho_{d1}}{\rho_1} \right) \left(\frac{\rho_1}{D} \right) u_1 t = 2 \times \frac{0.1}{160} \times 2,100 \times 12 \times 0.1 = 3 \text{ inches} \quad (C.1)$$

The equation of motion of the particles after they enter the probe (Reference 12) is:

$$C_D \left(\frac{\rho(u_d - Ku_1)^2}{2} \right) \left(\frac{\pi d^2}{4} \right) = - \frac{\pi d^3}{6} D u_d \frac{du_d}{dx} \quad (C.2)$$

Where: C_D = drag coefficient

d = effective particle diameter

ρ = air density in probe

$K = u_2/u_1$

Assuming C_D is constant, Equation C.2 can be integrated to give:

$$\frac{3C_D \rho_2 x}{4Dd} = \ln \frac{\frac{1}{\gamma} - 1}{\frac{u_d}{u_1} - 1} \frac{1}{\frac{1}{\gamma} - 1} \frac{1}{\frac{u_d}{u_1} - 1} \quad (C.3)$$

Equation C.3 is plotted in Figure C.2. If the following typical values are taken:

$$C_D = 0.46 \frac{\rho_2}{D} = \frac{0.18}{160}$$

$$\text{Then: } \frac{3C_D \rho_2}{4D} \frac{x}{d} = 19 \frac{x \text{ inches}}{d \text{ microns}} \quad (C.4)$$

Figure C.2 shows that if $x = 1.5$ inches, $d = 10$ microns and $K = 0.2$, then

$$x = 10 \times \frac{1.5}{10} = 1.5, \text{ and } \frac{u_d}{u_1} = 0.475 \text{ for } K = 0.2.$$

Since 0.46 is approximately the minimum C_D for a sphere with Reynolds numbers in the range of interest, the above result indicates that in 1.5 inches a 10-micron diameter particle should lose more than 53 percent of its velocity. Applying the momentum equation to an infinitesimal length of the inlet passage, one finds

$$-dp = \rho_2 u_2 du_2 + \rho_d u_1 du_d \quad (C.5)$$

Neglecting the first term on the right and integrating, one finds

$$\frac{p_m - p_t^1}{\rho_d u_1^2} = \left[1 - \frac{u_d}{u_1} \right] \quad (C.6)$$

where p_m is the pressure measured, and p_t is the pressure just inside the probe ($x = 0$) which, for

cause of turbulence in the flow). It appears, therefore, that the probe shown in Figure C.1 should not fill with dust if no particles larger than 1/8 inch become lodged in the passages.

The error due to flow through the probe,

$$\frac{p_t - p_m}{p_t - p_3}$$

was calculated and is plotted in Figure C.3 as a function of p_t/p_3 for one-dimensional, isentropic, compressible flow of pure air through the probe and for a contraction of area at the vent

$$\frac{A_2}{A_3} = 4/1.$$

For choked flow through the vent

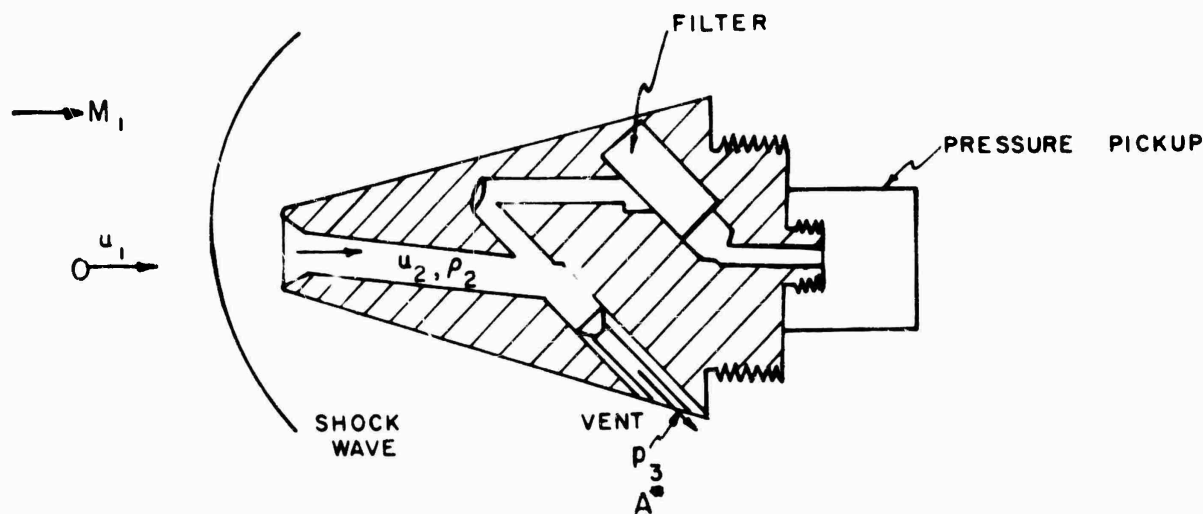


Figure C.1 Total-pressure probe design.

$K = 0$, would equal p_t , the gas-phase total pressure just upstream of the probe (neglecting corrections for angle of attack, Mach number, etc.) For the conditions assumed above, p_m should include 53 percent of the effect of the dust. Since most of the dust particles are smaller than 10 microns, and some particle deceleration occurs just ahead of the probe, the probe should indicate more than 53 percent of the dust momentum flux. If the mean particle size (by mass) is one micron, Figure C.3 indicates that the probe should indicate 80 percent of the dust effect for the previous conditions.

To test its internal configuration, the probe shown in Figure C.1 was machined from lucite and attached to a one-inch pipe leading to an air compressor and pressurized to p_t . Dust-laden air was blown through it, the flow of dust was observed, and p_m was measured with a manometer. This test showed that nearly all of several cubic inches of dust injected passed through the vent into the room, and only a few dust particles were coated on the passage leading to the filter. (A configuration tested previously, where the inlet passage was not inclined as in Figure C.1, filled with dust around the filter under similar conditions, probably be-

$$\frac{p_t}{p_3} > 1.9,$$

the Mach number inside the probe M_2 is 0.15 ($M_2 = 0.16$).

$$\frac{p_m}{p_t} = 0.985$$

$$K = \frac{u_2}{u_1} = \frac{\hat{M}_2}{M_1} = \frac{0.16}{M_1} \quad (C.7)$$

Data calculated from measured pressures are also plotted in Figure C.3. Measured and calculated values are in close agreement and indicate that for pure air the maximum error is 6 percent for low values of

$$M_1 \text{ (or } \frac{p_t}{p_3} \approx 1).$$

For supersonic flow past a cone (Taylor-Macoll theory), if $M_1 > 1.2$,

$$\frac{p_t}{p_3} > 1.9,$$

$$\gamma = \frac{u}{u_1}$$

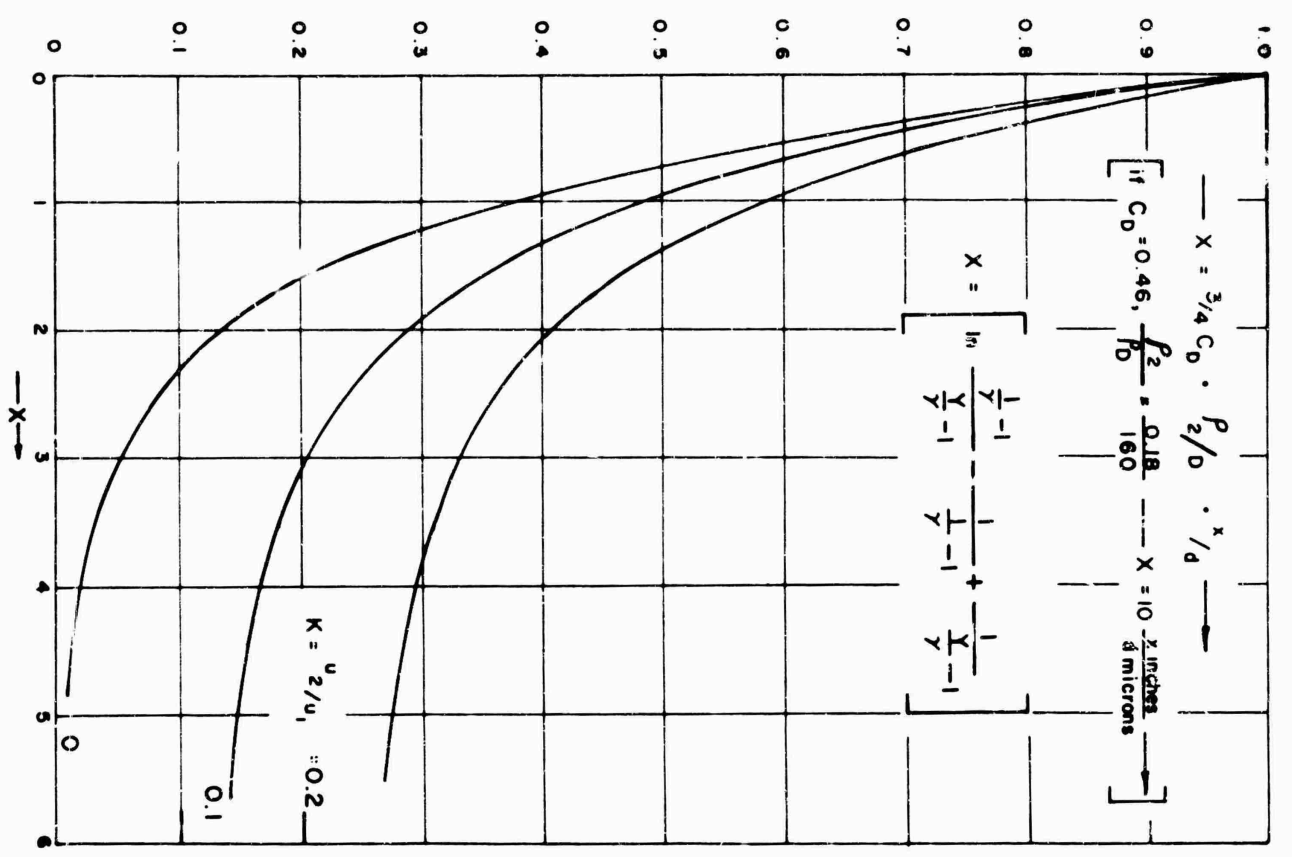


Figure C.2 Particle velocity ratio versus distance.

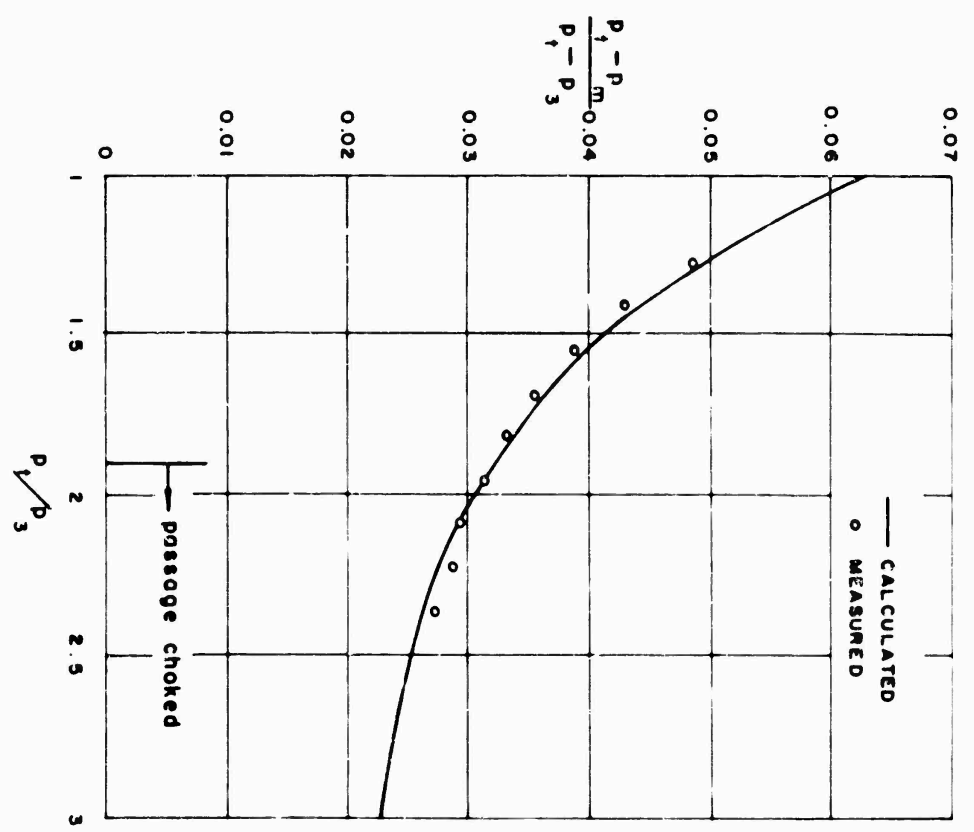


Figure C.3 Error versus pressure ratio.

the flow must be choked through the vent, and the error is less than 3 percent.

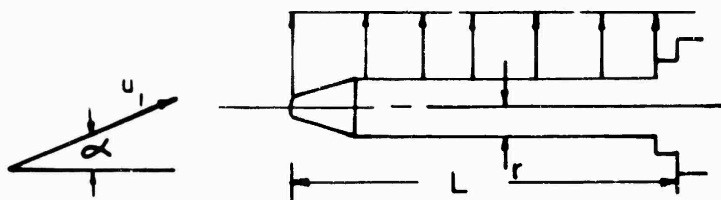
The calculations and measurements above were for pure air and for the vent discharging into still air. The effect of ambient air velocity at the vent should be to increase the area contraction ratio

$$\frac{A_2}{A_3}$$

because of choking at the vent. As a result the error decreases, but the possibility of filling the probe with dust increases.

The dynamic response of the probe to a step change in pressure was measured in a "pop chamber." An Ultradyne Corporation pressure transducer was used; the filter was a cylinder composed of wrapped wire; 20-psi steps in pressure were used. The rise time to 90 percent of the step was determined to be less than $2\frac{1}{2}$ msec; and to 100 percent of the step the rise time was $3\frac{1}{2}$ msec.

An estimation of fibre stress at the base of the probe is made with the following simplifying assumptions.



$$r = 1.5 \text{ in.}$$

$$L = 12 \text{ in.}$$

$$I = 2.42 \text{ in.}^4$$

Assume loading given by $q_1 = \frac{1}{2} \rho_1 u_1^2 = 2,000 \text{ psi}$, $\alpha = 30^\circ$. From Figure 7c of Reference 18 "local lifting pressure coefficient", β , for $\alpha = 30^\circ$ is taken:

$$\beta = \frac{p - p_1 - p(\alpha = 0)}{q_1} \quad (\text{C.8})$$

$\beta = 0.4$ on bottom surface of cylinder

$\beta = -0.2$ on top surface of cylinder

Then:

$$\text{loading/length} = 2r \times 0.6q_1$$

$$\text{Fibre stress at base} = S = \frac{Mc}{I}$$

$$M \cong \frac{L^2}{2} \times 1.2q_1r = \frac{12^2}{2} \times 1.2 \times 2,000 \times 1.5 \quad (\text{C.9})$$

$$= 259,000 \text{ in-lb}$$

$$S \cong \frac{259,000}{2.4} = 107,000 \text{ psi}$$

Compression $\cong 4,000 \text{ psi}$, and because $3(\sin 30^\circ) = 1.7052$:

$$\text{Shear} \cong \frac{0.6 \times 2,000 \times 3 \times 12}{\pi/4(3^2 - 1.7052)} = 9,000 \text{ psi}$$

From Bethlehem Steel Booklet 211, Page 60:

yield point = 110,000 psi,

tensile strength = 130,000 psi.

The probe should withstand the loading assumed. Transient stresses due to load application should be small because the period of the lowest mode of vibration is many times smaller than the estimated rise time of loading.

Appendix D
TEAPOT DATA REPROCESSED by METHODS
AGREED UPON by PARTICIPANTS in AFSWP-
SPONSORED MEETING 12 and 13 AUGUST 1958

TABLE D.1 OVERPRESSURE, SHOT 12, DESERT LINE

Gage	Ground Range	Gage Height	Arrival Time	Maximum Precursor	Time of Maximum Precursor	Main Shock Maximum Pressure	Time of Main Shock Maximum Pressure	Maximum Pressure*	Time of Maximum Pressure	Positive Phase Duration	Positive Phase Impulse	Wave-Form Type
	ft	ft	sec	psi	sec	psi	sec	psi	sec	sec	psi-sec	
1BA	750	0	0.104	81.0	0.115	164	0.133			0.1576	13.6	1
2BA	1,000	0	0.149	38.3	0.155	68.6	0.224			0.331	5.40	1
3P3	1,250	3	0.202	22.3	0.210	41.8	0.365			0.378	3.70	1
5B	1,500	0	0.265	19.7	0.275	29.9	0.520			0.535	4.85	1
5P3	1,500	3	0.265	16.0	0.275	47.4	0.517			0.535	5.84	1
5B10	1,500	10	0.269	—	—	25.7	0.290			†	†	—
5P10	1,500	10	0.268	17.3	0.235	32.4	0.520			0.535	4.87	1
6P10A	1,750	10	0.3465	10.7	0.365	15.0	0.615			0.634	4.05	1†
7B	2,000	0	0.4525	8.72	0.470	16.8	0.520			>0.548	>4.36	3
7P3	2,000	3	0.4525	10.5	0.470	21.1	0.530			>0.548	>5.83	3
7B10	2,000	10	0.458	—	—	21.9	0.560			†	†	—
7P10	2,000	10	0.4565	6.27	0.470	16.9	0.530			>0.544	>4.22	3
8P16A	2,250	10	0.599	5.28	0.610	13.5	0.680			>0.541	>3.73	3
9B	2,500	0	0.781	—	—	7.44	0.885			>0.619	>2.64	4
9P3	2,500	3	0.780	7.23	0.850	9.17	0.955			>0.620	>3.33	4
9B10	2,500	10	0.786	—	—	8.00	0.920			†	†	—
9P10	2,500	10	0.772	6.01	0.830	12.3	0.935			>0.618	>3.54	5
9P25	2,500	25	0.7885	2.06	0.770	9.97	0.955			>0.612	>3.47	5
9P40A	2,500	40	0.7915	3.65	0.795	7.84	0.920			>0.609	>2.72	5
11P3	2,750	3	0.987	2.67	0.995	7.25	1.150			>0.613	>2.58	5
12B	3,000	0	1.192	2.66	1.205	8.08	1.295			>0.608	>2.26	6
12P3	3,000	3	1.192	2.53	1.200	8.48	1.297			>0.608	>2.38	6
12P10	3,000	10	1.194	2.44	1.200	7.86	1.296			>0.606	>2.28	6
15B	3,500	0	1.6115	2.23	1.615	7.17	1.635			>0.589	>2.01	6
15P10	3,500	10	1.610	2.87	1.615	7.46	1.630			>0.590	>1.97	6
16P10	4,000	10	1.995	—	—	5.50	2.010			>0.605	>1.75	7
17B	4,500	0	2.3875	—	—	4.57	2.400			>0.613	>1.51	7
17P3	4,500	3	2.386	—	—	4.19	2.395			>0.614	>1.46	7
A-scaled to 1-kt radiochemical release at sea level												
1BA	257	0.0	0.0355	91.7	0.0393	186	0.0455			0.1969	5.19	1
2BA	342	0	0.0509	43.4	0.0530	77.7	0.0768			0.1131	2.06	1
3P3	428	1.0	0.0690	25.2	0.0718	47.2	0.1248			0.1292	1.41	1
5B	514	0	0.0906	22.3	0.0940	33.8	0.1777			0.1829	1.85	1
5P3	514	1.0	0.0906	18.1	0.0940	53.7	0.1767			0.1829	2.23	1
5B10	514	3.4	0.0919	—	—	29.1	0.0991			†	†	—
5P10	514	3.4	0.0916	19.6	0.0974	36.7	0.1777			0.1829	1.86	1
6P10A	599	3.4	0.1184	12.1	0.1248	17.0	0.2102			0.2167	1.55	1†
7B	685	0	0.1547	9.87	0.1606	19.0	0.1777			>0.1873	>1.66	3
7P3	685	1.0	0.1547	11.9	0.1606	23.9	0.1812			>0.1873	>2.23	3
7B10	685	3.4	0.1565	—	—	24.8	0.1914			†	†	—
7P10	685	3.4	0.1560	7.10	0.1606	19.1	0.1812			>0.1859	>1.61	3
8P10A	770	3.4	0.2047	5.98	0.2085	15.3	0.2324			>0.1849	>1.42	3
9B	856	0	0.2669	—	—	8.42	0.3025			>0.2116	>1.01	4
9P3	856	1.0	0.2666	8.18	0.2905	10.4	0.3264			>0.2119	>1.27	4
9B10	856	3.4	0.2687	—	—	9.06	0.3145			†	†	—
9P10	856	3.4	0.2673	6.60	0.2837	13.9	0.3196			>0.2112	>1.35	5
9P25	856	8.6	0.2695	2.33	0.2700	11.3	0.3264			>0.2092	>1.32	5
9P40A	856	13.7	0.2705	4.13	0.2717	8.87	0.3145			>0.2082	>1.04	5
11P3	942	1.0	0.3374	3.02	0.3401	8.51	0.3931			>0.2095	>0.98	5
12B	1,027	0	0.4074	3.03	0.4119	9.15	0.4428			>0.2078	>0.86	6
12P3	1,027	1.0	0.4074	2.86	0.4102	9.60	0.4433			>0.2078	>0.91	6
12P10	1,027	3.4	0.4081	2.99	0.4102	8.90	0.4430			>0.2071	>0.87	6
15B	1,198	0	0.5508	2.52	0.5520	8.12	0.5588			>0.2013	>0.77	6
15P10	1,198	3.4	0.5503	3.25	0.5522	8.43	0.5571			>0.2017	>0.75	6
16P10	1,370	3.4	0.6819	—	—	6.23	0.5870			>0.2068	>0.67	7
17B	1,541	0	0.8160	—	—	5.17	0.8203			>0.2095	>0.58	7
17P3	1,541	1.0	0.8155	—	—	4.74	0.8186			>0.2099	>0.56	7

* If different from main shock maximum pressure.

† Data uncertain



TABLE D.2 OVERPRESSURE, SHOT 12, WATER LINE

Gage	Ground Range	Gage Height	Arrival Time	Maximum Precursor	Time of Maximum Precursor	Main Shock Maximum Pressure	Time of Main Shock Maximum Pressure	Maximum Pressure*	Time of Maximum Pressure	Positive Phase Duration	Positive Phase Impulse	Wave Form Type
	ft	ft	sec	psi	sec	psi	sec	psi	sec	sec	psi-sec	
21BA	750	0	0.1185	—	—	170.	0.125	—	—	0.562	11.1	1†
22B	1,000	0	0.1695	30.2	0.185	69.8	0.200	—	—	0.551	7.55	1
23P3A	1,250	3	0.242	7.44	0.256	84.7	0.300	—	—	0.378	5.68	1
25B	1,500	0	0.3665	24.6	0.375	34.5	0.400	—	—	0.374	4.39	2
25P3	1,500	3	0.373	—	—	44.5	0.380	—	—	0.367	4.76	3
25B10	1,500	10	0.376	—	—	37.3	0.380	—	—	†	†	—
25P10	1,500	10	0.376	—	—	41.3	0.410	—	—	†	†	—
26P10A	1,750	10	0.493	—	—	35.2	0.500	—	—	0.364	4.30	2
27B	2,000	0	0.589	9.00	0.600	17.5	0.695	—	—	0.367	3.11	7
27P3	2,000	3	0.5865	14.8	0.605	20.2	0.695	—	—	0.511	3.35	1
27B10A	2,000	10	0.587	—	—	15.8	0.600	—	—	0.514	4.10	1
27P10	2,000	10	0.5865	12.1	0.595	5.0	0.695	—	—	†	†	—
29P10	2,250	10	0.7455	8.88	0.750	16.6	0.772	—	—	0.493	3.40	1
29B	2,500	0	0.914	—	—	11.8	0.960	—	—	0.514	3.16	6
29P3	2,500	3	0.913	—	—	13.6	0.940	—	—	0.566	2.68	7
29B10	2,500	10	0.914	—	—	12.9	0.915	—	—	0.427	1.89	7
29P10	2,500	10	0.913	—	—	13.1	0.960	—	—	†	†	—
29P25	2,500	25	0.913	—	—	14.1	0.915	—	—	0.567	3.14	7
29P40A	2,500	40	0.913	—	—	12.8	0.960	—	—	0.567	3.20	7
31P3	2,750	3	1.077	—	—	11.4	1.095	—	—	0.527	2.87	7
32BA	3,000	0	1.246	—	—	8.76	1.255	—	—	> 0.523	> 2.75	7
32P3	3,000	3	1.245	—	—	10.6	1.250	—	—	> 0.554	> 2.29	8
25P3X*	1,500	3	0.3715	—	—	49.8	0.380	—	—	> 0.555	> 2.43	8
25P3Y*	1,500	3	0.3575	32.6	0.375	42.0	0.425	—	—	0.389	4.59	—
29P3X*	2,500	3	0.914	—	—	14.6	0.965	—	—	0.222	3.35	—
29P3Y*	2,500	3	0.914	—	—	13.0	0.945	—	—	0.267	1.74	—
										> 0.486	> 2.95	—
A-scaled to 1-kt radiochemical release at sea level												
21BA	257	0	0.0405	—	—	192	0.0427	—	—	0.1921	4.24	1†
22B	342	0	0.0579	34.2	0.0632	79.0	0.0684	—	—	0.1883	2.88	1
23P3A	428	1.0	0.0827	8.42	0.0872	95.9	0.1025	—	—	0.1292	2.17	1
25B	514	0	0.1253	27.8	0.1282	39.1	0.1367	—	—	0.1278	1.68	2
25P2	514	1.0	0.1275	—	—	52.8	0.1299	—	—	0.1254	1.82	3
25B10	514	3.4	0.1285	—	—	3.2	0.1299	—	—	0.1244	1.65	—
25P10	514	3.4	0.1285	—	—	46.8	0.1401	—	—	0.1254	1.19	2
26P10A	599	3.4	0.1685	—	—	39.8	0.1709	—	—	0.1747	1.28	7
27B	685	0	0.2013	10.2	0.2051	19.8	0.2376	—	—	0.1757	1.56	1
27P3	685	1.0	0.2005	16.8	0.2068	22.9	0.2376	—	—	†	†	1
27B10A	685	3.4	0.2006	—	—	17.9	0.2051	—	—	0.1685	1.30	—
27P10	685	3.4	0.2005	13.7	0.2034	20.4	0.2376	—	—	0.1757	1.21	1
28P10	770	3.4	0.2548	10.1	0.2564	18.8	0.2639	—	—	0.1935	1.02	6
29B	856	0	0.3124	—	—	13.4	0.3281	—	—	0.1459	0.72	7
29P3	856	1.0	0.3121	—	—	15.4	0.3213	—	—	†	†	7
29B10	856	3.4	0.3124	—	—	14.6	0.3127	—	—	0.1938	1.20	—
29P10	856	3.4	0.3121	—	—	14.8	0.3291	—	—	0.1938	1.22	7
29P25	856	6.6	0.3121	—	—	16.0	0.3127	—	—	0.1801	1.10	7
29P40A	856	13.7	0.3121	—	—	14.6	0.3281	—	—	> 0.1788	> 1.05	7
31P3	942	1.0	0.3181	—	—	12.9	0.3743	—	—	> 0.1894	> 0.87	7
32BA	1,027	0	0.4259	—	—	9.92	0.4290	—	—	> 0.1897	> 0.93	8
32P3	1,027	1.0	0.4255	—	—	13.0	0.4273	—	—	0.1330	1.75	8
25P3X*	514	1.0	0.1270	—	—	53.4	0.1299	—	—	0.0759	1.28	—
25P3Y*	514	1.0	0.1222	36.9	0.1282	47.5	0.1453	—	—	0.0913	0.66	—
29P3X*	856	1.0	0.3086	—	—	16.5	0.3298	—	—	> 0.1661	> 1.13	—
29P3Y*	856	1.0	0.3124	—	—	14.7	0.3230	—	—	—	—	—

* If different from main shock maximum pressure.
 † Data uncertain.

~~SECRET~~

TABLE B.3 OVERPRESSURE, SHOT 12, ASPHALT LINE

Gage	Ground Range	Gage Height	Arrival Time	Maximum Precursor	Time of Maximum Precursor	Main Shock Maximum Pressure	Time of Main Shock Maximum Pressure	Maximum Pressure*	Time of Maximum Pressure	Positive Phase Duration	Positive Phase Impulse	Wave-Form Type
	ft	ft	sec	psi	sec	psi	sec	psi	sec	sec	psi-sec	
41BA	750	0	0.093	44.0	0.105	183	0.135			0.367	10.7	1
42BA	1,000	0	0.1335	34.6	0.160	78.1	0.230			0.427	8.06	1
43P3	1,250	3	0.183	22.4	0.200	30.8	0.365			0.457	5.80	1
45B	1,500	0	0.241	8.33	0.245	18.1	0.270			>0.559	>3.99	2
45P3	1,500	3	0.241	8.90	0.245	19.8	0.560			>0.559	>5.07	2-
45B10	1,500	10	0.244	—	—	21.2	0.270			†	†	—
45P10	1,500	10	0.2445	19.7	0.260	20.8	0.560			0.536	4.36	2
46P10	1,750	10	0.324	—	—	18.1	0.365			>0.578	>4.51	2
47B	2,000	0	0.418	—	—	13.8	0.440			>0.582	>3.57	3
47P3	2,000	3	0.418	—	—	15.4	0.450			>0.582	>3.74	4
47B10	2,000	10	0.421	—	—	12.2	0.445			†	†	—
47P10	2,000	10	0.421	—	—	13.2	0.465			>0.579	>3.64	4
48P10	2,250	10	0.5395	—	—	10.4	0.590			>0.561	>3.23	4
49B	2,500	0	0.674	—	—	6.60	0.730			>0.626	>2.32	4
49P3	2,500	3	0.674	—	—	8.63	0.720			>0.626	>3.39	4
49B10	2,500	10	0.679	—	—	6.38	0.700			†	†	—
49P25	2,500	25	0.688	—	—	6.90	0.755	6.98	0.840	>0.612	>2.61	7
49P40	2,500	40	0.695	—	—	6.60	0.720			>0.605	>2.81	7
51P3A	2,750	3	0.843	—	—	6.38	0.885			>0.457	>1.84	4
52B	3,000	0	1.034	—	—	4.25	1.075			>0.566	>1.41	5
52P3	3,000	3	1.032	—	—	4.51	1.190	4.63	1.310	>0.566	>1.93	5
A-scaled to 1-kt radiochemical release at sea level												
41BA	257	0	0.0318	49.8	0.036	207	0.046			0.125	4.08	1
42BA	342	0	0.0456	39.2	0.055	86.4	0.079			0.146	3.08	1
43P3	428	1.0	0.0625	25.4	0.068	34.9	0.125			0.156	2.21	1
45B	514	0	0.0824	9.43	0.082	20.5	0.092			0.191	>1.52	2
45P3	514	1.0	0.0824	10.1	0.082	22.4	0.191			0.191	>1.94	2-
45B10	514	3.4	0.0834	—	—	24.0	0.092			†	†	—
45P10	514	3.4	0.0836	22.3	0.089	23.5	0.191			0.183	1.66	2
46P10	596	3.4	0.1107	—	—	20.5	0.125			0.197	>1.72	2
47B	685	0	0.1429	—	—	15.6	0.150			0.199	>1.36	3
47P3	685	1.0	0.1429	—	—	17.4	0.154			0.199	>1.43	4
47B10	685	3.4	0.1439	—	—	13.8	0.152			†	†	—
47P10	685	3.4	0.1439	—	—	14.9	0.159			0.198	>1.39	4
48P10	770	3.4	0.1844	—	—	11.8	0.202			0.192	>1.23	4
49B	856	0	0.2304	—	—	7.47	0.250			0.214	>0.89	4
49P3	856	1.0	0.2304	—	—	9.77	0.246			0.214	>1.20	4
49B10	856	3.4	0.2321	—	—	7.22	0.239			†	†	—
49P25	856	8.6	0.2352	—	—	7.81	0.258	7.90	0.287	0.209	>1.00	7
49P40	856	13.7	0.2376	—	—	7.47	0.246			0.207	>1.07	7
51P3A	942	1.0	0.2881	—	—	7.22	0.302			0.156	>0.70	4
52B	1,027	0	0.3534	—	—	4.81	0.367			0.193	>0.54	5
52P3	1,027	1.0	0.3527	—	—	5.11	0.376	5.24	0.446	0.194	>0.74	5

* If different from main shock maximum pressure.

† Data uncertain.

TABLE D.4 OVERPRESSURE, SHOT 6, ASPHALT LINE

Gage	Ground Range	Gage Height	Arrival Time	Time of Maximum Precursor		Main Shock Maximum Pressure	Time of Main Shock Maximum Pressure		Time of Maximum Pressure	Positive Phase Duration	Positive Phase Impulse	Wave-Form Type
				ft	sec		psi	sec				
64B	1,300	0	0.343	7.65	0.365	10.1	0.405	0.477	2.71	2		
64P10A	1,300	10	0.3485	7.01	0.370	12.6	0.420	0.618	>3.34	2		
65BA	1,650	0	0.5265	—	—	7.17	0.630	0.554	2.25	4		
65P10	1,650	10	0.531	—	—	7.56	0.645	0.549	2.23	4		
66B	2,000	0	0.7555	—	—	4.22	0.825	0.545	1.52	7		
66P10	2,000	10	0.7575	—	—	3.62	0.830	0.910	1.98	4		
A-scaled to 1-kt radiochemical release at sea level												
64B	624	0	0.1604	8.90	0.1707	11.7	0.1894	0.2231	1.47	2		
64P10A	624	4.8	0.1630	8.15	0.1730	14.7	0.1964	0.2690	>1.82	2		
65BA	792	0	0.2462	—	—	8.34	0.2947	0.2591	1.22	4		
65P10	792	4.8	0.2483	—	—	8.79	0.3017	0.2568	1.21	4		
66B	961	0	0.3533	—	—	4.91	0.3859	0.4186	0.2549	4		
66P10	961	4.8	0.3543	—	—	6.59	0.3882	0.4256	0.2446	4		

* If different from main shock maximum pressure.

TABLE D.5 OVERPRESSURE, SHOT 6, DESERT LINE

Gage	Ground Range	Gage Height	Arrival Time	Time of Maximum Precursor		Main Shock Maximum Pressure	Time of Main Shock Maximum Pressure		Time of Maximum Pressure	Positive Phase Duration	Positive Phase Impulse	Wave-Form Type
				ft	sec		psi	sec				
61B	1,300	0	0.3945	9.30	0.410	14.1	0.440	0.595	0.396	2.55	2	
61P10A	1,300	10	0.399	6.62	0.410	20.0	0.465	0.485	0.351	3.13	2	
62B	1,650	0	0.6125	8.70	0.635	10.6	0.665	0.428	2.20	4		
62P10A	1,650	10	0.614	8.70	0.635	13.9	0.670	0.406	2.45	5		
63B	2,000	0	0.869	7.65	0.875	11.5	0.925	0.431	1.86	6		
63P10A	2,000	10	0.8695	9.44	0.875	12.2	0.925	0.431	2.09	6		
A-scaled to 1-kt radiochemical release at sea level												
61B	624	0	0.1845	10.6	0.1918	16.4	0.2058	0.2783	0.1665	1.39	2	
61P10A	624	4.8	0.1866	7.70	0.1918	23.3	0.2175	0.2268	0.1642	1.70	2	
62B	792	0	0.2865	10.1	0.2970	12.6	0.3110	0.2007	1.20	4		
62P10A	792	4.8	0.2872	10.1	0.2970	16.2	0.3134	0.1299	1.33	5		
63B	961	0	0.4064	8.78	0.4092	13.4	0.4326	0.2016	1.01	6		
63P10A	961	4.8	0.4067	11.0	0.4092	14.2	0.4326	0.2016	1.09	6		

* If different from main shock maximum pressure.



TABLE D.6 DYNAMIC PRESSURE, SHOT 12, DESERT LINE

NR - no record.

Gage	Ground Range	Gage Height	Arrival Time	Early Peak	Time of Early Peak	First Maximum Pressure	Time of First Maximum Pressure	Second Maximum Pressure	Time of Second Maximum Pressure	Wave-Form Type
	ft	ft	sec	psi	sec	psi	sec	psi	sec	
3Q3	1,250	3	0.205	—	—	141	0.220	180	0.345	1b
5Q3	1,500	3	0.267	—	—	172	0.278	107	0.475	1b
5Q10	1,500	10	0.269	—	—	122	0.300	119	0.445	1b
6Q10	1,750	10	0.347	—	—	17.1	0.370	111	0.410	2c
7Q3	2,000	3	0.453	7.13	0.465	26.9	0.485	44.7	0.510	3c
7Q10	2,000	10	0.459	3.37	0.465	37.6	0.515	68.8	0.535	3c
8Q10A	2,250	10	0.600	1.28	0.610	19.0	0.680	23.5	0.940	3c
9Q3A	2,500	3	0.781	3.99	0.830	8.46	0.855	10.2	0.875	4d
9Q10	2,500	10	0.784	1.58	0.830	8.12	0.865	14.6	0.935	5d
9Q25	2,500	25	0.7885	2.37	0.895	10.6	0.930	13.3	0.975	4d
9Q40	2,500	40	0.792	2.77	0.895	6.02	0.975	11.9	1.090	4d
11Q3	2,750	3	NR	NR	NR	NR	NR	NR	NR	NR
12Q3A	3,000	3	1.1915	—	—	0.26	1.215	1.75	1.295	6b
12Q10	3,000	10	NR	NR	NR	NR	NR	NR	NR	NR
15Q10A	3,500	10	1.610	—	—	0.07	1.615	1.31	1.625	6b
16Q10	4,000	10	1.995	—	—	0.71	2.010	—	—	7b
17Q3A	4,500	3	2.386	—	—	0.45	2.415	—	—	7b
A-scaled to 1-kt radiochemical release at sea level										
3Q3	-428	1.0	0.0701	—	—	160	0.0752	204	0.1179	1b
5Q3	514	1.0	0.0913	—	—	138	0.0950	121	0.1624	1b
5Q10	514	3.4	0.0919	—	—	138	0.1025	135	0.1521	1b
6Q10	599	3.4	0.1186	—	—	19.4	0.1265	126	0.1401	2c
7Q3	685	1.0	0.1548	8.07	0.1589	30.5	0.1658	50.6	0.1743	3c
7Q10	685	3.4	0.1569	3.81	0.1589	42.6	0.1760	77.9	0.1829	3c
8Q10A	770	3.4	0.2051	1.45	0.2085	21.5	0.2324	26.6	0.3213	3c
9Q3A	856	1.0	0.2669	4.52	0.2837	9.58	0.2922	11.5	0.2991	4d
9Q10	856	3.4	0.2680	1.79	0.2837	9.20	0.2957	16.5	0.3196	5d
9Q25	856	8.6	0.2695	2.68	0.3059	11.3	0.3179	15.1	0.3333	4d
9Q40	856	13.7	0.2707	3.14	0.3059	6.81	0.3333	13.5	0.3726	4d
11Q3	942	1.0	NR	NR	NR	NR	NR	NR	NR	NR
12Q3A	1,027	1.0	0.4073	—	—	0.29	0.4153	1.98	0.4426	6b
12Q10	1,027	3.4	NR	NR	NR	NR	NR	NR	NR	NR
15Q10A	1,198	3.4	0.5503	—	—	0.08	0.5520	1.48	0.5554	6b
16Q10	1,370	3.4	0.6819	—	—	0.80	0.6870	—	—	7b
17Q3A	1,541	1.0	0.8155	—	—	0.51	0.8254	—	—	7b

TABLE D.7 DYNAMIC PRESSURE, SHOT 12, WATER LINE

Gage	Ground Range	Gage Height	Arrival Time	Early Peak	Time of Early Peak	First Maximum Pressure	Time of First Maximum Pressure	Second Maximum Pressure	Time of Second Maximum Pressure	Wave-Form Type
	ft	ft	sec	psi	sec	psi	sec	psi	sec	
23Q3	1,250	3	0.255	—	—	240	0.272	85.5	0.325	1c
25Q3A	1,500	3	0.3755	—	—	30.0	0.380	52.1	0.425	3b
25Q10A	1,500	10	0.375	—	—	28.6	0.380	47.4	0.425	2b
26Q10	1,750	10	0.494	—	—	21.9	0.497	—	—	7b
27Q3	2,000	3	0.5865	—	—	24.1	0.645	32.6	0.680	1d
27Q10	2,000	10	0.5865	—	—	13.3	0.645	15.1	0.770	1d
28Q10A	2,250	10	0.7455	1.47	0.750	5.46	0.772	3.38	0.930	6b
29Q3A	2,500	3	0.9125	3.80	0.915	5.57	0.960	4.76	1.060	7c
29Q10	2,500	10	0.9125	—	—	3.48	0.915	4.48	1.070	7c
29Q25	2,500	25	0.913	—	—	4.24	0.915	—	—	7b
29Q40A	2,500	40	0.913	—	—	4.45	0.925	—	—	7b
31Q3	2,750	3	1.077	—	—	4.45	1.088	—	—	7b
32Q3	3,000	3	1.245	—	—	3.12	1.247	—	—	8a
25Q3X*	1,500	3	0.377	—	—	35.2	0.380	41.8	0.445	—
25Q3Y*	1,500	3	0.3735	—	—	204	0.460	—	—	—
29Q3X*	2,500	3	0.902	3.18	0.920	17.3	0.980	17.2	1.100	—
29Q3Y*	2,500	3	0.913	—	—	4.81	0.950	—	—	—
A-scaled to 1-kt radiochemical release at sea level										
23Q3	428	1.0	0.0872	—	—	272	0.0930	96.8	0.1111	1c
25Q3A	514	1.0	0.1283	—	—	34.0	0.1299	59.0	0.1453	3b
25Q10A	514	3.4	0.1281	—	—	32.4	0.1299	53.7	0.1453	2b
26Q10	599	3.4	0.1688	—	—	24.8	0.1659	—	—	7b
27Q3	685	1.0	0.2005	—	—	27.3	0.2205	36.9	0.2324	1d
27Q10	685	3.4	0.2005	—	—	15.1	0.2205	17.1	0.2632	1d
28Q10A	770	3.4	0.2548	1.66	0.2564	6.18	0.2639	3.83	0.3179	6b
29Q3A	856	1.0	0.3119	4.30	0.3127	6.31	0.3291	5.39	0.3623	7c
29Q10	856	3.4	0.3119	—	—	3.94	0.3127	5.07	0.3657	7c
29Q25	856	8.6	0.3121	—	—	4.80	0.3127	—	—	7b
29Q40A	856	13.7	0.3121	—	—	5.04	0.3162	—	—	7b
31Q3	942	1.0	0.3681	—	—	5.04	0.3719	—	—	7b
32Q3	1,027	1.0	0.4255	—	—	3.53	0.4262	—	—	8a
25Q3X*	514	1.0	0.1289	—	—	39.8	0.1299	47.3	0.1521	—
25Q3Y*	514	1.0	0.1277	—	—	231	0.1367	—	—	—
29Q3X*	856	1.0	0.3083	3.60	0.3145	19.6	0.3350	19.5	0.3760	—
29Q3Y*	856	1.0	0.3121	—	—	5.44	0.3247	—	—	—



TABLE D.8 DYNAMIC PRESSURE, SHOT 12, ASPHALT LINF

NR - no record.

Gage	Ground Range	Gage Height	Arrival Time	Early Peak	Time of Early Peak	First Maximum Pressure	Time of First Maximum Pressure	Second Maximum Pressure	Time of Second Maximum Pressure	Wave-Form Type
	ft	ft	sec	psi	sec	psi	sec	psi	sec	
43Q3A	1,250	3	0.186	—	—	109	0.195	199	0.340	1b
45Q3A	1,500	3	0.246	—	—	77.2	0.255	—	—	2d
45Q10	1,500	3	0.246	—	—	67.1	0.280	114	0.430	2c
46Q10A	1,750	10	0.325	4.07	0.335	20.2	0.390	38.3	0.425	2c
47Q3A	2,000	3	0.419	—	—	15.7	0.435	—	—	4c
47Q10A	2,000	10	0.423	—	—	13.1	0.515	13.2	0.720	4d
48Q10A	2,250	10	0.5395	3.49	0.560	8.47	0.585	14.6	0.640	4d
49Q3	2,500	3	0.678	—	—	5.68	0.705	9.85	0.930	4e
49Q10	2,500	10	0.679	2.20	0.720	7.50	0.820	5.3	0.900	4e
49Q25	2,500	25	0.688	1.76	0.730	7.35	0.845	88	0.930	4d
49Q40A	2,500	40	0.695	1.55	0.700	3.87	0.920	4.89	1.010	4d
51Q3	2,750	3	NR	NR	NR	NR	NR	NR	NR	NR
52Q3A	3,000	3	1.034	0.35	1.040	0.80	1.165	0.66	1.260	5c
A - scaled to 1-kt radiochemical release at sea level										
43Q3A	428	1.0	0.0636	—	—	123	0.0667	225	0.1162	1b
45Q3A	514	1.0	0.0841	—	—	87.4	0.0872	—	—	2d
45Q10	514	3.4	0.0841	—	—	76.0	0.0937	129	0.1479	2c
46Q10A	599	3.4	0.1111	4.61	0.1145	22.9	0.1333	43.4	0.1453	2c
47Q3A	685	1.0	0.1432	—	—	17.8	0.1477	—	—	4c
47Q10A	685	3.4	0.1446	—	—	14.8	0.1760	14.9	0.2393	4d
48Q10A	770	3.4	0.1844	3.95	0.1914	9.59	0.2000	16.5	0.2188	4d
49Q3	856	1.0	0.2317	—	—	6.43	0.2410	11.2	0.3179	4e
49Q10	856	3.4	0.2321	2.49	0.2461	8.49	0.2803	17.3	0.3076	4e
49Q25	856	8.6	0.2352	1.99	0.2495	8.32	0.2888	10.1	0.3179	4d
49Q40A	856	13.7	0.2376	1.75	0.2393	4.38	0.3145	5.54	0.3452	4d
51Q3	942	1.0	NR	NR	NR	NR	NR	NR	NR	NR
52Q3A	1,027	1.0	0.3534	0.40	0.3555	0.91	0.3982	0.75	0.4307	5c

TABLE D.9 DYNAMIC PRESSURE, SHOT C, DESERT LINE

NR - no record.

Gage	Ground Range ft	Gage Height ft	Arrival Time sec	Early Peak psi	Time of Early Peak sec	First Maximum Pressure psi	Time of First Maximum Pressure sec	Second Maximum Pressure psi	Time of Second Maximum Pressure sec	Wave-Form Type
61Q10	1,300	10	0.400	4.13	0.415	50.2	0.455	94.0	0.555	2c
62Q10	1,650	10	NR	NR	NR	NR	NR	NR	NR	NR
63Q10A	2,000	10	0.8695	—	—	1.90	0.880	3.19	0.925	6b
A-scaled to 1-kt radiochemical release at sea level										
61Q10	624	4.8	0.1871	4.80	0.1941	56.4	0.2128	109	0.2596	2c
62Q10	792	4.8	NR	NR	NR	NR	NR	NR	NR	NR
63Q10A	961	4.8	0.4067	—	—	2.21	0.4116	3.71	0.4326	6b

TABLE D.10 DYNAMIC PRESSURE, SHOT 6, ASPHALT LINE

Gage	Ground Range ft	Gage Height ft	Arrival Time sec	Early Peak psi	Time of Early Peak sec	First Maximum Pressure psi	Time of First Maximum Pressure sec	Second Maximum Pressure psi	Time of Second Maximum Pressure sec	Wave-Form Type
64Q10	1,300	10	0.352	2.16	0.370	19.8	0.440	64.6	0.550	2c
65Q10A	1,650	10	0.532	1.62	0.560	4.03	0.620	4.71	0.665	4c
66Q10A	2,000	10	0.7595	1.10	0.795	4.06	0.865	4.04	0.900	4d
A-scaled to 1-kt radiochemical release at sea level										
64Q10	624	4.8	0.1646	2.51	0.1730	23.0	0.2058	75.1	0.2572	2c
65Q10A	792	4.8	0.2488	1.88	0.2619	4.69	0.2900	5.48	0.3110	4c
66Q10A	961	4.8	0.3552	1.28	0.3718	4.72	0.4046	4.70	0.4209	4d

SECRET

Approved for release by NSA on 05-08-2014 pursuant to E.O. 13526

TABLE D. 11 CALCULATED MACH NUMBER AND DYNAMIC PRESSURE, SHOT 12, DESERT LINE

Station	Ground Range	Gage Height	Maximum Mach Number	Time of Maximum Mach Number	Maximum Dynamic Pressure	Time of Maximum Dynamic Pressure	Maximum Differential Pressure (pitot)	Time of Maximum Differential Pressure (pitot)
	ft	ft		sec	psi	sec	psi	sec
1	750	0	*	*	*	*	*	*
2	1,000	0	*	*	*	*	*	*
3	1,250	3†	2.12	0.325	81.4	0.350	180	0.345
5	1,500	3	1.83	0.475	62.5	0.278	122	0.278
5	1,500	10	1.96	0.450	61.0	0.300	122	0.300
5	1,500	10†	2.00	0.445	60.1	0.300	122	0.300
6	1,750	10†	1.80	0.410	52.9	0.410	111	0.410
7	2,000	3	1.30	0.510	30.5	0.510	44.7	0.510
7	2,000	10	1.60	0.735	40.7	0.535	88.8	0.535
7	2,000	10†	1.53	0.595	40.5	0.535	68.8	0.535
8	2,250	10†	1.15	0.940	17.1	0.940	23.5	0.940
9	2,500	3	0.84	0.875	9.55	0.875	10.2 (12.1)‡	0.875
9	2,500	10	1.07	0.935	15.6	0.935	14.6	0.935
9	2,500	10†	0.83	0.935	12.3	0.935	14.6 (19.6)	0.935
9	2,500	25†	0.86	1.380	11.1	0.975	13.3 (18.1)	0.975
9	2,500	40†	0.87	1.090	9.90	1.090	11.9 (16.6)	1.090
11	2,750	3	*	*	*	*	*	*
12	3,000	3	0.41	1.340	2.47	1.297	1.75 (1.83)	1.295
12	3,000	10	*	*	*	*	*	*
15	3,500	10	0.60	1.625	4.02	1.625	1.31 (1.51)	1.625
15	3,500	10†	0.31	1.625	1.28	1.625	1.31 (1.45)	1.625
16	4,000	10†	0.23	2.010	0.70	2.010	0.71 (0.79)	2.010
17	4,500	3	0.17	2.500	0.34	2.410	0.45 (0.47)	2.415

A-scaled to 1-kt radiochemical release at sea level

1	257	0	*	*	*	*	*	*
2	342	0	*	*	*	*	*	*
3	428	1.0†	2.12	0.1111	92.1	0.1196	204	0.1179
5	514	1.0	1.83	0.1624	70.8	0.0950	138	0.0950
5	514	3.4	1.96	0.1538	69.1	0.1025	138	0.1025
5	514	3.4†	2.00	0.1521	66.0	0.1025	138	0.1025
6	599	3.4†	1.80	0.1401	59.9	0.1401	126	0.1401
7	685	1.0	1.30	0.1743	34.5	0.1743	50.6	0.1743
7	685	3.4	1.60	0.2512	46.1	0.1829	77.9	0.1829
7	685	3.4†	1.53	0.2034	45.8	0.1829	77.9	0.1829
9	770	3.4†	1.15	0.3213	19.4	0.3213	26.6	0.3213
9	856	1.0	0.84	0.2991	10.8	0.2991	11.5 (13.7)‡	0.2991
9	856	3.4	1.07	0.3196	17.7	0.3196	16.5	0.3196
9	856	3.4†	0.83	0.3196	13.9	0.3196	16.5 (22.2)	0.3196
9	856	8.6†	0.86	0.4717	12.6	0.3333	15.1 (20.5)	0.3333
9	856	13.7†	0.87	0.3726	11.2	0.3726	13.5 (18.8)	0.3726
11	942	1.0	*	*	*	*	*	*
12	1,027	1.0	0.41	0.4580	2.80	0.4433	1.98 (2.07)	0.4426
12	1,027	3.4	*	*	*	*	*	*
15	1,198	3.4	0.60	0.5554	4.55	0.5554	1.48 (1.71)	0.5554
15	1,198	3.4†	0.31	0.5554	1.45	0.5554	1.48 (1.64)	0.5554
16	1,370	3.4†	0.23	0.6870	0.79	0.6870	0.80 (0.89)	0.6870
17	1,541	1.0	0.17	0.8545	0.38	0.8237	0.51 (0.53)	0.8254

* Gages necessary for Mach number calculation not present.

† P gage substituted for B gage in Mach number calculation.

‡ Parentheses enclose corrected q.



TABLE D.12 CALCULATED MACH NUMBER AND DYNAMIC PRESSURE, SHOT 12, ASPHALT LINE

Station	Ground Range	Gage Height	Maximum Mach Number	Time of Maximum Mach Number	Maximum Dynamic Pressure	Time of Maximum Dynamic Pressure	Maximum Differential Pressure (pitot)	Time of Maximum Differential Pressure (pitot)
	ft	ft		sec	psi	sec	psi	sec
41	750	0	*	*	*	*	*	*
42	1,000	0	*	*	*	*	*	*
43	1,250	3†	2.01	0.340	81.2	0.340	199	0.340
45	1,500	3	1.57	0.255	44.0	0.255	77.2	0.255
45	1,500	10	1.95	0.430	48.7	0.430	114	0.430
45	1,500	10†	1.94	0.430	49.0	0.430	114	0.430
46	1,750	10†	1.28	0.425	25.9	0.425	38.3	0.425
47	2,000	3	0.90	0.450	14.1	0.450	15.7 (19.9)‡	0.435
47	2,000	10	0.91	0.670	11.7	0.480	13.1‡ (17.7)	0.515
47	2,000	10†	0.92	0.700	11.1	0.515	13.1‡ (17.5)	0.515
48	2,250	10†	0.88	0.640	12.1	0.640	14.6‡ (20.6)	0.640
49	2,500	3	0.93	0.930	10.3	0.330	9.85	0.930
49	2,500	10	*	*	*	*	*	*
49	2,500	25†	0.77	0.890	7.72	0.930	8.88 (9.79)	0.930
49	2,500	40†	0.59	1.010	4.49	1.010	4.89 (5.44)	1.010
51	2,750	3	*	*	*	*	*	*
52	3,000	3	0.39	1.300	1.75	1.300	0.80 (0.84)	1.165

A-scaled to 1-kt radiochemical release at sea level

41	257	0	*	*	*	*	*	*
42	342	0	*	*	*	*	*	*
43	428	1.0†	2.01	0.1162	91.9	0.1162	225	0.1162
45	514	1.0	1.57	0.0872	49.8	0.0872	87.4	0.0872
45	514	3.4	1.95	0.1470	55.1	0.1470	129	0.1470
45	514	3.4†	1.94	0.1470	55.5	0.1470	129	0.1470
46	590	3.4†	1.28	0.1453	29.3	0.1453	43.4	0.1453
47	685	1.0	0.90	0.1538	16.0	0.1538	17.8 (22.5)‡	0.1487
47	685	3.4	0.91	0.2290	13.2	0.1641	14.8‡ (20.0)	0.1760
47	685	3.4†	0.92	0.2393	12.6	0.1760	14.8‡ (19.8)	0.1760
48	770	3.4†	0.88	0.2188	13.7	0.2188	16.5 (23.3)	0.2188
49	856	1.0	0.93	0.3179	11.7	0.3179	11.2	0.3179
49	856	3.4	*	*	*	*	*	*
49	856	8.6†	0.77	0.3042	8.74	0.3179	10.1 (11.1)	0.3179
49	856	13.7†	0.59	0.3452	5.08	0.3452	5.54 (6.16)	0.3452
51	942	1.0	*	*	*	*	*	*
52	1,027	1.0	0.39	0.4443	1.98	0.4443	0.91 (0.95)	0.3982

* Gages necessary for Mach number calculation not present.

† P gage substituted for B gage in Mach number calculation.

‡ Parentheses enclose corrected q.

‡ First maximum peak entered for comparison at same time.

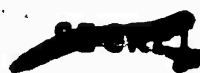


TABLE D.13 CALCULATED MACH NUMBER AND DYNAMIC PRESSURE, SHOT 6, DESERT LINE

Station	Ground Range	Gage Height	Maximum Mach Number	Time of Maximum Mach Number	Maximum Dynamic Pressure	Time of Maximum Dynamic Pressure	Maximum Differential Pressure (pitot)	Time of Maximum Differential Pressure (pitot)
	ft	ft		sec	psi	sec	psi	sec
61	1,300	10	1.77	0.555	45.8	0.555	94.0	0.555
61	1,300	10*	1.89	0.555	45.6	0.555	94.0	0.555
62	1,650	10	†	†	†	†	†	†
63	2,000	10	0.49	0.930	3.76	0.930	3.19 (3.55)‡	0.925
63	2,000	10*	0.43	0.930	3.06	0.925	3.19 (3.53)	0.925
A-scaled to 1-kt radiochemical release at sea level								
61	624	4.8	1.77	0.2596	53.3	0.2596	109	0.2596
61	624	4.8*	1.89	0.2596	53.0	0.2596	109	0.2596
62	792	4.8	†	†	†	†	†	†
63	961	4.8	0.49	0.4350	4.37	0.4350	3.71 (4.13)‡	0.4326
63	961	4.8*	0.43	0.4350	3.56	0.4326	3.71 (4.11)	0.4326

* P gage substituted for B gage in Mach number calculation.

† Gages necessary for Mach number calculation not present.

‡ Parentheses enclose corrected q.

TABLE D.14 CALCULATED MACH NUMBER AND DYNAMIC PRESSURE, SHOT 6, ASPHALT LINE

Station	Ground Range	Gage Height	Maximum Mach Number	Time of Maximum Mach Number	Maximum Dynamic Pressure	Time of Maximum Dynamic Pressure	Maximum Differential Pressure (pitot)	Time of Maximum Differential Pressure (pitot)
	ft	ft		sec	psi	sec	psi	sec
64	1,300	10	1.58	0.550	74.6	0.550	64.6	0.550
64	1,300	10*	1.68	0.550	33.7	0.550	64.6	0.550
65	1,650	10	0.59	0.665	4.65	0.665	4.71 (5.39)†	0.665
65	1,650	10*	0.56	0.665	4.35	0.665	4.71 (5.36)	0.665
66	2,000	10	0.66	0.890	5.05	0.890	4.06 (4.79)	0.865
66	2,000	10*	0.55	0.865	3.77	0.865	4.06 (4.60)	0.865
A-scaled to 1-kt radiochemical release at sea level								
64	624	4.8	1.58	0.2572	40.2	0.2572	75.1	0.2572
64	624	4.8*	1.68	0.2572	39.2	0.2572	75.1	0.2572
65	792	4.8	0.59	0.3110	5.41	0.3110	5.48 (6.27)†	0.3110
65	792	4.8*	0.56	0.3110	5.06	0.3110	5.48 (6.23)	0.3110
66	961	4.8	0.66	0.4163	5.87	0.4163	4.72 (5.57)	0.4046
66	961	4.8*	0.55	0.4046	4.38	0.4046	4.72 (5.35)	0.4046

* P gage substituted for B gage in Mach number calculation.

† Parentheses enclose corrected q.

TABLE D.15 CALCULATED MACH NUMBER AND DYNAMIC PRESSURE, SHOT 12, WATER LINE

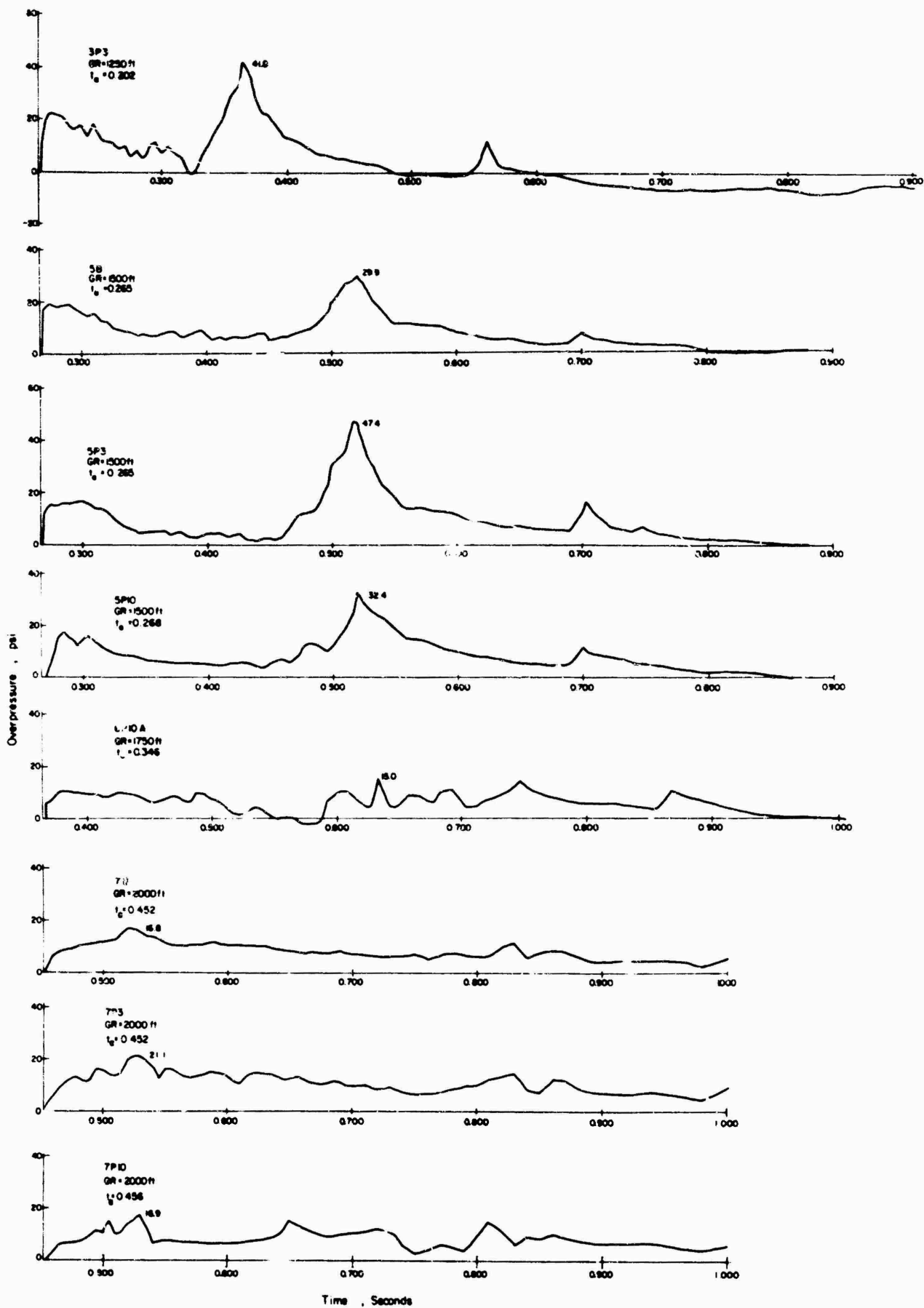
Station	Ground Range	Gage Height	Maximum Mach Number	Time of Maximum Mach Number	Maximum Dynamic Pressure	Time of Maximum Dynamic Pressure	Maximum Differential Pressure (pitot)	Time of Maximum Differential Pressure (pitot)
	ft	ft		sec	psi	sec	psi	sec
21	750	0	*	*	*	*	*	*
22	1,000	0	*	*	*	*	*	*
23	1,250	3†	2.25	0.272	89.6	0.285	240	0.272
25	1,500	3	1.28	0.380	38.7	0.425	52.1	0.425
25	1,500	10	1.22	0.380	34.7	0.380	47.4	0.425
25	1,500	10†	1.28	0.420	33.5	0.425	47.4	0.425
26	1,750	10†	0.76	0.497	19.0	0.497	21.9 (27.5)‡	0.497
27	2,000	3	1.23	0.680	22.9	0.680	32.6	0.680
27	2,000	10	0.85	0.630	11.4	0.770	15.1 (20.3)	0.770
27	2,000	10†	0.90	0.770	12.4	0.770	15.1 (21.9)	0.770
28	2,250	10†	0.50	0.772	5.14	0.772	5.46 (6.11)	0.772
29	2,500	3	0.58	0.940	5.68	0.940	5.57 (5.90)	0.960
29	2,500	10	0.68	0.915	6.76	0.915	4.48 (5.12)	1.070
29	2,500	10†	0.54	1.070	4.17	1.070	4.48 (5.08)	1.070
29	2,500	25†	0.46	0.950	4.02	0.915	4.24 (4.71)	0.915
29	2,500	40†	0.48	0.925	4.20	0.925	4.45 (4.97)	0.925
31	2,750	3†	0.50	1.088	4.18	1.088	4.45 (4.68)	1.088
32	3,000	3	0.53	1.250	4.26	1.250	3.12	1.247
25	1,500	3X	1.35	0.380	42.2	0.380	35.2‡	0.580
25	1,500	3Y	1.79	0.385	96.3	0.400	204	0.400
29	2,500	3Z	0.98	0.995	15.6	0.995	17.3	0.980
29	2,500	3Y	0.58	0.950	5.81	0.950	4.81 (5.14)	0.950
A-scaled to 1-kt radiochemical release at sea level								
21	257	0	*	*	*	*	*	*
22	342	0	*	*	*	*	*	*
23	428	1.0†	2.25	0.0930	101	0.0974	272	0.0930
25	514	1.0	1.28	0.1299	43.8	0.1453	59.0	0.1453
25	514	3.4	1.22	0.1299	39.3	0.1299	53.7	0.1453
25	514	3.4†	1.28	0.1436	37.9	0.1453	53.7	0.1433
28	599	3.4†	0.76	0.1699	21.5	0.1699	24.8 (31.1)‡	0.1699
27	685	1.0	1.23	0.2324	25.9	0.2324	36.9	0.2324
27	685	3.4	0.85	0.2153	12.9	0.2632	17.1 (23.0)	0.2632
27	685	3.4†	0.90	0.2632	14.0	0.2632	17.1 (24.8)	0.2632
28	770	3.4†	0.50	0.2639	5.82	0.2639	6.18 (6.92)	0.2639
29	856	1.0	0.58	0.3213	6.43	0.3213	6.31 (6.68)	0.3281
29	856	3.4	0.68	0.3127	7.65	0.3127	5.07 (5.80)	0.3657
29	856	3.4†	0.54	0.3657	4.72	0.3657	5.07 (5.75)	0.3657
29	856	8.6†	0.46	0.3247	4.55	0.3127	4.80 (5.33)	0.3127
29	856	13.7†	0.48	0.3162	4.75	0.3162	5.04 (5.63)	0.3162
31	942	1.0†	0.50	0.3719	4.73	0.3719	5.04 (5.30)	0.3719
32	1,027	1.0	0.53	0.4273	4.82	0.4273	3.53	0.402
25	514	1.0X	1.35	0.1299	47.8	0.1299	39.8‡	0.1299
25	514	1.0Y	1.79	0.1316	109	0.1367	231	0.1367
29	856	1.0X	0.98	0.3401	17.7	0.3401	19.6	0.3350
29	856	1.0Y	0.58	0.3247	6.58	0.3247	5.44 (5.82)	0.3247

* Gages necessary for Mach number calculation not present.
 † P gage substituted for B gage in Mach number calculation.
 ‡ Parentheses enclose corrected q.
 † First maximum peak entered for comparison at same time.

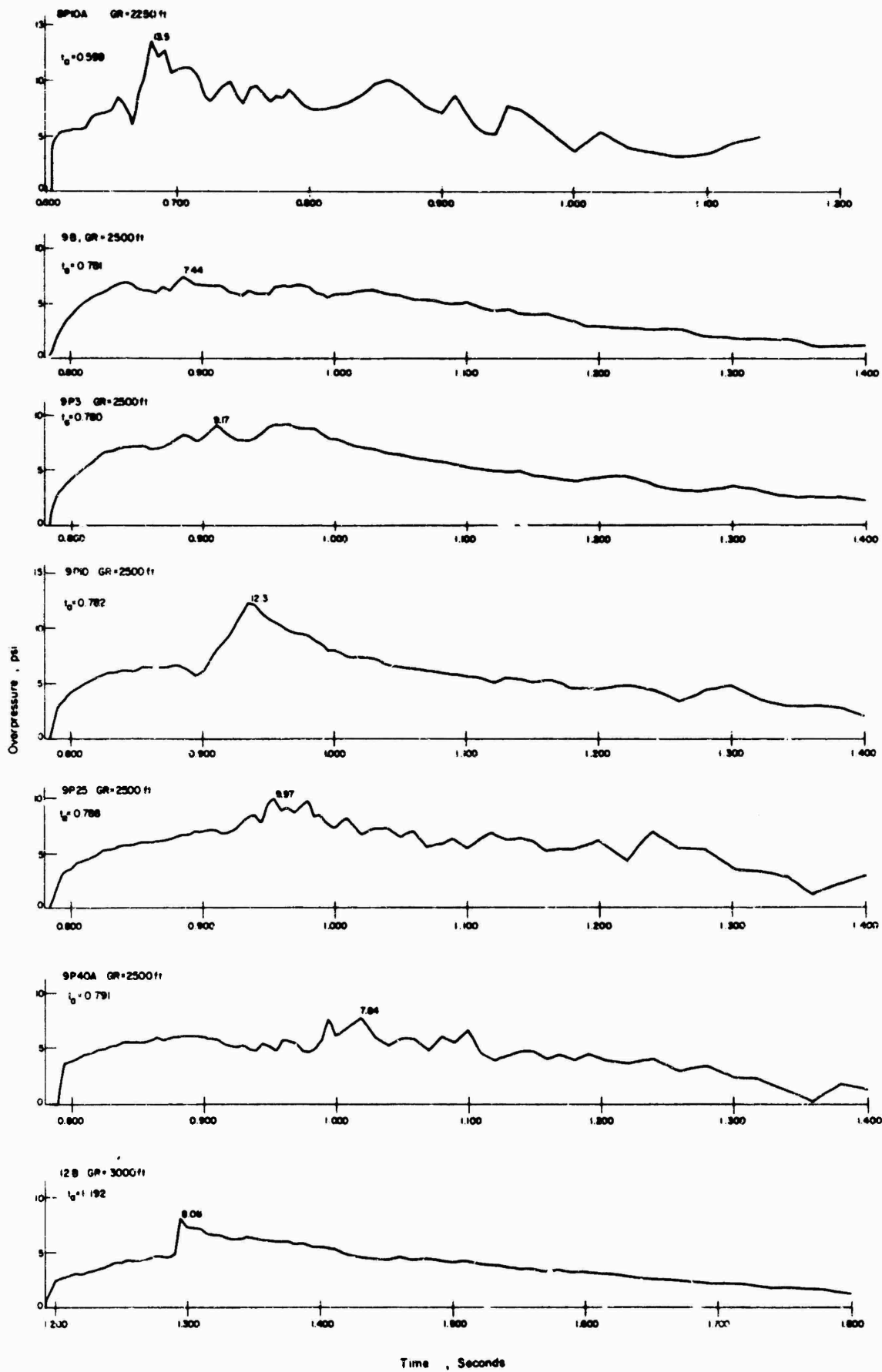


On the Mach number and dynamic overpressure (q^*) plots it will be noted that there are long vertical lines cutting through some of the records. In machine calculation the computer punches an "error" to indicated indefinable variations in Mach number and q^* under certain conditions. The vertical lines indicate the areas of error with the conditions coded by three numbers, 4, 5, and 6. The definition of these codes and therefore of these conditions is as follows:

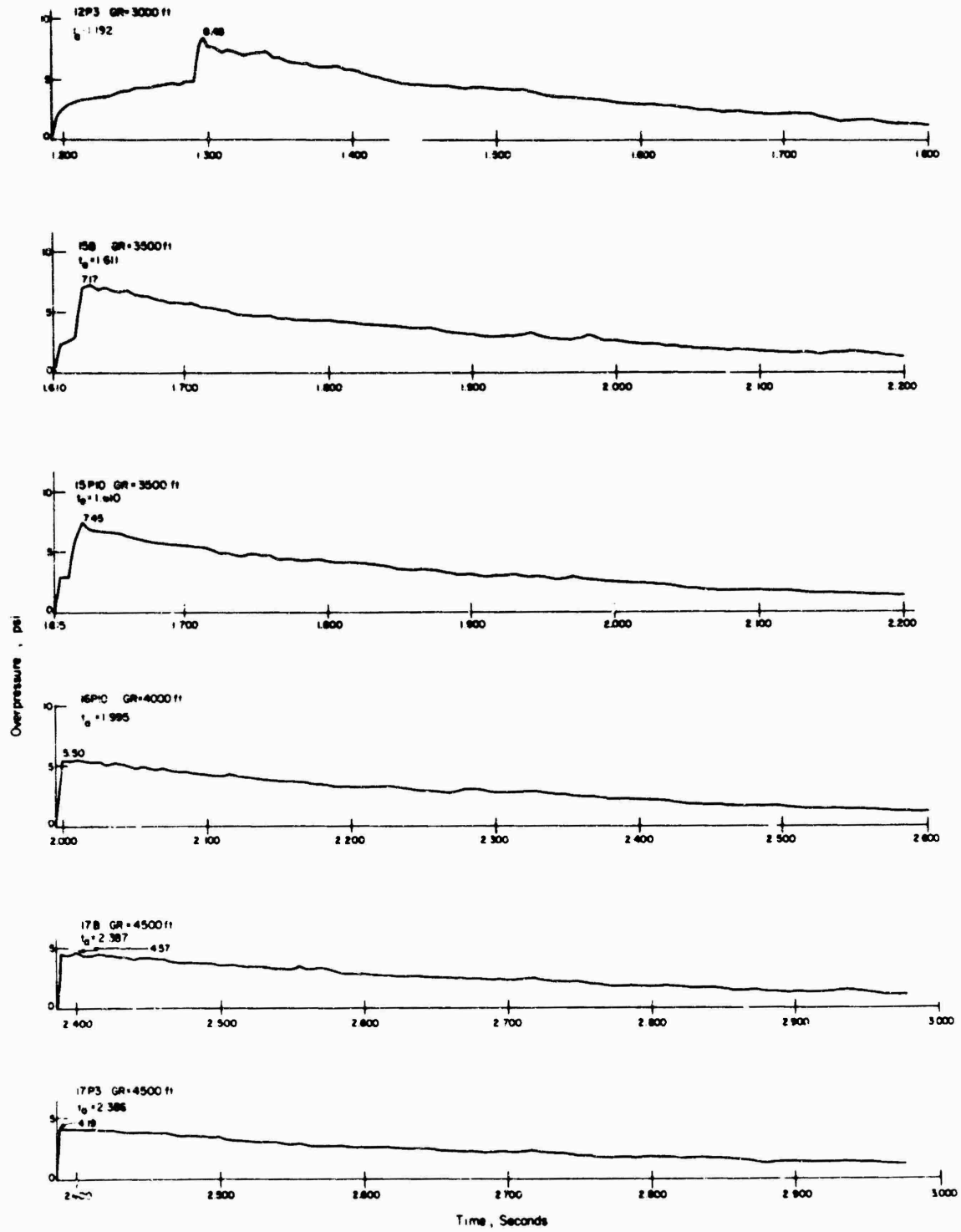
<u>Error No. Code</u>	<u>Definition of Condition</u>
4	$B = 0$
5	$P^* = P < 0$
6	$\frac{P^* + P_0}{B + P_0} < 1$



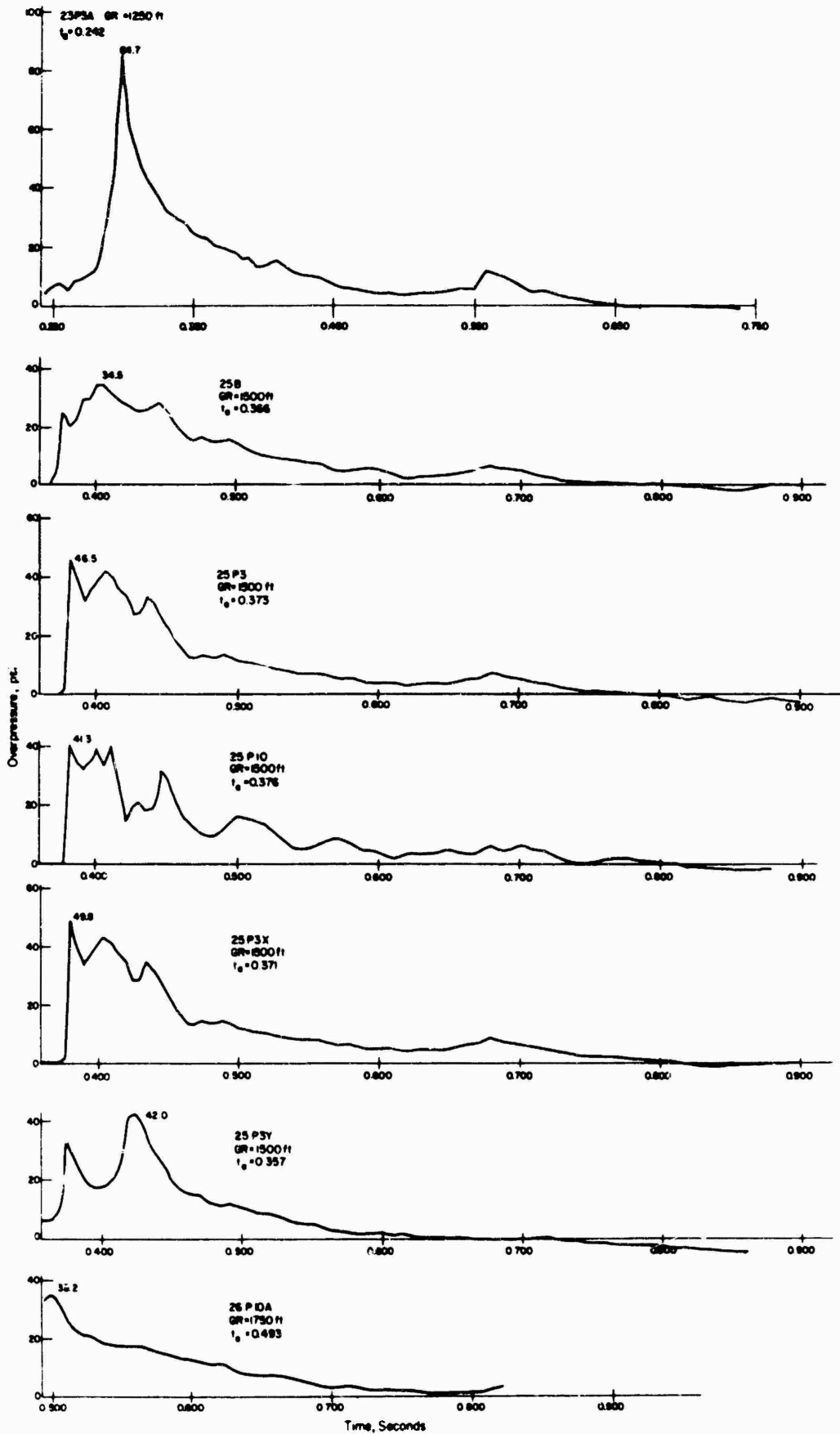
Overpressure versus time, Teapot Shot MET (12), Desert line.



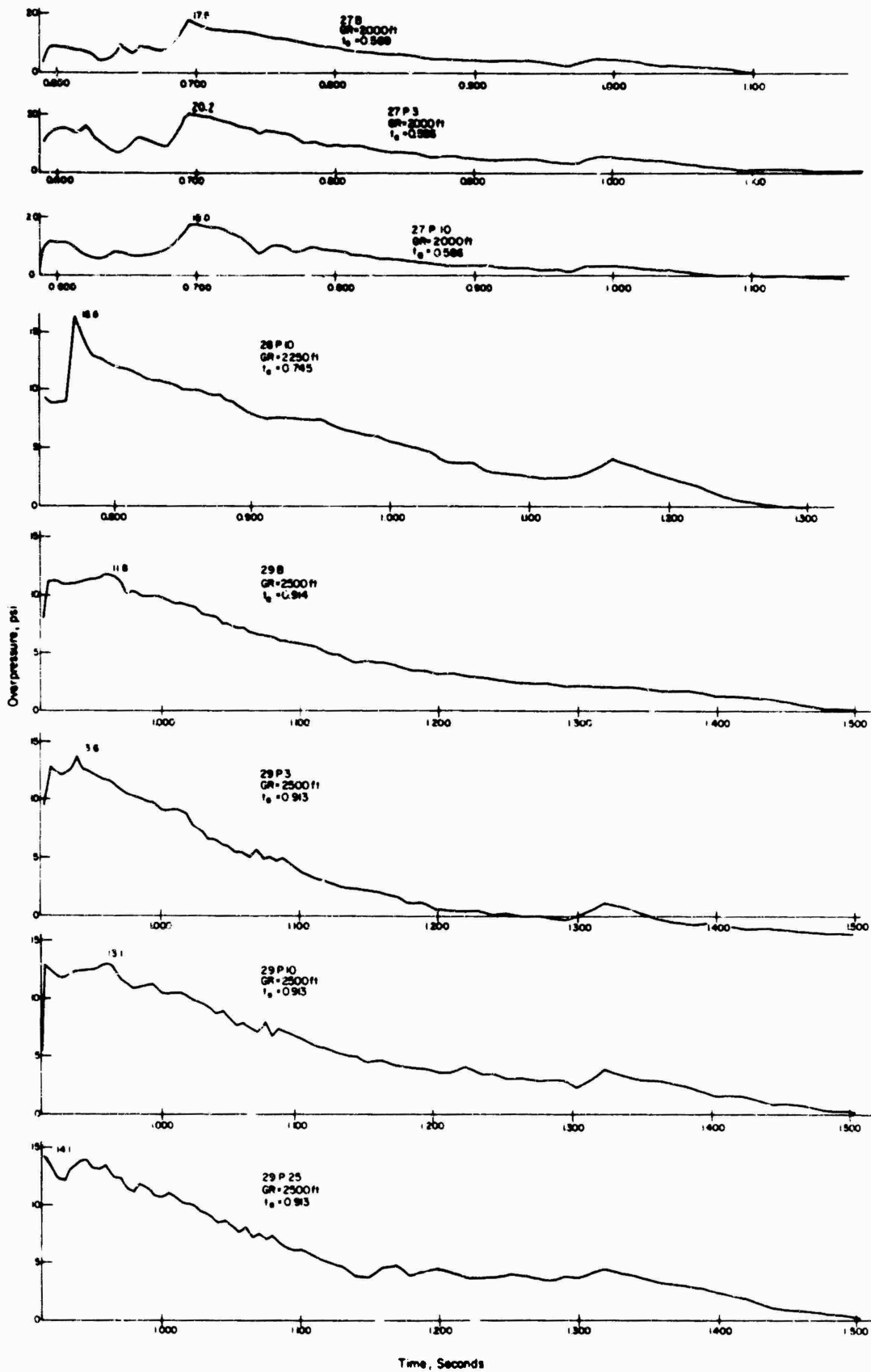
Overpressure versus time, Teapot Shot MET, Desert line.



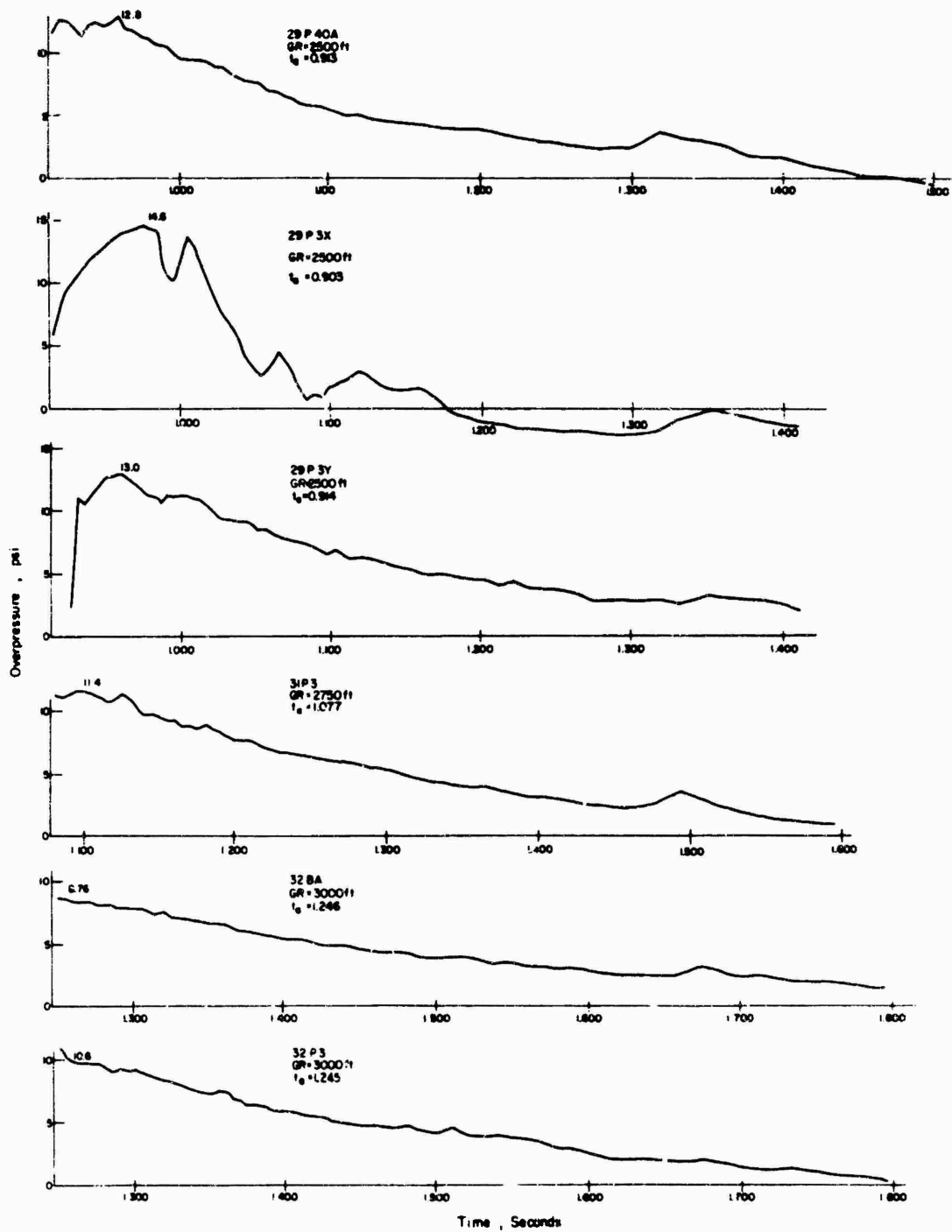
Overpressure versus time, Teapot Shot MET, Desert line.



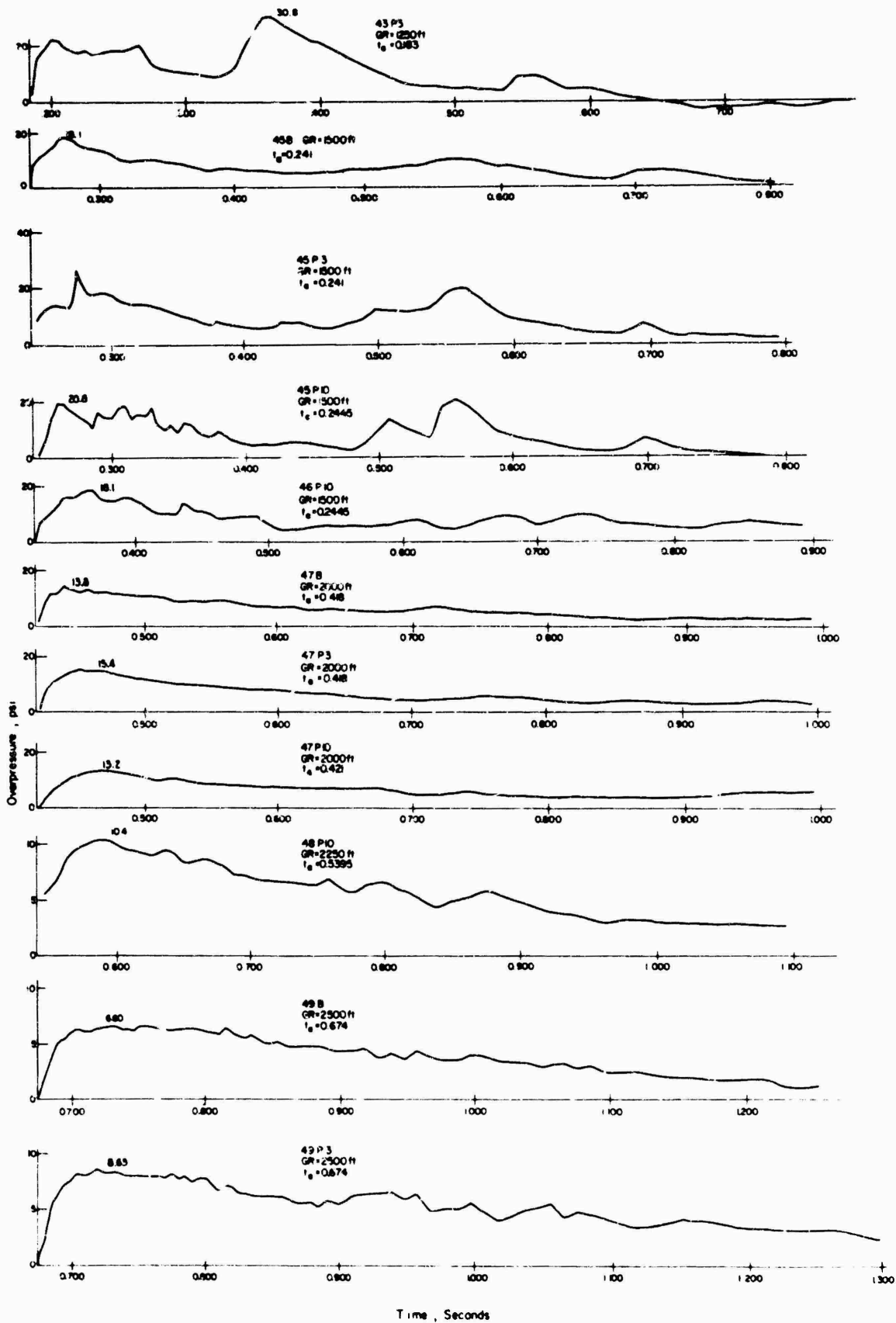
Overpressure versus time, Teapot Shot MET, Water line.



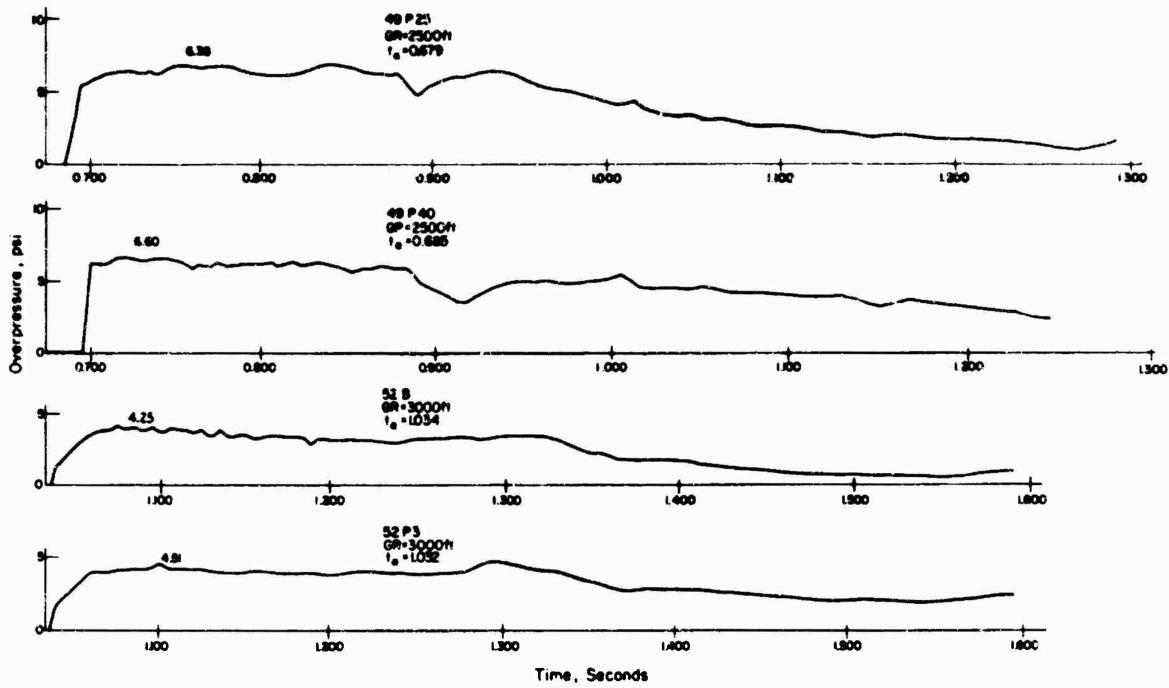
Overpressure versus time, Teapot Shot MET, Water line.



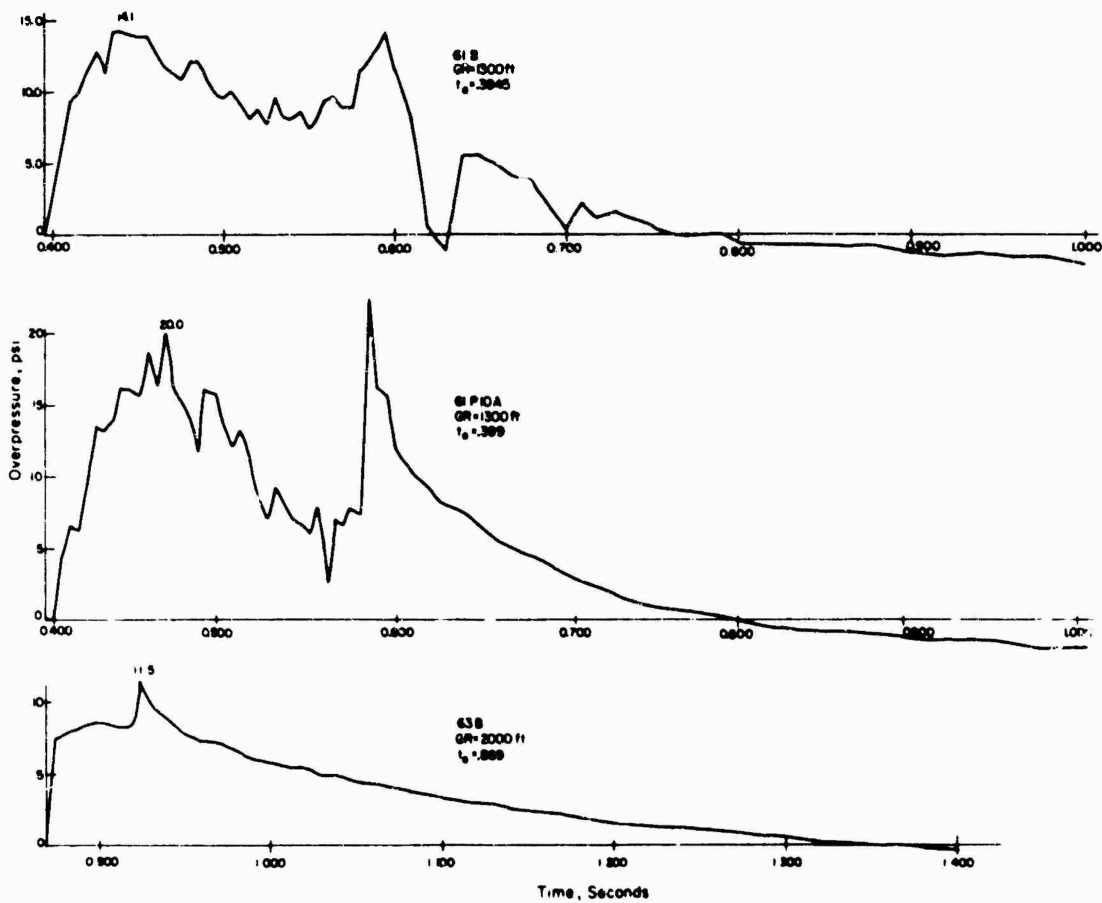
Overpressure versus time, Teapot Shot MET, Water line.



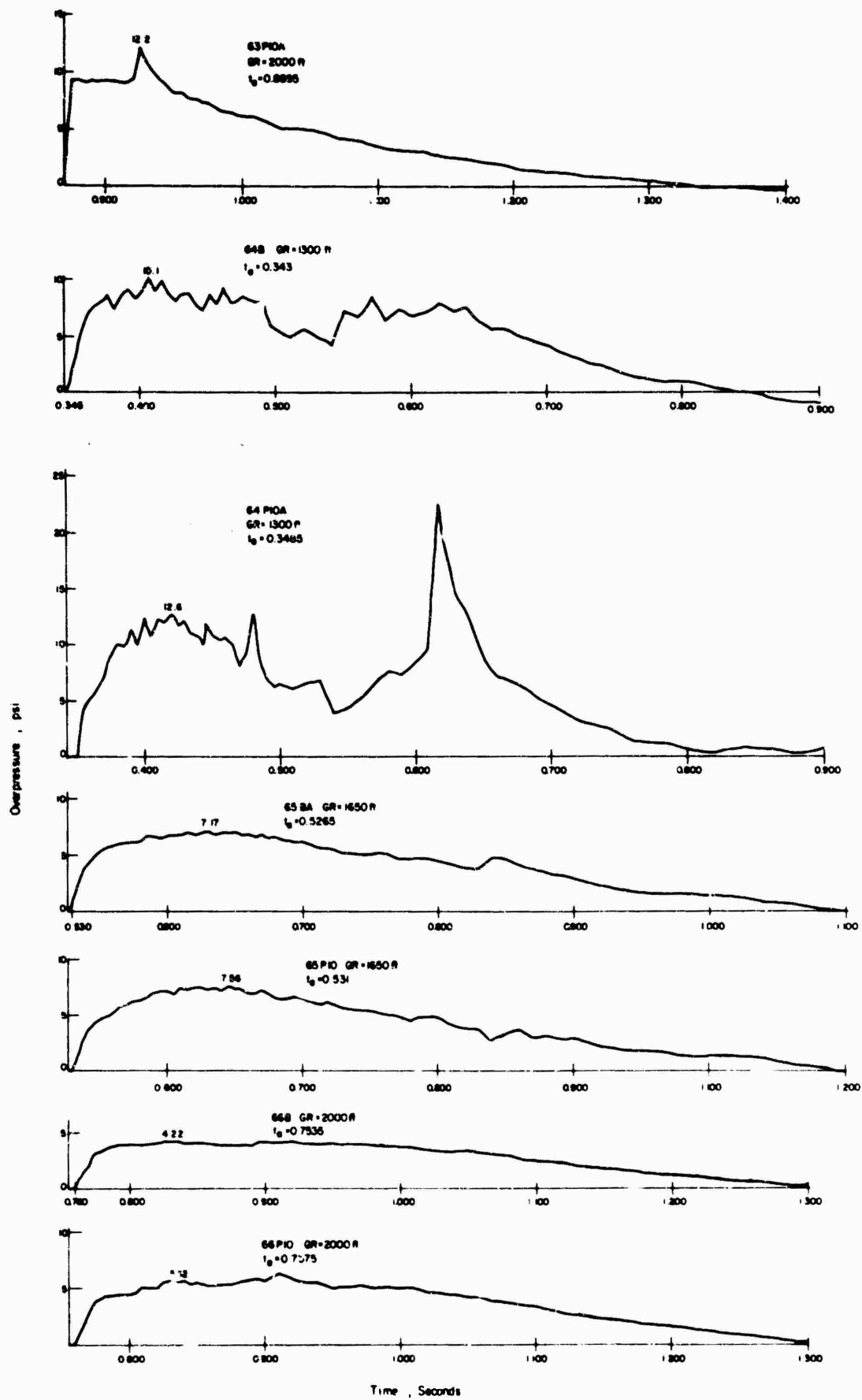
Overpressure versus time, Teapot Shot MET, Asphalt line.



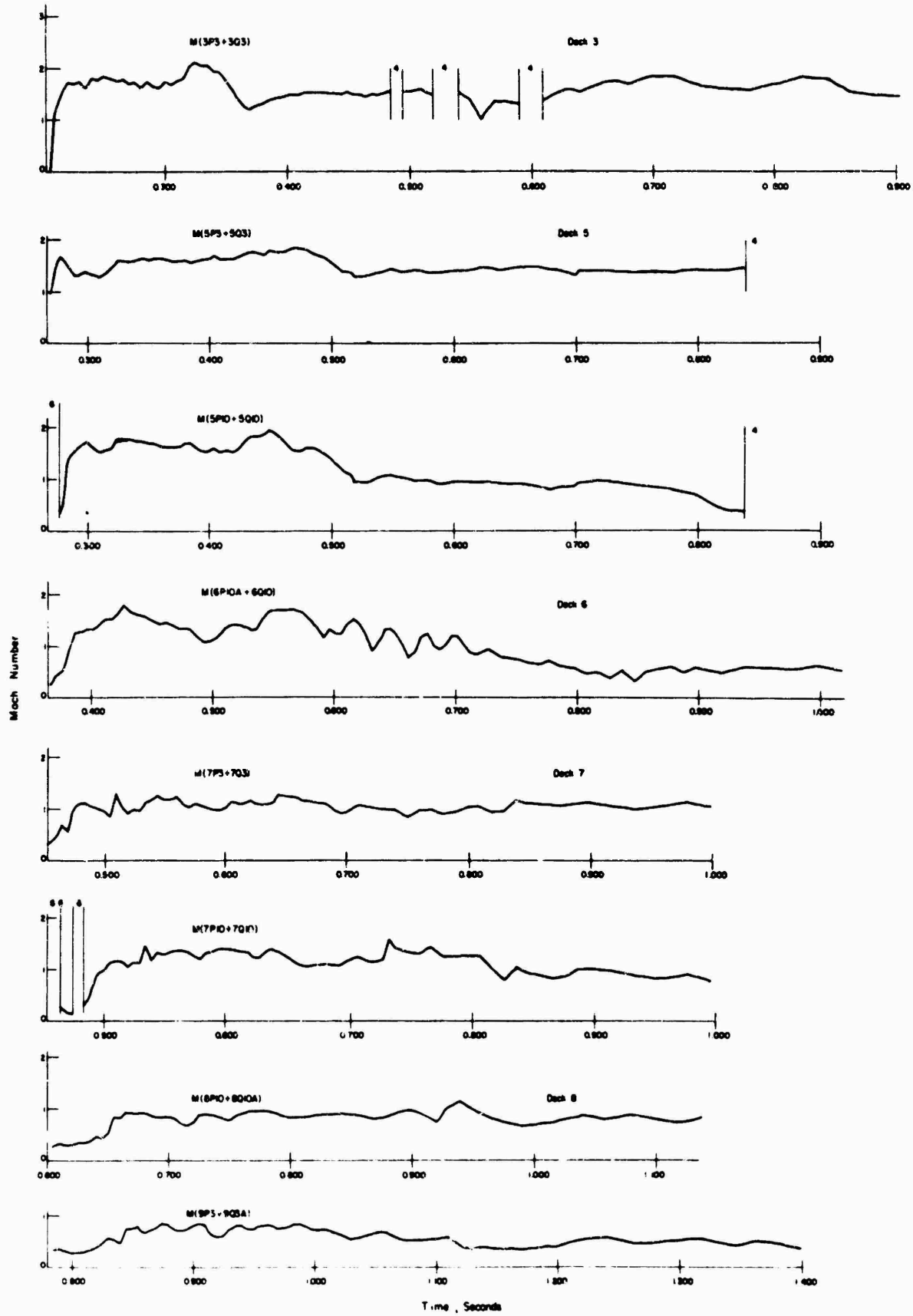
Overpressure versus time, Teapot Shot MET, Asphalt line.



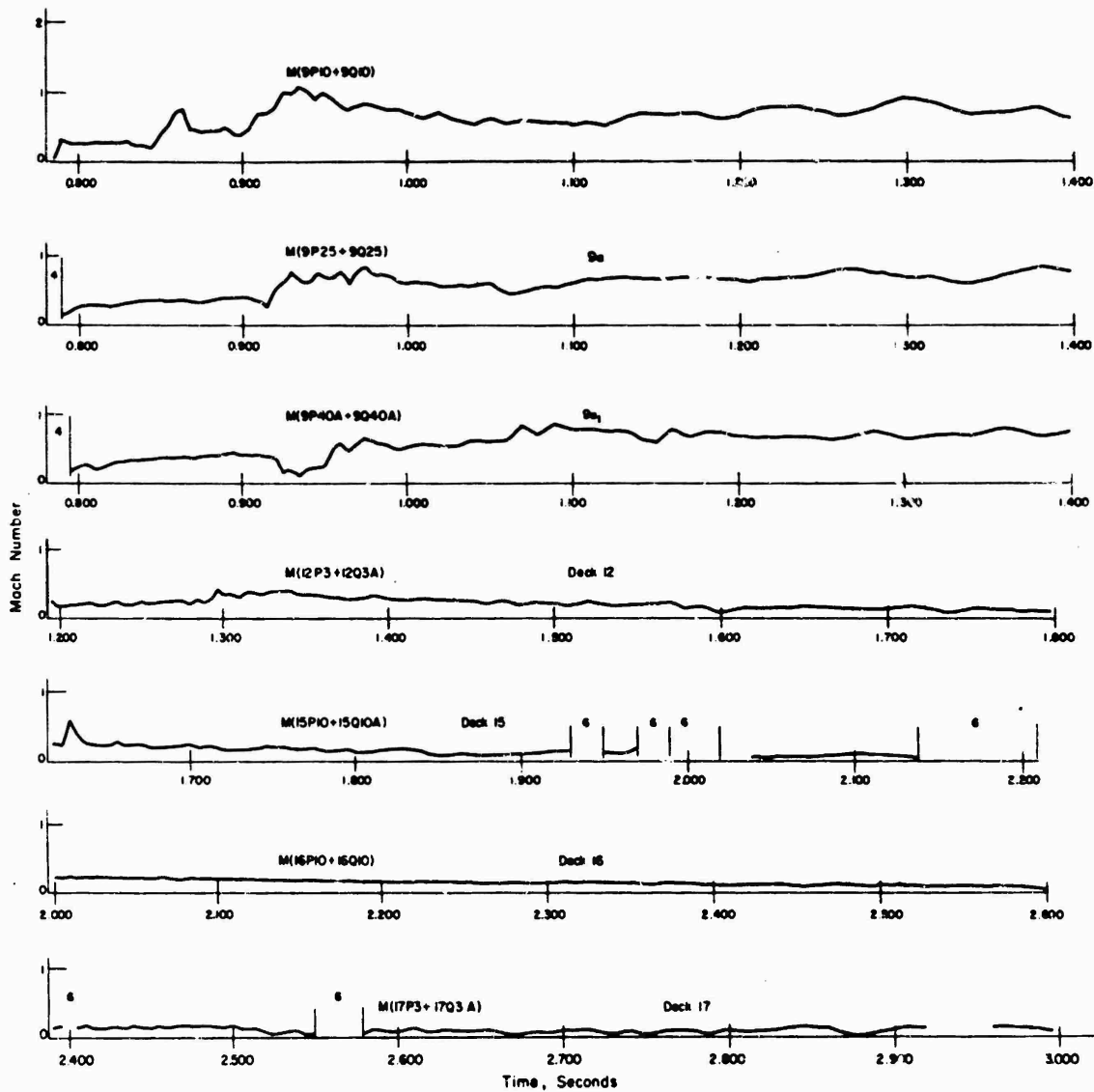
Overpressure versus time, Teapot Shot BEE (6).



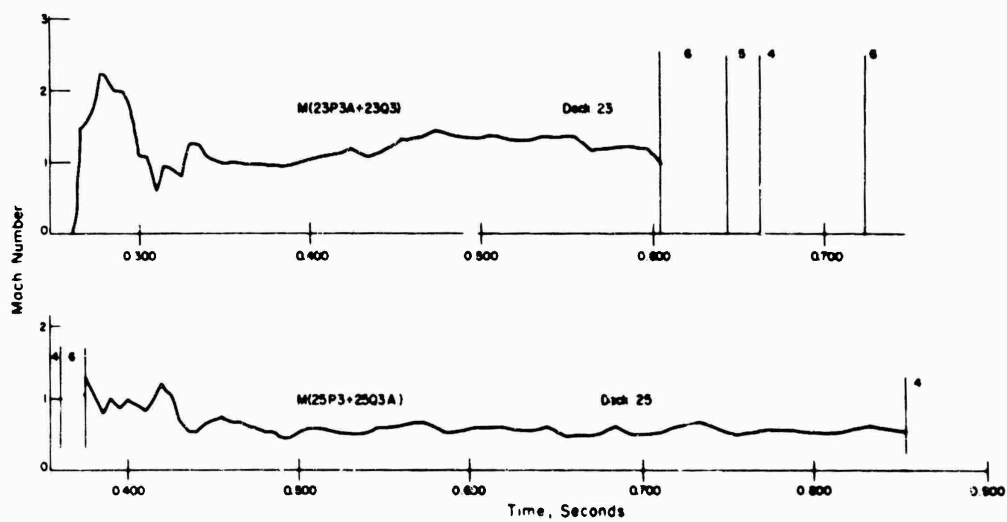
Overpressure versus time, Teapot Shot BEE.



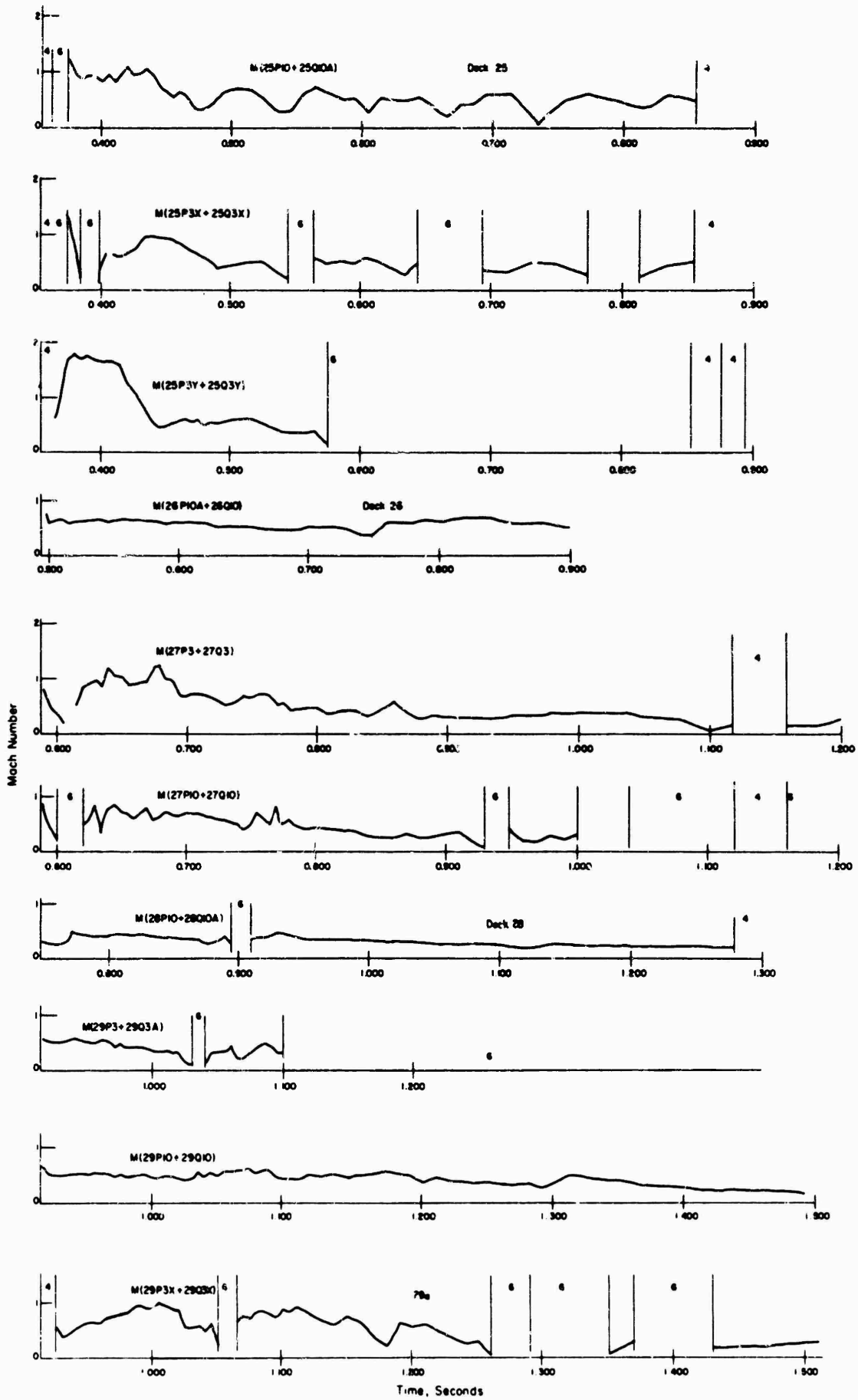
Mach number versus time, Teapot Shot MET, Desert line.



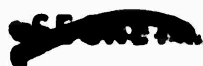
Mach number versus time, Teapot Shot MET, Desert line.

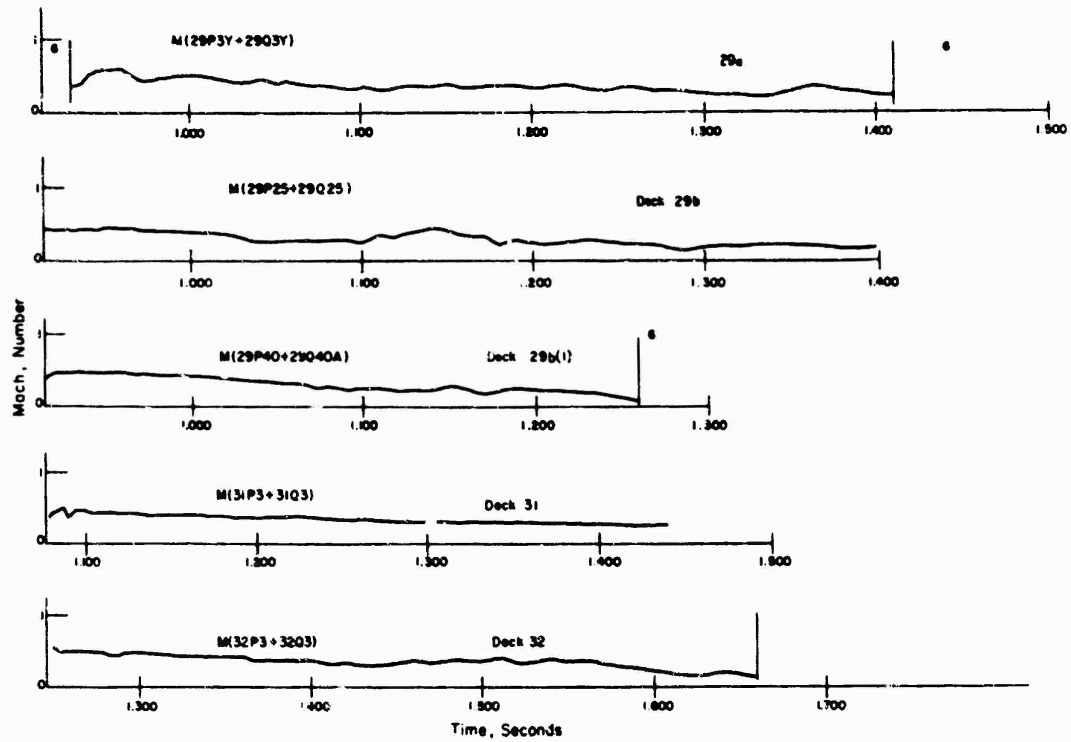


Mach number versus time, Teapot Shot MET, Water line.

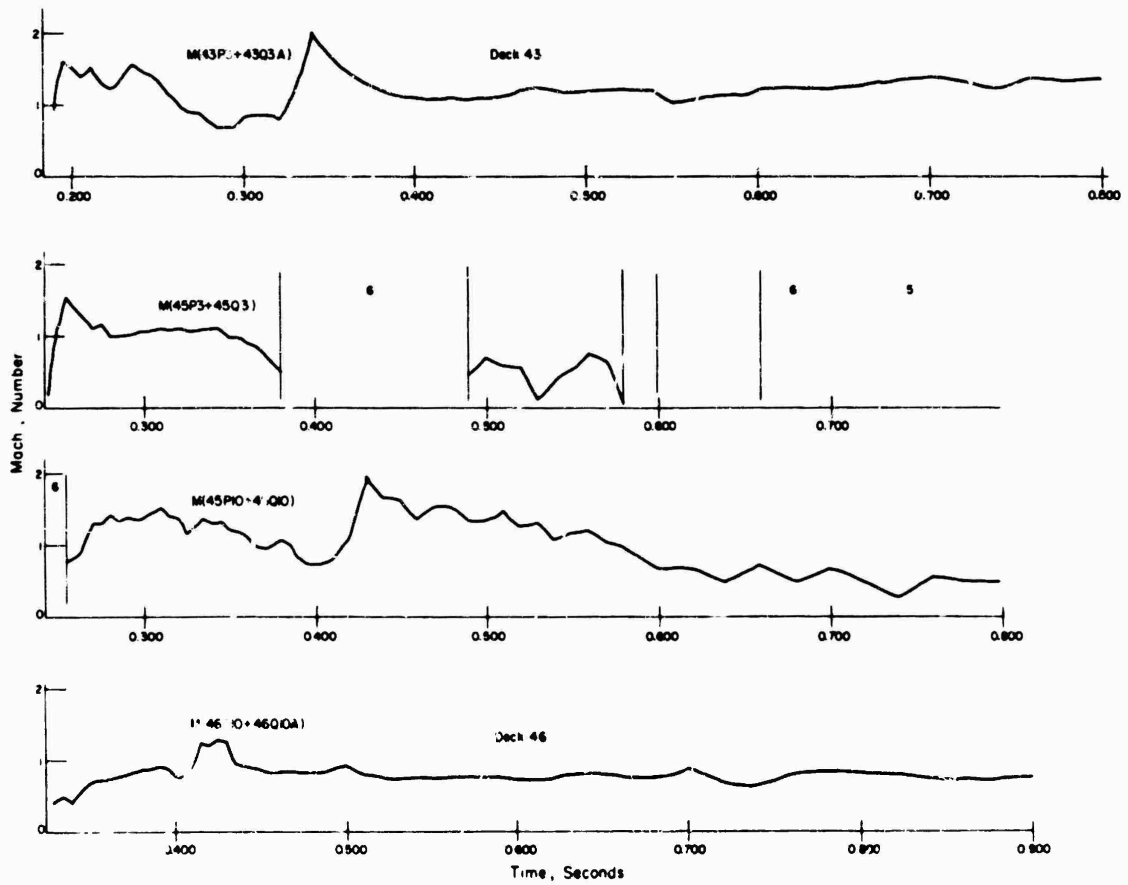


Mach number versus time, Teapot Shot MET, Water line.



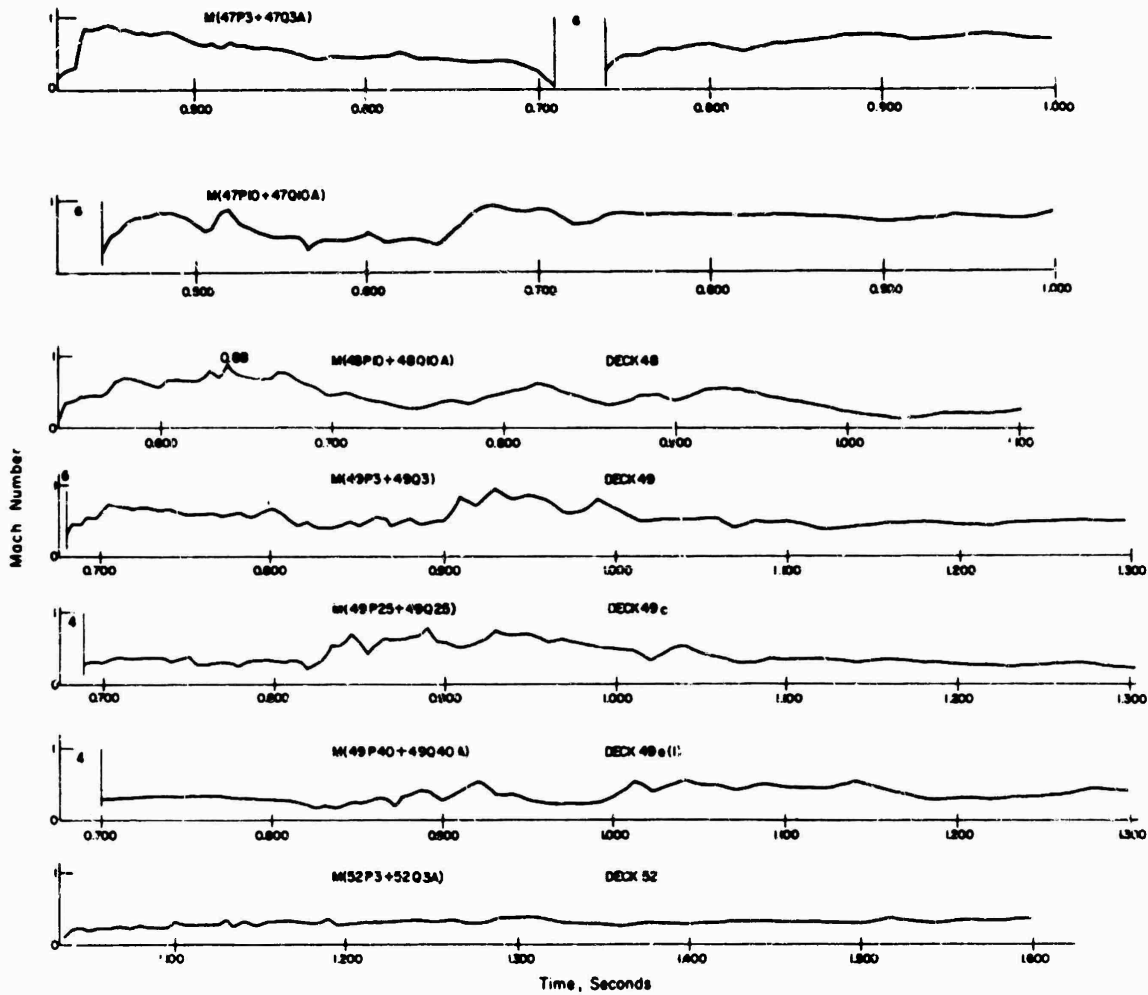


Mach number versus time, Teapot shot MET, Water line.

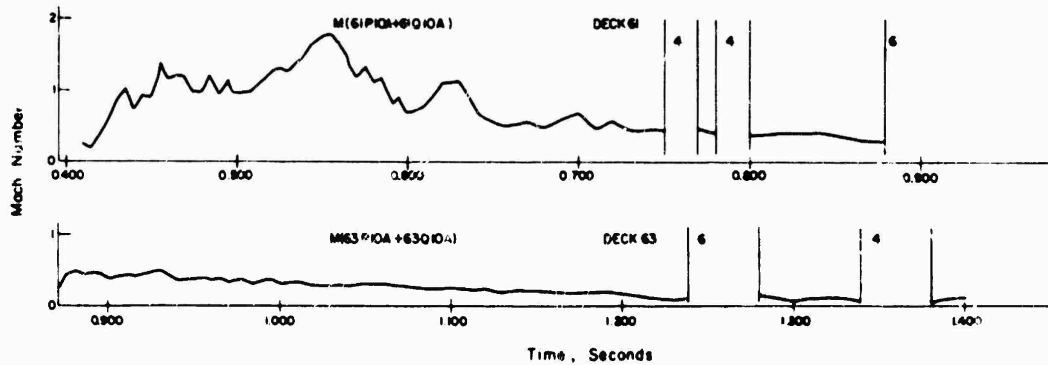


Mach number versus time, Teapot Shot MET, Asphalt line.



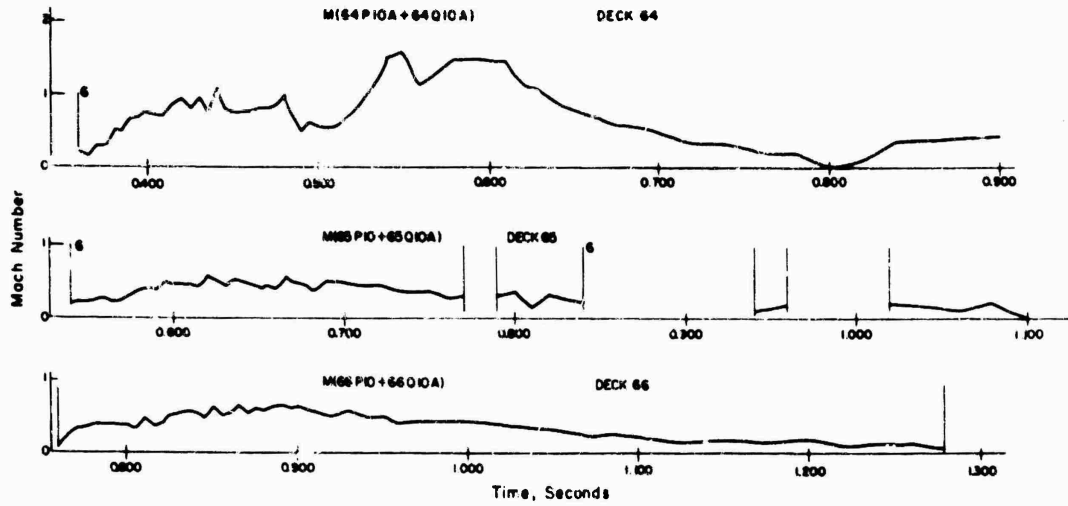


Mach number versus time, Teapot Shot MET, Asphalt line.

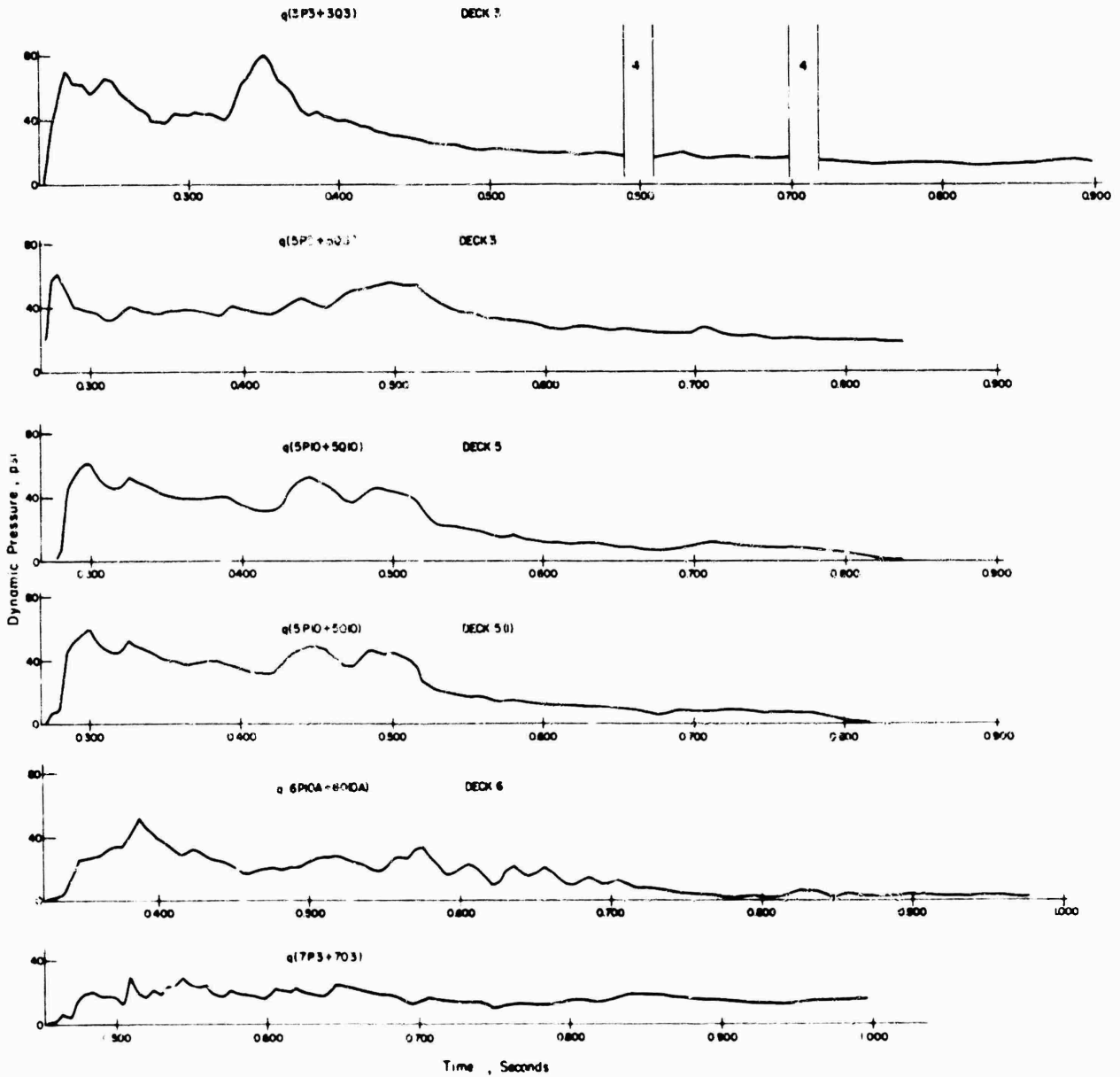


Mach number versus time, Teapot Shot BEE, Desert line.

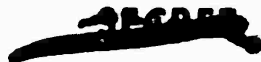


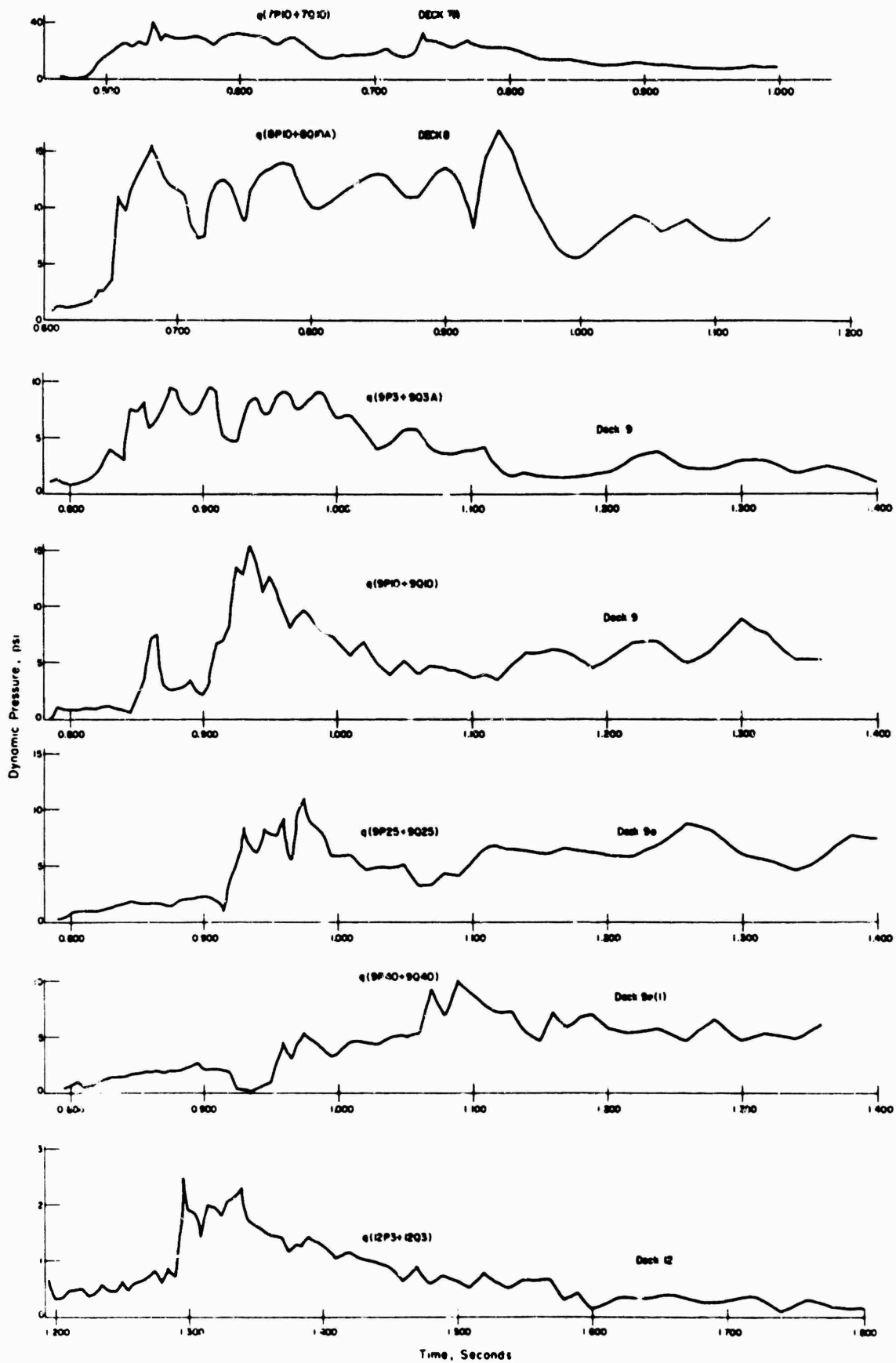


Mach number versus time, Teapot Shot BEE, Asphalt line.

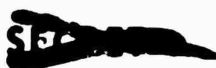


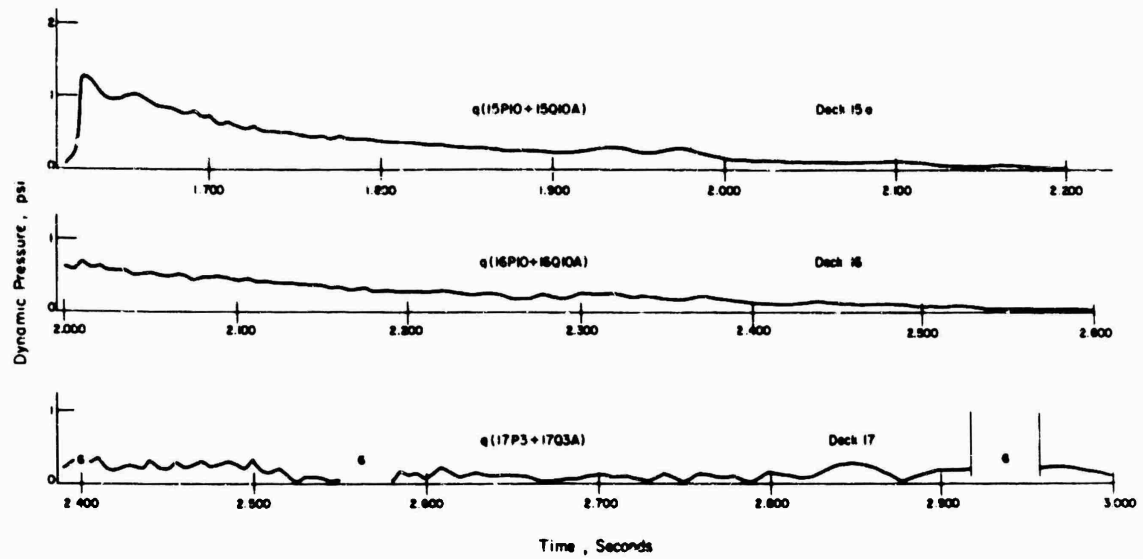
Dynamic pressure versus time, Teapot Shot MET, Desert line.



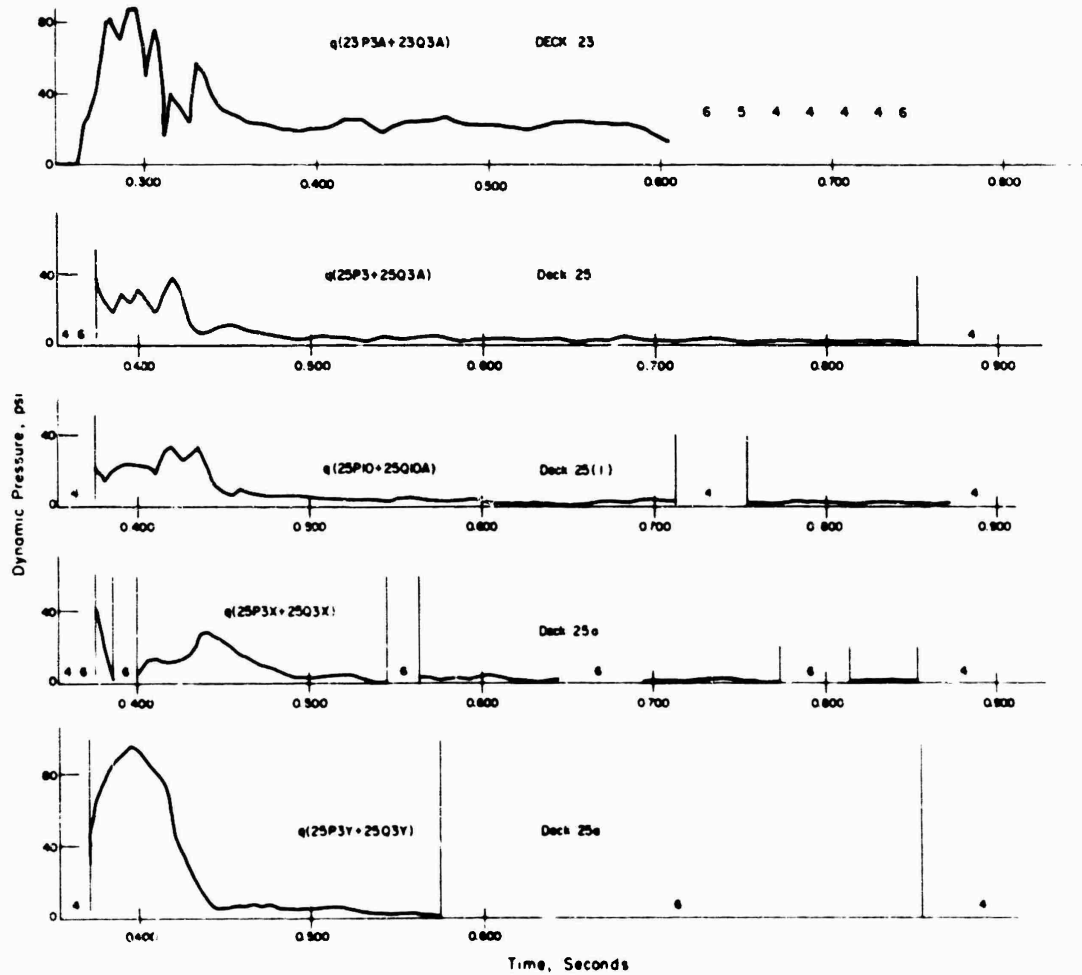


Dynamic pressure versus time, Teapot Shot MET, Desert line.

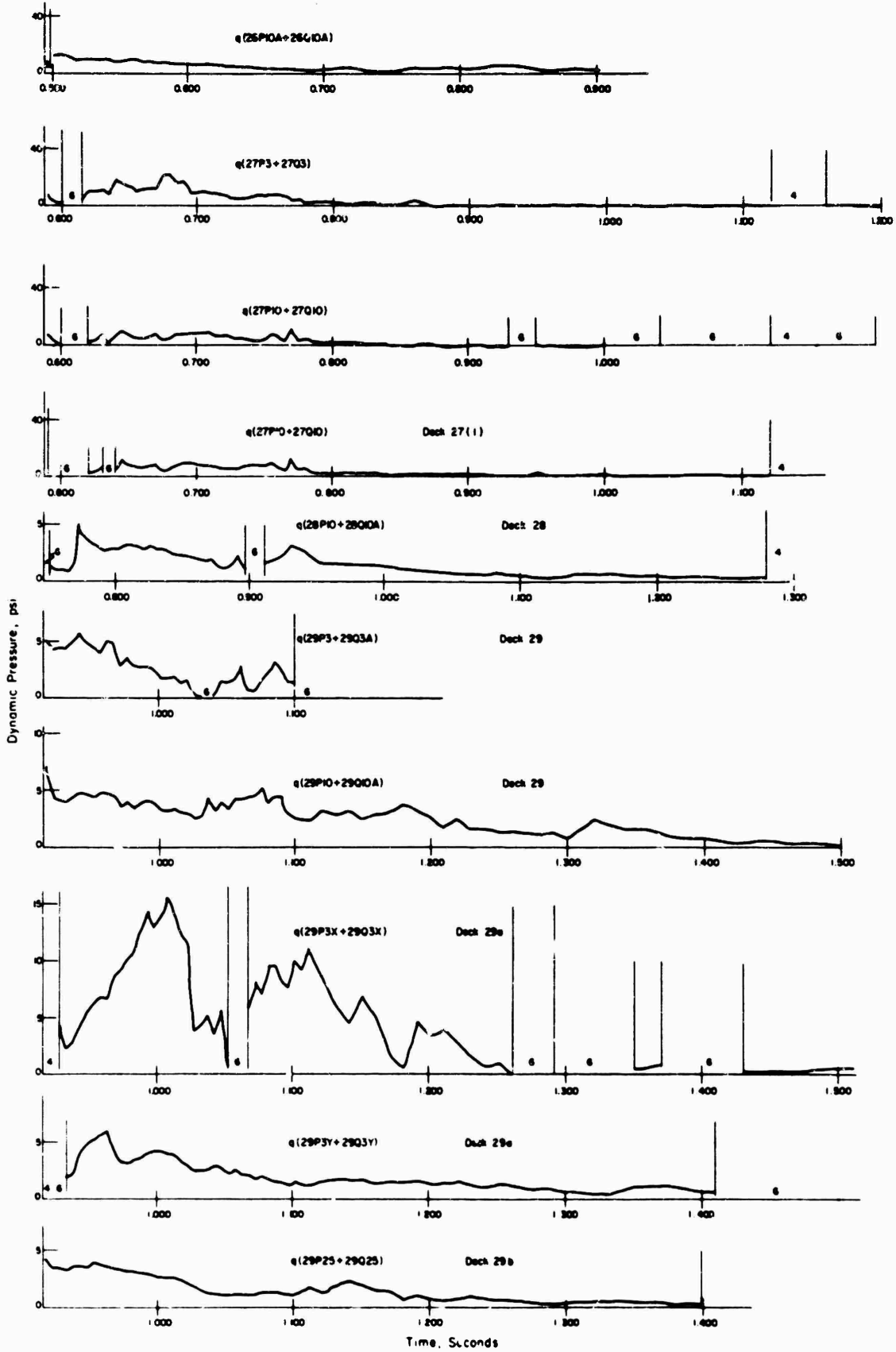




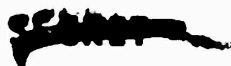
Dynamic pressure versus time, Teapot Shot MET, Desert line.

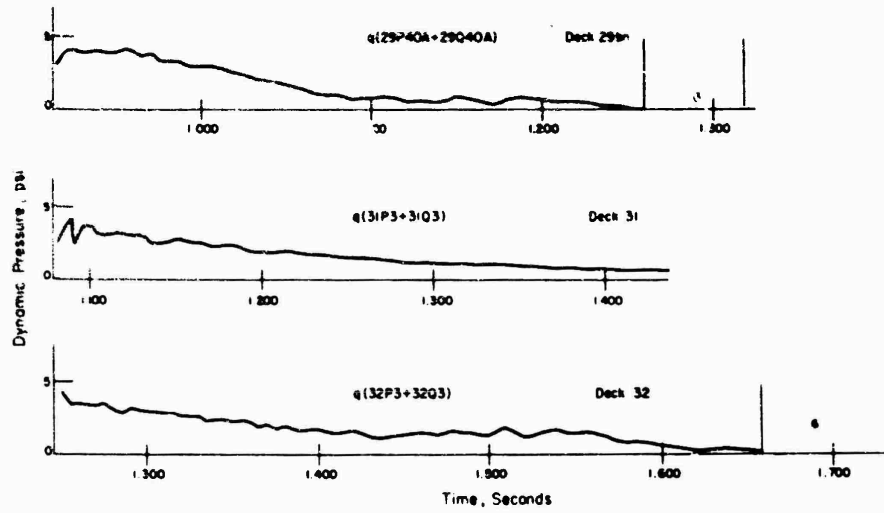


Dynamic pressure versus time, Teapot Shot MET, Water line.

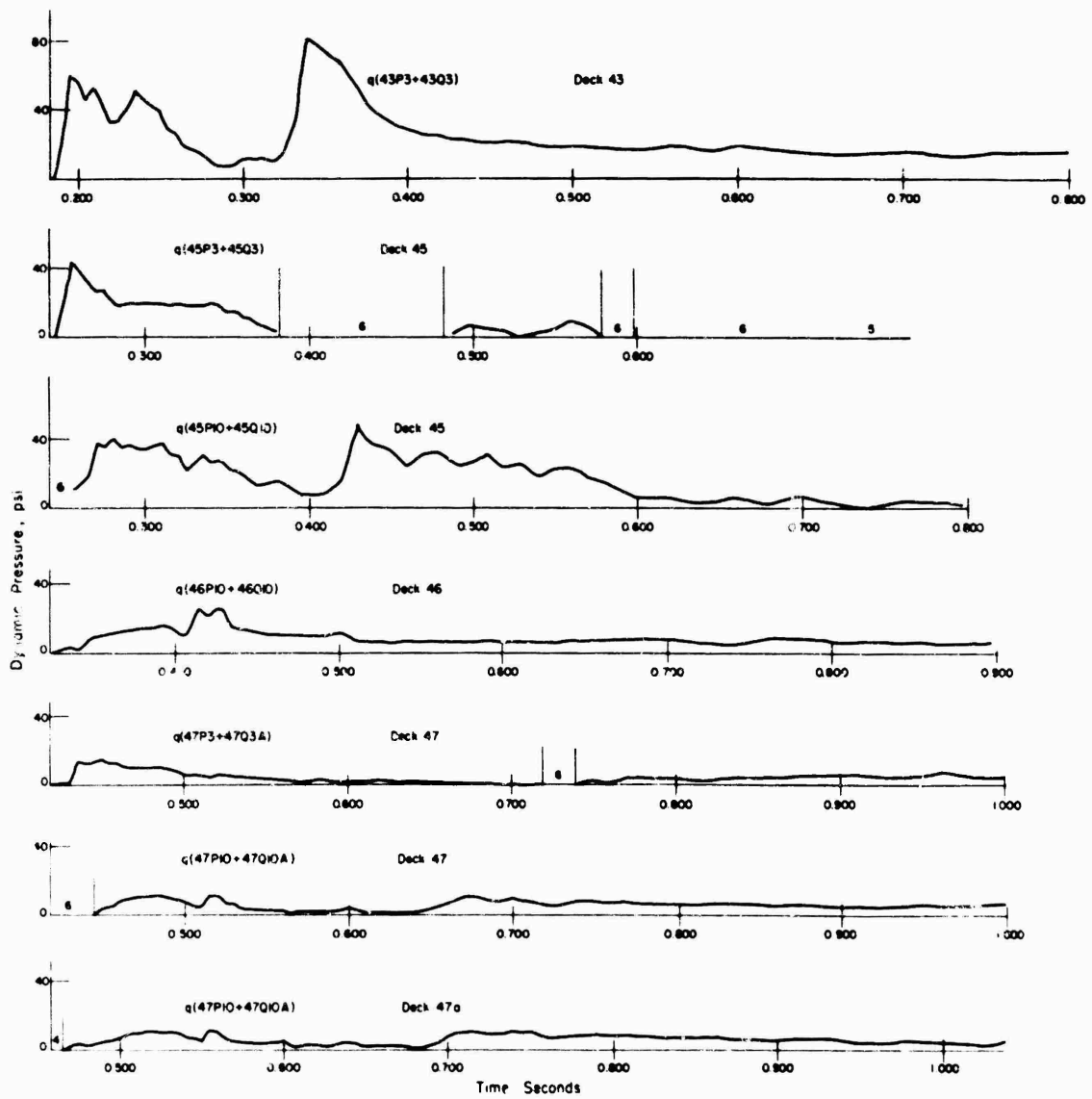


Dynamic pressure versus time, Teapot Shot MET, Water line.

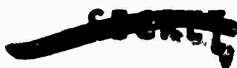


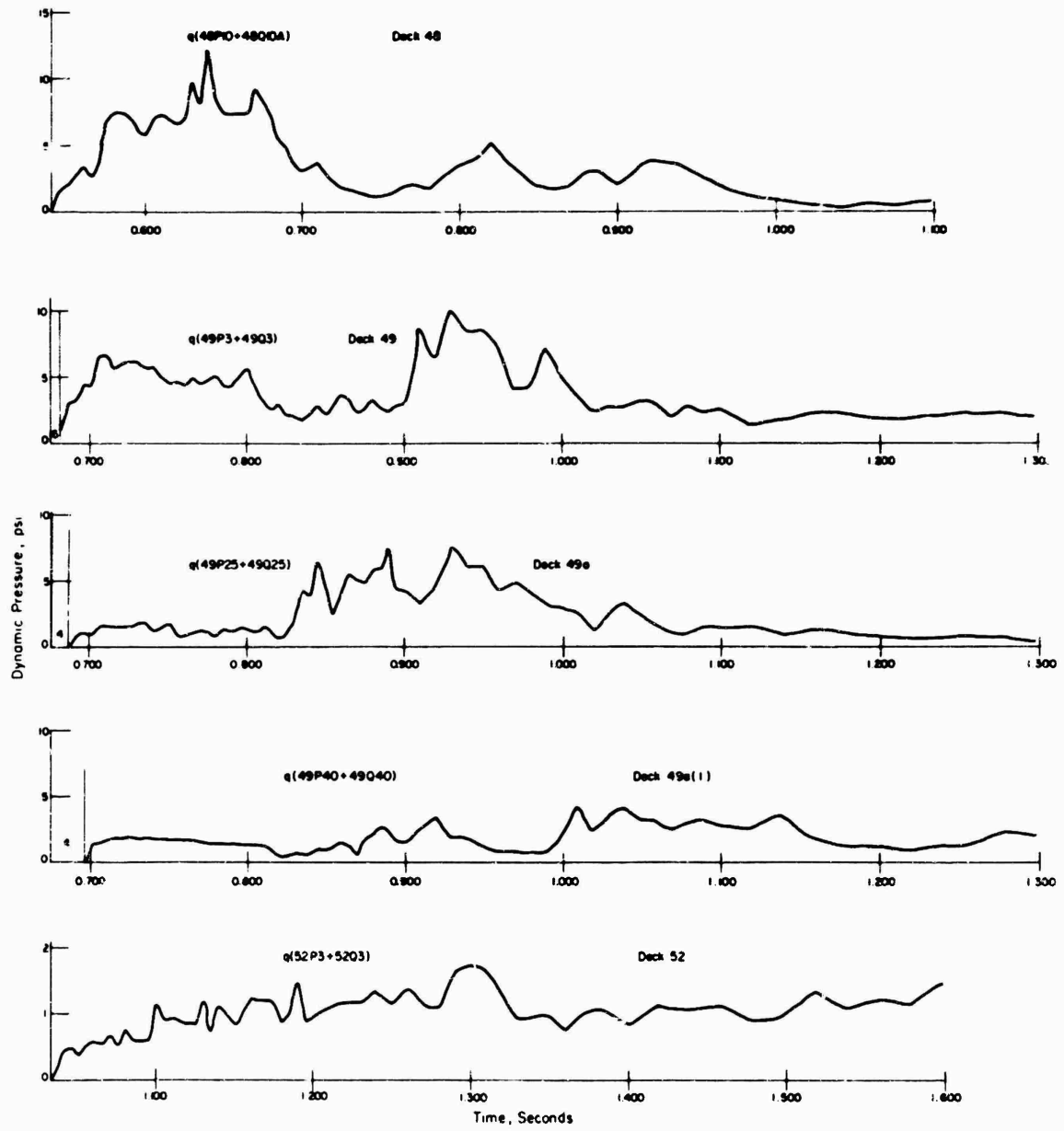


Dynamic pressure versus time, Teapot Shot MET, Water line.

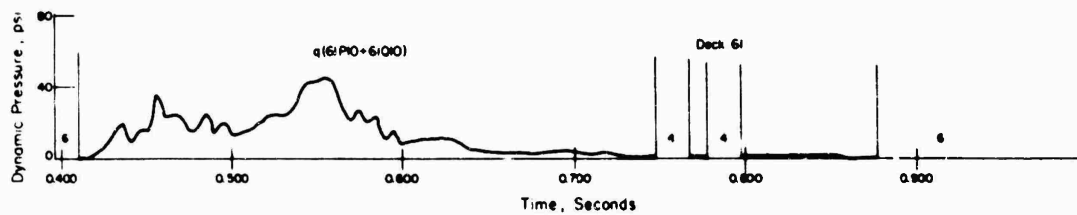


Dynamic pressure versus time, Teapot Shot MET, Asphalt line.

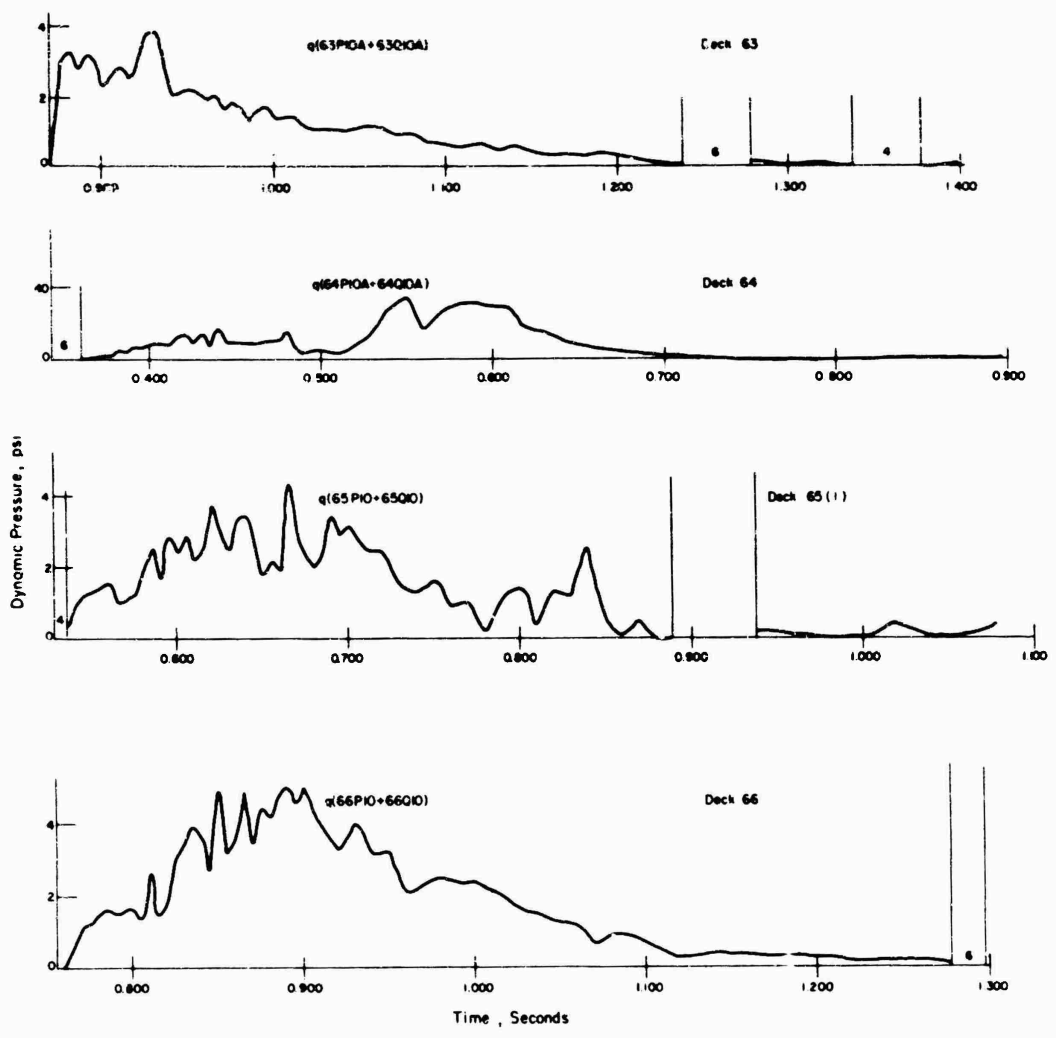




Dynamic pressure versus time, Teapot Shot MET, Asphalt line.



Dynamic pressure versus time, Teapot Shot BEE, Desert line.



Dynamic pressure versus time, Teapot Shot BEE, Asphalt line.

REFERENCES

1. Huntington K. Gilbert, Col., USAF, and Robert Q. Wilson, LCDR, USN; Final Report; Operation Buster, WT-412, July 1952; Armed Forces Special Weapons Project, Washington, D.C. Secret.
2. V. Salmon; "Air Pressure Versus Time"; Project 1.2, Operation Tumbler, WT-512, February 1953; Stanford Research Institute, Menlo Park, California; Secret Restricted Data.
3. L.M. Swift, and D.C. Sachs; "Air Pressure and Ground Shock Measurements"; Project 1.1b, Operation Upshot-Knothole, WT-711, January 1955; Stanford Research Institute, Menlo Park, California; Secret Formerly Restricted Data.
4. D.C. Sachs, L.M. Swift, and F.M. Sauer; "Airblast Overpressure and Dynamic Pressure Over Various Surfaces"; Project 1.10, Operation Teapot, WT-1109, September 1957; Stanford Research Institute, Menlo Park, California; Secret Formerly Restricted Data.
5. H.L. Brode; "Numerical Solution of Spherical Blast Waves"; Journal of Applied Physics, 26, 766, June 1955; Unclassified.
6. L.A. Schmidt, and F.B. Porzel; "Surface Effects on Blast Loading"; draft manuscript, prepared by Armour Research Foundation for Air Force Special Weapons Center, Kirtland AFB, New Mexico.
7. J. Von Neumann, and R.D. Richtmyer; "A Method for the Numerical Calculation of Hydrodynamic Shocks"; Journal of Applied Physics, 21, 232 - 237, March 1950.
8. R.V. Hess; "Interaction of Moving Shocks and Hot Layers"; Langley Aeronautical Laboratory, NACA TN-4002, Washington, May 1957; Unclassified.
9. A.H. Shapiro; "The Dynamics and Thermodynamics of Compressible Fluid Flow"; The Ronald Press Company, 1953, New York.
10. J.R. Banister, and F.H. Shelton; "Special Measurements of Dynamic Pressure Versus Time and Distance"; Project 1.11, Operation Teapot, WT-1110, February 1958; Sandia Corporation, Albuquerque, New Mexico; Secret Formerly Restricted Data.
11. C.D. Broyles; "Dynamic Pressures Versus Time and Supporting Air Blast Measurements"; Project 1.1d, Operation Upshot-Knothole, WT-714, February 1954; Sandia Corporation, Albuquerque, New Mexico; Secret Formerly Restricted Data.
12. J.L. Doussard, and A.H. Shapiro; "A Deceleration Probe for Measuring Stagnation Pressure and Velocity of a Particle-Laden Gas Stream"; report submitted under Office of Naval Research Contract N5 ori-07878, May 1955; Unclassified.
13. C.N. Kingery, C.H. Hoover, and J.H. Keefer; "Ground Surface Air-Blast Pressure Versus Distance"; Project 1.1, Operation Redwing, WT-1301, May 1960; Ballistic Research Laboratory, Aberdeen Proving Ground, Maryland; Secret Restricted Data.
14. P.A. Giragosian; "Wind Tunnel Calibration of a Pitot Static Probe, with Field Support Stand, in Pitch and Yaw Planes"; Report No. AA-949-W-1, January 1955; Cornell Aeronautical Laboratory; Official Use Only.
15. "Measuring Military Effects of Nuclear Weapons: A Manual for the Conduct of Full-Scale Field Tests"; prepared by Stanford Research Institute, Menlo Park, California, for Field Com-

mand, Armed Forces Special Weapons Project. Sandia Base, Albuquerque, New Mexico, December 1958; Official Use Only.

16. J. R. Kelso, editor; "Data Reduction Procedures for Nuclear Air-Blast Instrumentation"; AFSWP 1084, 15 April 1959; Secret Formerly Restricted Data.

17. W. Gracey; "Wind Tunnel Investigation of a Number of Total-Pressure Tubes at High Angles of Attack, Subsonic, Transonic, and Supersonic Speeds"; NACA TN-3641, May 1956; Unclassified.

18. E. W. Perkins, and D. M. Kuehn; "Comparison of the Experimental and Theoretical Distributions of Lift on a Spherically Inclined Body of Revolution at $M = 2$ "; NACA TN-3715, May 1956; Unclassified.

19. F. B. Hildebrand; "Introduction to Numerical Analysis"; McGraw-Hill Book Company, Inc., 1956; New York, New York.

20. "Summary Report of the Technical Director"; Operation Upshot-Knothole, WT-782, March 1955; Headquarters, Field Command, Armed Forces Special Weapons Project, Sandia Base, Albuquerque, New Mexico; Secret Restricted Data.

21. E. Glasstone, (editor), "The Effects of Nuclear Weapons"; Government Printing Office, 1958; Washington, D. C.

22. L. J. Vortman; "Effects of a Nonideal Shock Wave on Blast Loading of a Structure"; Project 34.1, Operation Plumbbob, ITR-1472, August 1957; Sandia Corporation, Albuquerque, New Mexico; Confidential Formerly Restricted Data.

23. J. W. Wistor and W. R. Perret; "Ground Motion Studies at High Incident Overpressure"; Project 1.5, Operation Plumbbob, ITR-1405, October 1957, Sandia Corporation, Albuquerque, New Mexico; Confidential Formerly Restricted Data.

24. W. E. Morris, J. Petes, E. R. Walthall, and F. J. Oliver; "Air Blast Measurements"; Projects 1.1a and 1.2, Operation Upshot-Knothole, WT-710, August 1954; Naval Ordnance Laboratory, White Oak, Silver Spring, Maryland; Secret Formerly Restricted Data.

25. J. R. Kelso, editor; "Proceedings on Air Blast Phenomena"; AFSWP-898, February 1957; Secret Formerly Restricted Data.

DISTRIBUTION

Military Distribution Category 12

ARMY ACTIVITIES

- 1 Deputy Chief of Staff for Military Operations, D/A, Washington 25, D.C. ATTN: Dir. of SW&R
- 2 Chief of Research and Development, D/A, Washington 25, D.C. ATTN: Atomic Div.
- 3 Assistant Chief of Staff, Intelligence, D/A, Washington 25, D.C.
- 4 Chief of Engineers, D/A, Washington 25, D.C. ATTN: ENGENB
- 5 Chief of Engineers, D/A, Washington 25, D.C. ATTN: ENGENB
- 6 Chief of Engineers, D/A, Washington 25, D.C. ATTN: ENGTB
- 7- 8 Office, Chief of Ordnance, D/A, Washington 25, D.C. ATTN: ORDTN
- 9- 11 Commanding General, U.S. Continental Army Command, Ft. Monroe, Va.
- 12 Director of Special Weapons Development Office, Headquarters COMARC, Ft. Bliss, Tex. ATTN: Capt. Chester I. Peterson
- 13 President, U.S. Army Artillery Board, Ft. Sill, Okla.
- 14 President, U.S. Army Air Defense Board, Ft. Bliss, Tex.
- 15 Commandant, U.S. Army Command & General Staff College, Ft. Leavenworth, Kansas. ATTN: ARCHIVES
- 16 Commandant, U.S. Army Armored School, Ft. Knox, Ky.
- 17 Commandant, U.S. Army Artillery and Missile School, Ft. Sill, Okla. ATTN: Combat Development Department
- 18 Commandant, U.S. Army Aviation School, Ft. Rucker, Ala.
- 19 Commandant, U.S. Army Infantry School, Ft. Benning, Ga. ATTN: C.D.S.
- 20 Commandant, U.S. Army Ordnance School, Aberdeen Proving Ground, Md.
- 21 Commandant, U.S. Army Ordnance and Guided Missile School, Redstone Arsenal, Ala.
- 22 Commanding General, Chemical Corps Training Comd., Ft. McClellan, Ala.
- 23 Commanding General, The Engineer Center, Ft. Belvoir, Va. ATTN: Asst. Cndt, Engr. School
- 24 Director, Armed Forces Institute of Pathology, Walter Reed Army Med. Center, 625 16th St., NW, Washington 25, D.C.
- 25 Commanding Officer, U.S. Army Research Lab., Ft. Knox, Ky.
- 26 Commandant, Walter Reed Army Inst. of Res., Walter Reed Army Medical Center, Washington 25, D.C.
- 27- 28 Commanding General, QM R&D Comd., QM R&D Cntr., Natick, Mass. ATTN: CBR Liaison Officer
- 29- 30 Commanding Officer, Chemical Warfare Lab., Army Chemical Center, Md. ATTN: Tech. Library
- 31 Commanding General, Engineer Research and Dev. Lab., Ft. Belvoir, Va. ATTN: Chief, Tech. Support Branch
- 32 Director, Watervays Experiment Station, P.O. Box 631, Vicksburg, Miss. ATTN: Library
- 33 Commanding Officer, Picatinny Arsenal, Dover, N.J. ATTN: ORDBB-F
- 34 Commanding Officer, Diamond Ord. Fuze Labs., Washington 25, D.C. ATTN: Chief, Nuclear Vulnerability Br. (230)
- 35- 36 Commanding General, Aberdeen Proving Grounds, Md. ATTN: Director, Ballistics Research Laboratory
- 37 Commanding General, Frankford Arsenal, Bridge and Tacony St., Philadelphia, Pa.
- 38 Commanding Officer, Watervliet Arsenal, Watervliet, New York. ATTN: ORDBF-RR
- 39 Commander, Army Rocket and Guided Missile Agency, Redstone Arsenal, Ala. ATTN: Tech Library
- 40 Commanding General, White Sands Missile Range, N. Mex. ATTN: ORDBS-JM-FL
- 41 Commander, Army Ballistic Missile Agency, Redstone Arsenal, Ala. ATTN: ORDAB-HT
- 42 Commanding General, Ordnance Tank Automotive Command, Detroit Arsenal, Centerline, Mich. ATTN: O.KMC-RO
- 43 Commanding General Ordnance Weapons Command, Rock Island, Ill.

- 44 Commanding General, U.S. Army Electronic Proving Ground, Ft. Huachuca, Ariz. ATTN: Tech. Library
- 45 Commanding General, USA Combat Surveillance Agency, 1124 N. Highland St., Arlington, Va.
- 46 Director, Operations Research Office, Johns Hopkins University, 6935 Arlington Rd., Bethesda 14, Md.
- 47 Commanding General, U. S. OGD Special Weapons-Ammunition Command, Dover, N.J.
- 48 Commander-in-Chief, U.S. Army Europe, APO 403, New York, N.Y. ATTN: Opot. Div., Weapons Br.

NAVY ACTIVITIES

- 49- 50 Chief of Naval Operations, D/N, Washington 25, D.C. ATTN: OP-03EG
- 51 Chief of Naval Operations, D/N, Washington 25, D.C. ATTN: OP-75
- 52- 53 Chief of Naval Research, D/N, Washington 25, D.C. ATTN: Code 811
- 54- 56 Chief, Bureau of Naval Weapons, D/N, Washington 25, D.C. ATTN: BLI-3
- 57- 61 Chief, Bureau of Naval Weapons, D/N, Washington 25, D.C. ATTN: RAAD-25
- 62 Chief, Bureau of Ordnance, D/N, Washington 25, D.C.
- Chief, Bureau of Naval Weapons, D/N, Washington 25, D.C. ATTN: SP-45
- 63 Chief, Bureau of Ships, D/N, Washington 25, D.C. ATTN: Code 423
- 64 Chief, Bureau of Yards and Docks, D/N, Washington 25, D.C. ATTN: D-440
- 65 Director, U.S. Naval Research Laboratory, Washington 25, D.C. ATTN: Mrs. Katherine H. Cass
- 66- 67 Commander, U.S. Naval Ordnance Laboratory, White Oak, Silver Spring 19, Md.
- 68 Director, Material Lab. (Code 900), New York Naval Shipyard, Brooklyn 1, N.Y.
- 69 Commanding Officer and Director, Navy Electronics Laboratory, San Diego 52, Calif.
- 70 Commanding Officer, U.S. Naval Mine Defense Lab., Panama City, Fla.
- 71- 72 Commanding Officer, U.S. Naval Radiological Defense Laboratory, San Francisco, Calif. ATTN: Tech. Info. Div.
- 73- 74 Commanding Officer and Director, U.S. Naval Civil Engineering Laboratory, Port Huenece, Calif. ATTN: Code L31
- 75 Commanding Officer, U.S. Naval Schools Command, U.S. Naval Station, Treasure Island, San Francisco, Calif.
- 76 Superintendent, U.S. Naval Postgraduate School, Monterey, Calif.
- 77 Commanding Officer, U.S. Fleet Sonar School, U.S. Naval Base, Key West, Fla.
- 78 Commanding Officer, U.S. Fleet Sonar School, San Diego 47, Calif.
- 79 Officer-in-Charge, U.S. Naval School, CEC Officers, U.S. Naval Construction Bn. Center, Port Huenece, Calif.
- 80 Commanding Officer, Nuclear Weapons Training Center, Atlantic, U.S. Naval Base, Norfolk 11, Va. ATTN: Nuclear Warfare Dept.
- 81 Commanding Officer, Nuclear Weapons Training Center, Pacific, Naval Station, San Diego, Calif.
- 82 Commanding Officer, U.S. Naval Damage Control Tng. Center, Naval Base, Philadelphia 12, Pa. ATTN: ABC Defense Course
- 83 Commanding Officer, Air Development Squadron 5, VX-5, China Lake, Calif.
- 84 Commanding Officer, Naval Air Material Center, Philadelphia 12, Pa. ATTN: Technical Data Br.
- 85 Commanding Officer, U.S. Naval Air Development Center, Johnsville, Pa. ATTN: NAS, Librarian

UNCLASSIFIED

66 Commanding Officer, U.S. Naval Medical Research Institute, National Naval Medical Center, Bethesda, Md. 136-137 Director, USAF Project RAND, VIA: USAF Liaison Office, The RAND Corp., 1700 Main St., Santa Monica, Calif.

87- 88 Commanding Officer and Director, David W. Taylor Model Basin, Washington 7, D.C. ATTN: Library 138 Commander, Rome Air Development Center, AMDC, Griffiss AFB, N.Y. ATTN: Documents Library, BCSEL-1

89 Commanding Officer and Director, U.S. Naval Engineering Experiment Station, Annapolis, Md. 139 Commander, Air Technical Intelligence Center, USAF, Wright-Patterson AFB, Ohio. ATTN: AFCIN-4Bla, Library

90 Commander, Norfolk Naval Shipyard, Portsmouth, Va. ATTN: Underwater Explosions Research Division 140 Assistant Chief of Staff, Intelligence, HQ. USAF, APO 633, New York, N.Y. ATTN: Directorate of Air Targets

91 Commandant, U.S. Marine Corps, Washington 25, D.C. ATTN: Code AO3E 141 Commander-in-Chief, Pacific Air Forces, APO 953, San Francisco, Calif. ATTN: PFCIE-MB, Base Recovery

9. Director, Marine Corps Landing Force, Development Center, MGS, Quantico, Va.

93 Commanding Officer, U.S. Naval CIC School, U.S. Naval Air Station, Glynco, Brunswick, Ga.

94-101 Chief, Bureau of Naval Weapons, Navy Department, Washington 25, D.C. ATTN: RR12

AIR FORCE ACTIVITIES

102 Hq. USAF, ATTN: Operations Analysis Office, Office, Vice Chief of Staff, Washington 25, D. C.

103 Director of Civil Engineering, HQ. USAF, Washington 25, D.C. ATTN: APOCE

104-114 Air Force Intelligence Center, Hq. USAF, ACS/I (AFCIN-3V1) Washington 25, D.C.

115 Director of Research and Development, DCS/D, Hq. USAF, Washington 25, D.C. ATTN: Guidance and Weapons Div.

116 The Surgeon General, Hq. USAF, Washington 25, D.C. ATTN: Bio.-Def. Pre. Med. Division

117 Commander, Tactical Air Command, Langley AFB, Va. ATTN: Doc. Security Branch

118 Commander, Air Defense Command, Fnt AFB, Colorado. ATTN: Assistant for Atomic Energy, ADLDC-A

119 Commander, Hq. Air Research and Development Command, Andrews AFB, Washington 25, D.C. ATTN: RDRWA

120 Commander, Air Force Ballistic Missile Div. Hq. AMDC, Air Force Unit Post Office, Los Angeles 45, Calif. ATTN: WRSOT

121-122 Commander, AF Cambridge Research Center, L. G. Hanscom Field, Bedford, Mass. ATTN: CRQST-2

123-127 Commander, Air Force Special Weapons Center, Kirtland AFB, Albuquerque, N. Mex. ATTN: Tech. Info. & Intel. Div.

128-129 Director, Air University Library, Maxwell AFB, Ala.

130 Commander, Lowry Technical Training Center (TW), Lowry AFB, Denver, Colorado.

131 Commandant, School of Aviation Medicine, USAF, Aerospace Medical Center (AFC), Brooks Air Force Base, Tex. ATTN: Col. Gerritt L. Hekhuis

132 Commander, 1009th Sp. Wpns. Squadron, Hq. USAF, Washington 25, D.C.

133-135 Commander, Wright Air Development Center, Wright-Patterson AFB, Dayton, Ohio. ATTN: WCACT (For WCOSI)

142 Director of Defense Research and Engineering, Washington 25, D.C. ATTN: Tech. Library

143 Chairman, Armed Services Explosives Safety Board, DOD, Building T-7, Gravelly Point, Washington 25, D.C.

144 Director, Weapons Systems Evaluation Group, Room 1E880, The Pentagon, Washington 25, D.C.

145-148 Chief, Defense Atomic Support Agency, Washington 25, D.C. ATTN: Document Library

149 Commander, Field Command, DASA, Sandia Base, Albuquerque, N. Mex.

150 Commander, Field Command, DASA, Sandia Base, Albuquerque, N. Mex. ATTN: FCTO

151-152 Commander, Field Command, DASA, Sandia Base, Albuquerque, N. Mex. ATTN: FCWT

153 Commander, JTF-7, Arlington Hall Station, Arlington 12, Va.

154 Administrator, National Aeronautics and Space Administration, 1520 "H" St., N.W., Washington 25, D.C. ATTN: Mr. R. V. Rhode

155 Commander-in-Chief, Strategic Air Command, Offutt AFB, Neb. ATTN: OANS

156 U.S. Documents Officer, Office of the United States National Military Representative - SRAPE, APO 55, New York, N.Y.

OTHER DEPARTMENT OF DEFENSE ACTIVITIES

ATOMIC ENERGY COMMISSION ACTIVITIES

157-159 U.S. Atomic Energy Commission, Technical Library, Washington 25, D.C. ATTN: For DMA

160-161 Los Alamos Scientific Laboratory, Report Library, P.O. Box 1663, Los Alamos, N. Mex. ATTN: Helen Redman

162-166 Sandia Corporation, Classified Document Division, Sandia Base, Albuquerque, N. Mex. ATTN: H. J. Smyth, Jr.

167-176 University of California Lawrence Radiation Laboratory, P.O. Box 808, Livermore, Calif. ATTN: Clovis J. Craig

177 Weapon Data Section, Office of Technical Information Extension, Oak Ridge, Tenn.

178-210 Office of Technical Information Extension, Oak Ridge, Tenn. (Surplus)

UNCLASSIFIED

UNCLASSIFIED DATA